Czech Technical University
in Prague

Faculty of Nuclear Sciences and Physical
Engineering

Department of Physics

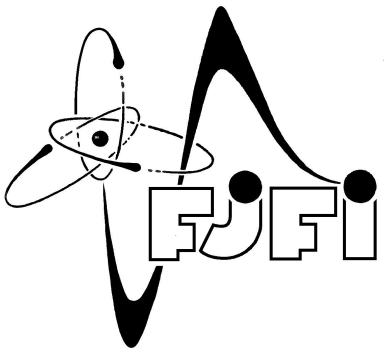

Ph.D. THESIS

Study of Antihadron Interactions with the Nuclear Medium

Ing. Jaroslava Hrtánková

Prague, 2017

Supervisor: RNDr. Jiří Mareš, CSc.

České vysoké učení technické
v Praze

Fakulta jaderná a fyzikálně inženýrská

Katedra fyziky

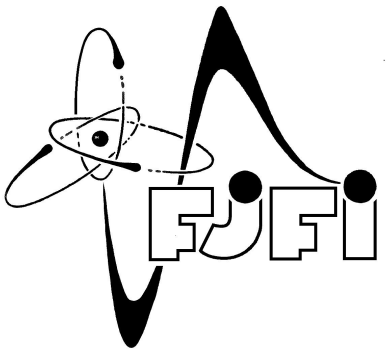

DIZERTAČNÁ PRÁCA

Štúdium interakcií antihadrónov s jadrovým prostredím

Ing. Jaroslava Hrtánková

Praha, 2017

Školiteľ: RNDr. Jiří Mareš, CSc.

Bibliographic entry

Author:	Ing. Jaroslava Hrtánková Czech Technical University in Prague Faculty of Nuclear Sciences and Physical Engineering Department of Physics
Thesis title:	Study of Antihadron Interactions with the Nuclear Medium
Kind of thesis:	Ph.D. thesis
Degree program	Application of Natural Sciences
Branch of study:	Nuclear Engineering
Supervisor:	RNDr. Jiří Mareš, CSc. Nuclear Physics Institute of the CAS Department of Theoretical Physics
Academic year:	2017/2018
Number of pages:	166
Keywords:	antihadron, interaction, nucleus, absorption, bound state

Bibliografický záznam

Autor:	Ing. Jaroslava Hrtánková České vysoké učení technické v Praze Fakulta jaderná a fyzikálně inženýrská Katedra fyziky
Názov práce:	Štúdium interakcií antihadrónov s jadrovým prostredím
Druh práce:	dizertačná práca
Študijný program:	Aplikácia prírodných vied
Obor štúdia:	Jadrové inžinierstvo
Školiteľ:	RNDr. Jiří Mareš, CSc. Ústav jaderné fyziky AV ČR, v. v. i. Oddelenie teoretickej fyziky
Akademický rok:	2017/2018
Počet strán:	166
Kľúčové slová:	antihadrón, interakcia, jadro, absorpcia, viazaný stav

Abstract

This thesis deals with the study of interactions of antihadrons ($\bar{H}$) with atomic nuclei. Nuclei are described within the framework of the Relativistic Mean-Field model and the antihadron–nucleus interactions are represented either by a phenomenological complex optical potential or by an optical potential constructed from microscopic models of antihadron–nucleon interactions. We explored the possibility of the existence of $\bar{H}$-nuclear quasi-bound states. We performed self-consistent calculations of the antiproton $\bar{p}$, antikaon K^-, and antihyperons $\bar{\Lambda}$, $\bar{\Sigma}$, $\bar{\Xi}$ bound states in selected nuclei. We found that all antihadrons feel a fairly attractive potential inside a nucleus. In the case of $\bar{p}$ and K^-, we took into account their strong absorption in the nuclear medium as well. We considered all possible effects which could lead to relatively long $\bar{p}$ and K^- lifetimes in the medium, including energy dependence of the optical potential and phase space suppression for the decay products. However, our self-consistent calculations revealed that the $\bar{p}$- and K^--nuclear quasi-bound states, if they ever exist, have sizable widths, comparable with or larger than their binding energies. This finding disproves the conjectures about the existence of narrow $\bar{p}$ and K^- bound states in many-body nuclear systems and disfavors their experimental observation.

Abstrakt

Táto práca sa zaoberá štúdiom interakcií antihadrónov ($\bar{H}$) s atómovými jadrami. Jadrá popisujeme v rámci relativistickej teórie stredných polí a antihadrón–jadrové interakcie sú sprostredkované buď prostredníctvom fenomenologického optického potenciálu alebo optickým potenciálom konštruovaným z mikroskopických modelov antihadrón–nukleónových interakcií. Skúmali sme hlavne možnosť existencie kvazivazaných stavov $\bar{H}$ v jadrách. Previedli sme selfkonzistentné výpočty viazaných stavov antiprotónu $\bar{p}$, antikaónu K^-, a antihyperónov $\bar{\Lambda}$, $\bar{\Sigma}$, $\bar{\Xi}$ vo vybraných atómových jadrách. Behom našich výpočtov sme zistili, že všetky uvažované antihadróny cítia vo vnútri jadra značne príťažlivý potenciál. V prípade $\bar{p}$ a K^- sme zahrnuli aj ich silnú absorpciu v jadrovom prostredí. Vzali sme do úvahy všetky možné efekty, ktoré by mohli viesť k relatívne dlhej dobe života $\bar{p}$ a K^- v jadrovom prostredí, ako je energetická závislosť optického potenciálu a potlačenie fázového priestoru pre rozpadové produkty. Avšak naše selfkonzistentné výpočty odhalili, že $\bar{p}$ a K^- kvazivazané stavy v jadrách, pokiaľ vôbec existujú, majú značné šírky, ktoré sú porovnateľné alebo väčšie ako ich väzbové enegie. Toto zistenie vyvracia domnienky o možnej existencii úzkych viazaných stavoch $\bar{p}$ a K^- v jadrových mnohočasticových systémoch a je tak nepriaznivé pre ich pozorovanie v experimentoch.

Prehlásenie

Prehlasujem, že som svoju dizertačnú prácu vypracovala samostatne a použila som iba podklady (literatúru, projekty, SW atd.) uvedené v priloženom zozname. Táto práca obsahuje výsledky výskumu uskutočneného v Ústavu jaderné fyziky Akademie věd České republiky, v. v. i. Pokiaľ nie je uvedená explicitná referencia, je dizertácia založená iba na originálnych článkoch autorky.

Nemám závažný dôvod proti použitiu tohto školského diela v zmysle zákona §60 Zákona č.121/2000 Sb., o práve autorskom, o právach súvisiacich s právom autorským a o zmene niektorých zákonov (autorský zákon).

Declaration

I declare that I wrote my Ph.D. thesis independently and exclusively within the use of cited bibliography. This thesis contains results of research conducted at Nuclear Physics Institute of the Czech Academy of Sciences. Unless an explicit reference is given, the thesis is based solely on the published papers of the author.

I agree with the usage of this thesis in the purport of the Act 121/2000 (Copyright Act).

V Prahe dňa .....

.....

Jaroslava Hrtánková

Acknowledgement

I wish to express my gratitude to my supervisor, Dr. Jiří Mareš, for his guidance, assistance and inspiring discussions throughout my whole Ph.D. study. I would also like to thank our collaborators, Prof. Eli Friedman and Prof. Avraham Gal, for useful comments and discussions with them and their hospitality during our stays in Jerusalem. Last but not least, I want to thank my family for their endless support and love during my study at the university.

Contents

Preface

This thesis is devoted to the study of interactions of antihadrons, namely the antiproton $\bar{p}$, antihyperons $\bar{\Lambda}$, $\bar{\Sigma}$, $\bar{\Xi}$, and the antikaon K^-, with atomic nuclei. It is a topical issue which provides us with information about the behavior of the antihadron $\bar{H}$ in the nuclear medium, such as its absorption and in-medium modifications. It may serve as a test of models of (anti)hadron–hadron interactions as well as models for nuclear structure calculations. Moreover, it may give us information about symmetries in nature, e.g., spin symmetry, G-parity ($\bar{p}$), chiral symmetry (K^-), and charge symmetry (hyperons in nuclei). Interactions between (anti)hadrons and nucleon(s) have been object of increased interest in recent years. Many scientific papers have been written about this issue and numerous international conferences have been held (e.g., HYP2015, LEAP2016, MESON2016, HADRON2017, EXA2017).

The thesis is organized as follows: In Chapter 1, an introduction to the topic is given, including physical motivation and an overview of the current status of the theoretical and experimental research in this field of physics. Chapter 2 contains a detailed description of the methodology used in this work: the Relativistic Mean-Field model for nuclear structure calculations and the applied $\bar{H}N$ interaction models. The values of parameters for various RMF models used in our calculations are given in Appendix A. A selection of the most important results of the study is presented in Chapter 3. First, we focus on the antibaryon (antihyperons and antiproton) behavior inside a nucleus without considering its absorption in the medium. We explore the dynamical response of the nuclear core to the extra antibaryon and discuss model dependence of the calculations. Then, we present results of the study of the antiproton–nucleus quasi-bound states in various nuclei using a phenomenological as well as microscopic optical potential, including the $\bar{p}$ annihilation in the nuclear medium. We consider all possible in-medium effects which could modify the $\bar{p}$ lifetime in nuclei. We evaluate the corresponding $\bar{p}$ widths self-consistently. Finally, we study the antikaon–nucleus quasi-bound states using an optical potential

derived from state-of-the-art meson–baryon interaction models. We compare the predictions for K^- binding energies and widths in all models considered and evaluate the effect of K^- multinucleon interactions on calculated observables. The results presented in this chapter represent highlights of our study; more results including detailed discussion can be found in our publications which are attached in Appendix B for completeness. A summary of the main findings and accomplishments of this work is given in Chapter 4, followed by an outlook on further advancement and future research.

Chapter 1

Introduction

The study of interactions of (anti)hadrons with nucleons and the nuclear medium at low and intermediate energies plays an important role in contemporary physics since it extends our knowledge of the basic laws and symmetries in nature. It allows, in principle, to establish connection between phenomena observed in (anti)hadronic reactions and underlying dynamics of QCD, the fundamental theory of strong interactions. The study of (anti)hadron interactions with the medium has not only implications for hadron and nuclear physics (including heavy-ion collisions) but also for astrophysics. In this chapter, we give a brief overview of the physics of antiprotons, antikaons and antihyperons, and their interactions with the nuclear medium at low energies.

1.1 Antiproton

The antiproton, the antiparticle of the proton, was discovered by Segré and Chamberlain at the Bevatron accelerator at Berkeley in 1955 [1] (see Fig. 1.1). Its observation supported the famous Dirac theory about existence of antiparticles. Since then the $\bar{p}$–nucleon and $\bar{p}$–nucleus interactions have been widely studied in many experiments. In the 1960's, the $\bar{p}$ annihilation was explored by stopping antiprotons in hydrogen- and deuterium-filled bubble chambers at Brookhaven National Laboratory (BNL) and CERN [2]. With the advent of the LEAR facility at CERN, which provided a high quality antiproton beam in the 80's, many dedicated experiments with $\bar{p}$ beams were performed [3]. The $\bar{p}$ elastic and inelastic scattering off nuclei and proton knock-out reactions were analyzed in order to get more information about the $\bar{p}$–nucleus potential. The measurements of the differential cross-section for the 48.6 MeV antiprotons scattered elastically off ^{12}C in the

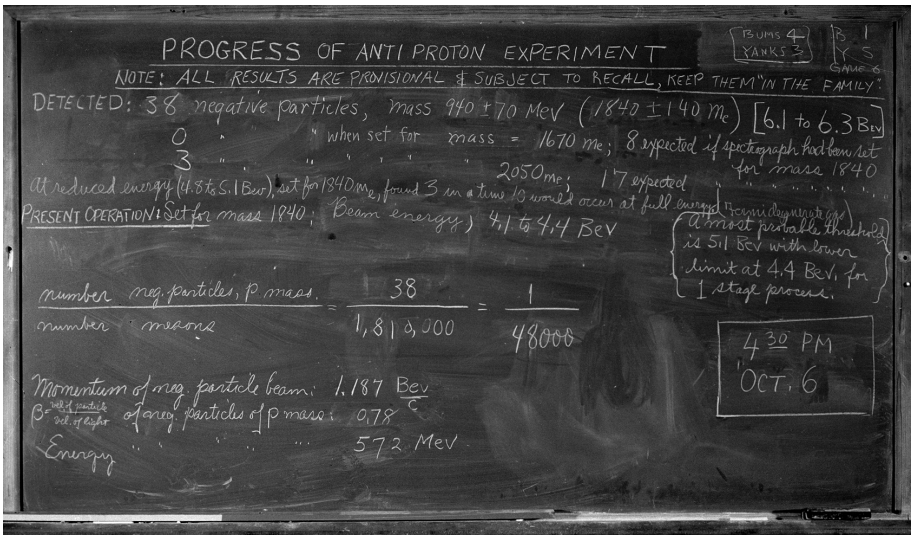

Figure 1.1: Antiproton discovery at Berkeley National Laboratory. Figure adapted from Ref. [5].

PS184 experiment [4] were in favor of an optical potential $V_{\rm opt}$ with a shallow attractive Re$V_{\rm opt}$ with the depth ≤ 70 MeV and an absorptive part Im$V_{\rm opt} \geq 2$Re$V_{\rm opt}$ [6]. Valuable information about the $\bar{p}$–nucleus optical potential has been provided by antiprotonic atoms [7,8]. The antiprotonic atom is a kind of an exotic atom which is created whenever an electron in an atomic orbit is replaced by a negatively charged (anti)hadron. As the (anti)hadron (e.g. $\bar{p}, \pi^-, \Sigma^-, K^-$) is much heavier than the electron it gets considerably closer to the nucleus. Consequently, it interacts with the atomic nucleus not only electromagnetically but also by strong interaction. The strong interaction causes energy shifts (ϵ) and widths (Γ) of atomic levels, which are measured by experiment. In the analysis of Ref. [9], 107 data points of X-ray and radiochemical data were fitted by an optical potential in a '$t\rho$' form with various shapes of the nuclear density distribution. The global fits led to a potential, the imaginary part of which outweighs the attractive real part. Unfortunately, the $\bar{p}$ optical potential could be determined reliably only at radii where the nuclear density reaches just a few per cent of the central nuclear density [7,8]. When extrapolated into the nuclear interior the potential has attractive real part about 110 MeV deep and the absorptive imaginary part about 160 MeV deep [9]. On the other hand, the $\bar{p}$ production in proton–nucleus and nucleus–nucleus collisions probes the $\bar{p}$ interaction (under different kinematical conditions) deep inside the medium and the data can be well described by Re$V_{\rm opt} \sim -$ (100 - 200) MeV [10–12].

The antiproton annihilation was widely studied in experiments at the LEAR

facility and at KEK (see [13] and references therein). The Crystal Barrel experiment explored $\bar{p}p$ and $\bar{p}d$ annihilation at rest and in flight [14]. The Obelix experiment focused on $\bar{p}$ and $\bar{n}$ interactions at rest and very low momenta. Experiments at KEK aimed to measure frequencies of $\bar{p}$ annihilation into two narrow mesons [15, 16].

The indications of relatively deep $\bar{p}$ potential in the medium led to conjectures about the possibility of the existence of antiproton–nucleon or $\bar{p}$–nucleus bound states [17, 18]. Signals for narrow $\bar{p}$ bound states were searched for in experiments at the LEAR facility [6] and at KEK [19–21]. However, no convincing evidence for such states was obtained [22].

Theoretical considerations about the $\bar{p}$–nucleus potential are based on symmetries between NN and $\bar{N}N$ interactions. In the framework of the meson-exchange theory, the long- and medium-range NN and $\bar{N}N$ potentials are related to each other by the G-parity transformation [23]. The $\bar{p}$–nucleus potential derived using the G-parity transformation is strongly attractive and has no repulsive core [24], which suggests that the antiproton should be bound deeply in the nucleus [25]. However, the $\bar{p}$ annihilation plays a crucial role in the $\bar{p}N$ and $\bar{p}$–nucleus interactions. It has a major contribution in the short-range part of the interaction and has to be taken into account thoroughly.

The above considerations about a deep $\bar{p}$–nucleus potential based on G-parity have stimulated many theoretical calculations [26–38]. In Refs. [26, 27], the G-parity transformed $\bar{p}$ coupling constants scaled by factor $\xi \in (0, 1\rangle$ were used to construct the $\bar{p}$–nucleus potential within phenomenological Relativistic Mean-Field (RMF) approach. The potential was then applied in calculations of $\bar{p}$ bound states in ^{16}O and ^{208}Pb, including the polarization of the nuclear core due to $\bar{p}$. They revealed large compression of a nucleus caused by the $\bar{p}$ with central density reaching values about 2 - 4 times the saturation density. The $\bar{p}$ binding energy reached up to ~ 1000 MeV for the strongly attractive $\bar{p}$ potential constructed using the G-parity transformation. Nuclear systems with several antiprotons were studied as well. The authors of Ref. [27] also studied the $\bar{p}$ annihilation in the nuclear medium. The $\bar{p}$ absorption in a dense environment should be a prompt process, however, when the antiproton is deeply bound in a nucleus, the phase space available for annihilation products could be considerably reduced. Consequently, many annihilation channels are suppressed or simply closed in the medium. Based on these assumptions the $\bar{p}$ lifetime in the medium was estimated to 2 - 20 fm/c [27].

The RMF model was employed to study the spin symmetry of antinucleon spectra in nuclei as well [32–34]. It was found that the spin symmetry is perfectly

conserved when the real part of the antinucleon potential derived using the G-parity transformation is adopted in the calculations.

Since the $\bar{p}$ causes significant polarization of the nuclear core, the possibility of cold nuclear compression due to $\bar{p}$ has been explored [26, 28, 31]. The Giessen Boltzmann-Uehling-Uhlenbeck (GiBUU) transport model [39] was used to calculate the time required for the formation of a compressed $\bar{p}$–nucleus system. The time needed to reach a compressed nucleus with the central density of order (2 - 3)ρ_0 was found to be about 4 - 10 fm, which is comparable with the estimated lifetime of $\bar{p}$ in a nucleus [27]. It was also demonstrated, that the $\bar{p}$ annihilation could lead to multifragmentation of the nucleus which might serve as a signature of the formation of a $\bar{p}$–nucleus bound state.

The GiBUU model was also applied to study the dynamics of the $\bar{p}$–nucleus interaction in a wide range of $\bar{p}$ momenta [29, 31]. It was used to fit the KEK data [40] on $\bar{p}$ absorption cross sections at $p_{\rm lab}$ = 470 - 880 MeV/c in order to fix the value of the scaling factor ξ for $\bar{p}$ coupling constants. The analysis yielded value $\xi = 0.22$ which corresponds to Re$V_{\rm opt} \simeq -150$ MeV at saturation density. Fits to the antiproton atom data gave a similar value of the scaling factor ξ = 0.2 - 0.3 [9].

The value of the scaling factor ξ represents a significant departure from G-parity, which could be attributed to various many-body effects in the medium and $\bar{p}$ absorption. However, it was argued recently by Gaitanos *et al.* [36, 37] that this deviation is due to missing momentum dependence of the mean fields in the standard RMF approach. They developed a non-linear derivative (NLD) model which accounts for the momentum and density dependence of the nuclear mean fields. They showed that the momentum dependence reduces the G-parity motivated $\bar{p}$ optical potential and yields its depth in agreement with available experimental data [35]. It was also demonstrated that the standard RMF approach with $\bar{p}$–meson couplings scaled by factor ξ = 0.2 - 0.3 reproduces the NLD results in average [38].

Though much effort has been devoted to the study of the $\bar{p}$–nucleus interaction within the RMF model, fully self-consistent calculations (including $\bar{p}$ absorption) of $\bar{p}$ bound states in various nuclei with a $\bar{p}$ optical potential consistent with experimental data have been missing.

Besides purely phenomenological approaches to the $\bar{p}N$ and $\bar{p}$–nucleus interaction, there exist microscopic models of the $\bar{N}N$ interaction as well. There are $\bar{N}N$ potential models based on boson exchange, such as the Paris $\bar{N}N$ potential [41], Bonn $\bar{N}N$ potential [42] or Zhou-Timmermans model [43]. Moreover, $\bar{N}N$ interaction models based on effective field theory (EFT) are being developed [44, 45].

Recently, the 2009 version of the Paris $\bar{N}N$ potential [41] was confronted by Friedman *et al.* with the $\bar{p}$-atom data and antinucleon interactions with nuclei up to 400 MeV/c, including elastic scattering and annihilation cross sections [46]. The analysis showed that higher partial waves have to be considered in order to describe the antiproton atom data well. It is to be noted that none of the microscopic models has been employed in the calculations of $\bar{p}$-nuclear bound states so far. Such calculations would supplement the phenomenological approaches used before and help to improve our knowledge of in-medium $\bar{p}$ interactions.

The research in $\bar{p}$ physics has gained renewed interest in the last decades. Recently, the data on $\bar{p}$ annihilation on ^{4}He from the Obelix spectrometer at CERN were analyzed [47, 48] in order to explore $\bar{p}$ annihilation with two and more nucleons [49, 50]. The possibility of formation of cold quark-gluon plasma or highly excited hadronic gas in such reaction was studied. Next, the BESIII experiment detected a near-threshold enhancement in the $\bar{p}p$ mass spectrum in the J/Ψ decay events. The data supports the existence of either a $\bar{p}p$ molecule-like state or a bound state [51]. It is to be noted that one of the observed resonant states in the BESIII experiment, $X(1835)$, was described by the 2009 version of the Paris $\bar{N}N$ potential, assuming that it originates from a $\bar{p}p$ bound state [41, 51].

New experimental facilities with $\bar{p}$ beams are being built. Currently, the FAIR facility in Darmstadt is under construction [52]. Here, physicists plan to collide antiproton beams of momenta 1 - 15 GeV/c with nuclei in order to study the hadron structure and their propagation in the nuclear medium [53]. These experiments are expected to provide us with new information about the $\bar{p}$–nucleus potential and $\bar{p}$ annihilation in the nuclear medium. Another experiments are planned in Japan at J-PARC facility where antiprotons from a secondary beam will be used in nuclear and particle physics experiments [54].

1.2 Antikaon

The detection of kaons and hyperons in cosmic rays in 1947 [55] started a new era in particle physics. The study of their lifetime led to the introduction of a new degree of freedom denoted by quantum number 'strangeness' which is not conserved in weak interactions. Further investigations of weak decays of kaons resulted in the discovery of CP violation in neutral kaon oscillations [56]. The attempts to find relations between baryons and mesons according to their charge and strangeness led to the idea that all (anti)hadrons are in fact composed of more elementary constituents,

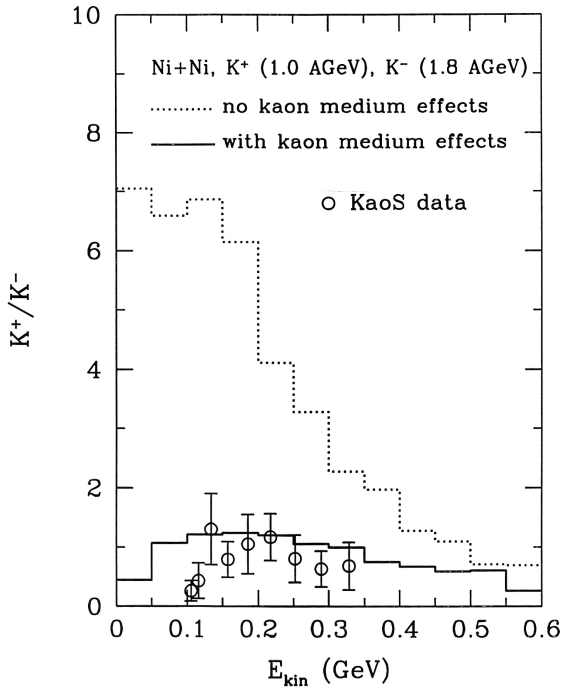

Figure 1.2: The kinetic energy spectra of K^+/K^- in Ni+Ni collisions. The dotted histogram denotes the result without kaon medium effect and the solid histogram accounts for medium effects. The experimental data are from the KaoS Collaboration [57].

quarks. Throughout the following years the theory of strong interactions, quantum chromodynamics (QCD), has been developed. At present, the interaction of the kaon with nucleons and its properties in the medium are connected with one of the basic symmetries in the nature — chiral symmetry of QCD. The kaon has been identified as a pseudo-Nambu-Goldstone bosons of spontaneously broken chiral $\mathrm{SU}(3)_R \times \mathrm{SU}(3)_L$ symmetry [58].

In the 80's, Kaplan and Nelson [59, 60] proposed the existence of kaon condensate in dense nuclear matter. Since then, the kaon properties in the medium have been widely studied, see e.g. [61–63]. Of special interest is the subthreshold kaon production in heavy-ion collisions which is sensitive to kaon properties in nuclear matter. The KaoS data showed that the measured K^+ to K^- ratio is consistent with unity, which is the indication of kaon in-medium modifications [57] (see Fig. 1.2). The knowledge of the kaon properties in the medium has consequences also in astrophysics. According to some scenarios, kaons are likely to appear in the inner core of a neutron star [64] (see also Fig. 1.3).

The study of interactions of (anti)kaons with nucleons and the nuclear medium

represents an important issue in current hadron physics. The starting point is the knowledge of (anti)kaon–nucleon interaction (for a comprehensive review see [65]). It is known that the K^+–nucleon as well as the K^+–nucleus interaction is weakly repulsive, see e.g. [8]. The situation with the K^-–nucleon interaction is different. The real part of the free K^-p scattering amplitude at and above threshold is repulsive based on the low-energy scattering and reaction data [66] and SIDDHARTA data on K^- hydrogen [67]. However, the $\bar{K}N$ interaction in the $I = 0$ channel is strongly attractive below threshold. The experimental information about the attractive nature of the subthreshold K^-N interaction comes from analyses of K^- atom data [7,8], the existence of the resonance $\Lambda(1405)$, considered an $I = 0$ $\bar{K}N$ quasi-bound state embedded in the resonant $\pi\Sigma$ continuum [68,69], and enhanced K^- production in heavy-ion collisions in the KaoS experiment at GSI [70–72].

The K^- atoms represent a unique probe of the K^-–nucleus potential at low energies and densities. The data consist of 65 energy-level shift, widths and transition yields, covering wide range of nuclei from kaonic hydrogen up to uranium. Global fits to the data using a phenomenological optical potential in a '$t\rho$' form [7] or potentials derived within the RMF approach yield real part of the K^-–nucleus potential fairly deep, about $\sim$ 100 - 200 MeV when extrapolated to the saturation density [73–75]. The absorptive part of these phenomenological potentials $\mathrm{Im}V_{K^-}(\rho_0) \sim -(60 - 80)$ MeV.

The existence of the resonance $\Lambda(1405)$, which lies 27 MeV below the $\bar{K}N$ threshold, was first predicted by Dalitz *et al.* [76,77] within a phenomenological study of $\bar{K}N$-$\pi\Sigma$ coupled channels. Later, the attractive nature of the $\bar{K}N$ interaction in this region was confirmed by Jülich meson–exchange model [78]. The precise determination of the structure of $\Lambda(1405)$ is closely related to the $\bar{K}N$ interaction below threshold. At present, there are still several theoretical explanations of its inner structure. Currently, the most accepted models view the $\Lambda(1405)$ as a meson–baryon molecule [68,69]. In this picture, the $\bar{K}N$ channel couples strongly to the $\pi\Sigma$ channel and strong K^- absorption in nuclear matter can thus be expected. Other models consider $\Lambda(1405)$ as a standard baryon with three quarks [79] or even a pentaquark [80].

The state-of-the-art theoretical framework for meson–baryon interactions is closely related to chiral perturbation theory (χPT) which was successfully applied to the description of the pion–nucleon interaction in the SU(2) sector (see e.g. Ref. [81] for a comprehensive overview). The existence of the $\Lambda(1405)$ resonance near threshold indicates strong nonperturbative dynamics of the $\bar{K}N$ interaction, which does

not allow direct application of χPT. Therefore, the $\bar{K}N$ interaction near threshold is described within the chiral SU(3) nonperturbative coupled-channel approach where resummation techniques based on the Lippmann–Schwinger [82,83] or Bethe–Salpeter equation [84–89] are used. Within these chirally-motivated coupled-channel models, the $\Lambda(1405)$ is generated dynamically as a two-pole structure assigned to the $\bar{K}N$ and $\pi\Sigma$ channels [90, 91]. Parameters of these models are fitted to available low-energy K^-N observables, such as the K^-p branching ratios [92, 93], K^-p scattering and reaction cross sections [66, 94, 95] and the $1s$ energy shift and width from kaonic hydrogen from SIDDHARTA experiment [67]. These models yield in-medium K^- potential shallower than phenomenological approaches, $\mathrm{Re}V_{K^-}(\rho_0) \sim -(50\text{ - }100)$ MeV [96–99].

The fact that the K^-N interaction is attractive in the subthreshold region has stimulated recently theoretical and experimental searches for K^- bound states in few-body systems as well as possible bound states of K^- in heavier nuclei. The relatively deeply bound K^- states in few-body systems, bound by ≈ 100 MeV, were suggested by Akaishi and Yamazaki [100]. For such deeply bound K^- the decay mode $K^-N \to \pi\Sigma$ would be kinematically forbidden which could lead to the existence of narrow K^- bound states. Since then, many theoretical calculations have been devoted to calculations of K^- bound states in the lightest nuclear systems, $\bar{K}NN$ [100–104] and $\bar{K}NNN$ [105, 106]. The theoretical calculations are based on various methods, such as Fadeev equations with coupled channels [102–104] or variational methods [105, 107], in which phenomenological or chiral K^- potentials are used. All the theoretical calculations agree that the K^-pp bound state exists, however, they differ in predictions of its binding energy and width.

The experimental situation regarding K^- bound states is unsettled as well: several candidates for the K^-pp bound state were reported by the FINUDA collaboration (Frascati) [108] or in analyses of the experiments OBELIX (CERN) [109] and DISTO (Saclay) [110]. All experimental results differ from each other and, moreover, the measured K^- binding energies and widths are far from all theoretical predictions. Therefore, new experiments are being planned and performed by the HADES [111] and LEPS [112] collaborations, and in the J-PARC E15 [113] and E27 experiments [114].

The possibility of K^- quasi-bound states in many-body nuclear systems was studied extensively as well. It is still not resolved if such K^- quasi-bound states could be directly observed in experiment. The calculations of K^- bound in ^{12}C up to ^{208}Pb were performed within the RMF approach [115–120] including K^- absorption

via a phenomenological imaginary potential in a $t\rho$ form fitted to K^- atom data. The authors of Refs. [117–119] took into account the polarization of the nuclear core due to K^-, phase space suppression for annihilation products and, moreover, they took into account the K^- absorption on two nucleons by adding a phenomenological ρ^2 term. Their calculations yielded K^- binding energies $B_{K^-} \geq 100$ MeV and widths $\Gamma_{K^-} \approx 50$ - 100 MeV. The core polarization due to K^- was found negligible. Nuclei containing several antikaons were calculated within the RMF model [117–119,121] as well as chiral approach [122–124] in order to study the onset of kaon condensation in a dense environment. The results suggest that the nuclear density reaches $(2 - 3)\rho_0$ where ρ_0 is the nuclear matter density and the K^- binding energy saturates with increasing number of K^- below 200 MeV. It is thus unlikely that kaon condensation occurs in strong-interaction self-bound strange hadronic matter [117–119].

Calculations based on chiral meson–baryon interaction models predict much shallower K^-–nucleus potential, about 50 - 100 MeV deep at ρ_0 [125–128]. In these calculations, the medium modification of K^-N amplitudes and self-consistent scheme for treating energy dependence of the amplitudes were taken into account. The chiral models yield considerably smaller K^- widths (up to ~ 40 MeV) than the phenomenological approach [115,116]. It is due to the fact that the chiral models include only the $K^-N \to \pi\Sigma$ conversion mode which becomes substantially suppressed in the medium. However, it is necessary to include $K^-NN \to YN$ ($Y = \Sigma, \Lambda$) conversion modes which become important in the medium. In Refs. [126–128], a phenomenological term representing K^- absorption on two nucleons was added to the chiral K^- single-nucleon potential. It was found that the two nucleon absorption contributes significantly to the K^- widths which then become comparable with the corresponding binding energies. However, these studies were performed only with one particular meson–baryon interaction model. Moreover, the K^- multinucleon processes should be taken into account more thoroughly, namely they contribute to the real part of the K^- optical potential as well. Recently, Sekihara et al. [129] evaluated the ratio of mesonic to nonmesonic K^- absorption within the chiral approach, however, it is not compatible with the K^- absorption data [130–132]. A proper chiral model for K^- interactions including multinucleon processes is still missing. Recently, Friedman and Gal [133] confronted all available meson–baryon interaction models with kaonic atom data and K^- single-nucleon absorption fractions from bubble chamber experiments. Moreover, the single-nucleon K^- potential derived from a chirally-motivated model was supplemented by a phenomenological term representing the K^- multinucleon processes. The parameters of the phenomenological

potential were fitted for each of the chiral model separately. Calculations of K^- bound states in many-body systems within all available chiral models including the K^- multinucleon interactions of Ref. [133] have been in high demand.

1.3 Antihyperons

Hyperons and antihyperons are (anti)baryons with non-zero strangeness. A hyperon (Λ, Σ, Ξ) embedded in a nucleus represents a suitable tool to probe the nuclear interior since it is not restricted by the Pauli principle. Hypernuclei (nuclei containing one or more hyperons) have been widely studied since the 80's by several experimental facilities, e.g., CERN, BNL, KEK or FINUDA (Italy). At present, there are still ongoing experiments at J-PARC (Japan), MAMI and GSI (Germany) or in J-LAB (USA). They provide valuable information about baryon–baryon interactions in the nuclear medium, nuclear structure, as well as weak interaction [134]. The knowledge of hyperon–nucleon and hyperon–hyperon interactions has implications for astrophysics. In a neutron star, the occurrence of hyperons emerges quite naturally at nuclear densities larger than about twice the nuclear density (see Fig. 1.3). However, the hyperonic equation of state (EOS) is expected to be very soft to explain recent observations of massive neutron stars with about twice the solar mass [135, 136]. This inconsistency is referred to as the 'hyperon puzzle'. Currently, many authors present hyperonic EOS's including repulsive three baryon forces which are then sufficiently stiff to stabilize two solar mass neutron star (see e.g. Refs. [137–140]). It seems that our incomplete understanding of the underlying baryon–baryon and even more subtle multi-body interactions in baryonic systems is the most probable reason for the hyperon puzzle [141–143].

There is rather limited amount of data on the hyperon–nucleon interaction — there are only ~ 600 low-momentum ΛN and ΣN scattering events, and almost no data on ΞN scattering [144]. The interaction of Λ and Ξ hyperons with nucleon(s) is attractive enough to support their binding in nuclei. The range of experimentally observed Λ hypernuclei is quite broad. So far, about 30 species have been observed, starting from the lightest hypernuclear system ${}^{3}_{\Lambda}$H up to the heavy hypernuclei ${}^{208}_{\Lambda}$Pb and ${}^{209}_{\Lambda}$Bi. Moreover, three nuclear systems with two Λ hyperons have been observed: ${}^{6}_{\Lambda\Lambda}$He [145], ${}^{10}_{\Lambda\Lambda}$Be [146] and ${}^{13}_{\Lambda\Lambda}$B [147], which provided us with unique information about the $\Lambda\Lambda$ interaction. Recently, the existence of the Ξ hypernucleus ${}^{14}_{\Xi}$N has been confirmed [148]. The Σ–nucleus optical potential is repulsive in the nuclear interior which does not support Σ-hypernuclear bound states, except the light hypernucleus

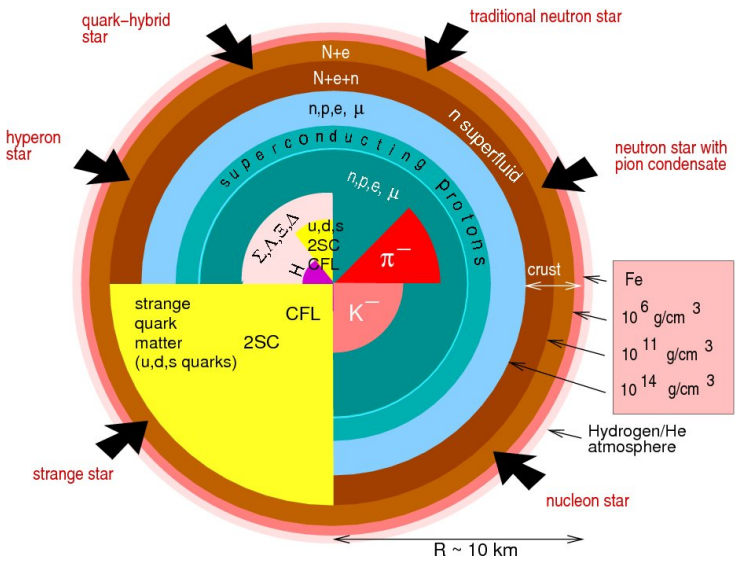

Figure 1.3: Conjectures about inner structure of a neutron star. Figure adapted from Ref. [150].

$^{4}_{\Sigma}$He [149].

Hyperon–antihyperon pairs are produced in $\bar{p}p$, $\bar{p}$–nucleus or nucleus–nucleus collisions. In general, the production of strangeness in nuclear collisions serves as a signal for the formation of quark-gluon plasma and represents an excellent tool to study QCD in the confinement regime [151, 152]. Moreover, quite recently the formation of antihypernuclei $^{3}_{\bar{\Lambda}}\bar{\mathrm{H}}$ and $^{4}_{\bar{\Lambda}}\bar{\mathrm{He}}$ was detected in heavy-ion collisions at RHIC (STAR) [153] and CERN (ALICE) [154]. The comparison of measured masses and lifetimes of antihypernuclei with those of hypernuclei is important for testing CPT symmetry in nature and may provide information about baryon–antibaryon asymmetry in the universe.

The antihyperon–nucleon ($\bar{Y}N$) interaction is much less known due to lack of experimental data. Few theoretical conjectures about the $\bar{Y}N$ interaction have appeared [155, 156], however, a proper microscopic model is missing. As in the $\bar{p}$ case, theoretical predictions based on the G-parity transformation can be made for the antihyperon–nucleus potential. In Ref. [27], the $\bar{\Lambda}$–nucleus potential was constructed within the RMF using the G-parity transformation of the Λ–nucleus potential. The calculations of $\bar{\Lambda}$ bound states in selected nuclei were performed. It was found that $\bar{\Lambda}$ is deeply bound ($\sim$ 600 MeV) inside a nucleus. The polarization of the nuclear core due to $\bar{\Lambda}$ was found to be less pronounced than in the case of $\bar{p}$ but still significant. The lifetime of $\bar{\Lambda}$ in the nuclear medium was discussed as well. Since the kaon which is present in the lowest mass $\bar{\Lambda}N$ annihilation channel is much heavier than

the pion, the phase space suppression for the annihilation products is expected to be more pronounced than in the case of $\bar{p}$ [27].

The authors of Ref. [157] applied the RMF approach with $\bar{\Lambda}$ coupling constants scaled by factor $\xi = 0.3$ to construct the $\bar{\Lambda}$–nucleus potential. Subsequently, they performed calculations of $\bar{\Lambda}$ bound states in various nuclei without considering the $\bar{\Lambda}$ absorption and found that spin symmetry is conserved in the $\bar{\Lambda}$ spectra.

It is desirable to study also $\bar{\Sigma}$– and $\bar{\Xi}$–nucleus interactions, either within the RMF model using properly scaled G-parity transformed hyperon–meson couplings or within microscopic models of $\bar{Y}N$ interaction. The antihyperon absorption in the nuclear medium should be taken into account as well.

In the forthcoming experiments at the FAIR facility, hyperon–antihyperon pairs will be produced in $\bar{p}$–nucleus interactions [52]. The measurement of transverse momentum asymmetry is expected to yield information about the depth of in-medium antihyperon potentials [158]. This would enable construction of more sophisticated $\bar{Y}$–nucleus interaction models.

The above overview demonstrates that despite considerable progress in this field of physics, there are still problems which remain unsolved. The present thesis is devoted to the study of selected issues in this area, aiming to contribute, at least partly, to their solution.

Chapter 2

Methodology

Our work is concerned with the study of interactions of antihadrons ($\bar{H} = \bar{p}, \bar{\Lambda}, \bar{\Sigma}, \bar{\Xi}$ and K^-) with nuclear many-body systems in which the mean-field concept is applicable. For the description of the nuclear density distribution ρ and the nuclear core itself we employ the Relativistic Mean-Field approach which has proved to be successful in calculations of nuclear structure as well as nuclear dynamics. The $\bar{H}$–nucleus interaction is described by a complex optical potential constructed either within the RMF phenomenology or using microscopic models.

First, we derive the real part of an $\bar{H}$–nucleus potential within the RMF approach using the G-parity motivated coupling constants. The imaginary part of the potential which covers the $\bar{H}$ absorption inside a nucleus is adopted from a phenomenological optical potential fitted to available experimental data.

Next, the $\bar{H}$ optical potential is constructed using scattering amplitudes derived from microscopic models of $\bar{H}N$ interactions, such as chiral and meson-exchange models. The equations of motion, namely the Dirac equation for $N, \bar{p}, \bar{\Lambda}, \bar{\Sigma}$ and $\bar{\Xi}$ and the Klein–Gordon equation for K^- and boson-exchange fields, are solved self-consistently. Modifications of the nuclear core due to the presence of $\bar{H}$ are taken into account as well.

We start this chapter with a brief introduction to the RMF model and derivation of relevant equations of motion. Then, we extend the RMF model to include antihadrons. Further, we present detailed description of the construction of an $\bar{H}$–nucleus optical potential within phenomenological and microscopic approaches and introduce a self-consistent scheme for treating its energy and density dependence.

2.1 Relativistic Mean-Field Model for Nucleus

In the RMF model [159–161], the nucleons are described as Dirac fields interacting strongly via the exchange of the following boson fields — the isoscalar-scalar field σ which is responsible for medium- and long-range attraction, the isoscalar-vector field ω which mediates short-range repulsion, the isovector-vector field ρ describing the isospin dependence of nuclear force, and the photon field A_μ which accounts for the electromagnetic interaction. The π and η meson fields with unnatural parity are not considered since we are dealing with nuclear states of well-defined parity.

The starting point of the model is the Lagrangian density containing nucleonic and effective mesonic degrees of freedom:

$$\begin{aligned}\mathscr{L} =&\bar{\psi}[i\gamma^\mu\partial_\mu - m_N - g_\sigma\sigma - g_\omega\gamma_\mu\omega^\mu - g_\rho\gamma_\mu\vec{\tau}\cdot\vec{\rho}^\mu - e\gamma_\mu\frac{1}{2}(1+\tau_3)A^\mu]\psi \\ &+\frac{1}{2}\left(\partial_\mu\sigma\partial^\mu\sigma - m_\sigma^2\sigma^2\right) - \frac{1}{2}(\frac{1}{2}\Omega_{\mu\nu}\Omega^{\mu\nu} - m_\omega^2\omega_\mu\omega^\mu) \\ &-\frac{1}{2}(\frac{1}{2}\vec{R}_{\mu\nu}\cdot\vec{R}^{\mu\nu} - m_\rho^2\vec{\rho}_\mu\cdot\vec{\rho}^\mu) - \frac{1}{4}F_{\mu\nu}F^{\mu\nu} \\ &-\frac{1}{3}g_2\sigma^3 - \frac{1}{4}g_3\sigma^4 + \frac{1}{4}d(\omega_\mu\omega^\mu)^2\ ,\end{aligned} \tag{2.1}$$

where m_N is the nucleon mass; m_σ, m_ω, m_ρ are the masses of the σ-, ω- and ρ-meson; g_σ, g_ω, g_ρ and e are the coupling constants of the meson and photon fields to nucleons, respectively. The g_2, g_3 and d couplings represent the strengths of the σ and ω self-interactions [162, 163]. The arrow denotes an isovector quantity and $\vec{\tau}$ is the triplet of Pauli matrices. The field tensors are defined as follows:

$$\begin{aligned}\Omega_{\mu\nu} &= \partial_\mu\omega_\nu - \partial_\nu\omega_\mu\ , \\ \vec{R}_{\mu\nu} &= \partial_\mu\vec{\rho}_\nu - \partial_\nu\vec{\rho}_\mu\ , \\ F_{\mu\nu} &= \partial_\mu A_\nu - \partial_\nu A_\mu\ .\end{aligned} \tag{2.2}$$

The nucleon is described by the isodoublet wave function

$$\psi = \begin{pmatrix}\psi_p \\ \psi_n\end{pmatrix}. \tag{2.3}$$

The parameters of the model, i.e., the meson masses and meson–nucleon coupling constants, are obtained by fitting properties of nuclear matter and selected

finite nuclei. Sets of these parameters define a specific RMF parametrization. In this thesis, we adopt the NL-SH [164] model and TM1(2) [163] models for heavy (light) nuclei. The values of the parameters of these models are listed in Table A.1.

The equations of motion for respective fields $q_i = \psi, \bar{\psi}, \sigma, \omega_\mu, \vec{\rho}_\mu, A_\mu$ are obtained using the principle of stationary action

$$\delta \int \mathscr{L}(q_i(x), \partial q_i(x), t)\ \mathrm{d}^4(x) = 0 \tag{2.4}$$

which yields Euler–Lagrange equations

$$\frac{\partial}{\partial x_\mu}\left[\frac{\partial \mathscr{L}}{\partial(\partial q_i/\partial x_\mu)}\right] - \frac{\partial \mathscr{L}}{\partial q_i} = 0\ . \tag{2.5}$$

The Lagrangian density (2.1) leads to nonlinear quantum field equations which are very complicated to be solved directly. Moreover, the coupling constants to the meson fields are expected to be large, perturbative approaches are thus not applicable. Therefore, reasonable approximations need to be involved in order to simplify the equations of motion: First, we replace all quantum fields by their expectation values which are classical fields. This is the so called *mean-field* approximation and it becomes more and more valid as the nuclear density increases:

$$\begin{aligned}
\sigma(x) \to \quad & \langle\sigma(x)\rangle \quad = \sigma_0(r)\ , \\
\omega_\mu(x) \to \quad & \langle\omega_\mu(x)\rangle \quad = \omega_0(r)\ , \\
\rho^i_\mu(x) \to \quad & \langle\rho^i_\mu(x)\rangle \quad = \rho^3_0(r)\ , \\
A_\mu(x) \to \quad & \langle A_\mu(x)\rangle \quad = A_0(r).
\end{aligned} \tag{2.6}$$

As a result of the mean-field approximation, nucleons are moving as independent particles in the corresponding mean fields. Furthermore, we work in the *no-sea* approximation which neglects all contributions from antiparticles (Dirac sea)[1]. The nucleon wave function can then be expanded in terms of single-particle states n

$$\psi = \sum_{n=1}^{A} \psi_n(x) a_n\ , \tag{2.7}$$

[1] One could argue that contribution from the Dirac sea should be taken into account since it may lead to the non-negligible contribution in the equations of motion. However, the RMF model is a phenomenological model with parameters fitted to the data. It means that the Dirac sea is to some extent absorbed in the coupling constants [165, 166].

where a denotes the nucleon annihilation operator and the summation runs only through A occupied positive-energy states in a nucleus. Moreover, we search for a solution of ground-state properties of magic nuclei which are spherical. Therefore, we assume time-reversal and rotational invariance, which implies that all space-like components of the vector fields and currents vanish and the fields will depend only on the radial coordinate r. Charge conservation implies that only the third component of the ρ field survives. We work in the static limit, i.e., all time derivatives of the fields vanish as well.

With the above assumptions the Lagrangian density from Eq. (2.1) acquires the form

$$\begin{aligned}\mathscr{L}_{\mathrm{RMF}} =&\bar{\psi}_n(i\gamma_\mu\partial^\mu - m_N - g_\sigma\sigma - g_\omega\gamma_0\omega_0 - g_\rho\gamma_0\tau_3\rho_0^3 - e\gamma_0\frac{1+\tau_3}{2}A_0)\psi_n \\ &- \frac{1}{3}g_2\sigma^3 - \frac{1}{4}g_3\sigma^4 + \frac{1}{4}d\omega_0^4 - \frac{1}{2}[(\nabla_i\sigma)^2 + m_\sigma^2\sigma^2] \\ &+ \frac{1}{2}[(\nabla_i\omega_0)^2 + m_\omega^2\omega_0^2] + \frac{1}{2}[(\nabla_i\rho_0)^2 + m_\rho^2\rho_0^2] + \frac{1}{2}(\nabla_i A_0)^2 \ .\end{aligned} \tag{2.8}$$

The Euler–Lagrange equations (2.5) lead to a set of coupled equations: the Dirac equation for nucleons

$$[-i\alpha\cdot\nabla + \beta(m_N + S) + V]\psi_n = \epsilon_n\psi_n \ , \tag{2.9}$$

where $\epsilon_n = i\partial_t\psi_n$ denotes nucleon single-particle energy, and the Klein–Gordon equations for scalar, vector and photon fields, respectively:

$$\begin{aligned}(-\triangle + m_\sigma^2 + g_2\sigma + g_3\sigma^2)\sigma &= -g_\sigma\rho_{\mathrm{S}} \ , \\ (-\triangle + m_\omega^2 + d\omega_0^2)\omega_0 &= g_\omega\rho_{\mathrm{V}} \ , \\ (-\triangle + m_\rho^2)\rho_0^3 &= g_\rho\rho_{\mathrm{I}} \ , \\ -\triangle A_0 &= e\rho_{\mathrm{C}} \ .\end{aligned} \tag{2.10}$$

The scalar S and vector V potentials entering the Dirac equation (2.9) are of the following form:

$$S = g_\sigma\sigma, \quad V = g_\omega\omega_0 + g_\rho\tau_3\rho_0^3 + e\frac{1+\tau_3}{2}A_0 \ .$$

The source terms on the r.h.s of Eq. (2.10) are scalar, vector, isovector and charge

densities, respectively, defined as

$$\begin{aligned}
\rho_{\mathrm{S}} = &\quad \langle 0| : \bar{\psi}\psi : |0\rangle &&= \sum_{n=1}^{A} \bar{\psi}_n \psi_n \ , \\
\rho_{\mathrm{V}} = &\quad \langle 0| : \psi^\dagger \psi : |0\rangle &&= \sum_{n=1}^{A} \psi_n^\dagger \psi_n \ , \\
\rho_{\mathrm{I}} = &\quad \langle 0| : \psi^\dagger \tau_3 \psi : |0\rangle &&= \sum_{n=1}^{A} \psi_n^\dagger \tau_3 \psi_n \ , \\
\rho_{\mathrm{C}} = &\quad \langle 0| : \psi^\dagger \tfrac{1+\tau_3}{2} \psi : |0\rangle &&= \sum_{n=1}^{A} \psi_n^\dagger \frac{1+\tau_3}{2} \psi_n \ .
\end{aligned} \tag{2.11}$$

Here, the symbol $\langle : \cdots : \rangle$ denotes the normal order product with respect to the nuclear ground state $|0\rangle$. The densities are normalized to yield a proper number of nucleons A, protons Z and neutrons N:

$$\begin{aligned}
\int &\quad \mathrm{d}x^3 \rho_{\mathrm{V}} = &&A \ , \\
\int &\quad \mathrm{d}x^3 \rho_{\mathrm{I}} = &&Z - N \ , \\
\int &\quad \mathrm{d}x^3 \rho_{\mathrm{C}} = &&Z \ .
\end{aligned} \tag{2.12}$$

The system of coupled equations (2.9) and (2.10) can now be solved numerically by iterative procedure. Once the nucleon and boson fields are determined, the total energy of the system can be calculated as

$$\begin{aligned}
E = &\int d^3x \mathscr{H} = \int d^3x \frac{\partial \mathscr{L}_{\mathrm{RMF}}}{\partial \dot{q}_i} \dot{q}_i - \mathscr{L}_{\mathrm{RMF}} \\
= &\sum_{n=1}^{A} \int d^3x \ \psi_n^\dagger [-i\alpha \cdot \nabla + \beta(m_N + S) + V] \psi_n \\
&+ \int d^3x \ \frac{1}{2}[(\nabla\sigma)^2 + m_\sigma^2 \sigma^2] - \frac{1}{2}[(\nabla\omega_0)^2 + m_\omega^2 \omega_0^2] - \frac{1}{2}(\nabla A_0)^2 - \frac{1}{2}[(\nabla\rho_0)^2 + m_\rho^2 \rho_0^2] \\
&+ \int d^3x \ \frac{1}{3} g_2 \sigma^3 + \frac{1}{4} g_3 \sigma^4 - \frac{1}{4} d\omega_0^4 \ .
\end{aligned} \tag{2.13}$$

The meson fields decay exponentially at large distances, which allows us to perform

partial integration, e.g., for the σ field

$$\begin{aligned}\int d^3x \frac{1}{2}[(\nabla\sigma)^2 + m_\sigma^2\sigma^2] &= \frac{1}{2}\int d^3x[\sigma(-\nabla^2 + m_\sigma^2)\sigma] \\ &= \frac{1}{2}\int d^3x(-g_\sigma\rho_{\rm S}\sigma - g_2\sigma^3 - g_3\sigma^4) \ ,\end{aligned} \tag{2.14}$$

and similarly for other fields. The part of Eq. (2.13) involving nucleon fields can be evaluated using the Dirac equation (2.9) and the following expression for the energy of the system is obtained

$$\begin{aligned}E = \sum_{n=1}^{A}\epsilon_n &- \frac{1}{2}\int {\rm d}^3x \ (g_\sigma\,\sigma\rho_{\rm S} + g_\omega\,\omega_0\rho_{\rm V} + g_\rho\,\rho_0^3\rho_{\rm I} + e\,A_0\rho_{\rm C}) \\ &- \frac{1}{2}\int {\rm d}^3x \ (\tfrac{1}{3}g_2\,\sigma^3 + \tfrac{1}{2}g_3\,\sigma^4 - \tfrac{1}{2}d\,\omega^4) \ .\end{aligned} \tag{2.15}$$

The total binding energy of a nucleus is then

$$\begin{aligned}E_B &= E + E_{\rm CMS} - Am_N \\ &= \textstyle\sum_{n=1}^{A}(\epsilon_n - m_N) \\ &- \frac{1}{2}\int {\rm d}^3x \ (g_\sigma\,\sigma\rho_{\rm S} + g_\omega\,\omega_0\rho_{\rm V} + g_\rho\,\rho_0^3\rho_{\rm I} + e\,A_0\rho_{\rm C}) \\ &- \frac{1}{2}\int {\rm d}^3x \ (\tfrac{1}{3}g_2\,\sigma^3 + \tfrac{1}{2}g_3\,\sigma^4 - \tfrac{1}{2}d\,\omega^4) \\ &- 30.75\ A^{-1/3}[{\rm MeV}] \ ,\end{aligned} \tag{2.16}$$

where $E_{\rm CMS} = -30.75\ A^{-1/3}$ is the center-of-mass correction to the total energy adopted from the harmonic oscillator shell model [167].

2.1.1 RMF Model with Density-Dependent Coupling Constants

Besides standard RMF models with constant couplings there exist also versions with density-dependent (DD) meson–nucleon couplings. The RMF model with the DD couplings represents a natural alternative which follows the Dirac-Bruckner (DB) theory of nuclear matter [168–170]. The DD model is as good as the nonlinear models with constant couplings in the description of properties of ordinary nuclear matter and finite nuclei. In addition, it yields equation of state for nuclear matter beyond the saturation point in agreement with the DB calculations [171]. The

specific form of density-dependence of the meson–nucleon couplings was introduced by Typel and Wolter [171] as follows:

$$g_i(\rho_{\rm V}) = g_i(\rho_0) f_i(x) \ , \quad i = \sigma, \omega \ , \tag{2.17}$$

where

$$f_i(x) = a_i \frac{1 + b_i(x + d_i)^2}{1 + c_i(x + d_i)^2} \ , \tag{2.18}$$

and the argument $x = \rho_{\rm V}/\rho_0$ with ρ_0 denoting the saturation density of nuclear matter. The coupling for the ρ meson has an exponential character

$$g_\rho(\rho_{\rm V}) = g_\rho(\rho_0) \exp[-a_\rho(x - 1)] \ . \tag{2.19}$$

The parameters $a_i,\ b_i,\ c_i, d_i$ and a_ρ are not independent and their values are obtained by fitting properties of nuclear matter and finite nuclei.

The DD RMF model starts from the same Lagrangian density (2.1), only the couplings are functions of the baryon density and the meson self-interaction terms are omitted, i.e., c_2, c_3 and d are set to zero. The Dirac equation for nucleons contains extra rearrangement term $\Sigma_{\rm R}$ stemming from the density-dependence of the scalar and vector potentials

$$[-i\alpha \cdot \nabla + \beta(m_N + S) + V + \Sigma_{\rm R}]\psi_n = \epsilon_n \psi_n \ . \tag{2.20}$$

The rearrangement term $\Sigma_{\rm R}$ is of the following form

$$\Sigma_{\rm R} = \frac{\partial g_\omega(\rho_{\rm V})}{\partial \rho_{\rm V}} \rho_{\rm V} \omega_0 + \frac{\partial g_\rho(\rho_{\rm V})}{\partial \rho_{\rm V}} \rho_{\rm I} \rho_0^3 - \frac{\partial g_\sigma(\rho_{\rm V})}{\partial \rho_{\rm V}} \rho_{\rm S} \sigma \ . \tag{2.21}$$

The equations for boson fields maintain their form (2.10) with the couplings replaced by the density-dependent ones. The rearrangement term $\Sigma_{\rm R}$ will appear in the expression for the total binding energy of a nucleus as well

$$\begin{aligned} E_B &= E_{\rm DD} + E_{\rm CMS} - A m_N \\ &= \textstyle\sum_{n=1}^{A} (\epsilon_n - m_N) \\ &- \frac{1}{2} \int {\rm d}^3x \, (g_\sigma(\rho_{\rm V})\, \sigma \rho_{\rm S} + g_\omega(\rho_{\rm V})\, \omega_0 \rho_{\rm V} + g_\rho(\rho_{\rm V})\, \rho_0^3 \rho_{\rm I} + e\, A_0 \rho_{\rm C} + 2\rho_{\rm V} \Sigma_{\rm R}) \\ &- 30.75 \ A^{-1/3} [{\rm MeV}] \ . \end{aligned} \tag{2.22}$$

2.2 Antihadron–Nucleus Interactions within Phenomenological Approach

The RMF formalism presented in Section 2.1 can be extended in a rather straightforward way to incorporate antihadrons ($\bar{H} = \bar{p}, \bar{\Lambda}, \bar{\Sigma}, \bar{\Xi}, K^-$) by introducing additional fields describing these antihadrons and their interactions with boson fields. The nuclear Lagrangian density is then supplemented by an appropriate Lagrangian density $\mathscr{L}_{\bar{H}}$. Moreover, in order to describe nuclear systems with more strange particles, 'hidden strangeness' scalar σ^* and vector ϕ meson fields that mediate the interaction exclusively between strange particles are introduced. However, since we are concerned with nuclei containing one strange antihadron at most, we do not consider these additional fields in this work. The RMF formalism extended in this way has been successfully applied in the description of Λ, Σ and Ξ hypernuclei [172–174], as well as $\bar{p}$ [26, 27, 175] and K^- [115–119] nuclei.

The $\bar{H}$–nucleus interaction is described by a complex optical potential, real part of which is constructed within the RMF model using the G-parity transformation of hadron–meson coupling constants. The absorption of $\bar{H}$ inside the nucleus is accounted for by means of the imaginary part of a purely phenomenological optical potential.

2.2.1 RMF Model for Nucleus with Antihadron

The Lagrangian density $\mathscr{L}_{\mathrm{RMF}}$ for the nucleonic sector (2.8) is extended by the Lagrangian density $\mathscr{L}_{\bar{H}}$ describing the interaction of *one* antihadron with the nuclear medium, $\mathscr{L}_{N+\bar{H}} = \mathscr{L}_{\mathrm{RMF}} + \mathscr{L}_{\bar{H}}$.

The interaction of an antibaryon $\bar{B}$ ($\bar{p}$ or antihyperon) with a nucleus is described by the following Lagrangian density:

$$\begin{aligned}\mathscr{L}_{N+\bar{B}} = \sum_{j=N,\bar{B}} \bar{\psi}_n^j (i\gamma_\mu \partial^\mu - m_j - g_{\sigma j}\sigma - g_{\omega j}\gamma_0\omega_0 - g_{\rho j}\gamma_0 I_3 \rho_0^3 - e\gamma_0(I_3 + \frac{1}{2}Y)A_0)\psi_n^j \\ - \frac{1}{3}g_2\sigma^3 - \frac{1}{4}g_3\sigma^4 + \frac{1}{4}d\omega_0^4 - \frac{1}{2}[(\nabla_i\sigma)^2 + m_\sigma^2\sigma^2] \\ + \frac{1}{2}[(\nabla_i\omega_0)^2 + m_\omega^2\omega_0^2] + \frac{1}{2}[(\nabla_i\rho_0^3)^2 + m_\rho^2(\rho_0^3)^2] + \frac{1}{2}(\nabla_i A_0)^2 \ ,\end{aligned} \tag{2.23}$$

where I_3 denotes the third component of isospin, Y stands for hypercharge, and $g_{\sigma\bar{B}}$, $g_{\omega\bar{B}}$ and $g_{\rho\bar{B}}$ denote the antibaryon–meson coupling constants.

The interaction of K^- with a nucleus is described by the Lagrangian density $\mathscr{L}_{N+K^-}$ which acquires the following form:

$$\begin{aligned}\mathscr{L}_{N+K^-} &= \bar{\psi}_n(i\gamma_\mu\partial^\mu - m_N - g_\sigma\sigma - g_\omega\gamma_0\omega_0 - g_\rho\gamma_0\tau_3\rho_0^3 - e\gamma_0\frac{1+\tau_3}{2}A_0)\psi_n \\ &- \frac{1}{3}g_2\sigma^3 - \frac{1}{4}g_3\sigma^4 + \frac{1}{4}d\omega_0^4 - \frac{1}{2}[(\nabla_i\sigma)^2 + m_\sigma^2\sigma^2] \\ &+ \frac{1}{2}[(\nabla_i\omega_0)^2 + m_\omega^2\omega_0^2] + \frac{1}{2}[(\nabla_i\rho_0^3)^2 + m_\rho^2(\rho_0^3)^2] + \frac{1}{2}(\nabla_i A_0)^2 \\ &- [(\nabla_i K^-)(\nabla_i K^+) + m_K^2 K^- K^+] - g_{\sigma K}m_K\sigma K^- K^+ \\ &+ (\epsilon_{K^-} + g_{\omega K}\omega_0 + g_{\rho K}\rho_0^3 + eA_0)^2 K^- K^+ \ ,\end{aligned} \tag{2.24}$$

where $\epsilon_{K^-} = i\partial_t K^-$ is the K^- single-particle energy, $K^{+(-)}$ denotes the (anti)kaon wave function, m_K is the kaon mass, and $g_{\sigma K}$, $g_{\omega K}$ and $g_{\rho K}$ denote (anti)kaon–meson coupling constants. The Lagrangian density (2.23) or (2.24) is a starting point for the derivation of the relevant equations of motion by techniques described in the previous section. Since the K^-–nucleus interaction has been extensively studied within the RMF model by Gazda *et al.* [117–119] we will further concentrate only to the description of antibaryon interactions with the nuclear medium.

The variational principle (2.4) leads to the following system of coupled equations: the Dirac equation for nucleons (2.9) and antibaryon

$$[-i\alpha\cdot\nabla + \beta(m_{\bar{B}} + S_{\bar{B}}) + V_{\bar{B}}]\psi_{\bar{B}} = \epsilon_{\bar{B}}\psi_{\bar{B}}, \tag{2.25}$$

where

$$S_{\bar{B}} = g_{\sigma\bar{B}}\sigma, \quad V_{\bar{B}} = g_{\omega\bar{B}}\omega_0 + g_{\rho\bar{B}}\rho_0^3 I_3 + e(I_3 + \frac{1}{2}Y)A_0 \ ,$$

and the equations of motion for boson fields which contain additional source terms on the r.h.s due to the presence of $\bar{B}$

$$\begin{aligned}(-\triangle + m_{\sigma^2} + g_2\sigma + g_3\sigma^2)\sigma &= -g_{\sigma N}\rho_{\rm S} - g_{\sigma\bar{B}}\rho_{\rm S\bar{B}} \ , \\ (-\triangle + m_{\omega^2} + d\omega_0^2)\omega_0 &= g_{\omega N}\rho_{\rm V} + g_{\omega\bar{B}}\rho_{\rm V\bar{B}} \ , \\ (-\triangle + m_{\rho^2})\rho_0^3 &= g_{\rho N}\rho_{\rm I} + g_{\rho\bar{B}}\rho_{\rm I\bar{B}} \ , \\ -\triangle A_0 &= e\rho_{\rm C} + e\rho_{\rm C\bar{B}} \ .\end{aligned} \tag{2.26}$$

Here, $\rho_{\rm S\bar{B}}$, $\rho_{\rm V\bar{B}}$, $\rho_{\rm V\bar{B}}$ and $\rho_{\rm C\bar{B}}$ are antibaryon scalar, vector, isovector and charge densities, respectively, normalized to unity.

The expression for the total binding energy of the system of A nucleons plus one antibaryon is then of the following form

$$\begin{aligned} E_B &= E + E_{\rm CMS} - A m_N - m_{\bar{B}} \\ &= \textstyle\sum_{n=1}^{A} (\epsilon_n - m_N) + (\epsilon_{\bar{B}} - m_{\bar{B}}) \\ &- \frac{1}{2} \int {\rm d}^3x \, (g_{\sigma N}\, \sigma \rho_S + g_{\omega N}\, \omega_0 \rho_V + g_{\rho N}\, \rho_0^3 \rho_I + e\, A_0 \rho_C) \\ &- \frac{1}{2} \int {\rm d}^3x \, (\tfrac{1}{3} g_2\, \sigma^3 + \tfrac{1}{2} g_3\, \sigma^4 - \tfrac{1}{2} d\, \omega^4) \\ &- \frac{1}{2} \int {\rm d}^3x \, (g_{\sigma \bar{B}}\, \sigma \rho_{S\bar{B}} + g_{\omega \bar{B}}\, \omega_0 \rho_{V\bar{B}} + g_{\rho \bar{B}}\, \rho_0^3 \rho_{I\bar{B}} + e\, A_0 \rho_{C\bar{B}}) \\ &- 30.75 \, (A+1)^{-1/3} [\text{MeV}] \, . \end{aligned} \tag{2.27}$$

The presence of $\bar{B}$ in a nucleus modifies the equations of motion for boson fields. This leads to polarization of the nuclear core, i.e., the nucleon single-particle energies and density distribution change. It was demonstrated by Mishustin *et al.* [27] that the insertion of $\bar{p}$ into a nucleus causes significant modification of the nuclear core, the central nuclear density reaches 2 - 3 times the saturation density. However, the standard nonlinear RMF models, TM1(2) [163] or NL-SH [164], do not have to describe correctly the behavior of a nucleus when extrapolated to such high nuclear densities. Therefore, we explored the antibaryon–nucleus interaction using the DD RMF model TW99 [171] as well.

In our DD RMF model, the Dirac equation for antibaryon maintains its original form (2.25), i.e, unlike the Dirac equation for nucleons it does not contain the additional rearrangement term $\Sigma_{\rm R}$. The equations for boson fields have the same form as in Eqs. (2.26), only the couplings are replaced by the density-dependent ones. The total binding energy for a nucleus with one antibaryon expressed within the DD RMF model is of the form

$$\begin{aligned} E_B &= E_{\rm DD} + E_{\rm CMS} - A m_N - m_{\bar{B}} \\ &= \textstyle\sum_{n=1}^{A} (\epsilon_n - m_N) + (\epsilon_{\bar{B}} - m_{\bar{B}}) \\ &- \frac{1}{2} \int {\rm d}^3x \, (g_{\sigma N}(\rho_{\rm V})\, \sigma \rho_{\rm S} + g_{\omega N}(\rho_{\rm V})\, \omega_0 \rho_{\rm V} + g_{\rho N}(\rho_{\rm V})\, \rho_0 \rho_{\rm I} + e\, A_0 \rho_{\rm C} + 2 \rho_{\rm V} \Sigma_{\rm R}) \\ &- \frac{1}{2} \int {\rm d}^3x \, (g_{\sigma \bar{B}}(\rho_{\rm V})\, \sigma \rho_{{\rm S}\bar{B}} + g_{\omega \bar{B}}(\rho_{\rm V})\, \omega_0 \rho_{{\rm V}\bar{B}} + g_{\rho \bar{B}}(\rho_{\rm V})\, \rho_0 \rho_{{\rm I}\bar{B}} + e\, A_0 \rho_{{\rm C}\bar{B}}) \\ &- 30.75 \, (A+1)^{-1/3} [\text{MeV}] \, . \end{aligned} \tag{2.28}$$

2.2.2 Antibaryon–Nucleus Interactions

An important ingredient of the $\bar{B}$–nucleus interaction model are the antibaryon–meson coupling constants. On the level of hadronic degrees of freedom the strong interaction is mediated by the exchange of mesons. One of the basic symmetries of the strong interaction is G-parity ($\hat{G} = \hat{C}\exp(-i\pi I_2)$ which involves charge conjugation $\hat{C}$ and rotation in isospin space) [23]. The G-parity transformation is usually applied in the construction of antinucleon–nucleon ($\bar{N}N$) interactions from meson-exchange models of nucleon–nucleon interactions. It seems to be quite natural to apply the G-parity transformation to the derivation of an antibaryon–nucleus potential within the RMF approach (the K^-–nucleus potential has been constructed in a similar way [115–119]).

The real part of the $\bar{B}$–nucleus optical potential is obtained by the G-parity transformation of the corresponding B–nucleus potential

$$U_{\bar{B}} = \sum_M G_M U_M \ . \tag{2.29}$$

Here, U_M denotes the potential generated by the exchange of meson M and G_M is the corresponding G-parity eigenvalue. The σ and ρ meson fields have a positive G-parity eigenvalue. However, the ω meson has a negative G-parity eigenvalue and the part of the potential generated by the ω exchange thus converts its sign. When expressed in terms of coupling constants we have

$$g_{\sigma\bar{B}} = g_{\sigma B}, \quad g_{\omega\bar{B}} = -g_{\omega B}, \quad g_{\rho\bar{B}} = g_{\rho B} \ . \tag{2.30}$$

The underlying hyperon couplings to the ω and ρ meson fields are derived using SU(6) symmetry relations [172,174]. The hyperon couplings to the σ fields are then obtained by fitting available experimental data on Λ hypernuclei [172], Σ atoms [173], and Ξ production in (K^+, K^-) reaction [176]. As a result, the hyperon–meson couplings are in the following relation to the nucleon–meson coupling constants:

$$\begin{aligned}
&g_{\sigma\Lambda} = 0.621 g_{\sigma N}, && g_{\omega\Lambda} = 2/3 g_{\omega N}, && g_{\rho\Lambda} = 0 \ , \\
&g_{\sigma\Sigma} = 0.5 g_{\sigma N}, && g_{\omega\Sigma} = 2/3 g_{\omega N}, && g_{\rho\Sigma} = 2/3 g_{\rho N} \ , \\
&g_{\sigma\Xi} = 0.299 g_{\sigma N}, && g_{\omega\Xi} = 1/3 g_{\omega N}, && g_{\rho\Xi} = g_{\rho N} \ .
\end{aligned} \tag{2.31}$$

Within the RMF model, the nuclear ground state is well described by an attractive scalar potential $S(0) \simeq -400$ MeV and a repulsive vector potential $V(0) \simeq 350$ MeV. The central potential acting on a nucleon in a nucleus is then $S(0)+V(0) \simeq -50$ MeV. Since the vector potential generated by the ω meson changes its sign under the G-parity transformation, the total potential acting on a $\bar{B}$ becomes strongly attractive, e.g., the $\bar{p}$ would feel the total central potential ≈ 750 MeV deep in the nuclear interior.

G-parity represents a valid concept for the long- and medium-range $\bar{B}$ potential. However, the $\bar{B}$ annihilation plays a crucial role in the $\bar{B}$–nucleus interactions. It has a major contribution in the short-range part of the interaction and it is not clear to what extent it affects the elastic part of the potential. Moreover, various many-body effects could cause deviations from the G-parity transformed coupling constants in the nuclear medium as well [27]. Therefore, G-parity should be regarded as a mere starting point to determine the $\bar{B}$–meson coupling constants in standard RMF models.

The depth of the $\bar{B}$ potential in the nuclear medium is still quite uncertain. The experiments with antiprotonic atoms, $\bar{p}$ scattering off nuclei and $\bar{p}$ production in proton–nucleus and nucleus–nucleus collisions suggest that the real part of the $\bar{p}$ potential should be in the range of $-(100$ - $300)$ MeV at normal nuclear density [7,9,29]. Therefore, following Refs. [27–31], we introduce a uniform scaling factor ξ for the $\bar{B}$–meson coupling constants:

$$g_{\sigma\bar{B}} = \xi\, g_{\sigma B}, \quad g_{\omega\bar{B}} = -\xi\, g_{\omega B}, \quad g_{\rho\bar{B}} = \xi\, g_{\rho B}\ . \tag{2.32}$$

In our calculations, we adopt the value $\xi = 0.2$ which provides the real part of the $\bar{p}$ potential consistent with $\bar{p}$ atom data [2]. It is to be noted that we assume the same value of the scaling factor ξ also for antihyperon–meson couplings due to lack of experimental information on antihyperon potential in the nuclear medium at low energies.

The equations of motion (2.9), (2.25) and (2.26) for a nucleus with antibaryon are derived on the Hartree level where each particle moves in mean fields created by *all* particles bound in the nucleus. It means that the (anti)baryon feels in addition a kind of 'attraction' as well as 'repulsion' from itself. In ordinary nuclei this self-interaction has only a minor (1/A) effect. However, the potential acting on the

[2]Recently, the Non-Linear Derivative model [38] was developed which incorporates momentum dependence of the mean fields and yields a $\bar{p}$ potential consistent with available experimental data while retaining the G-parity symmetry

antibaryon in a nucleus is much deeper than the potential acting on nucleons and the role of the $\bar{B}$ self-interaction could become pronounced. We verified that for the scaling factor $\xi = 0.2$ the effect of the $\bar{B}$ self-interaction is small and can be safely neglected [175].

$\bar{p}$ Absorption

The antibaryon annihilation in the nuclear medium is an indispensable part of a realistic model of the $\bar{B}$–nucleus interaction. In the present work, we take into account only the $\bar{p}$ absorption in a nucleus. The antihyperon absorption is not considered since there are no relevant data on the annihilation of antihyperons in the nuclear medium.

The $\bar{p}$ absorption in a nucleus is described by the imaginary part of an optical potential constructed in a '$t\rho$' form following optical model phenomenology [9]:

$$2\mu \mathrm{Im}V_{\mathrm{opt}}(r) = -4\pi \left(1 + \frac{\mu}{m_N}\frac{A-1}{A}\right) \mathrm{Im}b_0 \rho(r) \ , \tag{2.33}$$

where μ is the $\bar{p}$–nucleus reduced mass. The nuclear density distribution $\rho(r)$ is evaluated within the RMF model and the effective scattering length $\mathrm{Im}b_0 = 1.9$ fm, value of which was obtained by fitting $\bar{p}$ atom data [9].[3]

We assume that the global parameter $\mathrm{Im}b_0$ involves annihilation channels which are listed in Table 2.1 together with the corresponding branching ratios B_c. They are sorted according the number of mesons in the final state. Following Ref. [27], we include only direct decay channels, i.e., only non-resonant contributions and no further decay of produced mesons are taken into account. Moreover, we consider annihilation channels containing kaons.

The parameter $\mathrm{Im}b_0$ accounts for the $\bar{p}$ absorption at or very close to threshold. When considering the annihilation of the deeply-bound antiproton inside the nucleus, the phase space for annihilation products should be considerably reduced. We thus take into account the suppression of phase space by introducing suppression factors f_{s} for considered annihilation channels. The suppression factors f_s for

[3] The value of $\mathrm{Im}b_0$ was determined for a finite-range (FR) interaction, where original densities were replaced by 'folded' densities, while here it was applied to construct a zero-range '$t\rho$' potential. We checked that the RMF densities yield r.m.s. radii larger than the unfolded densities used in the $\bar{p}$ atom analysis and thus effectively approximate the FR 'folded' densities in Ref. [9].

two-body decay channels were evaluated with the help of the formula [177]:

$$f_{\rm s} = \frac{M^2}{s}\sqrt{\frac{[s-(m_1+m_2)^2][s-(m_1-m_2)^2]}{[M^2-(m_1+m_2)^2][M^2-(m_1-m_2)^2]}}\Theta(\sqrt{s}-m_1-m_2)\ , \qquad (2.34)$$

where m_1, m_2 are the masses of the annihilation products, $M = 2m_N$ and s is the Mandelstam variable. The energy available for the annihilation products at vacuum at rest is $\sqrt{s} = 2m_N$. In the nuclear medium this energy is reduced due to the binding of the antiproton and nucleon, and non-zero momenta of the annihilating partners. In the case of channels containing more than 2 particles in the final state the suppression factors $f_{\rm s}$ were calculated using the Monte Carlo simulation tool PLUTO [178]. They were evaluated as a ratio of Dalitz plot area for reduced $\sqrt{s}$ and vacuum $\sqrt{s} = 2m_N$. For channels containing more than 4 particles in the final

Table 2.1: The $\bar{p}N$ annihilation channels. Here, n_f is the number of decay products and B_c denotes the vacuum branching ratio of a particular decay channel† at rest. Table adapted from author's publication [175].

n_f	channel	B_c [%]	n_f	channel	B_c [%]
2	$2\pi^0$	0.07		$\pi^+\pi^-\pi^0$	1.8
	$\pi^+\pi^-$	0.31		$\pi_0 K_S K_L$	$6.7{\cdot}10^{-4}$
	$\pi^0\rho^0$	1.7		$\pi^\pm K^\mp K_S$	$2.7{\cdot}10^{-3}$
	$\pi^\pm\rho^\mp$	0.9		ωK^+K^-	$2.3{\cdot}10^{-3}$
	$\pi^0\omega$	0.6	4	$4\pi^0$	0.5
	$\rho^0\omega$	2.3		$\pi^+\pi^-2\pi^0$	7.8
	$\omega\eta$	1.5		$2\pi^+2\pi^-$	4.2
	2ω	3.0	5	$5\pi^0$	0.5
	K^+K^-	$1.0\ {\cdot}10^{-3}$		$\pi^+\pi^-3\pi^0$	20.1
	$K_S K_L$	$7.9{\cdot}10^{-4}$		$2\pi^+2\pi^-\pi^0$	10.4
3	$2\pi^0\eta$	0.7	6	$\pi^+\pi^-4\pi^0$	1.9
	$\pi^+\pi^-\eta$	1.3		$2\pi^+2\pi^-2\pi^0$	13.3
	$2\pi^0\omega$	2.6		$3\pi^+3\pi^-$	2.0
	$\pi^+\pi^-\omega$	6.6	7	$3\pi^+3\pi^-\pi^0$	1.9
	$\pi^+\pi^-\rho^0$	3.6		$2\pi^+2\pi^-3\pi^0$	4.0

†The non-strange annihilation channels and their branching ratios are taken from Ref. [27] (see also referencies therein). Branching ratios for channels containing kaons are taken from Ref. [14]

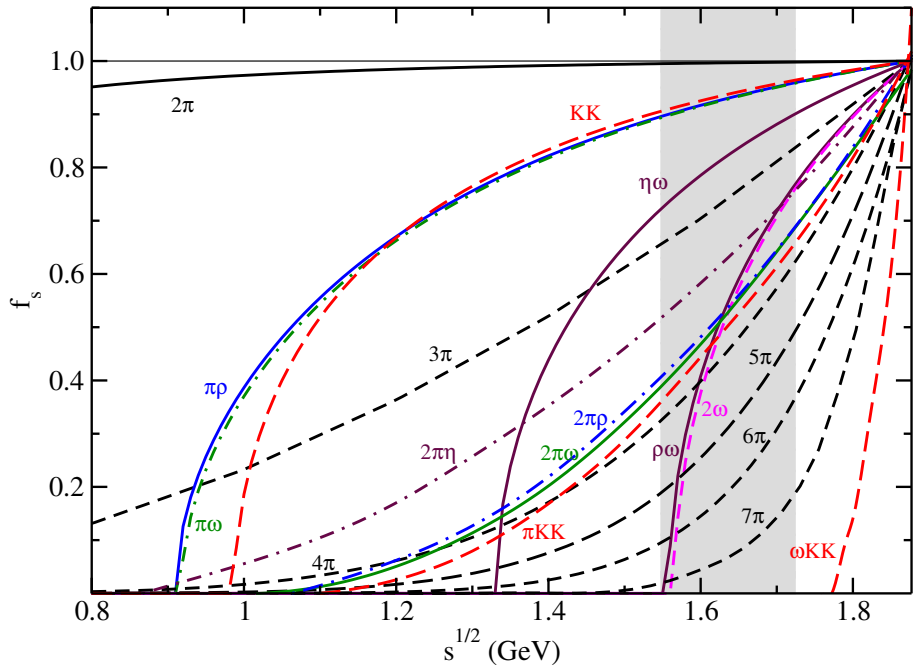

Figure 2.1: The phase space suppression factors $f_{\rm s}$ as a function of the c.m. energy $\sqrt{s}$. The range of $\sqrt{s}$ relevant for $\bar{p}$-nuclear states is denoted by gray area. Figure adapted from author's publication [175].

state we expressed the decay products in terms of two or three effective particles, i.e., we decomposed the n-body phase space ϕ_n into smaller subspaces for two or three effective particles according the formula [177]:

$$d\phi_n(P;p_1,\ldots,p_n) = d\phi_j(q;p_1,\ldots,p_j)\times d\phi_{n-j+1}(P;q,p_{j+1},\ldots,p_n)(2\pi)^3 dq^2 \ . \qquad (2.35)$$

Here, $q^2 = (\sum_{i=1}^{j} E_i)^2 - |\sum_{i=1}^{j} \vec{p}_i|^2$ with $j = 2$ or 3, P is the 4-momentum of the annihilating pair and p_i are the 4-momenta of the annihilation products.

The calculated suppression factors f_s for considered annihilations channels as a function of c.m. energy $\sqrt{s}$ are presented in Fig. 2.1. As the energy $\sqrt{s}$ decreases many channels become considerably suppressed or even closed. The shaded area denotes the energy region relevant for $\bar{p}$-nuclear state calculations.

The overall absorptive $\bar{p}$ potential, which is added to the real $\bar{p}$ potential constructed within the RMF model, acquires the form

$$\mathrm{Im}V_{\bar{p}}(r,\sqrt{s},\rho) = \sum_{\rm channel} B_c f_{\rm s}(\sqrt{s})\mathrm{Im}V_{\rm opt}(r) \ . \qquad (2.36)$$

2.3 Antihadron–Nucleus Interactions within Microscopical Approach

In this section, we present the construction of an $\bar{H}$–nucleus optical potential ($\bar{H} = \bar{p},\ K^-$) based on $\bar{H}N$ scattering amplitudes derived from microscopic models of $\bar{H}N$ interactions. In principle, one should construct the full many-body $\bar{H}$–nucleus amplitude from the two-body $\bar{H}N$ scattering amplitudes. However, this is an extremely difficult (or even unfeasible) task in the mass region considered in this work. Instead, we construct the $\bar{H}$–nucleus optical potential in a '$t\rho$' form following the multiple scattering theory [179]. The complicated many-body $\bar{H}$–nucleus amplitude is thus expressed as a sum of the $\bar{H}N$ amplitudes on each nucleon of the nuclear core.

The $\bar{p}$–nucleus optical potential is constructed using $\bar{p}N$ scattering amplitudes derived from the latest version of the Paris $\bar{N}N$ potential. This potential contains long- and medium-range meson-exchange interactions and a short-range phenomenological part describing the $\bar{N}N$ annihilation.

The theoretical description of the K^-N interaction is provided by chirally-motivated meson–baryon interaction models. We employ six different state-of-the-art meson–baryon interaction models and explore the model dependence of our calculations. Moreover, we consider K^- multinucleon interactions, which were found to be crucial to account for K^- atom data [133], in terms of a phenomenological optical potential.

2.3.1 Optical Potential

The optical potential describing the the S-wave $\bar{H}$–nucleus interaction is constructed in a '$t\rho$' form as follows:

$$2E_{\bar{H}}V_{\rm opt}(r) = -4\pi\left(F_0\frac{1}{2}\rho_p(r) + F_1\left(\frac{1}{2}\rho_p(r) + \rho_n(r)\right)\right)\ , \tag{2.37}$$

where $E_{\bar{H}} = m_{\bar{H}} - B_{\bar{H}}$ with $B_{\bar{H}} > 0$ being the antihadron binding energy, F_0 and F_1 are isospin 0 and 1 in-medium amplitudes, and $\rho_p(r)$ [$\rho_n(r)$] is the proton (neutron) density distribution calculated within the RMF NL-SH model [164]. The in-medium amplitudes F_0 and F_1 entering Eq. (2.37) are constructed from the free-space $\bar{H}N$ amplitudes using the multiple scattering approach of Wass *et al.* [180] (WRW) in

order to account for Pauli correlations in the nuclear medium

$$F_1 = \frac{\frac{\sqrt{s}}{m_N} f^{\rm S}_{\bar{H}n}(\sqrt{s})}{1+\frac{1}{4}\xi_k \frac{\sqrt{s}}{m_N} f^{\rm S}_{\bar{H}n}(\sqrt{s})\rho(r)} \ , \quad F_0 = \frac{\frac{\sqrt{s}}{m_N}[2f^{\rm S}_{\bar{H}p}(\sqrt{s}) - f^{\rm S}_{\bar{H}n}(\sqrt{s})]}{1+\frac{1}{4}\xi_k \frac{\sqrt{s}}{m_N}[2f^{\rm S}_{\bar{H}p}(\sqrt{s}) - f^{\rm S}_{\bar{H}n}(\sqrt{s})]\rho(r)} \ . \quad (2.38)$$

Here, $f^{\rm S}_{\bar{H}n}$ ($f^{S}_{\bar{H}p}$) denotes the free-space c.m. $\bar{H}n$ ($\bar{H}p$) S-wave scattering amplitude derived from the corresponding $\bar{H}N$ interaction model and $\rho(r) = \rho_p(r) + \rho_n(r)$. The factor $\sqrt{s}/m_N$ transforms the amplitudes from the two-body frame to the $\bar{H}$–nucleus frame. The Pauli correlation factor ξ_k is defined as follows

$$\xi_k = \frac{9\pi}{k_{\rm F}^2} \left(4 \int_0^\infty \frac{dr}{r} \exp(ikr) j_1^2(k_{\rm F} r) \right) \ , \quad (2.39)$$

where $j_1(k_{\rm F} r)$ is the spherical Bessel function, $k_{\rm F}$ is the Fermi momentum, the antihadron momentum $k = \sqrt{(\epsilon_{\bar{H}} - m_{\bar{H}})^2 - m_{\bar{H}}^2}$, $\epsilon_{\bar{H}} = -B_{\bar{H}} - {\rm i}\Gamma_{\bar{H}}/2$ ($B_{\bar{H}} > 0$), and $\Gamma_{\bar{H}}$ is the antihadron width. The integral in Eq.(2.39) can be solved analytically. The resulting expression is of the form

$$\xi_k = \frac{9\pi}{k_{\rm F}^2} \left[1 - \frac{q^2}{6} + \frac{q^2}{4} \left(2 + \frac{q^2}{6} \right) \ln \left(1 + \frac{4}{q^2} \right) - \frac{4}{3} q \left(\frac{\pi}{2} - \arctan \left(\frac{q}{2} \right) \right) \right] \ , \quad (2.40)$$

where $q = -ik/k_{\rm F}$. Since the $\bar{p}$ and K^- have both $I = 1/2$ the isospin structure of the in-medium amplitudes F_0 and F_1 (2.38) is the same in both cases.

Dirac Equation with Optical Potential

The binding energies $B_{\bar{p}}$ and widths $\Gamma_{\bar{p}}$ of $\bar{p}$ quasi-bound states in a nucleus are obtained by solving self-consistently the Dirac equation with the corresponding optical potential

$$[-i\alpha \cdot \nabla + \beta m_{\bar{p}} + V_{\rm opt}(r)]\psi_{\bar{p}} = \epsilon_{\bar{p}} \psi_{\bar{p}}, \quad (2.41)$$

where $m_{\bar{p}}$ is the mass of the antiproton and $\epsilon_{\bar{p}} = -B_{\bar{p}} - {\rm i}\Gamma_{\bar{p}}/2$. The optical potential $V_{\rm opt}$ enters the Dirac equation as the time component of a 4-vector. In order to test our computational code and verify numerical stability of our results obtained by solving the Dirac equation with a complex optical potential we performed comparable calculations using the Schrödinger equation as well. We set the same input for both equations and checked that they yield the same results. In Table 2.2, we present the $1s$ $\bar{p}$ binding energy and width in ^{16}O, calculated using the Dirac equation (2.41) and Schrödinger equation. The agreement of both equations is satisfactory.

Table 2.2: $1s$ $\bar{p}$ binding energy $B_{\bar{p}}$ and corresponding width $\Gamma_{\bar{p}}$ in ^{16}O (in MeV), calculated using the Dirac and Schrödinger equations.

$^{16}\mathrm{O}+\bar{p}$	Dirac eq.	Schrödinger eq.
$B_{\bar{p}}$	175.9	175.2
$\Gamma_{\bar{p}}$	263.7	263.4

Klein–Gordon Equation with Optical Potential

The calculations of K^-–nuclear quasi-bound states are based on solving the Klein–Gordon equation

$$\left[-\nabla^2 - \tilde{\omega}^2_{K^-} + m^2_{K^-} + \Pi_{K^-}(\omega_{K^-}, \rho(r))\right] \phi_{K^-} = 0 \ , \tag{2.42}$$

which yields antikaon binding energies B_{K^-} and widths Γ_{K^-}. Here, ϕ_{K^-} denotes the K^- wave function, $\tilde{\omega}_{K^-} = m_{K^-} - B_{K^-} - \mathrm{i}\Gamma_{K^-}/2 - V_C = \omega_{K^-} - V_C$, m_{K^-} is the K^- mass, $\Pi_{K^-} = 2\mathrm{Re}(\omega_{K^-})V_{\mathrm{opt}}(r)$ is the K^-–nucleus optical potential and $\rho(r)$ is the nuclear density distribution calculated within the RMF NL-SH model [164]. The Coulomb potential V_C introduced via the minimal substitution [181] was calculated within the RMF model as well.

2.3.2 Paris $\bar{N}N$ Potential

In this thesis, we adopt the 2009 version of the Paris $\bar{N}N$ potential model [41] in the description of the $\bar{p}$–nucleus interaction. The Paris $\bar{N}N$ potential consists of long-range one-pion exchange, correlated and uncorrelated two-pion exchange, and medium-range part represented by the ω and A_1 meson exchange. They are derived using the G-parity transformation of the corresponding NN potential. The short-range part of the $\bar{N}N$ potential responsible for the $\bar{p}$ annihilation is described by a phenomenological term. The parameters of the potential are obtained by fitting low-energy $\bar{p}N$ scattering data consisting of $\bar{p}N$ elastic and annihilation cross-sections (see [182, 183] and references therein) and strong interaction level shifts and widths in antiprotonic hydrogen [184, 185].

There exist other realistic $\bar{N}N$ potential models such as the Bonn $\bar{N}N$ meson-exchange model [42], Zhou–Timmermans model [43] or models based on chiral effective field theory (EFT), Bonn–Jülich chiral N^{2}LO [44] or N^{3}LO [45] potential models,

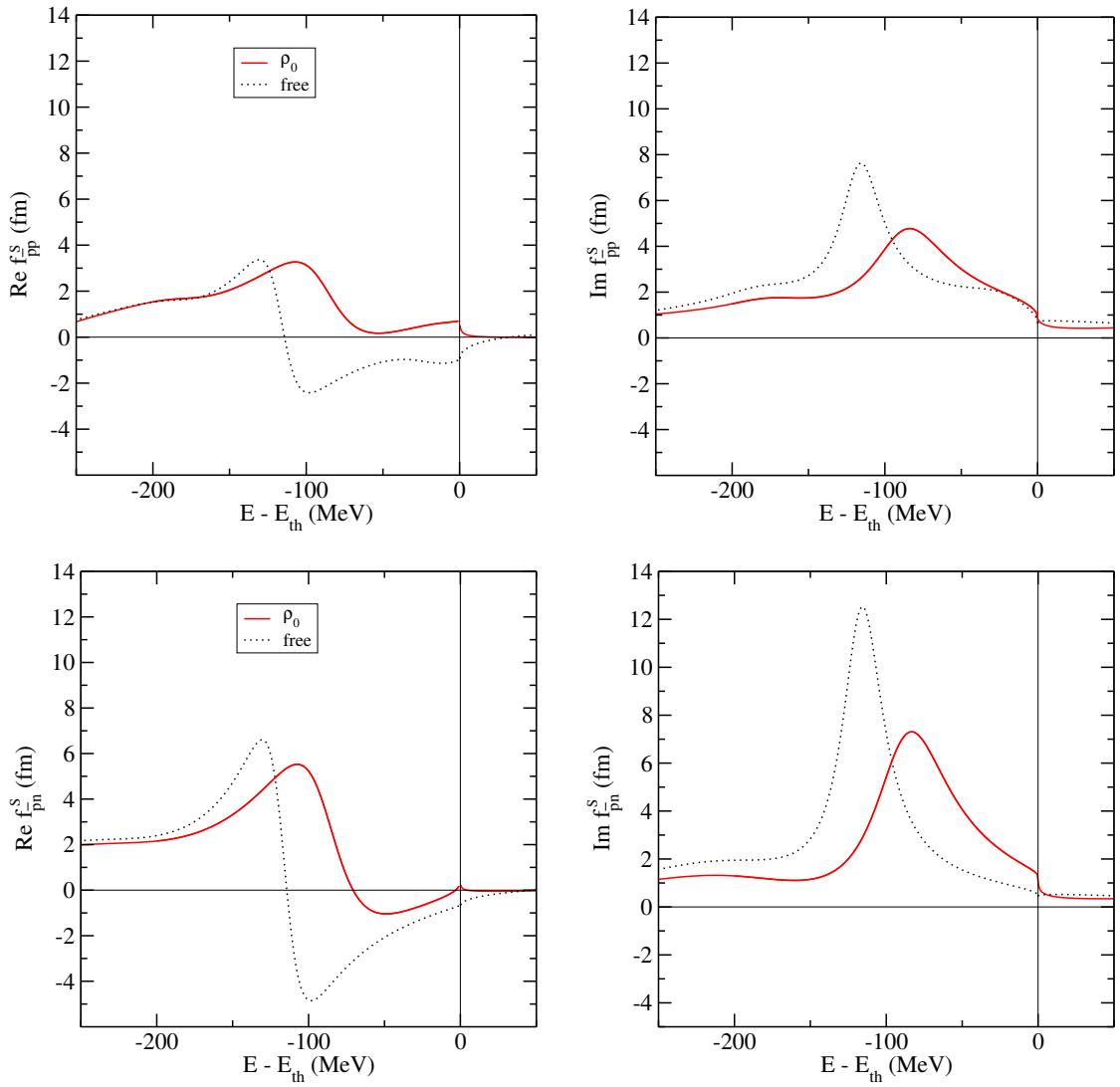

Figure 2.2: Energy dependence of the Paris 09 $\bar{p}p$ (top) and $\bar{p}n$ (bottom) S-wave c.m. amplitudes: in-medium (Pauli blocked) amplitudes for $\rho_0 = 0.17$ fm^{-3} (solid line) are compared with the free-space amplitudes (dotted line). Figure adapted from author's publication [186].

which could be applied to $\bar{p}$-nuclear states calculations as well. However, the Paris potential has been recently confronted with the antiproton atom data [46], which has stimulated us to apply it in the present calculations of $\bar{p}$-nuclear quasi-bound states.

The free-space c.m. S-wave $\bar{p}p$ and $\bar{p}n$ scattering amplitudes entering Eq. (2.38) are derived from the Paris $\bar{N}N$ potential as appropriate mixtures of isospin 0 and 1 $\bar{N}N$ amplitudes evaluated as angular momentum averages. In Fig. 2.2, we present free-space c.m. $\bar{p}p$ (top panel) and $\bar{p}n$ (bottom panel) S-wave scattering

amplitudes compared with medium modified amplitudes (2.38) at saturation density $\rho_0 = 0.17$ fm^{-3}. The amplitudes, plotted as a function of the energy shift $\delta\sqrt{s} = E - E_{\rm th}$, with $E_{\rm th} = m_N + m_{\bar{p}}$, vary considerably with the energy below threshold. The peaks of in-medium amplitudes are lower in comparison with the free-space ones and shifted by ≈ 30 MeV towards threshold. Moreover, the peaks of imaginary in-medium amplitudes are reduced much more than the peaks of real in-medium amplitudes. The real in-medium $\bar{p}p$ amplitude becomes attractive in the entire energy region below threshold. The real part of the in-medium $\bar{p}n$ amplitude is attractive for $\delta\sqrt{s} \leq -70$ MeV with a small repulsive dip near threshold.

P-wave Interaction

The analysis of $\bar{p}$ atom data [46] revealed that it is necessary to supplement the Paris S-wave potential by the P-wave interaction to make the real $\bar{p}$ potential attractive in the relevant low-density region of a nucleus. To incorporate the P-wave interaction in our model we supplement the r.h.s. of the S-wave optical potential in Eq. (2.37) [$2E_{\bar{p}}V^S_{\rm opt} = q(r)$] by a gradient term [46, 187, 188]:

$$2E_{\bar{p}}V_{\rm opt}(r) = q(r) + 3\nabla \cdot \alpha(r)\nabla \ . \tag{2.43}$$

The factor $2l + 1 = 3$ in the P-wave part is introduced to match the normalization of the Paris $\bar{N}N$ scattering amplitudes and

$$\alpha(r) = 4\pi\frac{m_N}{\sqrt{s}}\left(f^P_{\bar{p}p}(\delta\sqrt{s})\rho_p(r) + f^P_{\bar{p}n}(\delta\sqrt{s})\rho_n(r)\right) \ . \tag{2.44}$$

Here, $f^P_{\bar{p}p}(\delta\sqrt{s})$ and $f^P_{\bar{p}n}(\delta\sqrt{s})$ represent the P-wave $\bar{p}p$ and $\bar{p}n$ free-space c.m. scattering amplitudes, respectively. We do not consider any medium modifications of the P-wave amplitudes since we assume that the P-wave potential should contribute mainly near the surface of the nucleus due to its gradient form. The free-space $\bar{p}p$ and $\bar{p}n$ P-wave scattering amplitudes are plotted as a function of the energy shift $\delta\sqrt{s} = E - E_{\rm th}$ in Fig. 3.6. The amplitudes exhibit again considerable energy dependence below (but also above) threshold.

The analysis [46] also revealed that the optical potential constructed from the Paris S- and P-wave amplitudes fails to reproduce the $\bar{p}$ atom data. It is mainly due to the P-wave amplitude — its real and imaginary parts had to be scaled by different factors to get reasonable fit. On the contrary, the optical potential based on the Paris S-wave potential supplemented by a purely phenomenological P-wave

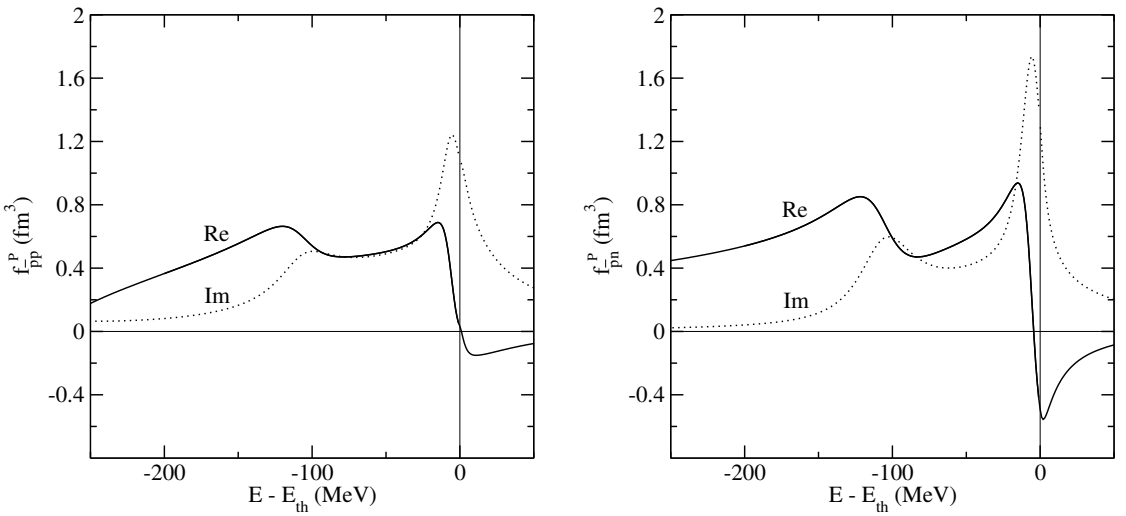

Figure 2.3: Energy dependence of the Paris 09 $\bar{p}p$ (left) and $\bar{p}n$ (right) P-wave c.m. free-space amplitudes. Figure adapted from author's publication [186].

term with $f^P_{\bar{p}N} = 2.9 + i1.8$ fm^3 fits the data well. In our calculations, we adopt both P-wave amplitudes, Paris as well as phenomenological, in order to study their effect on binding energies and widths of $\bar{p}$-nuclear states.

2.3.3 Chiral Coupled-Channel Meson–Baryon Interaction Models

Meson–baryon interactions at low and intermediate energies are currently described within microscopic models based on effective chiral Lagrangians that implement dynamics and symmetries of QCD. The existence of hadronic resonances at energies close to threshold hinders the use of perturbative approaches, such as the chiral perturbation theory. The state-of-the-art description of low-energy meson–baryon interactions is provided by the so called 'chirally-motivated meson–baryon coupled-channel interaction models' which represent synergy of chiral perturbation theory and coupled channel T-matrix resummation techniques [69,83,87–89,98,189]. The detailed description of these chiral models is beyond the scope of this thesis. Below, we present only the basic ingredients of their construction.

The meson–baryon interactions (including the $\bar{K}N$ interaction) are determined by solving coupled-channel Lippmann–Schwinger equation for the T-matrix

$$T_{ij} = V_{ij} + V_{ik} G_k T_{kj} \ , \tag{2.45}$$

where V_{ij} are matrix elements of the interaction matrix kernel, G_k stands for the intermediate state Green's function in a given channel and the indices ij run over the meson–baryon coupled channels. The following meson–baryon interaction channels are usually considered: $\bar{K}N$, $\pi\Lambda$, $\pi\Sigma$, $\eta\Lambda$, $\eta\Sigma$ and $K\Xi$. The meson–baryon potentials V_{ij} are constructed to match the equivalent amplitudes generated by the chiral Lagrangian at leading or next-to-leading order.

However, the multichannel form of the T-matrix (2.45) is not suitable for calculations of K^--nuclear bound states. Even in the most sophisticated three-body Faddeev equations for the $\bar{K}NN$ system, the problem is reduced to the 2 channel ($\bar{K}N$–$\pi\Sigma$) formalism [190–192]. In our calculations, we use the one-channel ($\bar{K}N$) reduction which preserves the full coupled-channel nature of the underlying dynamics [193]. For this purpose the one-channel T-matrix is constructed as follows

$$T_{11} \sim T_{\rm eff} = V_{\rm eff} + V_{\rm eff} G_1 T_{\rm eff} \ . \tag{2.46}$$

The effective potential $V_{\rm eff}$ is a sum of the bare interaction in channel 1 (the $\bar{K}N$ channel) and all contributions from the other $N-1$ channels

$$V_{\rm eff} = V_{11} + \sum_{2\leq i\leq N} V_{1i} G_i V_{i1} + \sum_{2\leq i,j\leq N} V_{1i} G_i T_{ij}^{(N-1)} G_j V_{j1} \ . \tag{2.47}$$

Here, $T_{ij}^{(N-1)}$ is the resummation of interactions in all channels except the channel 1. The free parameters of the interaction model are fitted to low-energy K^-N observables such as the K^-p total cross sections [66, 94, 95], threshold branching ratios [92, 93], and $1s$ energy shifts and widths of kaonic hydrogen [67].

In this thesis, we adopt 6 different chiral coupled-channel meson–baryon interaction models, namely: Prague (P) [83], Kyoto–Munich (KM) [87], Murcia (M1 and M2) [88], and Bonn (B2 and B4) [89]. They are all based on chiral SU(3) next-to-leading-order (NLO) Lagrangian but they differ in approaches to the solution of the coupled-channel equations and in applied fitting procedures (in the Bonn models higher partial waves were included in the fit whereas in the other models only S-waves were considered). The free-space S-wave c.m. scattering amplitudes f_{K^-p} and f_{K^-n} derived from all models considered in our work are plotted as a function of energy in Fig. 2.4. The K^-p amplitudes agree with each other at and above threshold (except the Bonn models B2 and B4) since they were fitted to the same data in this energy region. Below threshold, i.e., in the energy region relevant to K^--nuclear quasi-bound state calculations, the amplitudes differ from each other considerably.

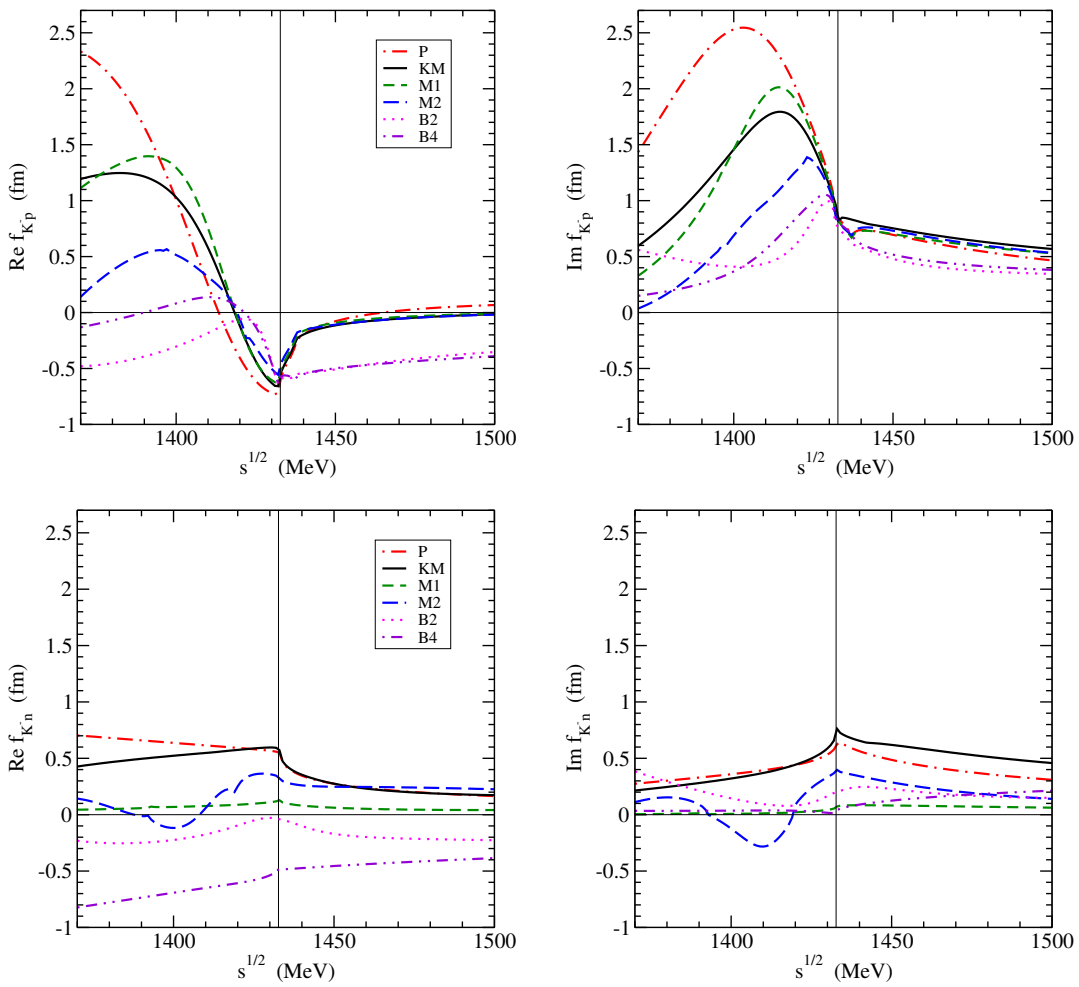

Figure 2.4: Energy dependence of real (left) and imaginary (right) parts of free-space c.m. K^-p (top) and K^-n (bottom) amplitudes in considered chiral models (see text for details). Thin vertical lines mark threshold energies. Figure adapted from author's publication [194].

Moreover, they exhibit strong energy dependence below threshold due to the existence of the $\Lambda(1405)$ resonance. On the other hand, the K^-n amplitudes in these models do not match each other even at and above threshold and their energy dependence is not so pronounced as in the K^-p case. The strong energy dependence of the K^-p amplitudes due to the $\Lambda(1405)$ requires a proper self-consistent scheme for the construction of the K^--nucleus optical potential. The method of treating the energy dependence will be discussed in the next section.

The free-space K^-p and K^-n scattering amplitudes enter the construction of in-medium amplitudes (2.38) which subsequently define the K^-–nucleus optical potential. The corresponding in-medium amplitudes at saturation density $\rho_0 = 0.17$ fm^{-3}

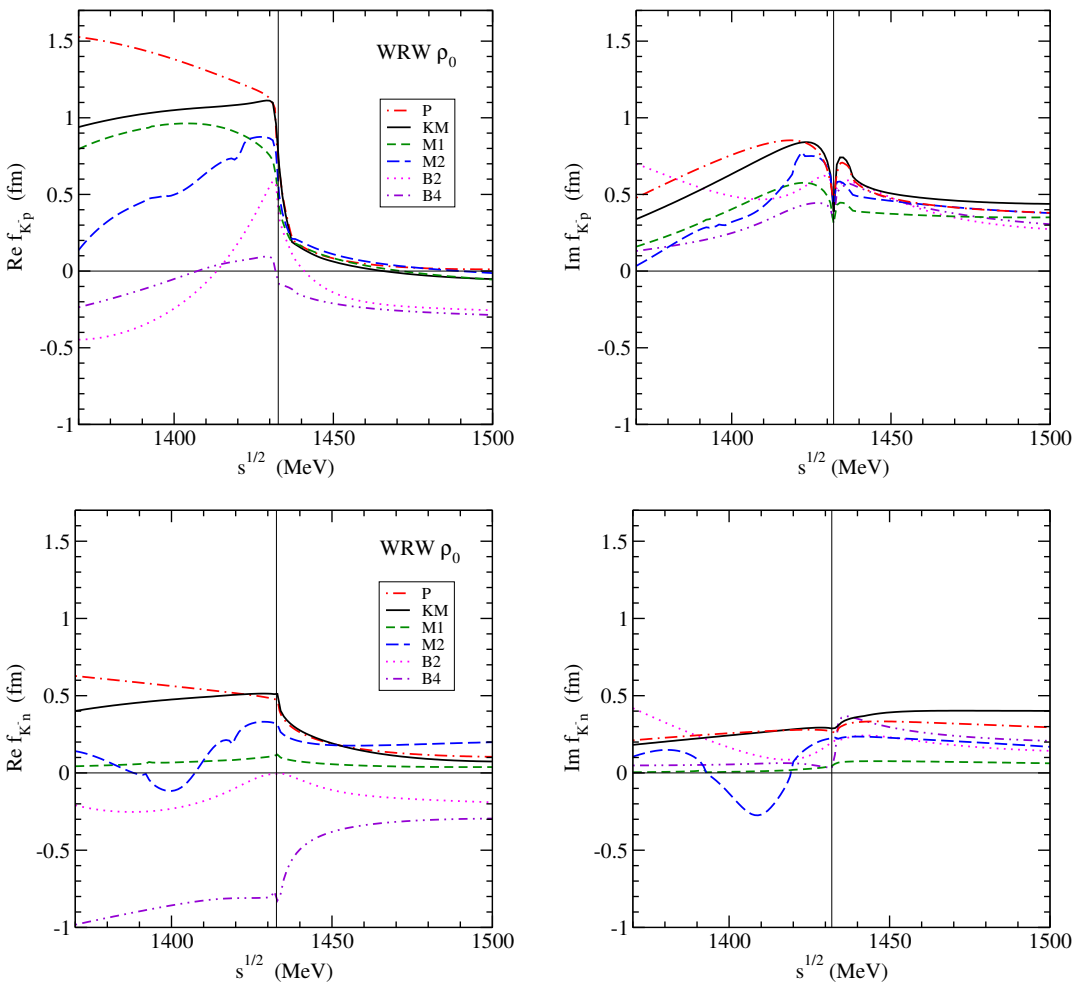

Figure 2.5: Energy dependence of real (left) and imaginary (right) parts of WRW modified c.m. K^-p (top) and K^-n (bottom) amplitudes at $\rho_0 = 0.17$ fm^{-3} in considered models. Thin vertical lines mark threshold energies. Figure adapted from author's publication [194].

are presented in Fig. 2.5. The WRW procedure significantly affects the K^-p amplitudes (see Fig. 2.4 for comparison). The real parts of the amplitudes become attractive in the entire energy region below threshold (except the Bonn models B2 and B4) and the imaginary parts are considerably lowered below threshold. On the other hand, the K^-n amplitudes exhibit only moderate changes in the medium.

In the P model, the Pauli correlations were previously accounted for in a different way (denoted further by 'Pauli'). They were incorporated directly in the Green's function G of Eq. (2.45) where the integration over the meson–baryon momenta was restricted to a region ensuring the nucleon intermediate energy to be above the Fermi level. Moreover, the effect of medium modifications of hadron masses was

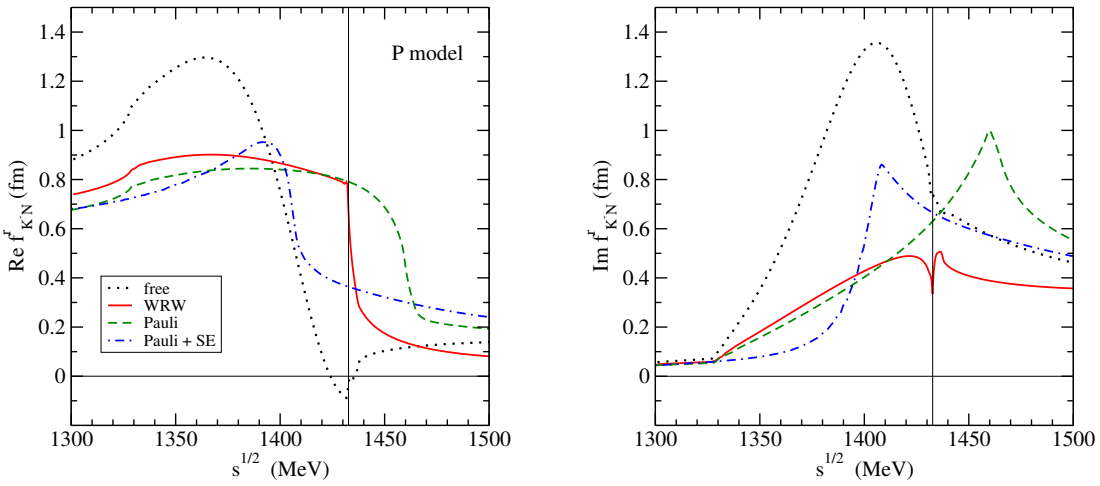

Figure 2.6: Energy dependence of free-space c.m. (dotted line) amplitude $f^r_{K^-N} = \frac{1}{2}(f^r_{K^-p} + f^r_{K^-n})$ compared with WRW modified amplitude (solid line), Pauli (dashed line), and Pauli + SE (dot-dashed line) modified amplitude at $\rho_0 = 0.17$ fm^{-3} in the P model (left: real parts, right: imaginary parts). The thin vertical line indicates the K^-N threshold. Figure adapted from author's publication [194].

considered in the P model by introducing hadron self-energies in the intermediate-state Green's functions [83]. We compared the in-medium amplitudes obtained by the WRW approach with the Pauli amplitudes in the P model to verify that both approaches yield comparable results. In Fig. 2.6, we present Pauli correlated and WRW modified reduced[4] in-medium amplitudes $f^r_{K^-N} = \frac{1}{2}(f^r_{K^-p} + f^r_{K^-n})$ at saturation density $\rho_0 = 0.17$ fm^{-3} as a function of energy. Both approaches yield very similar in-medium K^-N amplitudes below threshold. However, at and above threshold the behavior of Pauli and WRW amplitudes is different. In addition, Fig. 2.6 shows also the in-medium amplitudes including the hadron self-energies (denoted by 'Pauli+SE'). The Pauli+SE, Pauli and WRW modified amplitudes are quite similar to each other in the energy region relevant for K^--nuclear states calculations, but they differ significantly at and above threshold.

[4]In the P model, the amplitudes are given in a separable form $f_{K^-N} = g(p) f^r_{K^-N} g(p')$, where $g(p)$ is a momentum-space form factor (see Ref. [128])

K^- interactions with more nucleons

The above chiral models of meson–baryon interactions account for the K^- absorption on a single-nucleon (mesonic conversion mode)

$$K^-N \to \pi Y \ , \quad Y = \Sigma, \Lambda, \tag{2.48}$$

with threshold about 100 MeV and 180 MeV, respectively, below the total K^-N mass. The branching ratio for the K^- single-nucleon absorption at rest measured in bubble chamber experiments at CERN is about 80% [130–132]. However, in the nuclear medium the K^- absorption on two or more nucleons (nonmesonic decay mode), such as

$$K^-NN \to NY \ , \tag{2.49}$$

takes place as well. This mode with reaction rate of 20% at rest is dominated by the channel with $N\Sigma$ in the final state. It has threshold about 140 MeV lower than the single-nucleon absorption threshold. The multinucleon absorption is not implemented in chiral models and is usually described by a phenomenological potential [7, 8, 133].

When the antikaon is deeply-bound in a nucleus, the single-nucleon absorption mode becomes substantially suppressed or even closed and the K^- absorption on several nucleons prevails. Therefore, the K^- multinucleon interactions have to be taken into account for proper description of the K^- behavior in the nuclear medium. Recently, Friedman and Gal [133] supplemented the K^- single-nucleon potential constructed within all chiral meson–baryon interaction models mentioned above by a phenomenological term representing the K^- multinucleon interactions of the following form

$$2\mathrm{Re}(\omega_{K^-})V^{(2)}_{K^-} = -4\pi B(\frac{\rho}{\rho_0})^\alpha \rho \ . \tag{2.50}$$

The values of the complex amplitude B and positive exponent α were obtained by fitting kaonic atom data for each chiral model separately. They are listed together with their uncertainties in Table 2.3. The total K^- potential, expressed as a sum of the single-nucleon and multinucleon potentials, $V_{K^-} = V^{(1)}_{K^-} + V^{(2)}_{K^-}$, was confronted with available data. Only two models, P and KM, were found to reproduce simultaneously the kaonic atom data and branching ratios of K^- absorptions at rest [133]. It is to be noted that these models are equivalent to each other within uncertainties shown in Table 2.3.

In this work, we adopt all chiral models describing the K^-N interaction and

Table 2.3: Values of the complex amplitude B and exponent α of the phenomenological K^- multinucleon potential $V^{(2)}_{K^-}$ for all chiral meson–baryon interaction models considered in this work. Table adapted from author's publication [194]

	P1	KM1	P2	KM2
α	1	1	2	2
ReB (fm)	-1.3 ± 0.2	-0.9 ± 0.2	-0.5 ± 0.6	0.3 ± 0.7
ImB (fm)	1.5 ± 0.2	1.4 ± 0.2	4.6 ± 0.7	3.8 ± 0.7
	B2	B4	M1	M2
α	0.3	0.3	0.3	1
ReB (fm)	2.4 ± 0.2	3.1 ± 0.1	0.3 ± 0.1	2.1 ± 0.2
ImB (fm)	0.8 ± 0.1	0.8 ± 0.1	0.8 ± 0.1	1.2 ± 0.2

supplement them by the corresponding multinucleon potential $V^{(2)}_{K^-}$. We assume that the main contribution to the amplitude B (2.50) comes from the $K^-NN \to N\Sigma$ conversion. In order to account for phase space suppression for decay products in this channel in the nuclear medium we multiply ImB, which is a constant, by the kinematical suppression factor of the form

$$f_{\Sigma N} = \frac{M^3}{s^{3/2}} \sqrt{\frac{[s-(m_N+m_\Sigma)^2][s-(m_N-m_\Sigma)^2]}{[M^2-(m_N+m_\Sigma)^2][M^2-(m_N-m_\Sigma)^2]}} \Theta(\sqrt{s}-m_N-m_\Sigma) \ , \quad (2.51)$$

where $M = 2m_N + m_{K^-}$ and $\sqrt{s} = M - \delta\sqrt{s}$ [195].

The kaonic atom data probe reliably the real part of the K^-–nucleus potential only up to $\sim$ 25% of ρ_0 and its imaginary part up to $\sim$ 50% of ρ_0. The K^- multinucleon potential $V^{(2)}_{K^-}$ is not fully constrained at densities above these limits and its form is a matter of extrapolation. Therefore, we consider in our calculations different shapes of $V^{(2)}_{K^-}$ for $\rho(r) \geq 0.5\rho_0$. First, the form of Eq. (2.50) is applied in the entire density region (full density option, FD). Second, the potential $V^{(2)}_{K^-}$ is fixed at constant value $V^{(2)}_{K^-}(0.5\rho_0)$ for $\rho(r) \geq 0.5\rho_0$ (half density limit, HD). In the third approximation, the '$t\rho$' form of $V^{(2)}_{K^-}$ is assumed for densities $\rho(r) \geq 0.5\rho_0$ in Eq. (2.50), i.e. $V^{(2)}_{K^-} \sim -4\pi B(0.5)^\alpha \rho$ for $\rho(r) \geq 0.5\rho_0$ ($t\rho$ limit, TR).

2.4 Energy Dependence

The $\bar{H}N$ amplitudes introduced in the previous section exhibit strong energy dependence near and below threshold. This feature requires a proper self-consistent scheme for evaluating the $\bar{H}$ optical potential.

The suppression factors f_s (2.34), $f_{\Sigma N}$ (2.51) and the microscopic $\bar{p}N$ and K^-N scattering amplitudes discussed above are functions of energy given by the Mandelstam variable

$$s = (E_N + E_{\bar{H}})^2 - (\vec{p}_N + \vec{p}_{\bar{H}})^2 \ , \tag{2.52}$$

where $E_N = m_N - B_N$, $E_{\bar{H}} = m_{\bar{H}} - B_{\bar{H}}$, and B_N ($B_{\bar{H}}$) is the nucleon (antihadron) binding energy in a nucleus. When considering the $\bar{H}N$ interaction in the two-body c.m. frame the momentum dependent term vanishes, i.e., $\vec{p}_N + \vec{p}_{\bar{H}} = 0$ and Eq. (2.52) reduces to

$$\sqrt{s}_{\rm M} = \ m_{\bar{H}} + m_N - B_{\bar{H}} - B_N \ . \tag{2.53}$$

However, the annihilation of the antihadron with the nucleon takes place in a nucleus and the momentum dependent term in Eq. (2.52) can no longer be neglected [128]. It provides additional downward energy shift. Its proper self-consistent evaluation is crucial in $\bar{p}$-nuclear as well as K^--nuclear states calculations. Taking into account averaging over the angles $(\vec{p}_N + \vec{p}_{\bar{H}})^2 \approx \vec{p}_N^{\,2} + \vec{p}_{\bar{H}}^{\,2}$, Eq. (2.52) can be rewritten as

$$\sqrt{s}_{\rm J} = E_{\rm th}\left(1 - \frac{2(B_{\bar{H}} + B_{Nav})}{E_{\rm th}} + \frac{(B_{\bar{H}} + B_{Nav})^2}{E_{\rm th}^2} - \frac{T_{\bar{H}}}{E_{\rm th}} - \frac{T_{Nav}}{E_{\rm th}}\right)^{1/2} \ . \tag{2.54}$$

Here, $E_{\rm th} = m_N + m_{\bar{H}}$, B_{Nav} and T_{Nav} are the average binding and kinetic energy per nucleon, respectively, and $T_{\bar{H}}$ represents the $\bar{H}$ kinetic energy. The average binding energy per nucleon B_{Nav} is calculated self-consistently. The kinetic energies are evaluated as corresponding expectation values of the kinetic energy operator $\hat{T} = -\frac{\hbar^2}{2m}\triangle$.

In the studies of kaonic atoms and kaonic nuclei [126, 196, 197] the K^- kinetic energy is usually expressed within the local density approximation as

$$\frac{p_{K^-}^2}{2m_{K^-}} = -B_{K^-} - {\rm Re}V_{K^-} - V_C \ . \tag{2.55}$$

The nucleon kinetic energy is approximated within the Fermi gas model by

$$\frac{p_N^2}{2m_N} = T_N\left(\frac{\rho}{\bar{\rho}}\right)^{2/3} \ , \tag{2.56}$$

where $T_N = 23$ MeV is the average nucleon kinetic energy and $\bar{\rho}$ is the average nuclear density. The input for our K^--nuclear state calculations was adopted from the kaonic atoms analysis by Friedman and Gal [133], therefore we use similar kinematics in our calculations for the sake of consistency. The energy shift $\delta\sqrt{s} = \sqrt{s} - E_{\rm th}$ is expanded near threshold in terms of binding and kinetic energies (to leading order) and the energy argument is of the form:

$$\sqrt{s}_{\rm K} \approx E_{\rm th} - B_N - B_{K^-} - V_C - \beta_N T_N \left(\frac{\rho}{\bar{\rho}}\right)^{2/3} - \beta_{K^-}\left(-B_{K^-} - {\rm Re}V_{K^-}(r) - V_C\right) \ , \tag{2.57}$$

where $\beta_{N(K^-)} = m_{N(K^-)}/(m_N + m_{K^-})$ and $B_N = 8.5$ MeV is the average binding energy per nucleon. After introducing specific forms of density dependence ensuring that $\delta\sqrt{s} \to 0$ as $\rho \to 0$ in agreement with the low-density limit (for details see Ref. [198]) the energy $\sqrt{s}$ in Eq. (2.57) acquires the following form:

$$\sqrt{s}_{\rm E} = E_{\rm th} - B_N\frac{\rho}{\bar{\rho}} - \beta_N\left[B_{K^-}\frac{\rho}{\rho_{\rm max}} + T_N\left(\frac{\rho}{\bar{\rho}}\right)^{2/3} + V_C\left(\frac{\rho}{\rho_{\rm max}}\right)^{1/3}\right] + \beta_{K^-}{\rm Re}V_{K^-}(r) \ , \tag{2.58}$$

where $\rho_{\rm max}$ is the maximal value of the nuclear density. The K^- binding energy B_{K^-} is multiplied by $\rho/\rho_{\rm max}$, which ensures that the K^- kinetic energy expressed in Eq. (2.55) in terms of local density approximation is positive at any nuclear density.

We note that the $\bar{H}$ binding energy $B_{\bar{H}}$ (and ${\rm Re}V_{K^-}$) appears as an argument in the expression for $\sqrt{s}$, which in turn serves as an argument for f_s, $f_{\Sigma N}$, $V_{\rm opt}$ and Π_K in Eqs (2.36), (2.41), (2.42), and (2.51). Therefore, $\sqrt{s}$ has to be determined self-consistently, namely its value obtained by solving the Dirac or Klein–Gordon equation should agree with the value of $\sqrt{s}$ which serves as input in Eqs. (2.36), (2.37), (2.38), and (2.51).

Chapter 3

Results

In this chapter, we present selected results of our self-consistent calculations of antihadron quasi-bound states in nuclei across the periodic table. The results are unique and represent author's original contribution. They were published in prominent scientific journals. The key publications can be found in Appendix B of this thesis.

First, we studied $\bar{B}$–nucleus interactions within the phenomenological RMF approach. We performed calculations of $\bar{B}$ $(\bar{p}, \bar{\Lambda}, \bar{\Sigma}, \bar{\Xi})$ bound in $1s$ states of atomic nuclei with a purely real potential constructed using the G-parity transformation, thus neglecting the $\bar{B}$ absorption. The $\bar{B}$ coupling constants were properly scaled to get the $\bar{p}$ potential consistent with experimental data. We performed static as well as dynamical calculations. We explored the dynamical effects caused by $\bar{B}$ and model dependence of calculated $\bar{B}$ binding energies.

As a next step, we considered $\bar{p}$ absorption inside nuclei by adopting the imaginary part of a phenomenological optical potential. We took into account the phase space suppression for annihilation products and explored various procedures for evaluating the energy available for annihilation.

Then, we performed a similar study of $\bar{p}$-nuclear quasi-bound states with an optical potential based on the 2009 version of the Paris $\bar{N}N$ potential [41]. We considered in-medium modifications of the free-space S-wave scattering amplitudes. We explored the energy and density dependence of the S-wave $\bar{p}$–nucleus potential as well as the role of the $\bar{p}N$ P-wave interaction, and compared the predictions for $\bar{p}$ binding energies and widths with the phenomenological RMF approach.

We calculated K^--nuclear quasi-bound states using recent chiral coupled-channel

models of meson–baryon interactions. First, the K^- single-nucleon optical potential was constructed from the K^-N scattering amplitudes derived within six different meson–baryon interaction models and the model dependence of K^- binding energies and widths was studied. Then we supplemented the K^- single-nucleon optical potential by a phenomenological term describing K^- interactions with two and more nucleons. We explored the effect of the K^- multinucleon interactions on K^- binding energies and widths.

3.1 $\bar{B}$-Nuclear Quasi-Bound States

First, we explored $\bar{B}$-nuclear bound states within the RMF approach without considering $\bar{B}$ absorption in a nucleus. The real part of the $\bar{B}$–nucleus optical potential was constructed using the G-parity transformation of relevant coupling constants scaled by factor $\xi = 0.2$ in order to yield the $\bar{p}$ potential consistent with antiproton atom data. Due to the lack of information on antihyperon potential in the medium we assumed the same value of the scaling factor for antihyperon–meson couplings as well.

Below we present the most important results of this study published in *POS INPC2016 (2017) 280* and *Nucl. Phys.* ***A 945*** *(2016) 197*. These publications are attached in Appedix B.1 and B.2, respectively.

In Fig. 3.1, we present the potential acting on a baryon (B) in $1s$ state in ^{16}O (left) compared with the potential acting on an antibaryon ($\bar{B}$) in the same nucleus (right), calculated dynamically in the TM2 model and scaling factor $\xi = 0.2$. All antibaryons feel attractive potential due to the G-parity transformation (note that even $\bar{\Sigma}_0$ feels attraction inside the nucleus though the Σ_0 potential is repulsive). The potential acting on $\bar{B}$ is deeper than the one acting on B inside the nucleus, which indicates that the antibaryons would be bound more strongly than baryons. The $\bar{p}$ feels the deepest potential from all antibaryons. The antihyperon potential is shallower due to the weaker coupling to the meson fields [see Eq. (2.31)].

The antibaryon embedded in a nucleus affects the nuclear core. In order to explore the extent of the core polarization we performed static as well as dynamical calculations. In the static calculations, the core nucleus is not affected by the presence of extra $\bar{B}$ [i.e., the source terms from $\bar{B}$ are omitted from the r.h.s. of Eqs. (2.26)]. In the dynamical calculations, the polarization of the nuclear core due to $\bar{B}$, i.e., changes in the nucleon binding energies and densities, is taken into account [the source terms from $\bar{B}$ are considered in the r.h.s. of Eqs. (2.26)]. In Fig. 3.1, the

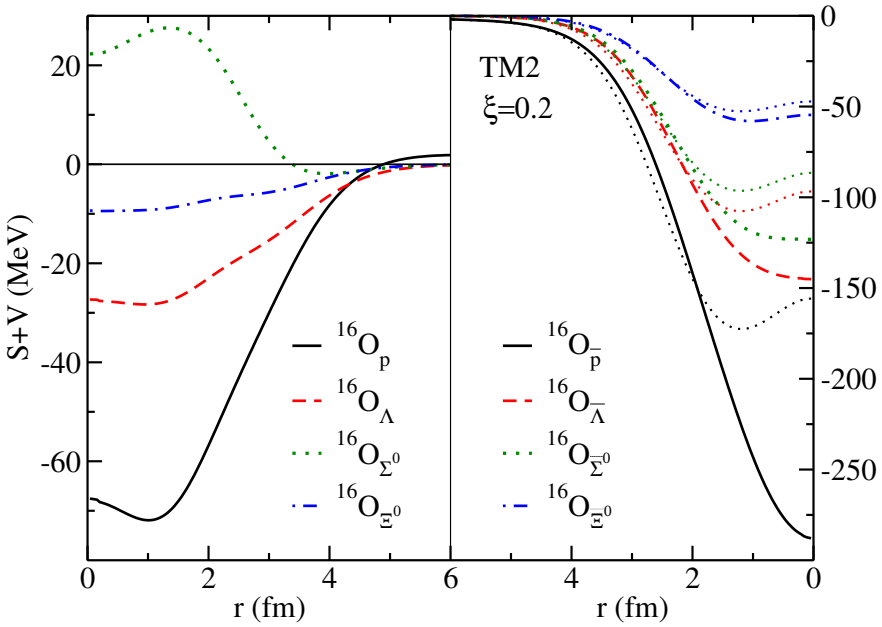

Figure 3.1: B–nucleus (left) and $\bar{B}$–nucleus (right) potentials in ^{16}O, calculated dynamically in the TM2 model for $\xi = 0.2$. $\bar{B}$–nucleus potentials calculated statically (thin dotted lines) are shown for comparison.

$\bar{B}$–nucleus potential calculated statically (right panel, thin dotted lines) is shown for comparison. The potential calculated statically is evidently shallower than the potential calculated dynamically for all antibaryons. The difference between the depth of the potential calculated statically and dynamically illustrates the extent of the core polarization. The antiproton causes the largest modification of the nuclear core, then follow $\bar{\Lambda}$, $\bar{\Sigma}_0$, and finally $\bar{\Xi}_0$ with almost negligible difference between the static and dynamical potentials. The strong polarization of the nuclear core by $\bar{p}$ was already demonstrated by Mishustin *et al.* [27, 28].

The $1s$ $\bar{B}$ binding energies in ^{6}Li, ^{12}C, ^{16}O, ^{40}Ca, ^{90}Zr, and ^{208}Pb are shown in Fig. 3.2, calculated dynamically in the TM1 and TM2 models with $\xi = 0.2$. Antiproton is the most bound antibaryon in all nuclei considered since it feels the deepest potential in the nuclear interior. The ordering of antihyperon binding energies corresponds to the depths of antihyperon potentials in Fig. 3.1. Charged antihyperons feel in addition Coulomb and isovector attraction or repulsion which modifies their binding energies accordingly (we denote the antiparticle to Σ^+ by symbol $\bar{\Sigma}^-$ and similarly for other antihyperons). The $\bar{B}$ binding energies are quite weakly A-dependent in a given model.

Next, we explored the model dependence of $\bar{B}$ binding energies. In Fig. 3.3, we

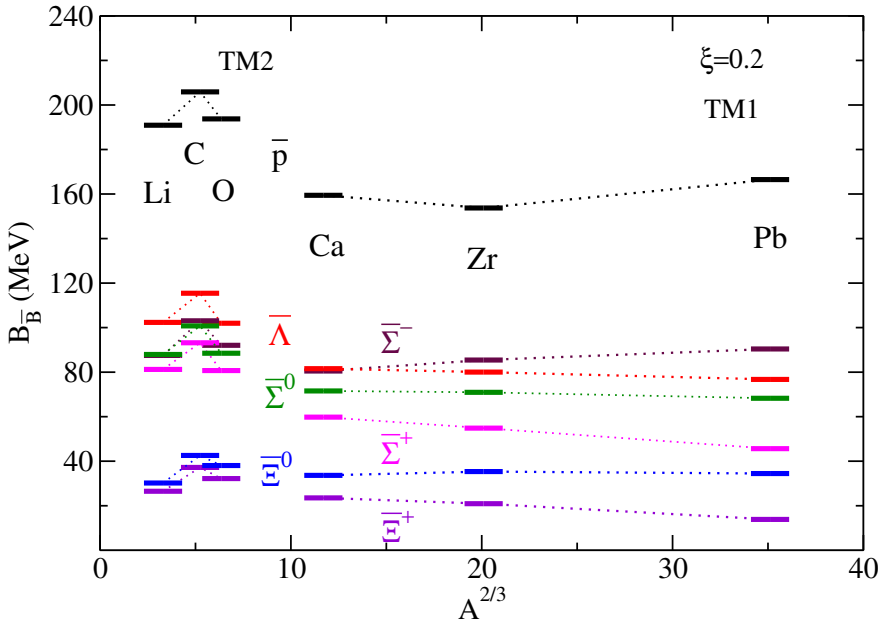

Figure 3.2: The A dependence of $\bar{B}$ $1s$ binding energies, calculated dynamically in the TM1 and TM2 models for $\xi = 0.2$.

present $1s$ $\bar{p}$ binding energies $B_{\bar{p}}$ in nuclei from ^{12}C to ^{208}Pb, calculated statically (left) and dynamically (right) in different RMF models. In the static calculations (and dynamical calculations alike), the $\bar{p}$ binding energies vary noticeably with the applied RMF model. There is a large inconsistency between $B_{\bar{p}}$ in light nuclei calculated using the TM2 model and $B_{\bar{p}}$ in the TM1 model for heavy nuclei (compare also $B_{\bar{p}}$ in ^{40}Ca for both TM1 and TM2)[1]. The same holds for $\bar{B}$ energies presented in Fig. 3.2. In the case of the NL-SH and TW99 models the $\bar{p}$ binding energy grows with increasing A, as expected, since the antiproton feels attraction from larger amount of nucleons (except ^{12}C with an extreme central density). The differences between the binding energies arise due to different magnitudes of the σ and ω fields provided by the applied models. In normal nuclei, the central nuclear potential is proportional to the difference of the scalar and vector potential and the resulting nuclear binding energies are almost model independent. However, the $\bar{p}$ potential is equal to the sum of the scalar and vector potential due to the G-parity transformation. Consequently, the differences between the total $\bar{p}$ potentials calculated within different RMF models in a given nucleus become more pronounced, which results in significant variations of the $\bar{p}$ binding energies.

[1]It is to be noted that TM model consists of two parameter sets TM1(2) for heavy (light) nuclei which, however, yield their binding energies in agreement with experiment [163].

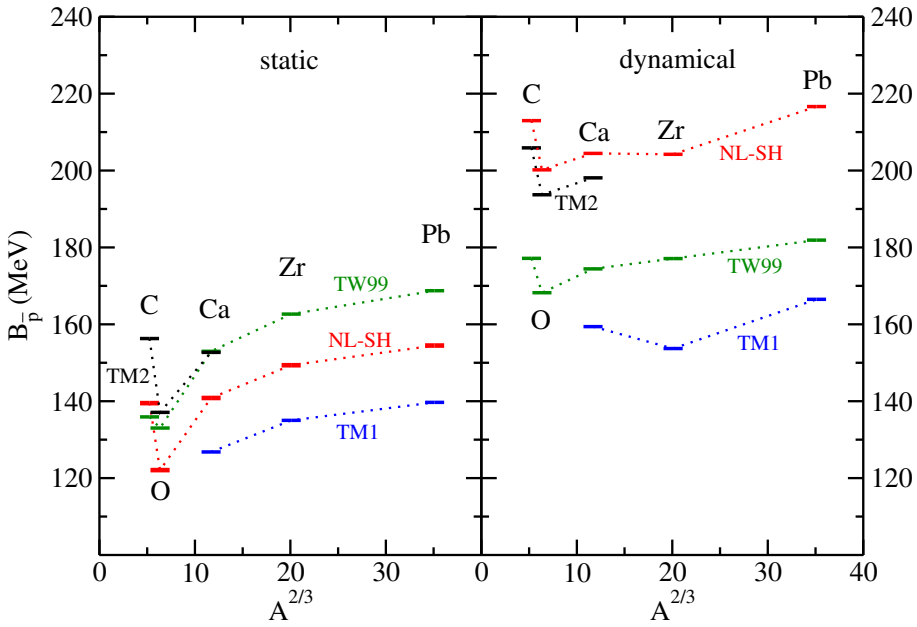

Figure 3.3: Binding energies of $1s$ $\bar{p}$-nuclear states across the periodic table calculated statically (left) and dynamically (right) using the TM2 (black), TM1 (blue), NL-SH (red) and TW99 (green) models. Figure adapted from author's publication [175].

Substantial differences between the $\bar{p}$ binding energies calculated statically and dynamically plotted in Fig. 3.3 indicate that the polarization of the nuclear core is significant. Indeed, the central core densities are almost twice as large as the saturation density ρ_0 . The $\bar{p}$ binding energies shown in the figure were calculated using the standard TM1, TM2, and NL-SH RMF models as well as the density-dependent TW99 model. We applied the TW99 model since the standard RMF models do not have to describe correctly the behavior of a nucleus when extrapolated to such high densities. But in the end, we found that the TW99 model gives similar results as the standard RMF models with constant couplings. The differences between the $\bar{p}$ binding energies calculated statically and dynamically vary with the applied RMF model. It seems that the decisive factor is nuclear compressibility, value of which is different in each model considered (see Table A.1). It expresses how rapidly the binding energy changes with the density. The larger is the value of compressibility the more pronounced is the increase of binding energy at a given density[2]. Indeed, the TW99 model gives the lowest value of the nuclear compressibility ($K = 240$ MeV) and, consequently, there is the smallest difference between $B_{\bar{p}}$ calculated statically

[2]It is to be noted that all models yield similar increase of the central nuclear density due to $\bar{p}$.

and dynamically. Then follow the TM1 and TM2 models with compressibilities $K = 280$ MeV and $K = 344$ MeV, respectively. The largest dynamical change of the $\bar{p}$ binding energy is observed for the NL-SH model with $K = 355$ MeV.

$\bar{p}$ Absorption in Nucleus

As a next step, we considered the $\bar{p}$ absorption in a nucleus and performed fully self-consistent calculations of $\bar{p}$-nuclear quasi-bound states. Below we present the most important results of this study published in *Nucl. Phys.* ***A 945*** *(2016) 197*. This publication is attached in Appedix B.2.

The $\bar{p}$ absorption is described by the phenomenological imaginary potential (2.33). Since the parameter $\mathrm{Im}b_0 = 1.9$ fm was determined by $\bar{p}$ absorption at threshold we introduced suppression factors which account for phase space reduction for annihilating products of the deeply bound antiproton. The suppression factors for decay channels are plotted in Fig. 2.1. The range of $\sqrt{s}$ relevant for our calculations, $\sqrt{s} \approx 1.55$ - 1.72 GeV, is denoted by the shaded area in Fig. 2.1. We took into account also kaon annihilation channels in our calculations (these channels were not considered in previous studies of $\bar{p}$ nuclei [27]). However, their contribution to the total $\bar{p}$ width was found negligible (5 MeV at most).

The extent of the phase space reduction and thus the size of suppression factors depend strongly on the c.m. energy $\sqrt{s}$. We considered various procedures for handling $\sqrt{s}$ and explored its effect on $\bar{p}$ widths. First, we adopted $\sqrt{s}$ in the two-body frame defined by Eq. (2.53) which was used in previous calculations by Mishustin *et al.* [27]. We allowed two scenarios — the annihilation of $\bar{p}$ with the nucleon with average binding energy, $B_N = B_{Nav}$ (denoted by M1) and annihilation with the proton in the $1s$ state, $B_N = B_{p1s}$ (denoted by M2). Next, we considered the contribution from kinetic energies of annihilating partners and used $\sqrt{s}$ of Eq. (2.54) expressed in the antiproton–nucleus frame. The kinetic energies were calculated self-consistently with constant (Jc) as well as reduced (Jr) (anti)nucleon masses in order to study the effect of the medium. For completeness, we adopted also the forms of $\sqrt{s}$ from Eqs. (2.57) and (2.58) (denoted by K and E, respectively) in the calculations of $\bar{p}$-nuclear quasi-bound states. These expressions were modified accordingly for the $\bar{p}$.

The effect of the suppression factors f_s is illustrated in Table 3.1. Here, we show binding energies $B_{\bar{p}}$ and widths $\Gamma_{\bar{p}}$ of the $1s$ $\bar{p}$-nuclear state in ^{16}O, calculated statically and dynamically using the real potential ('Real'), complex potential ('Complex'), and complex potentials including the suppression factors ('f_s(M1)' and

Table 3.1: Binding energies $B_{\bar{p}}$ and widths $\Gamma_{\bar{p}}$ (in MeV) of the $1s$ $\bar{p}$-nuclear state in ^{16}O, calculated dynamically (Dyn) and statically (Stat) within the TM2 model using the real and complex potentials consistent with $\bar{p}$–atom data (see text for details). Table adapted from author's publication [175].

	Real		Complex		f_s(M1)		f_s(Jr)	
	Dyn	Stat	Dyn	Stat	Dyn	Stat	Dyn	Stat
$B_{\bar{p}}$	193.7	137.1	175.6	134.6	190.2	136.1	191.5	136.3
$\Gamma_{\bar{p}}$	-	-	552.3	293.3	232.5	165.0	182.3	147.0

'f_s(Jr)'). When we compare calculations without and including $\bar{p}$ absorption ('Real' vs. 'Complex') we observe that $\bar{p}$ binding energies decrease noticeably when the $\bar{p}$ absorption is considered. The binding energies and widths calculated dynamically are much larger than those obtained in static calculations, which indicates that the polarization of the nuclear core is significant. When the phase space suppression is taken into account the $\bar{p}$ width is reduced by more than twice (compare 'Complex' and 'f_s(M1)' in the last row of Table 3.1). In addition, the $\bar{p}$ binding energy increases and becomes comparable with its 'Real' value. When the $\bar{p}$ and N momenta (see 'f_s(Jr)') are included self-consistently into $\sqrt{s}$, the $\bar{p}$ width is reduced by additional

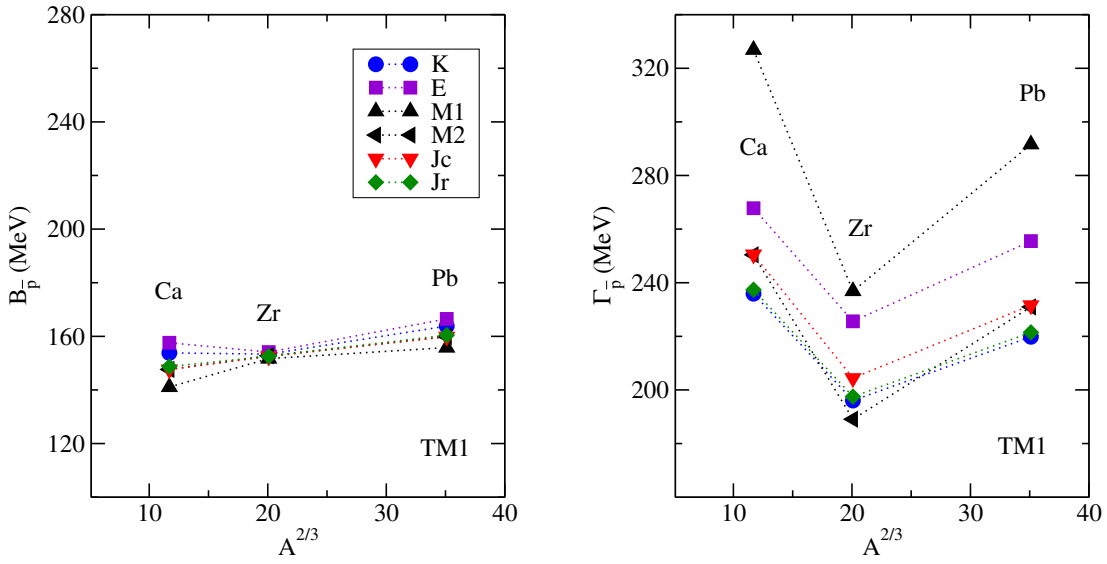

Figure 3.4: Binding energies (left panel) and widths (right panel) of $1s$ $\bar{p}$-nuclear states in selected nuclei, calculated dynamically using the TM1 model and different forms of $\sqrt{s}$ (see text for details). Figure adapted from author's publication [175].

≈ 50 MeV, but still remains sizable. The corresponding lifetime of the $\bar{p}$ in the nucleus is $\simeq 1$ fm/c. The response of the nuclear core to the extra $\bar{p}$ is not instant — it could possibly last longer than the lifetime of $\bar{p}$ inside a nucleus [28,31]. As a result, the antiproton annihilates before the nuclear core is fully polarized. Our static and dynamical calculations of $\bar{p}$ binding energies and widths may be thus considered as two limiting scenarios.

In Fig. 3.4, we present $1s$ $\bar{p}$ binding energies (left panel) and widths (right panel) in ^{40}Ca, ^{90}Zr, and ^{208}Pb, calculated dynamically for $\xi = 0.2$ and $\mathrm{Im}b_0 = 1.9$ fm within the same RMF model (TM1) but for different forms of $\sqrt{s}$. The $\bar{p}$ energies in a given nucleus calculated using different forms of $\sqrt{s}$ do not deviate much from each other. The $\bar{p}$ widths are sizable and exhibit much larger dispersion. The largest widths are predicted for $\sqrt{s}_{\mathrm{M1}}$ and the corresponding $\bar{p}$ binding energies are thus the smallest. We observe significant reduction of the $\bar{p}$ widths after including the momentum dependent terms in $\sqrt{s}$. It is due to the additional sizable downward energy shift coming from the $\bar{p}$ and nucleon kinetic energies which implies larger phase space suppression and thus smaller $\bar{p}$ widths. The kinetic energies calculated with reduced masses ($\sqrt{s}_{\mathrm{Jr}}$) are larger and, consequently, the $\bar{p}$ widths are smaller than those calculated using constant masses ($\sqrt{s}_{\mathrm{Jc}}$); the difference is up to 15 MeV in the TM1 model. The $\sqrt{s}_{\mathrm{M2}}$ yields similar $\bar{p}$ widths as $\sqrt{s}_{\mathrm{J}}$. However, in this case

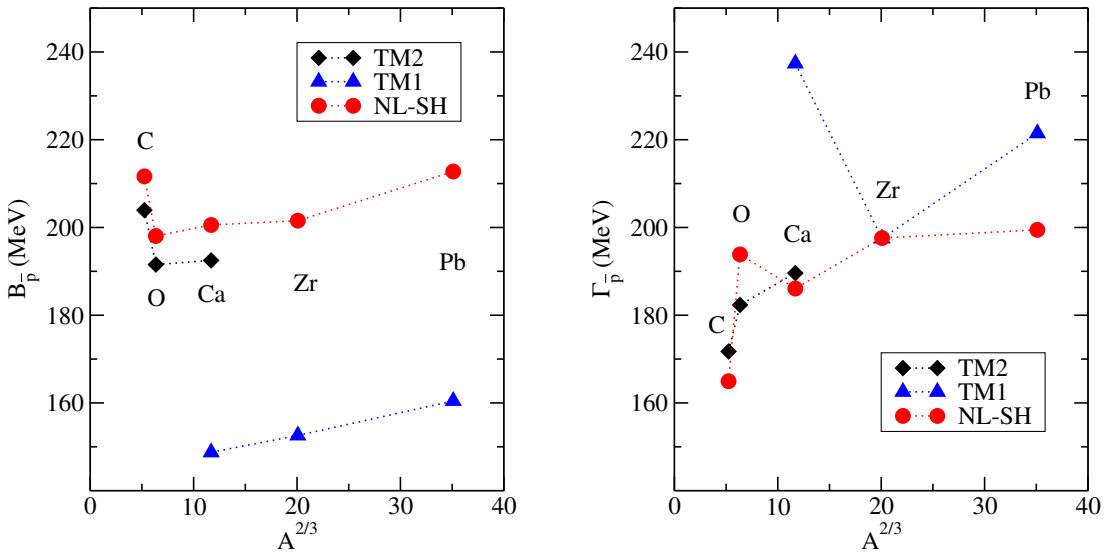

Figure 3.5: Binding energies (left panel) and widths (right panel) of $1s$ $\bar{p}$-nuclear states across the periodic table calculated dynamically for $\sqrt{s}_{\mathrm{Jr}}$ using the TM2 (black), TM1 (blue) and NL-SH (red) models. Figure adapted from author's publication [175].

the antiproton annihilates with the proton in the $1s$ state in the two-body frame ($B_{p1s} \gg B_{Nav}$). The $\sqrt{s}_{\rm K}$ from kaonic nuclei yields the $\bar{p}$ widths comparable with $\sqrt{s}_{\rm Jr}$. This agreement confirms reasonable approximations used in the evaluation of kinetic energies. However, when the low-density limit is taken into account ($\sqrt{s}_{\rm E}$) the $\bar{p}$ widths become by ≈ 30 MeV larger.

We studied the model dependence of $\bar{p}$ binding energies and widths as well. In Fig. 3.5, they are shown as a function of mass number A, calculated dynamically in the TM1, TM2 and NL-SH models for $\xi = 0.2$, Im$b_0 = 1.9$ fm, and $\sqrt{s}_{\rm Jr}$. The TM2 and NL-SH models yield similar $\bar{p}$ binding energies and widths in ^{12}C, ^{16}O and ^{40}Ca. On the other hand, the TM1 model predicts larger $\bar{p}$ widths than the TM2 and NL-SH models (except the case of ^{90}Zr). The $\bar{p}$ binding energies in this model are substantially lower than those in the TM2 and NL-SH models (see also Fig. 3.2).

Paris $\bar{N}N$ Potential

We performed self-consistent calculations of $\bar{p}$ quasi-bound states in nuclei across the periodic table using an optical potential constructed from $\bar{p}N$ scattering amplitudes derived from the 2009 version of the Paris $\bar{N}N$ potential [41]. First, we performed calculations using only the S-wave optical potential and explored its energy and density dependence. Then, we took into account the $\bar{p}N$ P-wave interaction and studied its effect on the $\bar{p}$ binding energies and widths. We performed static, as well as dynamical calculations and compared our results with the phenomenological RMF approach. Below we present the most important results of this study published in *Nucl. Phys.* ***A 969*** *(2018) 45*. This publication is attached in Appedix B.3.

As was demonstrated in the previous section, there is a strong model dependence of the dynamical effects caused by the extra $\bar{p}$ inside the nucleus which is attributed to different values of nuclear compressibility given by the applied RMF models (models with larger compressibility predict larger dynamical changes in $\bar{p}$ binding energies). In order to explore model dependence of the calculations with the Paris potential, we performed calculations using the RMF NL-SH [164] and TM(1)2 [163] models. We found that unlike the phenomenological RMF approach the present static as well as dynamical calculations based on Paris $\bar{N}N$ amplitudes yield quite similar results within the TM and NL-SH models, the differences in $\bar{p}$ binding energies and widths are up to 10 MeV. It is due to the energy dependence of the $\bar{p}N$ amplitudes which compensates the increase of the nuclear density. Namely, larger dynamical changes imply larger subthreshold energy shift and thus weaker

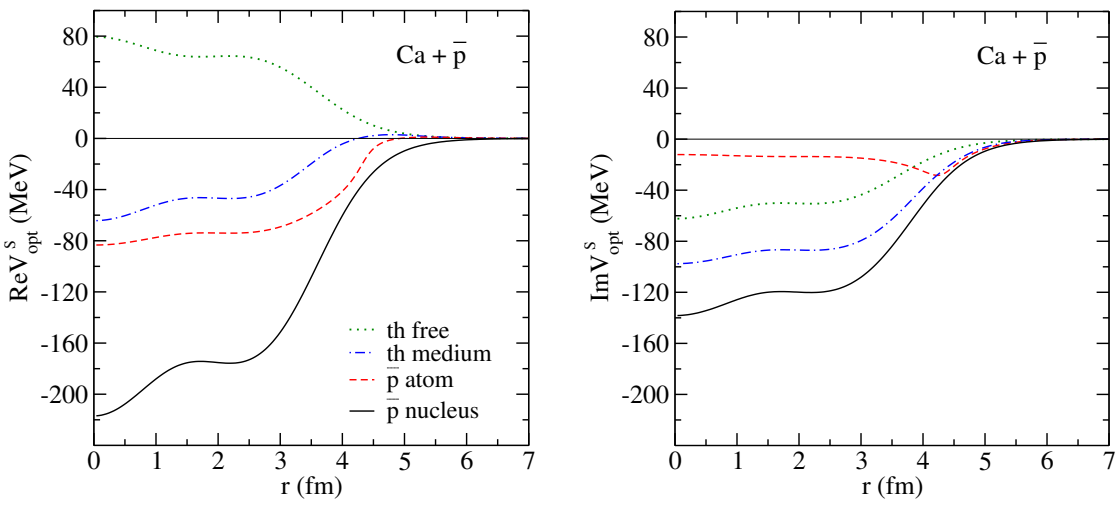

Figure 3.6: The potential felt by $\bar{p}$ at threshold ('th medium'), in the $\bar{p}$ atom and $\bar{p}$ nucleus, calculated for ^{40}Ca+$\bar{p}$ with in-medium Paris S-wave amplitudes and static RMF densities. The $\bar{p}$ potential calculated using free-space amplitudes at threshold is shown for comparison ('th free'). Figure adapted from author's publication [186].

$\bar{p}N$ amplitudes (see Fig. 2.2). We preferred the NL-SH model in the present work since the TM model consists of two different parameter sets – TM2 for light nuclei and TM1 for heavy nuclei.

The $\bar{p}N$ amplitudes are strongly energy and density dependent, as was shown in Fig. 2.2. Consequently, the depth and shape of the $\bar{p}$–nucleus potential depend greatly on the energies and densities pertinent to the processes under consideration. In Fig. 3.6 we present the $\bar{p}$ potential in ^{40}Ca calculated for different energies and densities: i) using the Paris free-space S-wave amplitudes at threshold (denoted by 'th free'), ii) using in-medium Paris S-wave amplitudes at threshold (denoted by 'th medium'), iii) using in-medium Paris S-wave amplitudes at energies relevant to $\bar{p}$ atoms (constructed following Ref. [46]), and iv) using in-medium Paris S-wave amplitudes at energies relevant to $\bar{p}$ nuclei ($\sqrt{s}_{\rm Jc}$). The $\bar{p}$ potential constructed using the free-space amplitudes has a repulsive real part and fairly absorptive imaginary part. When the medium modifications of the amplitudes are taken into account, the $\bar{p}$ potential becomes attractive and more absorptive. At the energies relevant to $\bar{p}$ atoms, the $\bar{p}$ potential is more attractive and weakly absorptive. Finally, at the energies relevant to $\bar{p}$ nuclei, the $\bar{p}$ potential is strongly attractive, however, also strongly absorptive. This demonstrates that proper self-consistent evaluation of the energy $\sqrt{s}$ is essential.

Next, we focus on the $\bar{p}$ binding energies and widths in various nuclei calculated

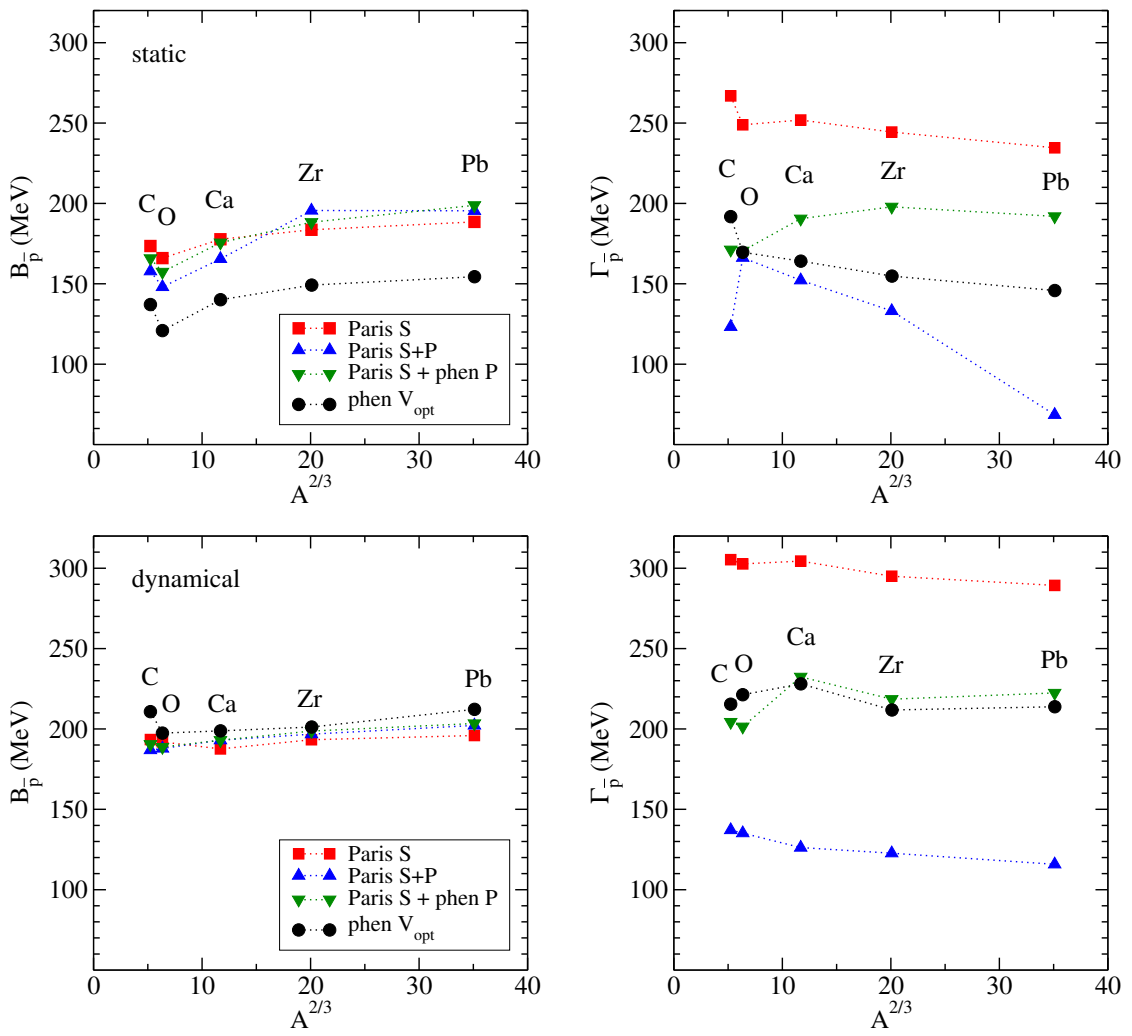

Figure 3.7: $1s$ $\bar{p}$ binding energies (left panel) and widths (right panel) in various nuclei, calculated statically (upper panel) and dynamically (lower panel) for $\sqrt{s}_{\rm Jc}$ using S-wave Paris potential (red squares), including phenomenological P-wave potential (green triangles down), Paris P-wave potential (blue triangles up) and phenomenological RMF potential (black circles).

statically and dynamically using the Paris $\bar{N}N$ potential and the role of the P-wave interaction. Throughout the calculations we used $\sqrt{s}_{\rm Jc}$ with self-consistently evaluated kinetic energies and constant (anti)nucleon masses.

In Fig. 3.7, we present $1s$ $\bar{p}$ binding energies (left) and widths (right) as a function of mass number A, calculated statically (top panel) and dynamically (bottom panel) with the Paris S-wave (squares), Paris $S+P$-wave (triangles up), and Paris S-wave + phen. P-wave (triangles down) potentials. The $\bar{p}$ binding energies and widths calculated within phenomenological RMF approach ('phen $V_{\rm opt}$', circles) are

shown for comparison. In dynamical and static calculations alike, both P-wave interaction terms, Paris as well as phenomenological, do not affect much the $\bar{p}$ binding energies — they are comparable with binding energies evaluated using only the S-wave potential. On the other hand, the $\bar{p}$ widths are reduced significantly when the phenomenological P-wave term is included in the $\bar{p}$ optical potential. The effect is even more pronounced for the Paris P-wave interaction.

The $\bar{p}$ widths calculated dynamically are noticeably larger than the widths calculated statically. It is caused by the increase of the central nuclear density, which exceeds the decrease of the $\bar{p}N$ amplitudes due to the larger energy shift with respect to threshold ($\delta\sqrt{s} \sim -255$ MeV in the dynamical case vs. $\delta\sqrt{s} \sim -200$ MeV in the static case). On the other hand, the $\bar{p}$ binding energies increase moderately and get closer to each other when the dynamical effects are taken into account. The $\bar{p}$ widths exhibit much large dispersion then the $\bar{p}$ binding energies for the different potentials.

The Paris S-wave + phen. P-wave potential yields very similar $\bar{p}$ widths as the phenomenological approach in the dynamical calculations. They are in the range of $\sim 200 - 230$ MeV, which means the $\bar{p}$ lifetime of 1 fm/c, and are comparable with the corresponding binding energies. The agreement between the phenomenological RMF and Paris S-wave + phen. P-wave potentials is quite impressive.

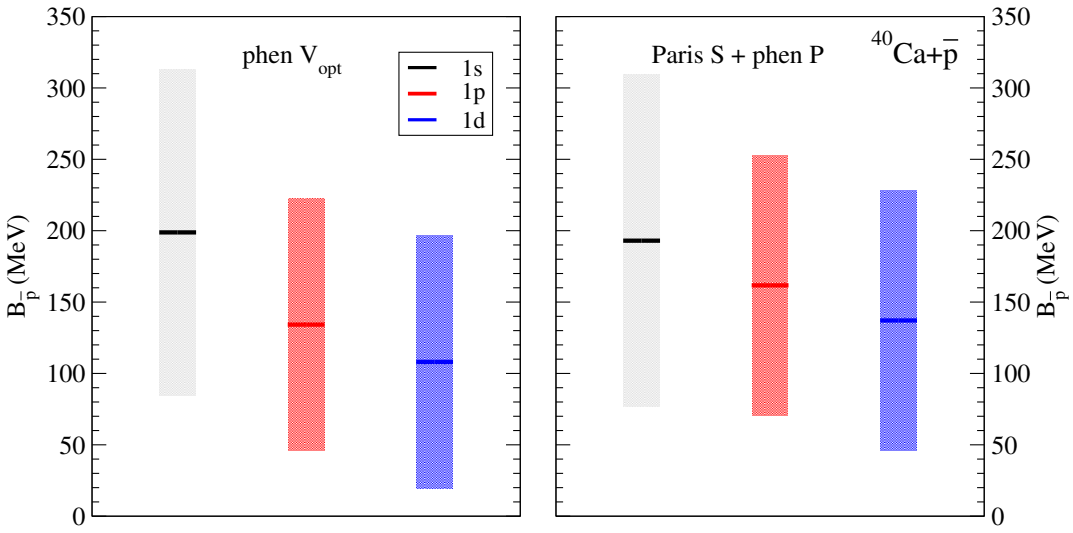

Figure 3.8: $1s$, $1p$, and $1d$ binding energies (lines) and widths (boxes) of $\bar{p}$ in ^{40}Ca calculated dynamically within the NL-SH model for $\sqrt{s}_{\rm Jc}$ with phenomenological $\bar{p}$ optical potential (left panel) and Paris S-wave + phen. P-wave potential (right panel). Figure adapted from author's publication [186].

Finally, we explored the $\bar{p}$ excited states in selected nuclei. Fig. 3.8 shows $\bar{p}$ spectra in ^{40}Ca calculated using the Paris S-wave + phen. P-wave potential and phenomenological RMF approach. The Paris S-wave + phen. P-wave potential yields the $1p$ and $1d$ binding energies slightly larger and thus the s-p and s-d level spacing smaller than the RMF approach. It is an effect of a broader $\bar{p}$ potential well generated by the Paris S-wave + phen. P-wave potential. Nevertheless, both approaches yield comparable $\bar{p}$ widths and the overall agreement is surprisingly good.

It is to be noted that there is no spin-orbit splitting of the p and d levels presented in Fig. 3.8 since the $V_{\rm opt}$ is a central potential constructed from angular momentum-averaged scattering amplitudes. In the RMF approach, the $\bar{p}$ binding energies in $1p$ and $1d$ spin doublets are nearly degenerate, the difference in $\bar{p}$ energies (as well as $\bar{p}$ widths) is up to ~ 1 MeV. This is in agreement with spin symmetry in antinucleon spectra within the RMF approach [32–34, 199]. In the left panel of Fig. 3.8 we show the spin-averaged $1p$ and $1d$ $\bar{p}$ binding energies and widths for better comparison with the results obtained with the central Paris potential.

3.2 K^--Nuclear Quasi-Bound States

We calculated K^- binding energies and widths in nuclei across the periodic table using the K^- optical potential derived within six current meson–baryon interaction models and compared the predictions. We took into account also K^- interactions with two and more nucleons in terms of a phenomenological optical potential. The parameters of this potential were fitted to kaonic atom data for each considered model separately.

Below we present the most important results of this study published in *Phys. Lett.* ***B 770*** *(2017) 342* and *Phys. Rev.* ***C 96*** *(2017) 015205*. These publications are attached in Appendix B.4 and B.5, respectively.

In our calculations of K^--nuclear states we considered only static RMF densities entering the optical potential (2.37). The core polarization due to the K^- should be taken into account. However, it was found that the polarization effects increase B_{K^-} by ≈ 6 MeV in ^{6}Li, by ≤ 2 MeV in ^{40}Ca, and by ≤ 0.5 MeV in ^{208}Pb [126]. In any case, the role of the nuclear polarization is less pronounced than the model dependence.

First, we constructed the K^- single-nucleon optical potential using the S-wave K^-N scattering amplitudes derived from the chiral meson–baryon interaction models presented in Chapter 2, Subsection 2.3.3. All the models yield different K^-N amplitudes below threshold (see Figs. 2.4 and 2.5), which indicates considerable model dependence of K^- binding energies and widths.

In Fig. 3.9, we present $1s$ K^- binding energies B_{K^-} and corresponding widths Γ_{K^-}, calculated self-consistently within the P, KM, M1, and M2 models using $\sqrt{s}_{\rm E}$ from Eq. (2.58). The calculated K^- binding energies are strongly model dependent, as expected. The binding energies B_{K^-} are gradually increasing with mass number A and their A-dependence is very similar in all models considered. On the other hand, the K^- widths are weakly A-dependent. The largest widths ($\simeq 40$ MeV) are predicted by the KM model. The P and M1 models yield K^- widths in heavy nuclei about three times smaller than the KM model. The M2 model yields similar widths as the KM model for ^{208}Pb and ^{90}Zr, while the widths in lighter nuclei are comparable with the P model widths. For the Bonn models B2 and B4, we did not obtain any K^--nuclear bound states because the real parts of the in-medium K^-N amplitudes are repulsive in the relevant subthreshold region (see Figs. 2.4 and 2.5).

The K^- widths obtained within all chiral models are smaller or comparable with the corresponding binding energies. Such result might stimulate searches for K^--

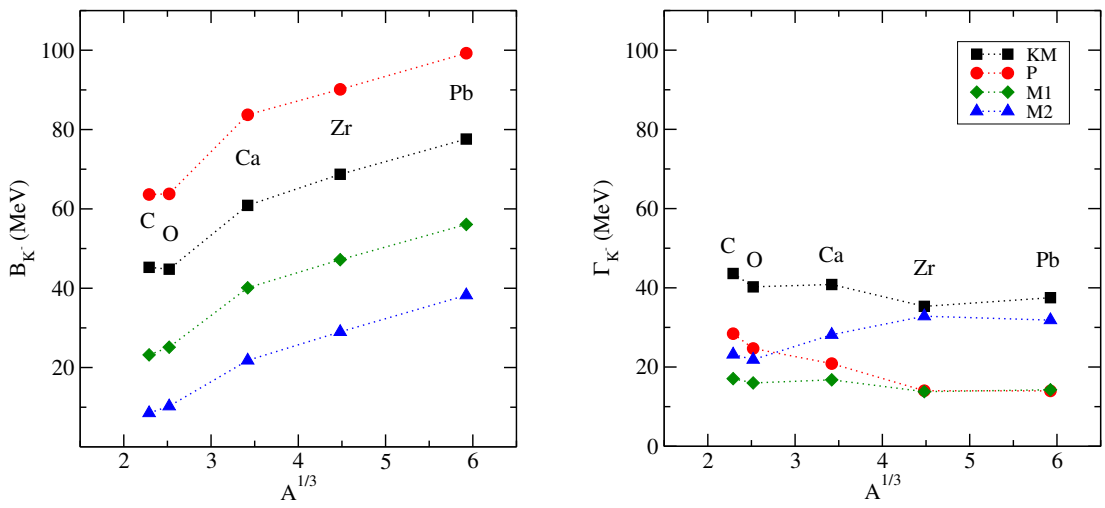

Figure 3.9: 1s K^- binding energies (left) and corresponding widths (right) in various nuclei calculated self-consistently in the P (circles), KM (squares), M1 (diamonds), and M2 (triangles) models. K^- multinucleon interactions are not considered. Figure adapted from author's publication [194].

nuclear bound states in many-body nuclear system. However, the chiral models take into account only the $K^-N \to \pi Y$ ($Y = \Lambda, \Sigma$) conversion mode. An inseparable component of every realistic description of K^- interactions in the nuclear medium is the absorption of K^- on two or more nucleons. Following Ref. [133], we supplemented the K^- single-nucleon potential from chiral models by the corresponding phenomenological multinucleon potential (2.50) and studied its impact on K^- binding energies and widths. The novelty of these calculations consists in the fact that the K^- multinucleon potential was constructed for each of the chiral models separately and that it involves besides K^- absorption also elastic K^- interactions.

In Fig. 3.10, we show real (left) and imaginary (right) parts of the total K^- potential, calculated self-consistently for ^{208}Pb+K^- in the KM model supplemented by the multinucleon potential $V^{(2)}_{K^-}$ from Eq. (2.50) with $\alpha = 1$ (KM1, top) and $\alpha = 2$ (KM2, bottom) for three different extrapolations of the multinucleon potential $V^{(2)}_{K^-}$ (for details see Chapter 2, Subsection 2.3.3). The gray shaded areas stand for uncertainties in $V^{(2)}_{K^-}$ due to the complex parameter B (see Table 2.3). We show also the underlying chirally-inspired K^- single-nucleon potential for comparison (denoted by 'KN'). The real parts of the K^- optical potential are affected by multinucleon interactions markedly less than its imaginary parts in all considered models. This has crucial consequences for the widths of K^--nuclear states. In the KM1 model, the FD, HD and TR options yield ReV_{K^-} shallower than the original single-nucleon

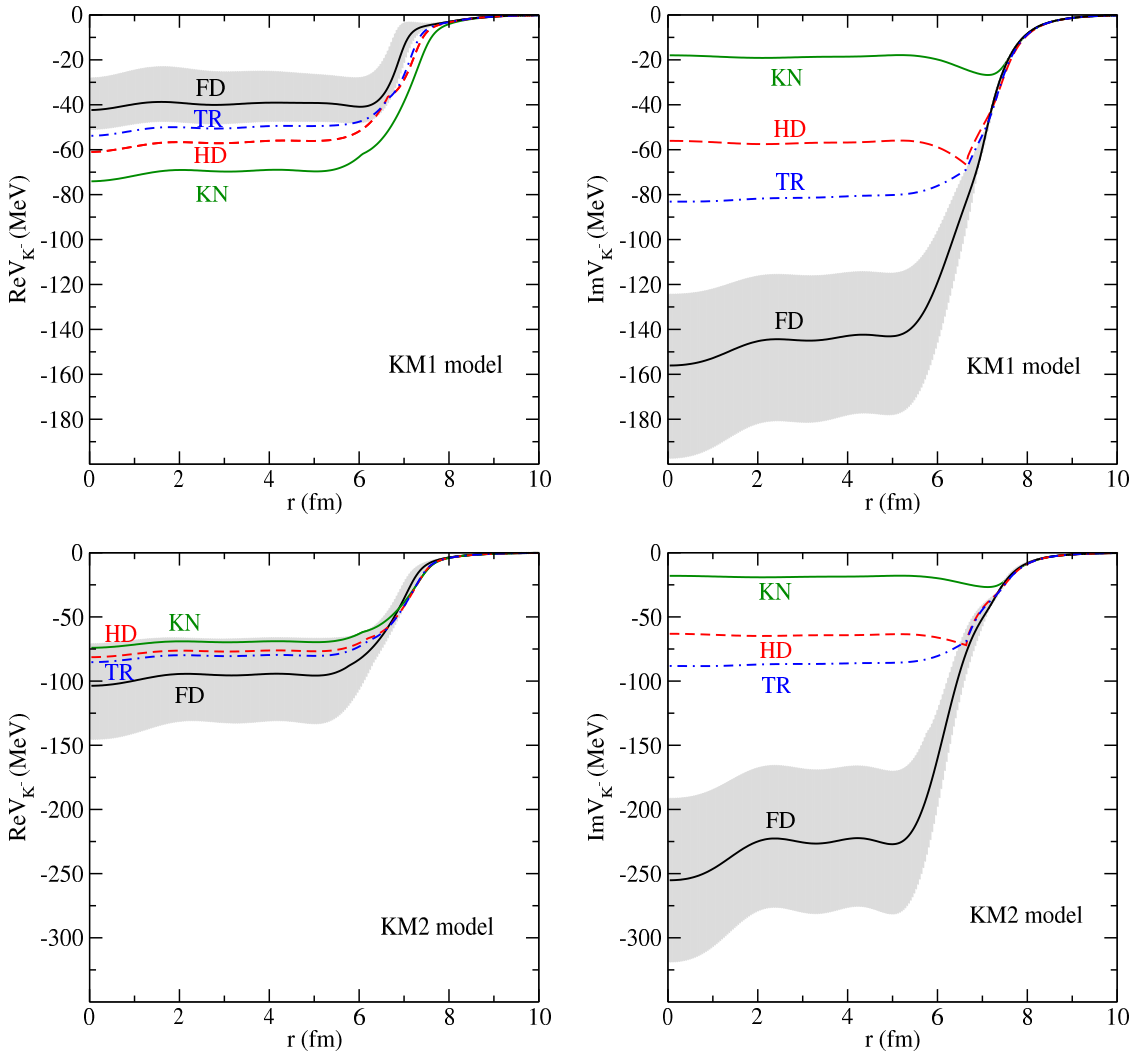

Figure 3.10: The real (left) and imaginary (right) parts of the K^- optical potential in the ^{208}Pb+K^- nucleus, calculated self-consistently in the KM1 (top) and KM2 (bottom) model, for three different versions of the K^- multinucleon potential (see text for details). The shaded area stands for uncertainties. The single-nucleon K^- potential (KN, green solid line) calculated in the KM model is shown for comparison.

$V^{(1)}_{K^-}$ potential. The same holds for the P1 and P2 models (not shown in the figure). In the KM2 model, the overall K^- real potential is deeper than the underlying K^- single-nucleon potential. The ReV_{K^-} potentials for HD, TR and FD options differ between each other up to ≈ 20 MeV in each interaction model. On the other hand, the imaginary parts of V_{K^-} exhibit much larger dispersion for different versions of $V^{(2)}_{K^-}$, as illustrated in Fig. 3.10, right panels. The K^- multinucleon absorption significantly deepens the imaginary part of the K^- optical potential. For the FD option of $V^{(2)}_{K^-}$, the KM model yields $|\mathrm{Im}V_{K^-}| \gg |\mathrm{Re}V_{K^-}|$ inside the nucleus for both

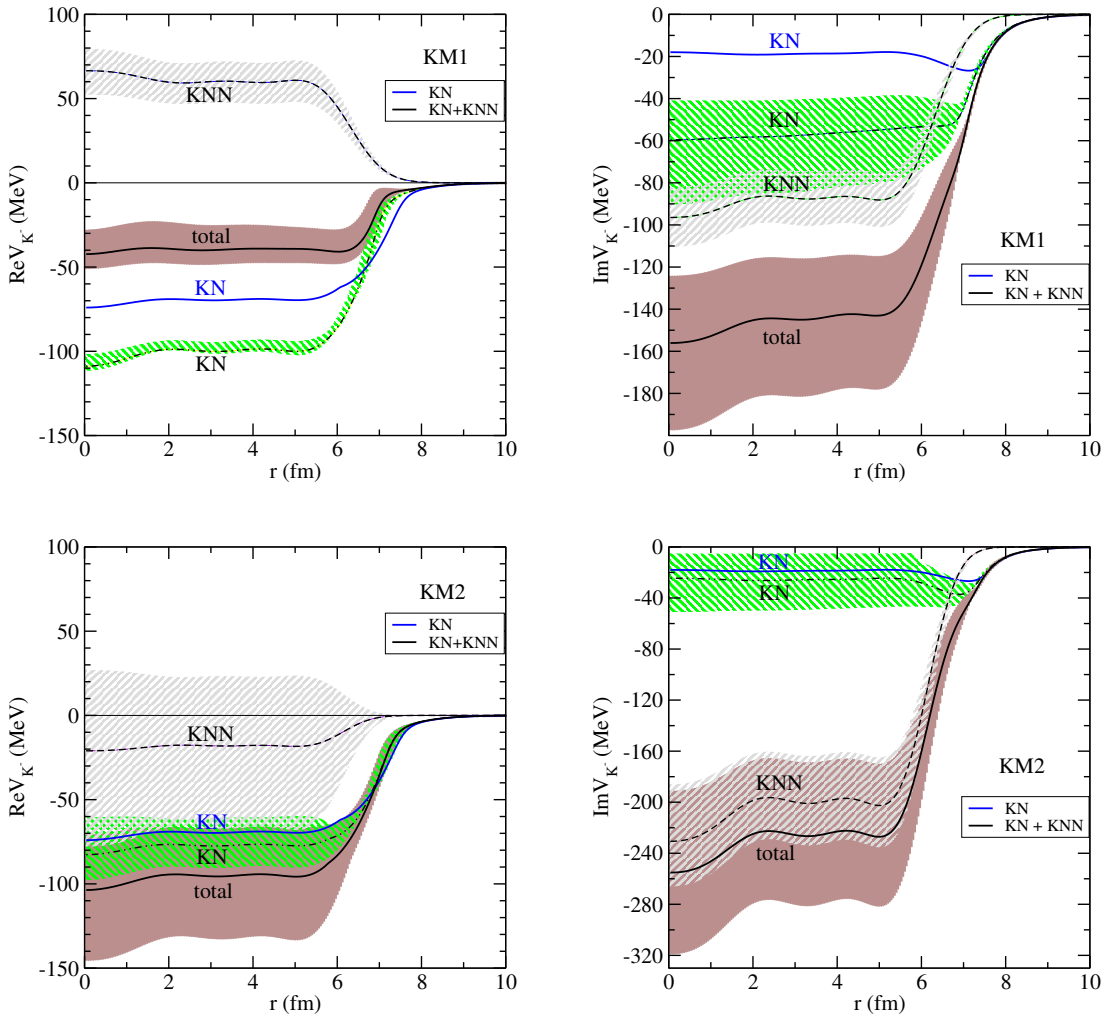

Figure 3.11: The respective contributions from K^-N (dashed dotted line) and K^-NN (dashed line) potentials to the total real (left) and imaginary (right) K^- optical potential in the ^{208}Pb+K^- nucleus, calculated self-consistently in the FD version of KM1 (top) and KM2 (bottom) models. The shaded areas denote the uncertainty bands. The K^- single-nucleon potential (KN, blue solid line) calculated in the KM model (i.e. w/o multinucleon interactions) is shown for comparison. Figure adapted from author's publication [194].

values of α, even when the uncertainties of the K^- multinucleon potential are taken into account. The same holds for the P model (not shown in the figure).

The individual contributions from the single-nucleon $V^{(1)}_{K^-}$ (denoted by 'KN') and multinucleon $V^{(2)}_{K^-}$ (denoted by 'KNN') potentials to the total K^- optical potential V_{K^-} including their uncertainties (shaded areas) are shown in Fig. 3.11, calculated self-consistently for ^{208}Pb+K^- in the KM1 (top panels) and KM2 model (bottom panels) and the FD version of $V^{(2)}_{K^-}$. We present the single-nucleon K^-N potential

(KN, blue solid line) derived from the K^-N amplitude model KM for comparison. The contribution from Re$V^{(2)}_{K^-}$ to the total real K^-–nucleus potential is repulsive in the KM1 model, as well as in the P1 and P2 models (not shown in the figure). As a result, the total K^-–nucleus potential including multinucleon processes is less attractive than the original single-nucleon K^-–nucleus potential. In the KM2 model, the contribution from $V^{(2)}_{K^-}$ brings additional attraction to the total potential due to positive sign of the effective amplitude ReB (see Table 2.3). The single-nucleon potential $V^{(1)}_{K^-}$ in the KM1 and KM2 models (as well as in P1 and P2 models) differs from the original single-nucleon K^-N potential due to the different subthreshold energy shift ($\delta\sqrt{s} \sim -85$ MeV in the KM model without the multinucleon interactions, $\delta\sqrt{s} \sim -50$ MeV in the KM1 model and $\delta\sqrt{s} \sim -80$ MeV in the KM2 model at normal nuclear density). The uncertainties in the K^-N part arise from variations of $\delta\sqrt{s}$ caused by the uncertainties in the total K^--nuclear potential.

The K^- multinucleon absorptions dramatically increase the depth of the total imaginary K^- potential as illustrated in the right panels of Fig. 3.11. The K^- multinucleon processes contribute substantially to K^- absorption mainly in the interior of a nucleus. The range of $V^{(2)}_{K^-}$ potential is considerably smaller than the range of the $V^{(1)}_{K^-}$ potential and thus in the surface region of a nucleus K^- single-nucleon absorption dominates in accordance with experimental findings [130–132].

Next, we evaluated the ratios of K^- single- and multinucleon absorptions as a function of nuclear radius (density). They are presented in Fig. 3.12. The ratios were expressed as fractions of Im$V^{(1)}_{K^-}$ and Im$V^{(2)}_{K^-}$ with respect to the total imaginary K^- potential ImV_{K^-}, calculated self-consistently for ^{208}Pb+K^- in the P and KM models for the FD option of $V^{(2)}_{K^-}$. The density ρ/ρ_0 (thin dotted line) is shown for comparison. Since the range of the corresponding potentials is different, the relative contributions of Im$V^{(1)}_{K^-}$ and Im$V^{(2)}_{K^-}$ to K^- absorption are changing with radius (density). At the nuclear surface, the K^- absorption on a single nucleon dominates, while it is reduced in the nuclear interior due to vicinity of $\pi\Sigma$ threshold and the multinucleon absorption prevails. The models with $\alpha = 2$ yield lower relative fraction of single-nucleon K^-N absorption in the nuclear medium than the models with $\alpha = 1$. It is due to the self-consistent value of $\sqrt{s}$ at ρ_0 which is closer to the $K^-N \to \pi\Sigma$ threshold in the case with $\alpha = 2$. The analysis of Ref. [133] showed that the fractions of K^- absorption on a single nucleon ($\sim 75\%$) and several nucleons ($\sim 25\%$) from the bubble chamber experiments are sensitive to about 15% of nuclear density (denoted in Fig. 3.12 by vertical black line). At this density, the ratios Im$V^{(2)}_{K^-}$/Im$V^{(1)}_{K^-}$ are lower than experimental fractions of K^- absorption at

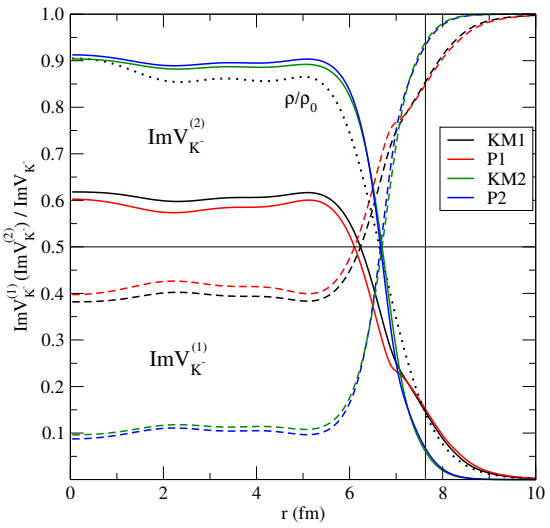

Figure 3.12: The ratio of $\mathrm{Im}V^{(1)}_{K^-}$ (dashed line) and $\mathrm{Im}V^{(2)}_{K^-}$ (solid line) potentials to the total K^- imaginary potential $\mathrm{Im}V_{K^-}$ as a function of radius, calculated self-consistently for ^{208}Pb+K^- system within the KM1, KM2, P1, and P2 models and FD option of the K^- multinucleon potential. The relative nuclear density ρ/ρ_0 (dotted line) and vertical lines denoting 15% of ρ_0 are shown for comparison. Figure adapted from author's publication [200].

rest [130–132] due to different self-consistent values of $\delta\sqrt{s}$ for kaonic and nuclear states. It is to be noted that the other options for multinucleon potential, HD and TR, yield similar fraction of K^- single-nucleon and multinucleon absorption inside the nucleus as the FD option.

Finally, in Table 3.2 we present $1s$ K^- binding energies B_{K^-} and widths Γ_{K^-}, calculated with the underlying K^- optical potentials $V_{K^-} = V^{(1)}_{K^-} + V^{(2)}_{K^-}$ within the KM and P models, respectively. These two models provide reasonable description of kaonic atom data as well as K^- single-nucleon absorption fractions. For comparison, we show also K^- binding energies and widths calculated only with the chirally-inspired K^- single-nucleon potential. The K^- widths increase considerably after including K^- multinucleon potential $V^{(2)}_{K^-}$, while K^- binding energies change less (they decrease in KM1, P1, and P2 models and increase in KM2 model)[3]. The HD and TR options of $V^{(2)}_{K^-}$ potential predict K^- widths of order $\sim$ 100 MeV and the binding energies much smaller than the corresponding widths in most nuclei. The FD multinucleon potentials $V^{(2)}_{K^-}$ do not even yield antikaon bound states in the

[3]For the FD variant of the P2 model, we had to scale huge imaginary part $\mathrm{Im}V_{K^-}$ by factor 0.8 in order to get fully converged self-consistent solution of the Klein–Gordon equation Eq. (2.42). The calculation with the unscaled imaginary potential is not numerically stable due to extremely strong K^- absorption — the non-converged $\Gamma_{K^-} > 500$ MeV while the corresponding $B_{K^-} < 15$ MeV.

Table 3.2: 1s K^- binding energies and widths (in MeV) in various nuclei calculated using the single nucleon K^-N KM amplitudes (denoted KN); plus a phenomenological amplitude $B(\rho/\rho_0)^\alpha$, where $\alpha = 1$ and 2, for half-density limit (HD), $t\rho$ option (TR), and full density option (FD). Table adapted from author's publications [194].

KM model			$\alpha = 1$			$\alpha = 2$		
		KN	HD	TR	FD	HD	TR	FD
^{6}Li	B_{K^-}	25	11	not	not	23	19	not
	Γ_{K^-}	45	116	bound	bound	122	160	bound
^{12}C	B_{K^-}	45	34	20	not	48	44	not
	Γ_{K^-}	44	114	182	bound	125	191	bound
^{16}O	B_{K^-}	45	34	25	not	48	46	not
	Γ_{K^-}	40	109	158	bound	121	167	bound
^{40}Ca	B_{K^-}	59	50	40	not	64	63	not
	Γ_{K^-}	37	113	164	bound	126	175	bound
^{90}Zr	B_{K^-}	69	56	47	17	72	71	30
	Γ_{K^-}	36	107	156	312	120	167	499
^{208}Pb	B_{K^-}	78	64	56	33	80	80	53
	Γ_{K^-}	38	108	153	273	122	163	429
P model			$\alpha = 1$			$\alpha = 2$		
		KN	HD	TR	FD	HD	TR	FD
^{6}Li	B_{K^-}	38	21	not	not	36	28	not
	Γ_{K^-}	40	112	bound	bound	133	183	bound
^{12}C	B_{K^-}	64	50	35	not	64	57	not
	Γ_{K^-}	28	96	165	bound	122	196	bound
^{16}O	B_{K^-}	64	50	39	not	63	59	not
	Γ_{K^-}	25	94	142	bound	117	169	bound
^{40}Ca	B_{K^-}	81	67	56	not	82	79	not
	Γ_{K^-}	14	95	145	bound	120	175	bound
^{90}Zr	B_{K^-}	90	74	62	19	87	85	not
	Γ_{K^-}	12	88	136	340	114	164	bound
^{208}Pb	B_{K^-}	99	82	70	37	96	92	47*
	Γ_{K^-}	14	92	137	302	117	163	412*

* the solution of the Klein-Gordon equation for ImV_{K^-} scaled by factor 0.8

vast majority of nuclei. We found 1s K^- quasi-bound states in ^{90}Zr and ^{208}Pb but the K^- binding energies of such states are small and widths are huge, one order of magnitude larger than the binding energies. These results are valid generally, even when the uncertainties in the multinucleon potential $V^{(2)}_{K^-}$ are taken into account.

We performed calculations also within the B2, B4, M1, and M2 models supple-

mented by relevant multinucleon interaction terms from Ref. [133]. The resulting K^- widths are again larger or comparable with the corresponding binding energies. Moreover, even the Bonn models B2 and B4 yield K^- bound states in nuclei after supplementing the K^- single-nucleon potential by the phenomenological K^- multinucleon potential which is strongly attractive.

Chapter 4

Summary & Outlook

In this work we studied interactions of antihadrons, namely the antiproton, antihyperons, and antikaon, with nuclear many-body systems. The antihadron–nucleus interactions were described by a phenomenological complex optical potential or by an optical potential constructed using recent microscopic models of antihadron–nucleon interactions. The structure of considered nuclei was calculated within the framework of the Relativistic Mean-Field model. We explored possibility of the existence of $\bar{H}$-nuclear quasi-bound states. Our fully self-consistent calculations yield unique predictions for the $\bar{H}$ binding energies and decay widths. They may serve as a guideline for experimentalists studying propagation of antihadrons in the nuclear medium or even searching for a possible hint of $\bar{H}$ quasi-bound states in nuclei.

First, we performed detailed calculations of $\bar{p}$, $\bar{\Lambda}, \bar{\Sigma}$, and $\bar{\Xi}$ bound states in selected nuclei across the periodic table within several parametrizations of the RMF model, not considering antibaryon absorption. We explored dynamical effects in nuclei caused by the antibaryon in the $1s$ nuclear state using the G-parity motivated $\bar{B}$–meson coupling constants properly scaled to yield $\bar{p}$ potential in agreement with available data. Due to lack of experimental information on antihyperon interactions, the same scaling was assumed for antihyperons as well. The estimate for $\bar{\Sigma}$– and $\bar{\Xi}$–nucleus potentials was given for the first time.

Next, we developed a model for the $\bar{p}$ absorption in the nuclear medium and performed first fully self-consistent calculations of $\bar{p}$ nuclei using a phenomenological optical potential consistent with $\bar{p}$ atom data. We took into account the phase space reduction for $\bar{p}$ annihilation products and evaluated suppression factors for relevant annihilation channels. The energy available for the annihilation products was calculated self-consistently, considering additional energy shift due to non-zero momenta of annihilating partners in the $\bar{p}$–nucleus system.

We carried out a comparable study of $\bar{p}$-nuclear quasi-bound states using a microscopic $\bar{N}N$ potential for the first time. The free-space $\bar{p}N$ amplitudes derived from the latest version of the Paris $\bar{N}N$ potential were modified using the multiple scattering approach in order to account for Pauli correlations in the medium. We explored the effect of the P-wave interaction on $\bar{p}$ binding energies and widths. Since the optical potential based on the Paris $S+P$-wave scattering amplitudes failed to fit the $\bar{p}$ atom data we considered the phenomenological P-wave term as well.

Finally, we calculated K^--nuclear quasi-bound states using K^-–nucleus optical potentials derived self-consistently from the microscopic K^-N amplitudes. The scattering amplitudes were obtained within several chirally-motivated meson–baryon coupled-channel models. We took into account the in-medium modification of the K^-N amplitudes by applying multiple scattering procedure WRW. We considered the K^- multinucleon interactions in terms of a phenomenological potential, parameters of which were fitted to the data for each of the chiral models separately. We explored the effect of the K^- multinucleon interactions on K^- binding energies and widths. Such a systematic study of K^--nuclear quasi-bound states was performed for the first time.

In our calculations, we confirmed that an antibaryon embedded in a nucleus causes significant modifications of the nuclear core. Its binding energy increases considerably and the central nuclear density reaches 2 - 3 times the saturation density. The most pronounced changes in the nuclear core are caused by the antiproton. We found that the extent of core polarization effects depends strongly on the applied RMF model.

Our calculations of $\bar{p}$ and K^- quasi-bound states in nuclei, which included their absorption in the nuclear medium, yielded the $\bar{p}$ and K^- widths larger or comparable with the binding energies (if such nuclear quasi-bound states ever exist). This fact disfavors experimental observation of such states.

In the case of $\bar{p}$-nuclear states we found good agreement between the results obtained using the phenomenological RMF potential and the Paris S-wave + phenomenological P-wave potential. These two potentials are consistent with antiprotonic atom data and $\bar{p}$ scattering off nuclei at low energies. Moreover, we found that the P-wave interaction almost does not affect the binding energies of $\bar{p}$-nuclear states. This is in sharp contrast to the case of $\bar{p}$ atoms where it was found necessary to include the P-wave interaction in order to increase attraction of the $\bar{p}$ optical potential [46].

The K^- binding energies and widths vary significantly with the applied chiral meson–baryon interaction model. After including the K^- multinucleon interactions, which are an inseparable ingredient of any realistic description of K^- propagation in the nuclear medium , we observed huge increase of the K^- widths and decrease of the corresponding binding energies. This feature is valid generally in chiral models which reproduce the experimental data from kaonic atoms and the K^- single-nucleon absorption fraction at rest from bubble chamber experiments. Another valuable finding is that due to the strong energy and density dependence of the $\bar{p}N$ and K^-N amplitudes, there exist no universal $\bar{p}$–nucleus or K^-–nucleus potential. Its depth and shape depend greatly on the energies and densities pertinent to the process under consideration.

In conclusion, it is to be noted that other microscopic $\bar{N}N$ models, such as the Bonn–Jülich chiral NNLO [44] and N^{3}LO [45] EFT potential models or Zhou–Timmermans model [43], should be applied to the description of $\bar{p}$ interaction with the nuclear medium. Comparison between these $\bar{N}N$ interaction models could bring valuable information about in-medium $\bar{p}$ interactions in the direct confrontation with the data from $\bar{p}$ atoms and $\bar{p}$ scattering off nuclei, as well as predictions for $\bar{p}$-nuclear quasi-bound states. Next, more realistic models of the antihyperon–nucleus interactions, including their absorption in the medium, should be developed in the near future. The knowledge of $\bar{B}$–nucleus potentials derived within different theoretical approaches could be then used in the simulations of antibaryon interactions with nuclei under kinematical conditions relevant to the processes to be studied at FAIR [52, 53].

Regarding the K^-N interaction, the description of K^- multinucleon processes within microscopic approaches, such as the chirally-motivated coupled-channel model, is needed. Moreover, though the formation of K^- bound states in nuclear many-body systems seems to be improbable due to the sizable absorption of K^- on two or more nucleons, it is desirable to explore the role of the K^- multinucleon interactions in few-body systems as well.

References

[1] O. Chamberlain *et al.*, Phys. Rev. **100** (1955) 947.

[2] R. Armenteros, B. French, *High-Energy Physics*. Vol. **4**, (Academic Press New York 1969).

[3] T. Walcher, Ann. Rev. Nucl. Part. Sci. **38** (1988) 67.

[4] D. Garetta *et al.*, Phys. Lett. **B 135** (1984) 266; Phys. Lett. **B 139** (1984) 464(E).

[5] Antiproton Discovery, Symmetry Magazin [online] URL:<https://www.symmetrymagazine.org/article/october-2009/antiproton-discovery>.

[6] G. E. Walker, Ch. D. Goodman, C. Olmer (Eds.), *Antinucleon– and Nucleon–Nucleus Interaction*, (Plenum Press 1985).

[7] C. J. Batty, E. Friedman, A. Gal, Phys. Rep. **287** (1997) 385.

[8] E. Friedmam, A. Gal, Phys. Rep. **452** (2007) 89.

[9] E. Friedman, A. Gal, J. Mareš, Nucl. Phys. **A 761** (2005) 283.

[10] S. Teis, W. Cassing, T. Maruyama, U. Mosel, Phys. Rev. **C 50** (1994) 388.

[11] C. Spieles *et al.*, Phys. Rev. **C 53** (1996) 2011.

[12] A. Sibirtsev *et al.*, Nucl. Phys. **A 632** (1998) 131.

[13] E. Klempt, C. J. Batty, J.-M. Richard, Phys. Rept. **413** (2005) 197.

[14] C. Amsler, Rev. Mod. Phys. **70** (1998) 1293.

[15] M. Chiba *et al.*, Phys. Rev. **D 39** (1989) 3227.

[16] M. Chiba *et al.*, J. Phys. Soc. Jap. **69** (2000) 1356.

[17] C. Y. Wong, A. K. Kerman, G. R. Satchler, A. D. MacKellar, Phys. Rev. **C 29** (1984) 574.

[18] A. J. Baltz, C. B. Dover, M. E. Sainio, A. Gal, G. Toker, Phys. Rev. **C 32** (1985) 1272.

[19] M. Chiba *et al.*, Phys. Lett. **B 177** (1986) 217.

[20] M. Chiba *et al.*, Phys. Lett. **B 202** (1988) 447.

[21] M. Chiba *et al.*, Phys. Rev. **C 60** (1999) 035204.

[22] L. Tauscher, *Antiproton–nucleon and antiproton–nucleus bound states*, Proc. 8th European Symposium on Nucleon-antinucleon Interactions, Thessaloniki, 1–5 Sep 1986, pp.247-257.

[23] T. D. Lee, C. N. Yang, Nuovo Cim. **3** (1956) 749.

[24] R. Machleidt, Adv. Nucl. Phys. **19** (1988) 189.

[25] H.-P. Dürr, E. Teller, Phys. Rev. **101** (1956) 494; H.-P. Dürr, Phys. Rev. **103** (1956) 469.

[26] T. Bürvenich, I. N. Mishustin, L. M. Satarov, J. A. Maruhn, H. Stöcker, W. Greiner, Phys. Lett. **B 542** (2002) 261.

[27] T. J. Bürvenich, W. Greiner, I. N. Mishustin, L. M. Satarov, H. Stöcker, Phys. Rev. **C 71** (2005) 035201.

[28] A. B. Larionov, I. N. Mishustin, L. M. Satarov, W. Greiner, Phys. Rev. **C 78** (2008) 014604.

[29] A. B. Larionov, I. A. Pschenichnov, I. N. Mishustin, W. Greiner, Phys. Rev. **C 80** (2009) 021601.

[30] A. B. Larionov, I. N. Mishustin, I. A. Pschenichnov, L. M. Satarov, W. Greiner, Acta Phys. Polon. **B 41** (2010) 299.

[31] A. B. Larionov, I. N. Mishustin, L. M. Satarov, W. Greiner, Phys. Rev. **C 82** (2010) 024602.

[32] X. T. He, S. G. Zhou, J. Meng, E. G. Zhao, W. Scheid, Eur. Phys. J. **A 28** (2006) 265.

[33] R. Lisboa, M. Malheiro, P. Alberto, M. Fiolhais, A. S. de Castro, Phys. Rev. **C 81** (2010) 064324.

[34] H. Liang, W. H. Long, J. Meng, N. Van Giai, Eur. Phys. J. **A 44** (2010) 119.

[35] T. Gaitanos, M. Kaskulov, H. Lenske, Phys. Lett. **B 703** (2011) 193.

[36] T. Gaitanos, M. Kaskulov, U. Mosel, Nucl. Phys. **A 828** (2009) 9.

[37] T. Gaitanos, M. Kaskulov, Nucl. Phys. **A 899** (2013) 133.

[38] T. Gaitanos, M. Kaskulov, Nucl. Phys. **A 940** (2015) 181.

[39] The GiBUU model [online] URL:<http://gibuu.physik.uni-giessen.de/GiBUU>.

[40] K. Nakamura *et al.*, Phys. Rev. Lett. **52** (1984) 731.

[41] B. El-Bennich, M. Lacombe, B. Loiseau, S. Wycech, Phys. Rev. **C 79** (2009) 054001.

[42] T. Hippchen, K. Holinde, W. Plessas, Phys. Rev. **C 39** (1989) 761.

[43] D. Zhou, R. G. E. Timmermans, Phys. Rev. **C 86** (2012) 044003.

[44] K. W. Kang, J. Haidenbauer, U.-G. Meißner, JHEP **1402** (2014) 113.

[45] L.-Y. Dai, J. Haidenbauer, U.-G. Meißner, JHEP **1707** (2017) 78.

[46] E. Friedman, A. Gal, B. Loiseau, S. Wycech, Nucl. Phys. **A 934** (2015) 101.

[47] P. Montagna *et al.*, Nucl. Phys. **A 700** (2002) 159.

[48] A. Panzarasa, P. Salvini, G. Bendiscioli, P. Montagne, N. Zappa, Nucl. Phys. **A 747** (2005) 448.

[49] E. Hernandéz, E. Oset, Nucl. Phys. **A 494** (1989) 533.

[50] E. Hernandéz, E. Oset, Z. Phys. **A 341** (1992) 201.

[51] M. Ablikim *et al.* (BESIII Collaboration), Phys. Rev. Lett. **117** (2016) 042002.

[52] The FAIR facility [online]
URL:<http://www.fair-center.eu/index.php?id=1>.

[53] The PANDA experiment [online]
URL:<https://panda.gsi.de/>.

[54] H. Noumi, Few-Body Syst. **54** (2013) 813.

[55] G. D. Rochester, C. C. Butler, Nature **160** (1947) 855.

[56] J. H. Christenson, J. W. Cronin, V. L. Fitch, R. Turlay, Phys. Rev. Lett. **13** (1964) 138.

[57] G. Q. Li, C.-H. Lee, G. E. Brown, Nucl. Phys. **A 625** (1997) 372.

[58] N. Kaiser, T. Waas, W. Weise, Nucl. Phys. **A 612** (1997) 297.

[59] B. D. Kaplan, A. E. Nelson, Phys. Lett. **175** (1986) 57.

[60] A. E. Nelson, B. D. Kaplan, Phys. Lett. **B 192** (1987) 193.

[61] C.-H. Lee, Phys. Rep. **275** (1996) 255.

[62] H. Heiselberg, M. Hjorth-Jensen, Phys. Rep. **328** (2000) 237.

[63] A. Ramos, J. Schaffner-Bielich, J. Wambach, Lect. Notes Phys. **578** (2001) 175.

[64] P. J. Ellis, R. Knorren, M. Prakash, Phys. Lett. **B 349** (1995) 11.

[65] V. Metag, M. Nanova, E. Ya. Paryev, Prog. Part. Nucl. Phys. **97** (2017) 199.

[66] D. Evans *et al.*, J. Phys. **G 9** (1983) 885.

[67] M. Bazzi *et al.* (SIDDHARTA collaboration), Phys. Lett. **B 704** (2011) 113; Nucl. Phys. **A 881** (2012) 88.

[68] M. Jones, R. H. Dalitz, R. R. Horgan, Nucl. Phys. **B 129** (1977) 45.

[69] W. Weise, Nucl. Phys. **A 835** (2010) 51.

[70] R. Barth *et al.* (KaoS Collaboration), Phys. Rev. Lett. **78** (1997) 4007.

[71] F. Laue *et al.* (KaoS Collaboration), Phys. Rev. Lett.**82** (1999) 1640.

[72] W. Scheinast *et al.* (KaoS Collaboration), Phys. Rev. Lett. **96** (2006) 072301.

[73] E. Friedman, A. Gal, C. J. Batty, Phys. Lett. **B 308** (1993) 6;
Nucl. Phys. **A 579** (1994) 518.

[74] E. Friedman, A. Gal, J. Mareš, A. Cieplý, Phys. Rev. **C 60** (1999) 024314.

[75] J. Mareš, E. Friedman, A. Gal, Nucl. Phys. **A 770** (2006) 84.

[76] R. H. Dalitz, S. F. Tuan, Phys. Rev. Lett. **2** (1959) 425.

[77] R. H. Dalitz, T. C. Wong, G. Rajasekaran, Phys. Rev. **153** (1967) 1617.

[78] A. Müller-Groeling, K. Holinde, J. Speth, Nucl. Phys. **A 513** (1990) 557.

[79] N. Isgur, G. Karl, Phys. Rev. **D 18** (1978) 4187.

[80] T. Inoue, Nucl. Phys. **A 790** (2007) 530.

[81] S. Scherer, Adv. Nucl. Phys. **27** (2003) 277.

[82] N. Kaiser, P. B. Siegel, W. Weise, Nucl. Phys. **A 594** (1995) 325.

[83] A. Cieplý, J. Smejkal, Nucl. Phys. **A 881** (2012) 115.

[84] E. Oset and A. Ramos, Nucl. Phys. **A 635** (1998) 99.

[85] B. Borasoy, R. Nissler, W. Weise, Eur. Phys. J. **A 25** (2005) 79.

[86] B. Borasoy, U.-G. Meißner, R. Nissler, Phys. Rev. **C 74** (2006) 055201.

[87] Y. Ikeda, T. Hyodo, W. Weise, Nucl. Phys. **A 881** (2012) 98.

[88] Z. H. Guo, J. A. Oller, Phys. Rev. **C 87** (2013) 035202.

[89] M. Mai, U.-G. Meißner, Nucl. Phys. **A 900** (2013) 51.

[90] J. A. Oller, U.-G. Meißner, Phys. Lett. **B 500** (2001) 263.

[91] D. Jido, J. A. Oller, E. Oset, A. Ramos, U.-G. Meißner, Nucl. Phys. **A 725** (2003) 181.

[92] D. N. Tovee *et al.*, Nucl. Phys. **B 33** (1971) 493.

[93] R. J. Nowak *et al.*, Nucl. Phys. **B 139** (1978) 61.

[94] A. D. Martin, Nucl. Phys. **B 179** (1981) 33.

[95] J. Ciborowski *et al.*, J. Phys. **G 8** (1982) 13.

[96] G. E. Brown, M. Rho, Nucl. Phys. **A 596** (1996) 503.

[97] T. Waas, N. Kaiser, W. Weise, Phys. Lett. **B 379** (1996) 34.

[98] A. Ramos, E. Oset, Nucl. Phys. **A 671** (2000) 481.

[99] A. Cieplý, E. Friedman, A. Gal, J. Mareš, Nucl. Phys.**A 696** (2001) 173.

[100] Y. Akaishi, T. Yamazaki, Phys. Rev. **C 65** (2002) 044005; T. Yamazaki, Y. Akaishi, Phys. Lett. **B 535** (2002) 70.

[101] T. Yamazaki, Y. Akaishi, Phys. Rev. **C 76** (2007) 045201.

[102] N. V. Shevchenko, A. Gal, J. Mareš, Phys. Rev. Lett. **98** (2007) 082301.

[103] J. Révai, N. V. Shevchenko, Phys. Rev. **C 90** (2014) 034004.

[104] Y. Ikeda, T. Sato, Prog. Theor. Phys. **124** (2010) 533.

[105] N. Barnea, A. Gal, E. Z. Liverts, Phys. Lett. **B 712** (2012) 132.

[106] S. Marri, S. Z. Kalantari, Eur. Phys. J. **A 52** (2016) 282.

[107] A. Doté, T. Hyodo, W. Weise, Phys. Rev. **C 79** (2009) 014003.

[108] M. Angello *et al.*, Phys. Rev. Lett. **94** (2005) 212303.

[109] G. Bendiscioli *et al.*, Nucl. Phys. **A 789** (2007) 222.

[110] T. Yamazaki *et al.*, Phys. Rev. Lett. **104** (2010) 132502.

[111] L. Fabbietti *et. al.*, Nucl. Phys. **A 914** (2013) 60.

[112] A. O. Tokiyasu *et al.*, Phys. Lett. **B 728** (2014) 616.

[113] S. Ajimura *et al.*, Nucl. Phys. **A 914** (2013) 315.

[114] Y. Ichikawa *et al.*, Few-Body Syst. **54** (2013) 1191.

[115] J. Mareš, E. Friedman, A. Gal, Phys. Lett. **B 606** (2005) 295.

[116] J. Mareš, Nucl. Phys. **A 804** (2008) 296.

[117] D. Gazda, E. Friedman, A. Gal, J. Mareš, Phys. Rev. **C 76** (2007) 05520402.

[118] D. Gazda, E. Friedman, A. Gal, J. Mareš, Phys. Rev. **C 77** (2008) 045206.

[119] D. Gazda, E. Friedman, A. Gal, J. Mareš, Phys. Rev. **C 80** (2009) 035205.

[120] X. M. Zhong, G. X. Peng, L. Li, P. Z. Ning, Phys. Rev. **C 74** (2006) 034321.

[121] J. Schaffner, I. N. Mishustin, Phys. Rev. **C 53** (1996) 1416.

[122] T. Muto, T. Maruyama, T. Tatsumi, Phys. Rev. **C 79** (2009) 035207.

[123] T. Muto, Phys. Rev. **C 77** (2008) 015810.

[124] T. Muto, Nucl. Phys. **A 804** (2008) 322.

[125] W. Weise, R. Härtle, Nucl. Phys. **A 804** (2008) 173.

[126] D. Gazda, J. Mareš, Nucl. Phys. **A 881** (2012) 159.

[127] A. Cieplý, E. Friedman, A. Gal, D. Gazda, J. Mareš, Phys. Rev. **C 84** (2011) 045206.

[128] A. Cieplý, E. Friedman, A. Gal, D. Gazda, J. Mareš, Phys. Lett. **B 702** (2011) 402.

[129] T. Sekihara, J. Yamagata-Sekihara, D. Jido, Y. Kanada-En'yo, Phys. Rev. **C 86** (2012) 065205.

[130] H. Davis, F. Oppenheimer, W. L. Knight, F. R. Stannard, O. Treutler, Nuovo Cimento **53 A** (1968) 313.

[131] J. W. Moulder, N. E. Garret, L. M. Tucker, W. M. Bugg, G. T. Condo, H. O. Cohn, R. D. McCulloch, Nucl. Phys. **B 35** (1971) 332.

[132] C. Vander Velde-Wilquet, J. Sacton, J. H. Wickens, D. N. Tovee, D. H. Davis, Nuovo Cimento **39 A** (1977) 538.

[133] E. Friedman, A. Gal, Nucl. Phys. **A 959** (2017) 66.

[134] P. Bydžovský, A. Gal, J. Mareš (Eds.), *Topics in Strangeness Nuclear Physics*, Lect. Notes Phys. **724** (2007) 1.

[135] P. B. Demorest, T. Pennucci, S. M. Ransom, M. S. E. Roberts, J. W. T. Hessels, Nature **467** (2010) 1081.

[136] J. Antoniadis *et al.*, Science **340** (2013) 6131.

[137] B. Bhowmick *et al.*, Phys. Rev. **C 89** (2014) 065806.

[138] J. Rikovska Stone *et al.*, Nucl. Phys. **792** (2007) 341.

[139] H. Togashi *et al.*, Phys. Rev. **C 93** (2016) 035808.

[140] L. Tolos, M. Centelles, A. Ramos, Astrophys. J. **834** (2017) 3.

[141] M. Isaka, Y. Yamamoto, Th. A. Rijken, Phys. Rev. **C 95** (2017) 044308.

[142] D. Lonardoni *et al.*, Phys. Rev. Lett. **114** (2015) 092301.

[143] Y. Yamamoto *et al.*, Phys. Rev. **C 90** (2014) 045805.

[144] B. F. Gibson, E. V. Hungerford, Phys. Rep. **257** (1995) 350.

[145] D. J. Prowse, Phys. Rev. Lett. **17** (1966) 782.

[146] M. Danysz *et al.*, Nucl. Phys. **49** (1963) 121.

[147] S. Aoki *et al.*, Prog. Theor. Phys. **85** (1991) 87.

[148] K. Nakazawa *et al.*, Prog. of Theoretical and Experimental Physics **3** 2015 033D02.

[149] S. Bart *et al.*, Phys. Rev. Lett. **83** (1999) 5238.

[150] The NEUMATT Project [online]
URL:<https://web.infn.it/CSN4/IS/Linea5/NEUMATT/NEUMATT.html>.

[151] M. Papenbrock, EPJ Web Of Conf. **113** (2016) 05005.

[152] C. Greiner, S. Leupold, J. Phys. **G 27** (2001) L95.

[153] STAR Collaboration, Science **328** (2010) 58.

[154] ALICE Collaboration, Phys. Lett. **B 754** (2016) 360.

[155] D. B. Lichtenberg, Phys. Rev. **113** (1959) 1309.

[156] J. Cugnon, J. Vandermeulen, Phys. Rev. **C 39** (1989) 181.

[157] Ch.-T. Song, J.-M. Yao, J. Meng, Chin. Phys. Lett. **28** (2011) 092101.

[158] J. Pochodzalla, Phys. Lett. **B 669** (2008) 306.

[159] B. D. Serot, J. D. Walecka, Adv. Nucl. Phys. **16** (1986) 1.

[160] P.-G. Reinhardt, Rep. Prog. Phys. **52** (1989) 439.

[161] Y. K. Gambhir, P. Ring, A. Thimet, Ann. Phys. **198** (1990) 132.

[162] J. Boguta, A. R. Bodmer, Nucl. Phys. **A 292** (1977) 413.

[163] Y. Sugahara, H. Toki, Nucl. Phys. **A 579** (1994) 557.

[164] M. M. Sharma, M. A. Nagarajan, P. Ring, Phys. Lett. **B 312** (1993) 377.

[165] S. A. Chin, Ann. Phys. **108** (1977) 301.

[166] Z. Zhou, J. Mang, P. Ring, Phys. Lett. **B 254** (1991) 325.

[167] P.-G. Reinhard, M. Rufa, J. Maruhn, W. Greiner, J. Friedrich, Z. Phys. **A 323** (1986) 13.

[168] C. J. Horowitz, B. D. Serot, Nucl. Phys. **A 464** (1987) 613.

[169] B. ter Haar, R. Malfliet, Rhys. Rep. **149** (1987) 207.

[170] R. Brockmann, R. Machleidt, Phys. Rev. **C 42** (1990) 1965.

[171] S. Typel, H. H. Wolter, Nucl. Phys. **A 656** (1999) 331.

[172] J. Mareš, B. K. Jennings, Phys. Rev. **C 49** (1994) 2472.

[173] J. Mareš, E. Friedman, A. Gal, B. K. Jennings, Nucl. Phys. **A 594** (1995) 311.

[174] J. Schaffner, C. B. Dover, A. Gal, C. Greiner, D. J. Millener, H. Stöcker, Ann. Phys. **235** (1994) 35.

[175] J. Hrtánková, J. Mareš, Nucl. Phys. **A 945** (2016) 197.

[176] P. Khaustov *et al.*, Phys. Rev. **61** (2000) 054603.

[177] Particle data group [online], `<http://pdg.lbl.gov/2013/reviews/rpp2013-rev-kinematics.pdf>`.

[178] A Monte Carlo Simulation tool PLUTO [online], `<http://www-hades.gsi.de/?q=pluto>`.

[179] H. Feshbach, *Theoretical Nuclear Physics: Nuclear Reactions*, (John Wiley & Sons, Inc. 1992)

[180] T. Wass, M. Rho, W. Weise, Nucl. Phys. **A 617** (1997) 449.

[181] E. E. Kolomeitsev, N. Kaiser, W. Weise, Phys. Rev. Lett. **90** (2003) 092501.

[182] B. El-Bennich, M. Lacombe, B. Loiseau, R. Vinh Mau, Phys. Rev. **C 59** (1999) 2313.

[183] F. Iazzi *et al.* (OBLEIX Collaboration), Phys. Lett. **B 475** (2000) 378.

[184] M. Augsburger *et al.*, Nucl. Phys. **A 658** (1999) 149.

[185] D. Gotta *et al.*, Nucl. Phys. **A 660** (1999) 1283.

[186] J. Hrtánková, J. Mareš, Nucl. Phys. **A 969** (2018) 45.

[187] M. B. Johnson, G. R. Satchler, Annals of Physics **248** (1996) 134.

[188] M. Ericson, T. E. O. Ericson, Annals of Physics **36** (1966) 323.

[189] M. Lutz, Phys. Lett. **B 426** (1998) 12.

[190] N. V. Shevchenko, A. Gal, J. Mareš, Phys. Rev. Lett. **98** (2007) 082301.

[191] N. V. Shevchenko, A. Gal, J. Mareš, J. Révai, Phys. Rev. **C 76** (2007) 044004.

[192] Y. Ikeda, T. Sato, Phys. Rev. **C 76** (2007) 035203.

[193] T. Hyodo, W. Weise, Phys. Rev. **C 77** (2008) 035204.

[194] J. Hrtánková, J. Mareš, Phys. Rev. **C 96** (2017) 015205.

[195] J. Mareš, E. Friedman, A. Gal, Phys. Lett. **B 606** (2005) 295.

[196] E. Friedman, A. Gal, Nucl. Phys. **A 899** (2013) 60.

[197] A. Gal, Nucl. Phys. **A 914** (2013) 270.

[198] E. Friedman, A. Gal, Nuc. Phys. **A 899** (2013) 60.

[199] J. N. Ginocchio, Phys. Rep. **414** (2005) 165.

[200] J. Hrtánková, J. Mareš, Phys. Lett. **B 770** (2017) 342.

List of Author's Publications

Publications in Scientific Journals

1. J. Hrtánková, J. Mareš,
   Calculations of antiproton-nucleus quasi-bound states using the Paris $\bar{N}N$ potential,
   Nucl. Phys. **A 969** (2018) 45,
   arXiv:1708.06204 [nucl-th].

2. J. Hrtánková, J. Mareš,
   K^--nuclear states: Binding energies and widths,
   Phys. Rev. **C 96** (2017) 015205,
   arXiv:1704.07205 [nucl-th].

3. J. Hrtánková, J. Mareš,
   Are there any narrow K^--nuclear states?,
   Phys. Lett. **B 770** (2017) 342,
   arXiv:1703.01788 [nucl-th].

4. P. Veselý, E. Hyama, J. Hrtánková, J. Mareš,
   Sensitivity of Λ single-particle energies of the ΛN spin-orbit coupling to the nuclear core structure in p-shell and sd-shell hypernuclei,
   Nucl. Phys. **A 954** (2016) 260,
   arXiv:1605.05646 [nucl-th].

5. J. Hrtánková, J. Mareš,
   Interaction of antiprotons with nuclei,
   Nucl. Phys. **A 945** (2016) 197,
   arXiv:1510.07409 [nucl-th].

6. J. Hrtánková, J. Mareš,
   Interaction of antiproton with nuclei,
   Hyperfine Interactions **234** (2015) 93,
   arXiv:1502.05523 [nucl-th].

Conference Proceedings

1. J. Hrtánková, J. Mareš,
   Calculations of antiproton-nucleus quasi-bound states based on the Paris $\bar{N}N$ potential model,
   Proc. International Conference on Exotic Atoms and Related Topics (EXA2017),
   EPJ Web Conf. (2018), subm.

2. J. Hrtánková, J. Mareš,
   Antikaon in the nuclear medium and the role of K^- multinucleon interactions,
   Proc. International Conference on Exotic Atoms and Related Topics (EXA2017),
   EPJ Web Conf. (2018), subm.

3. E. Friedman, A. Gal, A. Cieplý, J. Hrtánková, J. Mareš,
   Studies of mesic atoms and nuclei,
   Proc. International Conference on Hadron Spectroscopy and Structure (HADRON2017),
   POS HADRON2017 (2018) 203, subm.,
   arXiv:1711.11371 [nucl-th].

4. J. Hrtánková, J. Mareš,
   Calculations of $\bar{p}$-nuclear states within the Paris $\bar{N}N$ potential model,
   Proc. FAIRNESS 2017,
   J. Phys. Conf. Ser. (2017), accepted for publication.

5. J. Hrtánková, J. Mareš,
   Calculations of kaonic nuclei based on chiral meson-baryon coupled-channel interaction models,
   Proc. 55th International Winter Meeting on Nuclear Physics (BORMIO2017),
   POS BORMIO2017 (2017), accepted for publication.

6. J. Hrtánková, J. Mareš,
   Antibaryon interactions with the nuclear medium,
   Proc. International Nuclear Physics Conference (INPC2016),
   POS INPC2016 (2017) 280,
   arXiv:1710.02045 [nucl-th].

7. J. Hrtánková, J. Mareš,
   Interaction of antiprotons with nuclei ,
   Proc. 12th International Conference on Low Energy Antiproton Physics (LEAP2016),
   JPS Conf. Proc. **18** (2017) 011032,
   arxiv:1711.10258 [nucl-th].

8. J. Hrtánková, A. Cieplý, J. Mareš,
   Calculations of kaonic nuclei based on chiral meson-baryon coupled-channel interaction models,
   Proc. 15th International Workshop on Meson Physics (MESON2016),
   EPJ Web Conf. **130** (2016) 02006,
   arXiv:1612.04087 [nucl-th].

9. J. Hrtánková, J. Mareš,
   Antibaryon - nucleus bound states,
   Proc. FAIRNESS 2014
   J. Phys. Conf. Ser. **599** (2015) 012007,
   arXiv:1411.7536 [nucl-th].

Conference Presentations

1. ECT* Workshop on Advances and Open Problems in Low-Energy Nuclear and Hadronic Strangeness Physics (ASTRA2017),
   Trento, Italy, October 23 - 27, 2017.
   (oral presentation)

2. International Conference on Exotic Atoms and Related Topics (EXA2017),
   Vienna, Austria, September 11 - 15, 2017.
   (oral presentation)

3. FAIRNESS 2017,
   Sitges, Spain, May 29 - June 3, 2017.
   (oral presentation)

4. 55th International Winter Meeting on Nuclear Physics,
   Bormio, Italy, January 23 - 27, 2017.
   (oral presentation)

5. International Nuclear Physics Conference (INPC2016),
   Adelaide, Australia, September 11 - 16, 2016.
   (oral presentation)

6. 15th International Workshop on Meson Physics (MESON2016),
   Cracow, Poland, June 2 - 7, 2016.
   (oral presentation)

7. 12th International Conference on Low Energy Antiproton Physics (LEAP2016),
   Kanazawa, Japan, March 6 - 11, 2016.
   (oral presentation + poster)

8. ECT* Workshop on Frontiers in Hadron and Nuclear Physics with Strangeness and Charm,
   Trento, Italy, October 19 - 23, 2015.
   (oral presentation)

9. ECT* Workshop on Achievements and Perspectives in Low-Energy QCD with Strangeness,
   Trento, Italy, October 27 - 31, 2014.
   (oral presentation)

10. FAIRNESS 2014,
    Vietri sul Mare, Italy, September 22 - 27, 2014.
    (oral presentation)

11. International Conference on Exotic Atoms and Related Topics (EXA2014),
    Vienna, Austria, September 15 - 19, 2014.
    (oral presentation)

12. 26th Indian-Summer School & SPHERE School on Low Energy Hadron Physics,
    Prague, Czech Republic, September 3 - 7, 2014.
    (oral presentation)

13. 3rd International School for Strangeness Nuclear Physics,
    Tokai + Sendai, Japan, February 13 - 19, 2014.
    (oral presentation + poster)

14. 4th International Conference on Nuclear Fragmentation,
    Kemer, Turkey, September 29 - October 6, 2013.
    (oral presentation + poster)

15. Winter School of Experimental Nuclear Physics, FNSPE, CTU in Prague,
    Bílý Potok, Czech Republic, January 12 - 19, 2013.
    (oral presentation)

16. 3 KK Conference,
    Banská Bystrica, Slovak Republic, January 4, 2013.
    (oral presentation)

17. 1st International School for Strangeness Nuclear Physics,
    Tokai + Sendai, Japan, February 12 - 18, 2012.
    (poster)

Appendix A

RMF Model Parametrizations

In this thesis we use the following RMF parametrizations: the NL-SH model [164], the TM1(2) models for heavy (light) nuclei [163], and the density-dependent model TW99 [171]. These models contain values of meson masses and meson–nucleon

Table A.1: The values of meson masses and coupling constants in the TM1, TM2, NL-SH and TW99 models. The characteristics of nuclear matter (saturation density ρ_0, binding energy per nucleon E/A, and nuclear compressibility K) calculated within the given models are shown for comparison.

		TM1	TM2	NL-SH	TW99
m_N	(MeV)	938	938	939	939
m_σ	(MeV)	511.198	526.443	526.059	550
m_ω	(MeV)	783	783	783	783
m_ρ	(MeV)	770	770	763	763
$g_{\sigma N}$		10.0289	11.4694	10.444	10.7285
$g_{\omega N}$		12.6139	14.6377	12.945	13.2902
$g_{\rho N}$		9.2644	9.3566	8.766	7.3220
g_2	(fm^{-1})	-7.2325	-4.4440	-6.9099	0
g_3		0.6183	4.6076	-15.8337	0
d		71.3075	84.5318	0	0
ρ_0	(fm^{-3})	0.145	0.132	0.146	0.153
E/A	(MeV)	-16.3	-16.2	-16.3	-16.3
K	(MeV)	281	344	355	240

Table A.2: The parameters of the density-dependent meson–nucleon couplings in the TW99 model.

a_σ	c_σ	c_σ	d_σ	a_ρ
1.365469	0.226061	0.409704	0.901995	0.515
a_ω	b_ω	c_ω	d_ω	-
1.402488	0.172577	0.344293	0.983955	-

coupling constants which were obtained by fitting properties of nuclear matter and selected finite nuclei, such as saturation point, binding energies, and charge RMS radii. The values are listed in Table A.1. The NL-SH and TM models are so called 'nonlinear' since they contain σ and ω self-interactions with extra couplings g_2, g_3 and d. These models proved themselves to be reliable in the description of nuclear matter properties as well as characteristics of finite nuclei. The density-dependent model TW99 contains in addition parameters for the density-dependent meson-nucleon couplings [see Eqs. (2.18) and (2.19)] which are listed in Table A.2. This model does not contain meson self-interaction terms and it is capable of describing nuclear matter and finite nuclei properties in similar fashion as the nonlinear models.

Appendix B

Selected Publications

PROCEEDINGS OF SCIENCE

Antibaryon interactions with the nuclear medium

Jaroslava Hrtánková*, **Jiří Mareš**

Nuclear Physics Institute, 250 68 Řež, Czech Republic
E-mail: hrtankova@ujf.cas.cz

This contribution deals with our recent study of antibaryon interactions with the nuclear medium within the relativistic mean-field approach using antibaryon coupling constants consistent with available experimental data. We performed calculations of $\bar{B}$ ($\bar{B} = \bar{p}, \bar{\Lambda}, \bar{\Sigma}, \bar{\Xi}$) bound states in selected nuclei. Due to the lack of information on the in-medium antihyperon annihilation near threshold only the $\bar{p}$ absorption was considered. It was described by the imaginary part of a phenomenological optical potential fitted to $\bar{p}$-atom data. The annihilation was treated dynamically, taking into account explicitly the reduced phase space for annihilation products in the nuclear medium, as well as the compressed nuclear density due to the antiproton. The energy available for the annihilation products was evaluated self-consistently, considering additional energy shift due to particle momenta in the $\bar{p}$-nucleus system. Corresponding $\bar{p}$ widths were significantly reduced, however, they still remain sizable. Next, the $\bar{p}$-nucleus interaction was constructed using the latest version of the Paris $\bar{N}N$ potential. Related scattering amplitudes were used to define the complex $\bar{p}$ optical potential in the nuclear medium. The resulting $\bar{p}$ $1s$ binding energies are about 10% smaller and widths about 20% larger than those obtained with the phenomenological approach.

The 26th International Nuclear Physics Conference
11-16 September, 2016
Adelaide, Australia

*Speaker.

PoS(INPC2016)280

1. Introduction

The antibaryon–nucleus interaction is an interesting and topical issue in view of the future experiments at FAIR facility. Its study could provide us with information about the behavior of an antibaryon inside the medium as well as nuclear dynamics. Moreover, it could serve as a test for models of (anti)hadron–hadron interactions. In particular, much attention was devoted to the $\bar{p}$-nucleus interaction and possible existence of $\bar{p}$-nuclear quasi-bound states [1]. It was argued in Ref. [1] that the phase space for $\bar{p}$ annihilation products in the medium could be substantially suppressed so that $\bar{p}$ could live relatively long inside the nucleus.

In this contribution, we report on our recent self-consistent calculations of $\bar{B}$ bound states in various nuclei using G-parity motivated coupling constants. Special attention was devoted to calculations of $\bar{p}$-nuclear bound states, which were performed using a phenomenological optical potential as well as microscopic Paris $\bar{N}N$ potential.

In Section 2, we briefly introduce the model used in our calculations. Our results are presented in Section 3 and conclusions are drawn in Section 4.

2. Model

The interactions of an antibaryon with A nucleons are studied within the relativistic mean-field approach (RMF) [2]. In this model, the (anti)baryons interact among each other by the exchange of the scalar (σ) and vector ($\omega_\mu, \vec{\rho}_\mu$) meson fields, and the massless photon field A_μ. The equations of motion are derived from the standard Lagrangian density $\mathscr{L}_N$ extended by the Lagrangian density $\mathscr{L}_{\bar{B}}$ describing the antibaryon interaction with the nuclear medium using the variational principle (see Ref. [3] for details). The Dirac equations for nucleons and antibaryon read:

$$[-i\vec{\alpha}\vec{\nabla} + \beta(m_j + S_j) + V_j]\psi_j^\alpha = \varepsilon_j^\alpha \psi_j^\alpha, \quad j = N, \bar{B}\,, \tag{2.1}$$

where

$$S_j = g_{\sigma j}\sigma, \quad V_j = g_{\omega j}\omega_0 + g_{\rho j}\rho_0\tau_3 + e_j\frac{1+\tau_3}{2}A_0 \tag{2.2}$$

are the scalar and vector potentials, respectively. Here, α denotes single particle states, m_j stands for (anti)baryon masses and $g_{\sigma j}, g_{\omega j}, g_{\rho j}$, and e_j are (anti)baryon coupling constants to corresponding fields. The Klein–Gordon equations for the meson fields involve additional source terms due to the antibaryon:

$$\begin{aligned}
(-\triangle + m_{\sigma^2} + g_2\sigma + g_3\sigma^2)\sigma &= -g_{\sigma N}\rho_{SN} - g_{\sigma\bar{B}}\rho_{S\bar{B}}\,,\\
(-\triangle + m_{\omega^2} + d\omega_0^2)\omega_0 &= g_{\omega N}\rho_{VN} + g_{\omega\bar{B}}\rho_{V\bar{B}}\,,\\
(-\triangle + m_{\rho^2})\rho_0 &= g_{\rho N}\rho_{IN} + g_{\rho\bar{B}}\rho_{I\bar{B}}\,,\\
-\triangle A_0 &= e_N\rho_{QN} + e_{\bar{B}}\rho_{Q\bar{B}}\,,
\end{aligned} \tag{2.3}$$

where $m_\sigma, m_\omega, m_\rho$ are the masses of considered mesons and $\rho_{Sj}, \rho_{Vj}, \rho_{Ij}$ and ρ_{Qj} are the scalar, vector, isovector and charge densities, respectively. The system of coupled Dirac (2.1) and Klein–Gordon (2.3) equations is solved self-consistently by iterative procedure.

The values of the nucleon–meson coupling constants and meson masses were adopted from the nonlinear RMF models TM1(2) [4] for heavy (light) nuclei and from the NL-SH model [5].

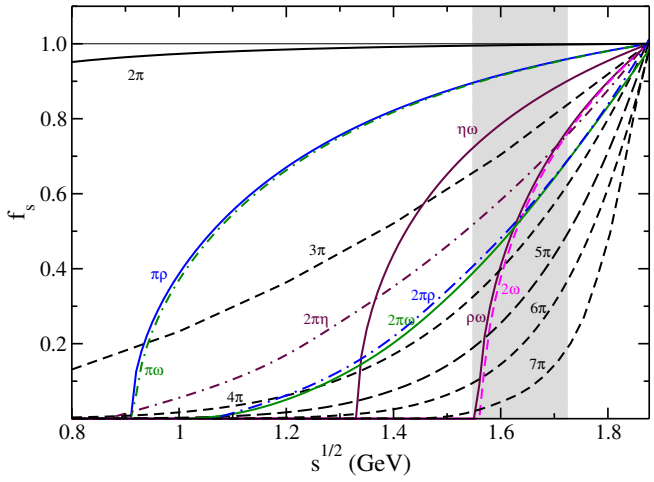

Figure 1: The phase space suppression factor f_s as a function of the center-of-mass energy $\sqrt{s}$.

The hyperon–meson coupling constants for the ω and ρ fields were derived using SU(6) symmetry relations. The values of the σ coupling constants were obtained from fits to available experimental data — Λ hypernuclei [6], Σ atoms [7], and Ξ production in (K^+,K^-) reaction [8].

The $\bar{B}$–nucleus interaction is constructed from the B–nucleus interaction with the help of the G-parity transformation: the potential generated by the exchange of the ω meson changes sign due to the G-parity and becomes attractive. The G-parity is surely a valid concept for the long and medium range $\bar{B}$ potential. It yields a very deep $\bar{B}$-nucleus potential, e. g., the $\bar{p}$ potential would be about 750 MeV deep inside a nucleus. However, the $\bar{B}$ annihilation, which is a dominant process in the short range interaction, and various many-body effects could cause significant deviations from the G-parity values in the nuclear medium. Indeed, the experiments with antiprotonic atoms [9] and $\bar{p}$ scattering off nuclei at low energies [10] suggest that the real part of the $\bar{p}$-nucleus potential is $100-300$ MeV deep in the nuclear interior. Therefore, we introduce a scaling factor ξ for the antibaryon–meson coupling constants which are in the following relation to the baryon–meson couplings:

$$g_{\sigma\bar{B}} = \xi\, g_{\sigma N}, \quad g_{\omega\bar{B}} = -\xi\, g_{\omega N}, \quad g_{\rho\bar{B}} = \xi\, g_{\rho N}\ . \tag{2.4}$$

In this work, we consider the value of $\xi = 0.2-0.3$ which is in accordance with the experimental data fits. We assume the same scaling for antihyperons, as well, due to the lack of experimental information on antihyperon interactions.

The realistic description of $\bar{B}$-nucleus interaction should involve $\bar{B}$ absorption in the medium. In our calculations, only the $\bar{p}$ absorption in a nucleus has been considered since we found no experimental information on antihyperon annihilation in the medium. The $\bar{p}$ absorption is described by the imaginary part of the optical potential in a '$t\rho$' form adopted from optical model phenomenology [9]:

$$2\mu \mathrm{Im}V_{\mathrm{opt}}(r) = -4\pi\left(1+\frac{\mu}{m_N}\frac{A-1}{A}\right)\mathrm{Im}b_0\rho(r)\ , \tag{2.5}$$

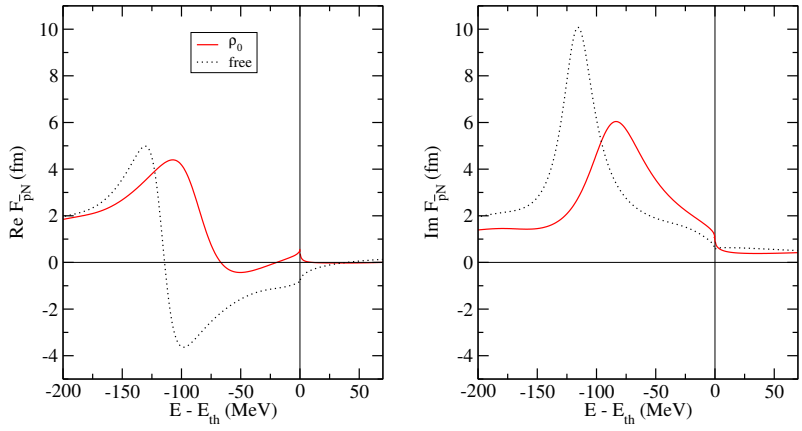

Figure 2: Energy dependence of the Paris 09 $\bar{p}N$ S-wave amplitudes: Pauli blocked amplitude for $\rho_0 = 0.17$ fm^{-3} (solid lines) is compared with free-space amplitude (dotted lines).

where μ is the $\bar{p}$–nucleus reduced mass. The density $\rho(r)$ is evaluated dynamically within the RMF model, while the parameter $\mathrm{Im}b_0 = 1.9$ fm is determined by fitting the $\bar{p}$ atom data [9]. The effective scattering length $\mathrm{Im}b_0$ describes the $\bar{p}$ absorption at threshold and, therefore, we evaluate the suppression factor f_s for a given decay channel to account for reduction of the phase space available for decay products of the $\bar{p}$ annihilation in the nuclear medium. The absorptive $\bar{p}$ potential then acquires the form

$$\mathrm{Im}V_{\bar{p}}(r,\sqrt{s},\rho) = \sum_{\text{channel}} B_c f_s(\sqrt{s})\mathrm{Im}V_{\text{opt}}(r)\ , \tag{2.6}$$

where B_c is the branching ratio for a given channel (see Ref. [3] for details). The calculated phase space suppression factors as a function of $\sqrt{s}$ for all channels considered are depicted in Figure 1.

Next, we construct the $\bar{p}$ optical potential using the S-wave $\bar{p}N$ scattering amplitudes derived from the latest version of the Paris $\bar{N}N$ potential [11]. The free-space amplitudes are modified using the multiple scattering approach of Wass et al. [12] to account for Pauli correlations in the medium. The in-medium isospin 1 and 0 amplitudes are of the form

$$F_1 = \frac{f_{\bar{p}n}(\delta\sqrt{s})}{1+\frac{1}{4}\xi_k\frac{\sqrt{s}}{m_N}f_{\bar{p}n}(\delta\sqrt{s})\rho}\ , \qquad F_0 = \frac{[2f_{\bar{p}p}(\delta\sqrt{s})-f_{\bar{p}n}(\delta\sqrt{s})]}{1+\frac{1}{4}\xi_k\frac{\sqrt{s}}{m_N}[2f_{\bar{p}p}(\delta\sqrt{s})-f_{\bar{p}n}(\delta\sqrt{s})]\rho}\ . \tag{2.7}$$

Here, $f_{\bar{p}n}$ and $f_{\bar{p}p}$ denote the free-space amplitudes as a function of $\delta\sqrt{s} = \sqrt{s} - E_{\text{th}}$; ρ is the nuclear core density distribution and ξ_k is taken from Ref. [13]. In Figure 2, there are free-space $\bar{p}N$ amplitudes compared with the in-medium modified amplitudes at ρ_0 as a function of energy. Both amplitudes vary significantly with energy below threshold. The peaks of the in-medium amplitudes are lower in comparison with the free-space amplitudes and are shifted towards threshold. The S-wave optical potential is of the following form:

$$2E_{\bar{p}}V_{\text{opt}} = -4\pi\frac{\sqrt{s}}{m_N}\left(F_0\frac{1}{2}\rho_p + F_1\left(\frac{1}{2}\rho_p+\rho_n\right)\right)\ , \tag{2.8}$$

where ρ_p (ρ_n) is the proton (neutron) density distribution and the factor $\sqrt{s}/m_N$ transforms the in-medium amplitudes to the $\bar{p}$-nucleus frame.

The energy relevant for the $\bar{p}$ scattering amplitudes and suppression factors in the nuclear medium is defined by Mandelstam variable

$$s = (E_N + E_{\bar{p}})^2 - (\vec{p}_N + \vec{p}_{\bar{p}})^2 \,, \tag{2.9}$$

where $E_N = m_N - B_{Nav}$, $E_{\bar{p}} = m_{\bar{p}} - B_{\bar{p}}$, B_{Nav} and $B_{\bar{p}}$ are the average binding energy per nucleon and the $\bar{p}$ binding energy, respectively. In the two-body c.m. frame $\vec{p}_N + \vec{p}_{\bar{p}} = 0$ and Eq. (2.9) reduces to

$$\sqrt{s} = \; m_{\bar{p}} + m_N - B_{\bar{p}} - B_{Nav} \quad \text{(M)}. \tag{2.10}$$

However, in the $\bar{p}$-nucleus frame the momentum dependent term in Eq. (2.9) is no longer negligible [14] and provides additional downward energy shift. Then the Mandelstam variable can be rewritten as

$$\sqrt{s} = E_{th}\left(1 - \frac{2(B_{\bar{p}} + B_{Nav})}{E_{th}} + \frac{(B_{\bar{p}} + B_{Nav})^2}{E_{th}^2} - \frac{1}{E_{th}}T_{\bar{p}} - \frac{1}{E_{th}}T_{Nav}\right)^{1/2} \quad \text{(J)}, \tag{2.11}$$

where T_{Nav} is the average kinetic energy per nucleon and $T_{\bar{p}}$ represents the $\bar{p}$ kinetic energy. The kinetic energies were calculated as the expectation values of the kinetic energy operator $T_j = -\frac{\hbar^2}{2m_j^{(*)}}\triangle$, where $m_j^* = m_j - S_j$ is the (anti)nucleon reduced mass.

3. Results

First, we performed self-consistent calculations of $1s$ $\bar{B}$ bound states in various nuclei using the RMF model with G-parity motivated coupling constants, introduced in previous section. Then, we considered the $\bar{p}$ absorption inside the nucleus. The $\bar{p}$ absorption was described by the imaginary

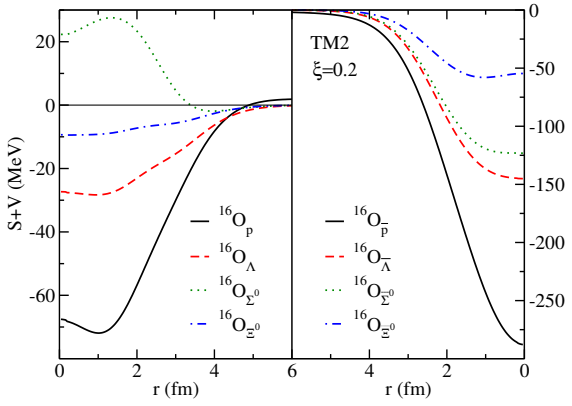

Figure 3: The B–nucleus (left) and $\bar{B}$–nucleus (right) potentials in ^{16}O, calculated dynamically in the TM2 model for $\xi = 0.2$.

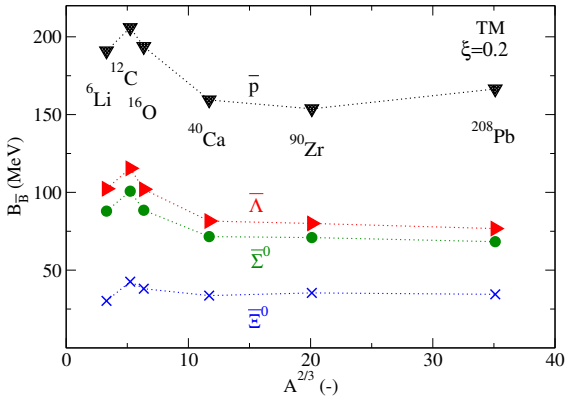

Figure 4: The A dependence of $\bar{B}$ 1s binding energies, calculated dynamically in the TM model for $\xi = 0.2$.

part of the phenomenological optical potential. Finally, we studied $\bar{p}$ quasi-bound states within the latest version of the Paris $\bar{N}N$ potential.

In Figure 3, there is the total potential acting on an extra baryon and extra antibaryon in the 1s state in ^{16}O, calculated dynamically (i. e., the core polarization effect due to $\bar{B}$ was considered) in the TM2 model. All antibaryons feel attractive potential due to the G-parity transformation (note that even $\bar{\Sigma}_0$ feels attraction inside the nucleus). The depth of the potential felt by $\bar{B}$ is deeper than the one felt by B inside the nucleus and indicates that the antibaryons would be strongly bound in the medium. Figure 4 presents corresponding 1s binding energies of $\bar{B}$ bound in nuclei across the periodic table, calculated dynamically in the TM model and $\xi = 0.2$. The $\bar{p}$ is the most bound antibaryon in all nuclei considered since it feels the deepest potential inside the medium. The $\bar{\Lambda}$, $\bar{\Sigma}_0$ and $\bar{\Xi}_0$ are bound less due to the weaker couplings to the meson fields. It is to be noted that the presented binding energies were calculated in two models, the TM2 model for ^{6}Li, ^{12}C and ^{16}O and the TM1 model for ^{40}Ca, ^{90}Zr and ^{208}Pb. These two models yield different values of

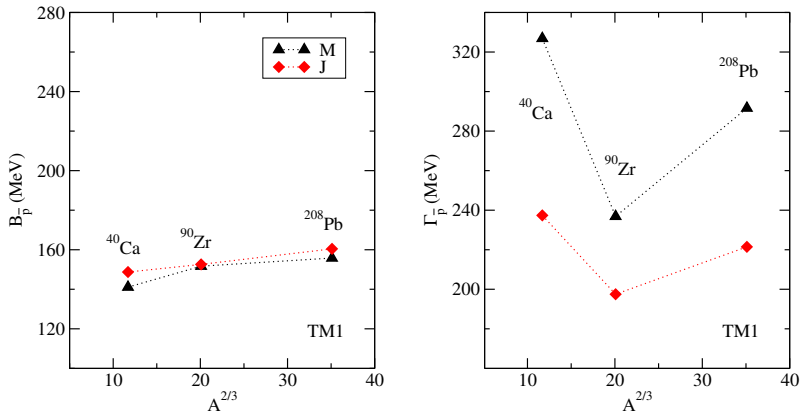

Figure 5: Binding energies (left panel) and widths (right panel) of 1s $\bar{p}$-nuclear states in selected nuclei, calculated dynamically using the TM1 model for different $\sqrt{s}$.

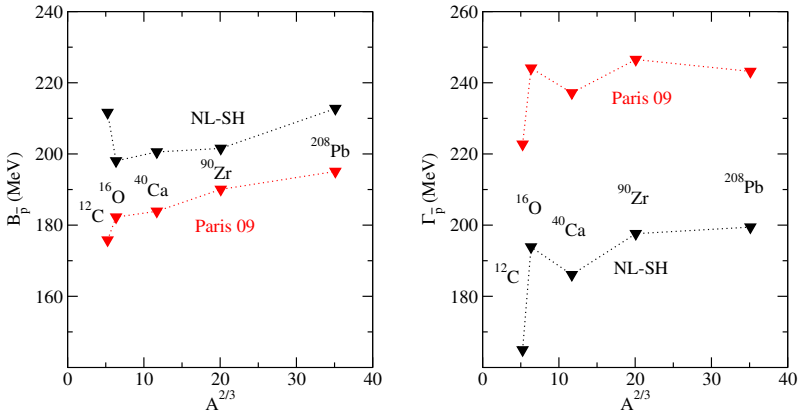

Figure 6: Binding energies (left panel) and widths (right panel) of $1s$ $\bar{p}$-nuclear states in selected nuclei, calculated dynamically for $\sqrt{s} = \mathrm{J}$ using the Paris $\bar{N}N$ S-wave potential (red) and phenomenological approach within the NL-SH model (black).

nuclear compressibility and different magnitudes of the σ and ω fields and, therefore, the binding energies do not grow with the increasing mass number A as would be expected (see Ref. [3] for more details).

Next, we considered the $\bar{p}$ absorption inside the nucleus by adding the imaginary part of the phenomenological potential to the real $\bar{p}$-nucleus potential evaluated within the RMF approach. In Figure 5, there are binding energies (left panel) and widths (right panel) of the $1s$ $\bar{p}$-nuclear states in various nuclei, calculated dynamically in the TM1 model. The presented results were calculated for $\sqrt{s}$ in the two-body frame (M) and laboratory frame (J). The two versions of $\sqrt{s}$ yield similar $\bar{p}$ binding energies. The energies in a given nucleus are not much affected by the $\bar{p}$ absorption (compare with Figure 4). On the other hand, the $\bar{p}$ widths are sizable in the two-body c.m. frame and are significantly reduced after including the momentum dependent term in $\sqrt{s}$. However, they still remain large.

We performed a comparable study of $\bar{p}$-nuclear quasi-bound states using the microscopic Paris $\bar{N}N$ S-wave potential. The resulting $1s$ $\bar{p}$ binding energies and corresponding widths are presented in Figure 6. The $\bar{p}$ binding energies and widths calculated using the phenomenological approach within the NL-SH model are shown for comparison. The Paris S-wave potential yield smaller $\bar{p}$ binding energies than the phenomenological potential in all nuclei considered. The $\bar{p}$ widths exhibit the same A dependence, however, they are much larger than those calculated with the phenomenological potential. It is to be noted that the Paris $\bar{N}N$ potential contains sizable P-wave interaction which should be included in the calculations. Such calculations have been performed recently and will be published elsewhere.

4. Conclusions

We performed self-consistent calculations of antibaryon-nucleus bound states in selected nuclei. First, the $\bar{B}$-nucleus potential was constructed within the RMF approach using the G-parity motivated coupling constants properly scaled to fit available experimental data. The real parts of the

potentials felt by $\bar{B}$ inside nuclei are attractive and fairly deep due to the G-parity transformation. In our calculations, we considered only the $\bar{p}$ absorption inside the nucleus so far. The absorption was described by the imaginary part of the phenomenological potential. The phase space suppression factors entering the phenomenological potential were evaluated self-consistently using $\sqrt{s}$ for the two-body frame and $\bar{p}$-nucleus frame. It was found that the energy shift due to N and $\bar{p}$ momenta significantly reduces the $\bar{p}$ widths. However, they still remain sizable for potentials consistent with $\bar{p}$-atom data. Next, we performed calculations of $\bar{p}$-nuclear quasi-bound states using the optical potential constructed from the Paris $\bar{N}N$ S-wave scattering amplitudes. The free-space $\bar{p}N$ amplitudes were modified in order to account for Pauli correlations in medium. The resulting $1s$ $\bar{p}$ binding energies are about 10% smaller and widths about 20% larger than those calculated with the phenomenological approach.

Acknowledgments

We wish to thank E. Friedman, A. Gal and S. Wycech for valuable discussions, and B. Loiseau for providing us with the $\bar{N}N$ amplitudes. This work was supported by the GACR Grant No. P203/15/04301S.

References

[1] T. J. Bürvenich, W. Greiner, I. N. Mishustin, L. M. Satarov, H. Stöcker, *Phys. Rev.* **C 71** (2005) 035201.

[2] B. D. Serot, J.D. Walecka, *Adv. Nucl. Phys.* **16** (1986) 1.

[3] J. Hrtánková, J. Mareš, *Nucl. Phys.* **A 945** (2016) 197.

[4] Y. Sugahara, H. Toki, *Nucl. Phys.* **A 579** (1994) 557.

[5] M. M. Sharma, M.A. Nagarajan, P. Ring, *Phys. Lett.* **B 312** (1993) 377.

[6] J. Mareš, B. K. Jennings, *Phys. Rev.* **C 49** (1994) 2472.

[7] J. Mareš, E. Friedman, A. Gal, B. K. Jennings, *Nucl. Phys.* **A 594** (1995) 311.

[8] P. Khaustov et al., *Phys. Rev.* **61** (2000) 054603.

[9] E. Friedman, A. Gal, J. Mareš, *Nucl. Phys.* **A 761** (2005) 283.

[10] G. E. Walker, Ch. D. Goodman, C. Olmer (Eds.), *Antinucleon– and Nucleon–Nucleus Interaction*, Plenum Press, New York 1985.

[11] B. El-Bennich, M. Lacombe, B. Loiseau, S. Wycech, *Phys. Rev.* **C 79** (2009) 054001.

[12] T. Wass, M. Rho, W. Weise, *Nucl. Phys.* **A 617** (1997) 449.

[13] E. Friedman, A. Gal, *Nucl. Phys.* **A 959** (2017) 66.

[14] A. Cieplý, E. Friedman, A. Gal, D. Gazda, J. Mareš, *Phys. Lett.* **B 702** (2011) 402.

Available online at www.sciencedirect.com

ScienceDirect

Nuclear Physics A 945 (2016) 197–215

NUCLEAR PHYSICS A

www.elsevier.com/locate/nuclphysa

Interaction of antiprotons with nuclei

Jaroslava Hrtánková *, Jiří Mareš

Nuclear Physics Institute, 250 68 Řež, Czech Republic

Received 3 September 2015; received in revised form 6 October 2015; accepted 24 October 2015

Available online 28 October 2015

Abstract

We performed fully self-consistent calculations of $\bar{p}$-nuclear bound states using a complex $\bar{p}$-nucleus potential accounting for $\bar{p}$-atom data. While the real part of the potential is constructed within the relativistic mean-field (RMF) model, the $\bar{p}$ annihilation in the nuclear medium is described by a phenomenological optical potential. We confirm large polarization effects of the nuclear core caused by the presence of the antiproton. The $\bar{p}$ annihilation is treated dynamically, taking into account explicitly the reduced phase space for annihilation from deeply bound states as well as the compressed nuclear density due to the antiproton. The energy available for the products of $\bar{p}$ annihilation in the nuclear medium is evaluated self-consistently, considering the additional energy shift due to transformation from the $\bar{p}N$ system to $\bar{p}$-nucleus system. Corresponding $\bar{p}$ widths in the medium are significantly suppressed, however, they still remain considerable for the $\bar{p}$ potential consistent with experimental data.

Keywords: Antiproton–nucleus interaction; Antiproton annihilation; Antiproton nuclear bound states

1. Introduction

The study of the interaction of antiprotons with nuclei is a source of valuable information about the behavior of antiproton in nuclear matter, the in-medium $\bar{p}N$ interactions, as well as nuclear dynamics. Experiments aiming at exploring the $\bar{p}$-nucleon interaction have been performed since the discovery of the antiproton in 1955 [1]. The antiproton–proton annihilation was

* Corresponding author.
E-mail address: hrtankova@ujf.cas.cz (J. Hrtánková).

http://dx.doi.org/10.1016/j.nuclphysa.2015.10.005

studied at the Brookhaven National Laboratory (BNL) and CERN in the 1960s [2] (see also [3] and the references therein).

Theoretical considerations about the $\bar{p}$-nucleus interaction are based on symmetry between NN and $\bar{N}N$ potentials. In the framework of a meson exchange model, the real part of an $\bar{N}N$ potential constructed using the G-parity transformation is strongly attractive [4], which led to conjectures about deeply bound $\bar{p}$ states in nuclei [5–7]. The possibility of existence of antiproton–nucleon or antiproton–nucleus quasi-bound states was studied in experiments at the LEAR facility at CERN [8]. The $\bar{p}$ elastic and inelastic scattering off nuclei and proton knock-out reactions were analyzed in order to extract information about the $\bar{p}$-nucleus potential. The measurements of the differential cross-section for the $\bar{p}$ elastic scattering off ^{12}C at 46.8 MeV favor a shallow attractive $\mathrm{Re}V_{\mathrm{opt}}$ with the depth ≤ 70 MeV and an absorptive part $\mathrm{Im}V_{\mathrm{opt}} \geq 2\mathrm{Re}V_{\mathrm{opt}}$ [8]. On the other hand, $\bar{p}$ production in proton–nucleus and nucleus–nucleus collisions is well described by $\mathrm{Re}V_{\mathrm{opt}} \sim -(100\text{–}200)$ MeV [9]. Despite considerable efforts, no convincing evidence for existence of $\bar{p}N$ or $\bar{p}$-nucleus bound states has been found [10,11].

Unique information about the $\bar{p}$-nucleus optical potential near threshold has been provided by analyses of strong interaction energy shifts and widths of $\bar{p}$-atomic levels [12–14]. Global fits of 107 data points of X-ray and radiochemical data led to the $\bar{p}$ potential with an attractive real part about 110 MeV deep and an absorptive imaginary part about 160 MeV deep when extrapolated into the nuclear interior [14]. However, the $\bar{p}$-atom data probe reliably the $\bar{p}$-nucleus potential at the far periphery of the nucleus and model dependent extrapolations to the nuclear interior are a source of large uncertainties. Very recently Friedman et al. [15] applied $\bar{N}N$ scattering amplitudes of the latest version of the Paris $\bar{N}N$ potential [16] to construct the $\bar{p}$-nucleus optical potential and demonstrated the importance of P-wave amplitudes to account for the $\bar{p}$-atom data.

The $\bar{p}$-nucleus interaction has attracted renewed interest in recent years at the prospect of future experiments with $\bar{p}$ beams at the FAIR facility at GSI [17]. The $\bar{p}$-nuclear bound states and the possibility of their formation have been studied in Refs. [18–23] within the relativistic mean-field approach [24,25] by employing the G-parity transformation of nucleon–meson coupling constants. A scaling factor ξ was introduced to vary the depth of the $\bar{p}$-nucleus potential [18–22]. This scaling factor which represents departure from the G-parity symmetry can be then fitted to yield the $\bar{p}$ potential consistent with available experimental data. The calculations predicted strong binding of the antiproton inside a nucleus and large compression of the nuclear core induced by the presence of $\bar{p}$. The $\bar{p}$ annihilation in the nuclear medium was studied as well [18]. Partial widths were evaluated with the help of vacuum annihilation cross sections for considered annihilation channels and the phase space suppression for $\bar{p}$ annihilation from deeply bound states was taken into account. The lifetime of $\bar{p}$ in a nucleus was estimated to be in the range of 2–20 fm/c.

In Refs. [21,22] the Giessen Boltzmann–Uehling–Uhlenbeck (GiBUU) transport model [26] was applied to $\bar{p}$-nucleus interactions in a wide range of $\bar{p}$-beam momenta. The GiBUU model was used to fit the KEK data [27] on $\bar{p}$ absorption cross sections at $p_{\mathrm{lab}} = 470\text{–}880$ MeV/c to fix the value of the scaling factor $\xi = 0.22$, which corresponds to $\mathrm{Re}V_{\mathrm{opt}} \simeq 150$ MeV deep at normal nuclear density. Dynamical response of selected nuclei to the incident antiproton together with the probability that the antiproton reaches the dense nuclear environment before it annihilates was examined. The time required for the nuclear compression was found to be within the range of the $\bar{p}$ lifetime calculated in Ref. [18].

Recently, Gaitanos et al. [28,29] developed a non-linear derivative (NLD) model which accounts for momentum dependence of the nuclear mean fields, which is missing in standard RMF models. This momentum dependence reduces the G-parity motivated $\bar{p}$ optical potential and

yields its depth in agreement with available experimental data. It was demonstrated that the RMF approach with antiproton–meson couplings scaled by a factor $\xi = 0.2$–0.3 can reproduce the NLD results in average [30].

In this work, we performed fully self-consistent calculations of $\bar{p}$ nuclear bound states using a complex $\bar{p}$-nucleus potential consistent with $\bar{p}$-atom data, aiming at analyzing in detail various effects which could have impact on calculated $\bar{p}$-nuclear characteristics. In particular, we explored dynamical response of the nuclear core to the presence of the deeply bound antiproton. In view of appreciable densities in the interior of $\bar{p}$ nuclei, it is desirable to check how reliable are the underlying RMF models in such highly dense nuclear matter. We therefore applied in our calculations various RMF models which yield different compressibilities of nuclear matter, including the TW99 model with density-dependent couplings [31], and compared their predictions. Annihilation widths in the nuclear medium depend strongly on the energy available for the decay products of the deeply bound antiproton, as well as the density of the surrounding nuclear medium. It is thus imperative to perform fully dynamical calculations of $\bar{p}$-nuclear states using a complex $\bar{p}$ potential which incorporates main features of the $\bar{p}$-nucleus interaction, while taking into account self-consistently the additional energy shift corresponding to the transformation from the 2 c.m. $\bar{p}N$ annihilation to $\bar{p}N$ annihilation in a nucleus. The procedure for self-consistent handling the sub-threshold energy dependence was recently applied in calculations of kaonic atoms, and kaonic and η nuclear states using chirally motivated $\bar{K}N$ amplitudes [32–37].

The paper is organized as follows. In Section 2, we briefly describe the applied RMF model for calculating $\bar{p}$ nuclear states, discuss the underlying $\bar{p}$-nucleus interaction and $\bar{p}$ absorption in the nuclear medium including self-consistent schemes for evaluating the energy $\sqrt{s}$ which enters phase space suppression factors. In Section 3, we present selected results of our calculations of $\bar{p}$ quasi-bound states in various nuclei across the periodic table in order to demonstrate dynamical effects in the nuclear core caused by the antiproton, model dependence of the calculations, and the role of various factors that determine $\bar{p}$ widths in the nuclear medium. Conclusions are summarized in Section 4.

2. Model

The interaction of an antiproton with a nucleus is studied within the relativistic mean-field model [24,25]. In this model, the interaction among (anti)nucleons is mediated by the exchange of the scalar (σ) and vector (ω_μ, $\vec{\rho}_\mu$) meson fields, and the massless photon field A_μ. In order to incorporate the $\bar{p}$ into the model we extended the standard Lagrangian density for nucleonic sector by the Lagrangian density which describes the antiproton interaction with the nuclear medium:

$$\begin{aligned}\mathcal{L} = &\sum_{j=N,\bar{p}} \bar{\psi}_j [i\gamma^\mu \partial_\mu - m_j - g_{\sigma j}\sigma - g_{\omega j}\gamma_\mu \omega^\mu - g_{\rho j}\gamma_\mu \vec{\tau}\cdot\vec{\rho}^\mu - e\gamma_\mu \frac{1}{2}(1+\tau_3)A^\mu]\psi_j \\ &+ \frac{1}{2}\left(\partial_\mu\sigma\,\partial^\mu\sigma - m_\sigma^2\sigma^2\right) - \frac{1}{2}(\frac{1}{2}\Omega_{\mu\nu}\Omega^{\mu\nu} - m_\omega^2\omega^\mu\omega_\mu) \\ &- \frac{1}{2}(\frac{1}{2}\vec{R}_{\mu\nu}\cdot\vec{R}^{\mu\nu} - m_\rho^2\vec{\rho}_\mu\cdot\vec{\rho}^\mu) - \frac{1}{4}F_{\mu\nu}F^{\mu\nu} \\ &- \frac{1}{3}g_2\sigma^3 - \frac{1}{4}g_3\sigma^4 + \frac{1}{4}d(\omega^\mu\omega_\mu)^2\,, \end{aligned} \tag{1}$$

where m_j denotes the mass of the (anti)nucleon; m_σ, m_ω, m_ρ are the masses of the considered meson fields; $g_{\sigma j}$, $g_{\omega j}$, $g_{\rho j}$ and e are the (anti)nucleon couplings to corresponding fields – g_2, g_3 and d represent the strengths of the σ and ω field self-interactions. The field tensor fulfills $F_{\mu\nu} = \partial_\mu F_\nu - \partial_\nu F_\mu$, and correspondingly for the $\Omega_{\mu\nu}$ and $\vec{R}_{\mu\nu}$.

The equations of motion are derived using the variational principle employing the mean-field and no-sea approximations. Furthermore, we are dealing with stationary states and spherically symmetric nuclei. We assume that single particle states do not mix isospin, i.e., only the neutral component of the isovector ρ-meson field is considered. The Dirac equations for nucleons and antiproton then read:

$$[-i\vec{\alpha}\vec{\nabla} + \beta(m_j + S_j) + V_j]\psi_j^\alpha = \epsilon_j^\alpha \psi_j^\alpha, \quad j = N, \bar{p}\ , \tag{2}$$

where

$$S_j = g_{\sigma j}\sigma, \quad V_j = g_{\omega j}\omega_0 + g_{\rho j}\rho_0\tau_3 + e_j\frac{1+\tau_3}{2}A_0 \tag{3}$$

are the scalar and vector potentials and α denotes single particle states. The equations of motion for the boson fields acquire additional source terms due to the presence of $\bar{p}$:

$$\begin{aligned}
(-\triangle + m_\sigma^2 + g_2\sigma + g_3\sigma^2)\sigma &= -g_{\sigma N}\rho_{SN} - g_{\sigma\bar{p}}\rho_{S\bar{p}}\ ,\\
(-\triangle + m_\omega^2 + d\omega_0^2)\omega_0 &= g_{\omega N}\rho_{VN} + g_{\omega\bar{p}}\rho_{V\bar{p}}\ ,\\
(-\triangle + m_\rho^2)\rho_0 &= g_{\rho N}\rho_{IN} + g_{\rho\bar{p}}\rho_{I\bar{p}}\ ,\\
-\triangle A_0 &= e_N\rho_{QN} + e_{\bar{p}}\rho_{Q\bar{p}}\ ,
\end{aligned} \tag{4}$$

where $\rho_{\mathrm{S}j}$, $\rho_{\mathrm{V}j}$, $\rho_{\mathrm{I}j}$ and $\rho_{\mathrm{Q}j}$ are the scalar, vector, isovector, and charge densities, respectively. The coupled system of the equations of motion Eq. (2) and Eq. (4) is solved fully self-consistently by iterative procedure.

The nucleon–meson coupling constants and meson masses were adopted from the nonlinear RMF model TM1 for heavy nuclei and TM2 for light nuclei [38]. These two RMF parametrizations proved successful in the description of ground state characteristics of ordinary nuclei in the corresponding mass regions, however, it is not guaranteed that they will provide consistent account of the properties of $\bar{p}$ nuclei (e.g. $\bar{p}$ and total binding energies), particularly their A dependence. Moreover, since TM1 and TM2 yield quite different compressibilities of nuclear matter, they could predict different size of the nuclear core modifications due to the antiproton. We thus performed calculations of selected $\bar{p}$ nuclei using the RMF NL-SH parametrization [39] as well, and studied model dependence of our results.

The antiproton placed in a nucleus causes strong polarization effects resulting in the high central density of the nuclear core, reaching up to 4 times the nuclear matter density. The application of standard RMF models for the description of nuclear matter at such densities has to be considered as extrapolation. Therefore, we employed also the density-dependent RMF model [31] which is more suitable for the description of dense nuclear matter. In the density-dependent model, the nucleon–meson couplings are a function of the nucleon density $\rho_{\mathrm{V}N}$

$$g_{iN}(\rho_{\mathrm{V}N}) = g_{iN}(\rho_0)\, f_i(x)\ , \quad i = \sigma, \omega\ , \tag{5}$$

where

$$f_i(x) = a_i\frac{1 + b_i(x + d_i)^2}{1 + c_i(x + d_i)^2}\ , \tag{6}$$

and $x = \rho_{VN}/\rho_0$, where ρ_0 represents the saturation density of nuclear matter. The coupling of the ρ meson has an exponential character

$$g_{\rho N}(\rho_{VN}) = g_{\rho N}(\rho_0)\exp[-a_\rho(x-1)] \,. \tag{7}$$

The parameters a_i, b_i, c_i, d_i and a_ρ are fitted to Dirac–Brueckner calculations of nuclear matter and constrained by conditions on the functions $f_i(x)$ [31]. The density dependence of the nucleon–meson couplings leads to an extra term Σ_R in the Dirac equation for nucleons

$$[-i\vec{\alpha}\vec{\nabla} + \beta(m_N + S_N) + V_N + \Sigma_R]\psi_N^\alpha = \epsilon_N^\alpha \psi_N^\alpha \,, \tag{8}$$

where

$$\Sigma_R = \frac{\partial g_{\omega N}}{\partial \rho_{VN}}\rho_{VN}\omega_0 + \frac{\partial g_{\rho N}}{\partial \rho_{VN}}\rho_{IN}\rho_0 - \frac{\partial g_{\sigma N}}{\partial \rho_{VN}}\rho_{SN}\sigma \,. \tag{9}$$

The Klein–Gordon equations for the meson fields retain their form as in Eq. (4) only the couplings become a function of density.

The equations of motion in the RMF model are derived on the Hartree level where each nucleon moves in mean fields created by *all* nucleons bound in the nucleus. Consequently, the nucleon feels in addition a kind of "attraction" as well as "repulsion" from itself. In ordinary nuclei this self-interaction has only a minor (1/A) effect.[1] However, the potential acting on the antiproton in a nucleus is much deeper than the potential acting on nucleons and so the impact of the $\bar{p}$ self-interaction could become pronounced. In order to explore the role of the $\bar{p}$ self-interaction, we performed calculations where the $\bar{p}$ source terms were omitted in the Klein–Gordon equations for the boson fields acting on the antiproton, i.e.

$$(-\triangle + m_M^2)\Phi_{\bar{p}} = g_{MN}\rho_{MN} \cancel{+ g_{M\bar{p}}\rho_{M\bar{p}}} \tag{10}$$

and compared them with the results of regular calculations according to Eq. (4). The impact of the unphysical $\bar{p}$ self-interaction depends on the depth of the $\bar{p}$ potential. The deeper is the $\bar{p}$ potential the larger is the role of the $\bar{p}$ self-interaction. We will demonstrate in the following section that the effect of the $\bar{p}$ self-interaction is negligible for the $\bar{p}$ potential consistent with available experimental data.

2.1. $\bar{p}$-nucleus interaction

On the level of hadron degrees of freedom the strong interaction between nucleons is understood as a meson exchange process. When going from the NN interaction to $\bar{N}N$ interaction the G-parity transformation, which consist of charge conjugation and rotation in isospin space, seems to be a natural link for the medium and long range part of the interaction which is governed by the meson exchange. To describe the $\bar{p}$-nucleus interaction we thus make use of the G-parity transformation. The real part of the $\bar{p}$-nucleus potential is obtained by the transformation of the nucleon–nucleus potential

$$U_{\bar{p}} = \sum_M G_M U_M \,, \tag{11}$$

where U_M denotes the potential generated by the exchange of the meson M and G_M is the G-parity eigenvalue for the corresponding meson field. When expressed in terms of coupling constants we have

[1] It is to be noted that the self-interaction is directly subtracted in the Hartree–Fock formalism.

$$g_{\sigma\bar{p}} = g_{\sigma N}, \quad g_{\omega\bar{p}} = -g_{\omega N}, \quad g_{\rho\bar{p}} = g_{\rho N} \ . \tag{12}$$

Within the RMF approach the nuclear ground state is well described by an attractive scalar potential $S(0) \simeq -400$ MeV and a repulsive vector potential $V(0) \simeq 350$ MeV. The central potential acting on a nucleon in a nucleus is then $S(0) + V(0) \simeq -50$ MeV. Since the vector potential generated by the ω meson exchange changes its sign under the G-parity transformation, the total $\bar{p}$ potential would be strongly attractive and ≈ 750 MeV deep in the nuclear interior.

We should stress that G-parity is surely a valid concept for the long and medium range $\bar{p}$ potential. However, the $\bar{p}$ annihilation plays a crucial role in the $\bar{p}N$ and $\bar{p}$-nucleus interactions. It has a major contribution in the short range region and it is not clear to what extent it affects the elastic part of the interaction. Moreover, various many-body effects could cause deviations from the G-parity values in the nuclear medium as well [18]. Therefore G-parity should be regarded as a mere starting point to determine the $\bar{p}$-meson coupling constants in standard RMF models. It is to be noted that a recent approach [30] which incorporates the momentum dependence of the mean fields yields the $\bar{p}$ potential consistent with in-medium antinucleon phenomenology while retaining the G-parity symmetry.

The form of the $\bar{p}$ potential in the nuclear medium is still quite uncertain, despite considerable experimental as well as theoretical efforts in the past. Following Refs. [18–22] we introduce a uniform scaling factor $\xi \in \langle 0, 1\rangle$ for the $\bar{p}$-meson coupling constants:

$$g_{\sigma\bar{p}} = \xi\, g_{\sigma N}, \quad g_{\omega\bar{p}} = -\xi\, g_{\omega N}, \quad g_{\rho\bar{p}} = \xi\, g_{\rho N} \tag{13}$$

to control the strength of the $\bar{p}$-nucleus interaction. The experiments with antiprotonic atoms, $\bar{p}$ scattering off nuclei and $\bar{p}$ production in proton–nucleus and nucleus–nucleus collisions suggest that the real part of the $\bar{p}$ potential should be in the range of $-$(100–300) MeV at normal nuclear density [12,14,21] which corresponds to $\xi = 0.2$–0.3.

For the real part of the $\bar{p}$-nucleus potential we adopted the value $\xi = 0.2$ which provides the $\bar{p}$ potential consistent with $\bar{p}$-atom data. It is to be stressed here that due to sizable modifications of the nuclear core caused by the deeply bound antiproton, the dynamically evaluated $\bar{p}$ potential becomes considerably deeper than the corresponding potential deduced from the analysis of $\bar{p}$ atoms, as will be demonstrated in Section 4.

2.1.1. $\bar{p}$ annihilation

The annihilation of the antiproton in the nuclear medium is an inseparable part of any realistic description of the $\bar{p}$-nucleus interaction. Since the RMF approach does not address directly the $\bar{p}$ absorption in a nucleus, we adopted the imaginary part of the optical potential in a '$t\rho$' form from optical model phenomenology [14]:

$$2\mu \mathrm{Im} V_{\mathrm{opt}}(r) = -4\pi \left(1 + \frac{\mu}{m_N}\frac{A-1}{A}\right) \mathrm{Im} b_0 \rho(r) \ , \tag{14}$$

where μ is the $\bar{p}$-nucleus reduced mass. While the density $\rho(r)$ was treated as a dynamical quantity evaluated within the RMF model, the global parameter $\mathrm{Im}b_0 = 1.9$ fm adopted from Ref. [14], was fitted to $\bar{p}$ atom data. It is to be noted that the value of $\mathrm{Im}b_0$ was determined for a finite-range (FR) interaction, where original densities were replaced by 'folded' densities, while here it was applied to construct a zero-range '$t\rho$' potential. We checked that the RMF densities in the present work yield r.m.s. radii larger than the unfolded densities used in the $\bar{p}$ atom analysis and thus effectively approximate the FR 'folded' densities in Ref. [14].

In our calculations we considered that $\mathrm{Im}b_0$ involves annihilation channels with corresponding branching ratios B_c listed in Table 1. They are sorted according the number of mesons in final

Table 1
The annihilation channels for $\bar{p}N$ at rest in vacuum. Here, n_f is the number of decay products and B_c denotes the branching ratio of a particular decay channel[a].

n_f	Channel	B_c [%]	n_f	Channel	B_c [%]
2	$2\pi^0$	0.07		$\pi^+\pi^-\pi^0$	1.8
	$\pi^+\pi^-$	0.31		$\pi_0 K_S K_L$	$6.7 \cdot 10^{-4}$
	$\pi^0\rho^0$	1.7		$\pi^\pm K^\mp K_S$	$2.7 \cdot 10^{-3}$
	$\pi^\pm\rho^\mp$	0.9		$\omega K^+ K^-$	$2.3 \cdot 10^{-3}$
	$\pi^0\omega$	0.6	4	$4\pi^0$	0.5
	$\rho^0\omega$	2.3		$\pi^+\pi^-2\pi^0$	7.8
	$\omega\eta$	1.5		$2\pi^+2\pi^-$	4.2
	2ω	3.0	5	$5\pi^0$	0.5
	K^+K^-	$1.0 \cdot 10^{-3}$		$\pi^+\pi^-3\pi^0$	20.1
	$K_S K_L$	$7.9 \cdot 10^{-4}$		$2\pi^+2\pi^-\pi^0$	10.4
3	$2\pi^0\eta$	0.7	6	$\pi^+\pi^-4\pi^0$	1.9
	$\pi^+\pi^-\eta$	1.3		$2\pi^+2\pi^-2\pi^0$	13.3
	$2\pi^0\omega$	2.6		$3\pi^+3\pi^-$	2.0
	$\pi^+\pi^-\omega$	6.6	7	$3\pi^+3\pi^-\pi^0$	1.9
	$\pi^+\pi^-\rho^0$	3.6		$2\pi^+2\pi^-3\pi^0$	4.0

[a] The non-strange annihilation channels and their branching ratios are taken from Ref. [18] (see also references therein). Branching ratios for channels containing kaons are taken from Ref. [41].

state. We included only direct decay channels, i.e. only non-resonant contributions and no further decay of produced mesons were taken into account, as in Ref. [18]. Moreover, we considered annihilation channels containing kaons.

The energy available for $\bar{p}N$ annihilation in vacuum at rest is $\sqrt{s} = m_{\bar{p}} + m_N$. In the nuclear medium, this energy is reduced due to the binding of the antiproton and nucleon. Consequently, the phase space available for annihilation products should be substantially suppressed for deeply bound $\bar{p}$, which might lead to a relatively long living antiproton in the nuclear interior [18].

We took into account the suppression of phase space by introducing corresponding suppression factors f_s. For the two body decay channels f_s were evaluated with the help of the formula [40]:

$$f_s = \frac{M^2}{s}\sqrt{\frac{[s-(m_1+m_2)^2][s-(m_1-m_2)^2]}{[M^2-(m_1+m_2)^2][M^2-(m_1-m_2)^2]}}\,\Theta(\sqrt{s}-m_1-m_2)\,, \tag{15}$$

where m_1, m_2 are the masses of the annihilation products and $M = m_{\bar{p}} + m_N$. For channels containing more than 2 particles in the final state the suppression factors f_s were calculated with the help of the Monte Carlo simulation tool PLUTO [42]. To compute the suppression factors for the channels containing more than 4 particles in the final state we expressed the decay products in terms of two or three effective particles. The n-body phase space ϕ_n was then decomposed into smaller subspaces according the formula [40]

$$d\phi_n(P; p_1, \ldots, p_n) = d\phi_j(q; p_1, \ldots, p_j) \times d\phi_{n-j+1}(P; q, p_{j+1}, \ldots, p_n)(2\pi)^3 dq^2, \tag{16}$$

where $q^2 = (\sum_{i=1}^{j} E_i)^2 - |\sum_{i=1}^{j} \vec{p}_i|^2$, P is the 4-momentum of the annihilating pair and p_i are the 4-momenta of the annihilation products. The suppression factor was expressed as a ratio of Dalitz plot area for reduced $\sqrt{s}$ and vacuum $\sqrt{s} = 2m_N$. The phase space suppression factors

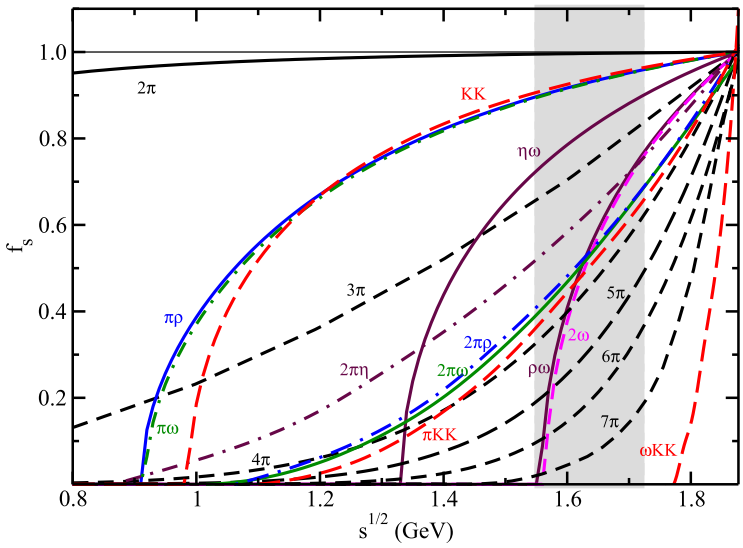

Fig. 1. The phase space suppression factors f_s as a function of the c.m. energy $\sqrt{s}$. The range of $\sqrt{s}$ relevant for $\bar{p}$-nuclear states is denoted by gray area.

for considered annihilation channels are plotted as a function of the center-of-mass energy $\sqrt{s}$ in Fig. 1.

The energy available for the annihilation in the medium is given by Mandelstam variable

$$s = (E_N + E_{\bar{p}})^2 - (\vec{p}_N + \vec{p}_{\bar{p}})^2 \,, \tag{17}$$

where $E_N = m_N - B_N$, $E_{\bar{p}} = m_{\bar{p}} - B_{\bar{p}}$, and B_N ($B_{\bar{p}}$) is the nucleon ($\bar{p}$) binding energy. In the two-body c.m. frame $\vec{p}_N + \vec{p}_{\bar{p}} = 0$ and Eq. (17) reduces to

$$\sqrt{s} = m_{\bar{p}} + m_N - B_{\bar{p}} - B_N. \tag{18}$$

This form of $\sqrt{s}$ was considered in Ref. [18]. However, when the annihilation of the antiproton with a nucleon takes place in a nucleus, the momentum dependent term in Eq. (17) is no longer negligible [32] and provides additional downward energy shift to that stemming from the binding energies $B_{\bar{p}}$ and B_N. Taking into account averaging over the angles $(\vec{p}_N + \vec{p}_{\bar{p}})^2 \approx \vec{p}_N^{\,2} + \vec{p}_{\bar{p}}^{\,2}$, Eq. (17) can be rewritten as

$$\sqrt{s} = E_{th}\left(1 - \frac{2(B_{\bar{p}} + B_{Nav})}{E_{th}} + \frac{(B_{\bar{p}} + B_{Nav})^2}{E_{th}^2} - \frac{1}{E_{th}}T_{\bar{p}} - \frac{1}{E_{th}}T_{Nav}\right)^{1/2}, \tag{19}$$

where $E_{th} = 2m_N$, B_{Nav} and T_{Nav} is the average binding and average kinetic energy per nucleon, respectively, and $T_{\bar{p}}$ represents the $\bar{p}$ kinetic energy. The kinetic energies of the nucleon and the antiproton were calculated as the expectation values of the kinetic energy operator $T_j = -\frac{\hbar^2}{2m_j^*}\Delta$, where $m_j^* = m_j - S_j$ is the (anti)nucleon reduced mass.

In the studies of K^--nuclear potentials [32,33], the momentum dependence in $\sqrt{s}$ was transformed into the density dependence. The nucleon kinetic energy was approximated within the Fermi gas model by $T_N(\frac{\rho_N}{\rho_0})^{2/3}$, where $T_N = 23$ MeV, and the kaon kinetic energy was expressed within the local density approximation by $T_K \approx -B_K - \mathrm{Re}\mathcal{V}_K(r)$, where $\mathcal{V}_K = V_K + V_C$ and V_C is the K^- Coulomb potential, which led to the expression

$$\sqrt{s} = m_N + m_K - B_{Nav} - \xi_N B_K + \xi_K \mathrm{Re}\mathcal{V}_K(r) - \xi_N T_N(\frac{\rho_N}{\rho_0})^{2/3}, \tag{20}$$

where $\xi_{N(K)} = \frac{m_{N(K)}}{m_N + m_K}$. In more recent calculations of kaonic atoms [34,35] and η-nuclear bound states [36,37], $\delta\sqrt{s} = \sqrt{s} - m_N - m_H$ was adjusted to respect the low density limit $\delta\sqrt{s} \to 0$ upon $\rho \to 0$:

$$\delta\sqrt{s} = -B_{Nav}\frac{\rho_N}{\bar{\rho}_N} - \xi_N B_H \frac{\rho_N}{\rho_0} - \xi_N T_N (\frac{\rho_N}{\rho_0})^{2/3} + \xi_H \mathrm{Re}V_H(r) - \xi_N V_C (\frac{\rho_N}{\rho_0})^{1/3}, \qquad (21)$$

where $\bar{\rho}_N$ is the average nucleon density and $H = K, \eta$ (for η mesons, the last term in Eq. (21) is zero).

The absorptive $\bar{p}$ potential used fully self-consistently in our calculations of $\bar{p}$-nucleus states acquires the form

$$\mathrm{Im}V_{\bar{p}}(r, \sqrt{s}, \rho) = \sum_{\text{channel}} B_c f_s(\sqrt{s}) \mathrm{Im}V_{\text{opt}}(r). \qquad (22)$$

3. Results

We adopted the formalism introduced in Section 2 to detailed calculations of $\bar{p}$ bound states in selected nuclei across the periodic table. First, we did not consider the $\bar{p}$ absorption and explored various dynamical effects in these nuclei caused by the antiproton in the $1s$ nuclear state using the G-parity motivated $\bar{p}$-meson coupling constants scaled by the factor ξ (Eq. (13)). We studied model dependence of the calculations, as well as the effect of the $\bar{p}$ self-interaction. We confirmed previous findings of Mishustin et al. [18] who had revealed that the insertion of the $\bar{p}$ into the nucleus causes significant polarization of the nuclear core. Then, we took into account the $\bar{p}$ absorption in the nuclear medium and performed first fully self-consistent calculations of $\bar{p}$ nuclei using an optical potential consistent with $\bar{p}$ atom data [14]. Selected results of our calculations are presented in the following subsections.

3.1. Dynamical effects and model dependence

In order to explore the extent of dynamical effects in the nuclear core due to the presence of $\bar{p}$, we performed *static* as well as *dynamical* calculations of $\bar{p}$ nuclei. In static calculations the antiproton source terms are omitted in the right hand sides of *all* equations of motion (4). When the exact G-parity symmetry is assumed for the $\bar{p}$ coupling constants, the antiproton potential is about 800 MeV deep in ^{16}O calculated statically within the TM2 model. When calculated dynamically, the $\bar{p}$ potential reaches nearly 1700 MeV in all nuclei considered. The dynamical effects are thus considerable and should not be neglected. The binding energies of $\bar{p}$ in the $1s$ state are 1212.4 MeV in $^{16}\mathrm{O}_{\bar{p}}$ (TM2 model) and 1107.5 MeV in $^{208}\mathrm{Pb}_{\bar{p}}$ (TM1 model). The corresponding total binding energies are $B = 1259.9$ MeV and $B = 2651.2$ MeV for $^{16}\mathrm{O}_{\bar{p}}$ and $^{208}\mathrm{Pb}_{\bar{p}}$, respectively (compare with $B = 128.9$ MeV for ^{16}O and $B = 1634.8$ MeV for ^{208}Pb).

The antiproton embedded in the nucleus causes its compression and the nuclear core density increases, particularly in the vicinity of $\bar{p}$ where it reaches ∼3–4 times the normal nuclear density. The effect is more pronounced in lighter nuclei where the antiproton, which is localized in the central region of the nucleus up to ≈1.5 fm, affects the whole nucleus. In heavier nuclei, the increase in the core density distribution is significant only in the central region of the nucleus, $r \leq 2$ fm.

Standard RMF models need not be reliable at such high nuclear densities occurring in $\bar{p}$ nuclei. Therefore, we also performed calculations using the density-dependent model TW99 [31] which is considered more suitable for the description of dense nuclear matter. The TW99 model

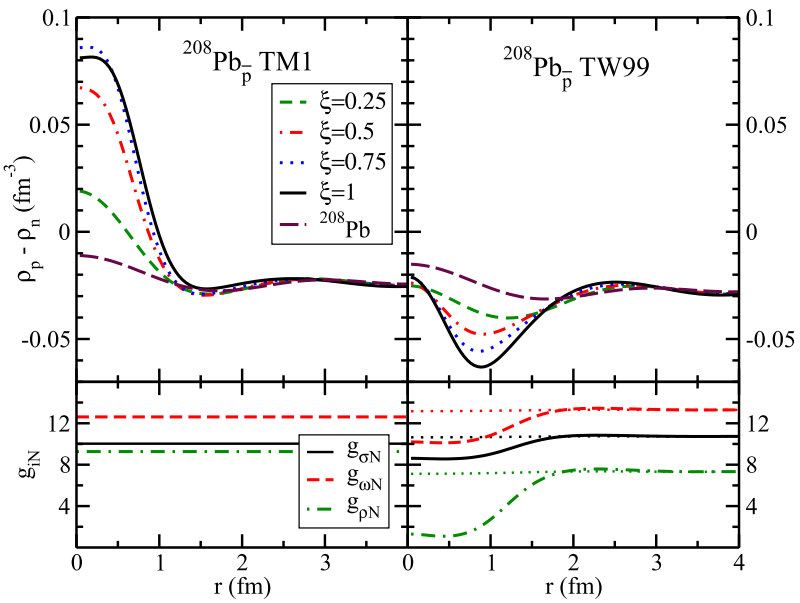

Fig. 2. The isovector density distribution in $^{208}\mathrm{Pb}_{\bar{p}}$ calculated dynamically for different values of the scaling parameter ξ within the TM1 model (upper left panel) and DD TW99 model (upper right panel). The radial dependence of the nucleon–meson couplings is shown in the lower panels.

yields approximately the same depth of the $\bar{p}$ potential and somewhat higher nuclear core densities than the TM model. This is due to the lower compressibility of the TW99 model – compare $K = 240$ MeV in the TW99 model, $K = 344$ MeV in the TM2 model, and $K = 280$ MeV in the TM1 model. The only qualitative difference between the TM and TW99 models concerns the isovector density distribution, $\rho_p(r) - \rho_n(r)$. In Fig. 2, we present comparison of isovector densities in $^{208}\mathrm{Pb}_{\bar{p}}$ calculated dynamically within the TM1 and TW99 models for different values of the scaling factor ξ. In the TM1 model (left panel), the density of protons exceeds the density of neutrons in the central region of the nucleus. Protons are more concentrated around the $\bar{p}$ than neutrons because they feel strong isovector attraction which together with Coulomb attraction from the antiproton surpass the Coulomb repulsion among protons. The rearrangement of the nuclear structure is sizeable even in light nuclei. In the TW99 model (right panel) we observe the opposite effect. Neutrons are more concentrated in the center of the nucleus where the antiproton is localized. This is due to the decreasing strength of the isovector ρ meson coupling with increasing nucleon density as can be seen in the lower panel of Fig. 2. Consequently, protons feel much weaker isovector attraction and neutrons much weaker isovector repulsion in the center of the nucleus. The isovector rearrangement of the nuclear structure is now less pronounced in light nuclei containing less nucleons.

During our dynamical calculations we noticed that the central $\bar{p}$ density $\rho_{\bar{p}}(0)$ reaches its maximum for $\xi \approx 0.5$ and then starts to decrease, as illustrated in the left part of Fig. 3. Here, we present the $\bar{p}$ density distribution in $^{208}\mathrm{Pb}_{\bar{p}}$, calculated dynamically for different values of ξ using the TM1 model. This sudden decrease of the central $\bar{p}$ density is due to the $\bar{p}$ self-interaction (see Section 2) which causes sizable effects on the calculated observables when the $\bar{p}$ potential in the nuclear medium is very deep. When the $\bar{p}$ self-interaction is subtracted (right panel) the $\rho_{\bar{p}}(0)$ increases gradually with ξ and saturates at much higher values of ξ. Fig. 4 shows the nuclear core density distribution in $^{208}\mathrm{Pb}_{\bar{p}}$, calculated dynamically in the TM1 model with (left)

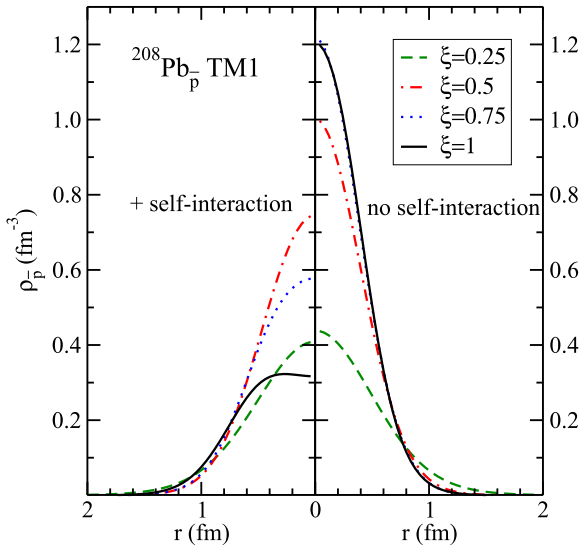

Fig. 3. The $\bar{p}$ density distribution in $^{208}\mathrm{Pb}_{\bar{p}}$, calculated dynamically for different values of ξ in the TM1 model with (left) and without (right) the $\bar{p}$ self-interaction.

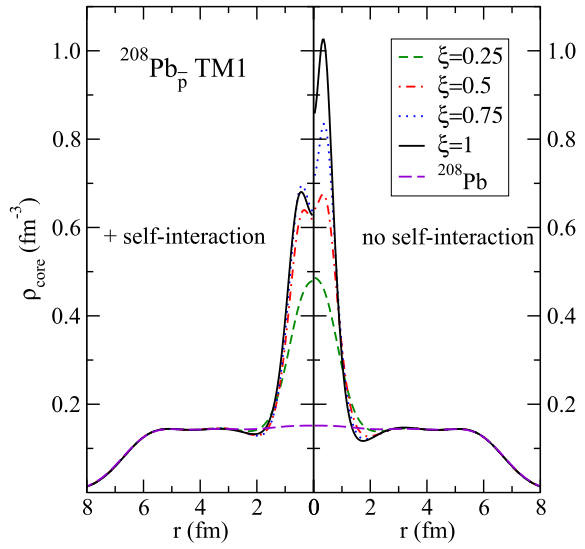

Fig. 4. The core density distribution in $^{208}\mathrm{Pb}_{\bar{p}}$, calculated dynamically for different values of ξ in the TM1 model with (left) and without (right) the $\bar{p}$ self-interaction. The case of ^{208}Pb is shown for comparison.

and without (right) the $\bar{p}$ self-interaction. It follows a similar trend as the $\bar{p}$ density distribution, but it saturates at a different value of ξ.

In Fig. 5, we compare scalar $S_{\bar{p}}$ and vector $V_{\bar{p}}$ potentials acting on the $\bar{p}$ in ^{208}Pb, calculated dynamically using the TM1 model with and without the $\bar{p}$ self-interaction. When the $\bar{p}$ self-interaction is included (left panel), the scalar potential $S_{\bar{p}}$ is deeper than the vector potential $V_{\bar{p}}$. The difference between their depths grows with increasing value of the scaling factor – for $\xi = 1$, $S_{\bar{p}}(0)$ is twice as deep as $V_{\bar{p}}(0)$. When the $\bar{p}$ self-interaction is subtracted (right panel), the $\bar{p}$ scalar potential is comparable or even shallower than the vector potential, the difference between their depths being much smaller now.

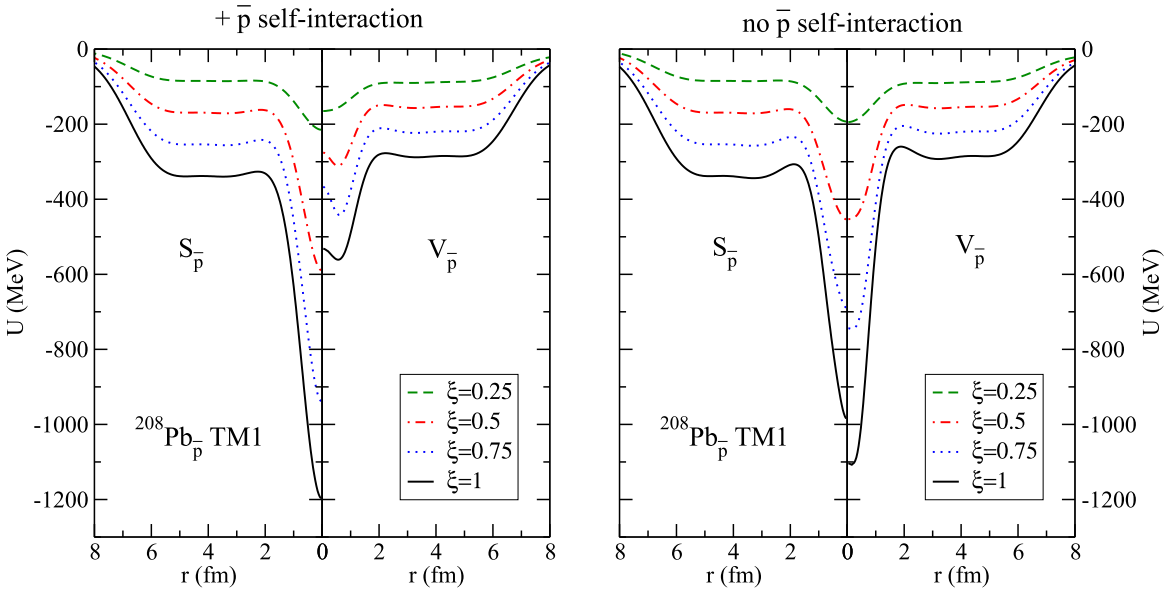

Fig. 5. Scalar $S_{\bar{p}}$ and vector $V_{\bar{p}}$ potentials felt by $\bar{p}$ in ^{208}Pb, calculated dynamically for different values of ξ in the TM1 model with (left panel) and without (right panel) the $\bar{p}$ self-interaction.

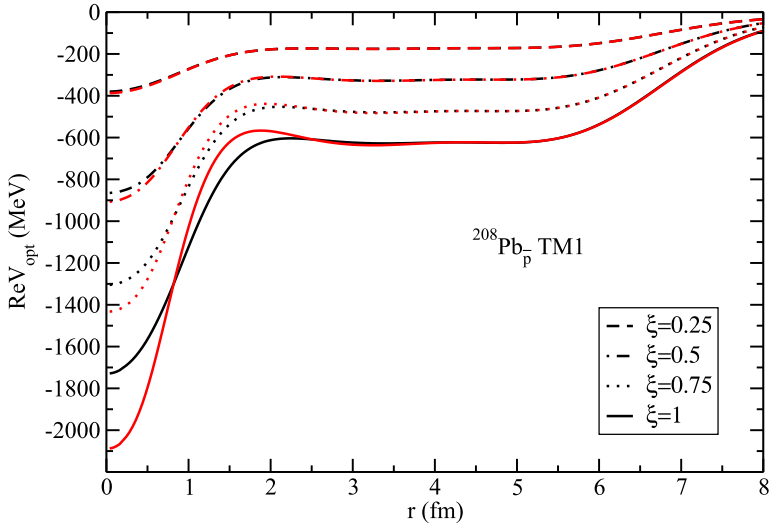

Fig. 6. The real part of the optical potential acting on $\bar{p}$ in ^{208}Pb, calculated dynamically for different values of ξ in the TM1 model with (black lines) and without (red lines) the $\bar{p}$ self-interaction. (For interpretation of the references to color in this figure legend, the reader is referred to the web version of this article.)

The interplay between the value of $S_{\bar{p}} - V_{\bar{p}}$, the $\bar{p}$ single particle energy, and the $\bar{p}$ rest mass affects the large component of the solution of the Dirac equation for the underlying $\bar{p}$ wave function which controls the density distribution. As the difference between the scalar and vector potential increases with ξ in the case with the $\bar{p}$ self-interaction, a sudden change of sign occurs in the solution of the Dirac equation for the large component of the $\bar{p}$ wave function. Consequently, the density starts to decrease. It should be noted that the change of sign appears also in the case without the $\bar{p}$ self-interaction but at much higher values of ξ.

Fig. 6 shows the total potential acting on $\bar{p}$ in ^{208}Pb, calculated dynamically for selected values of ξ within the TM1 model with (black lines) and without (red lines) the $\bar{p}$ self-interaction.

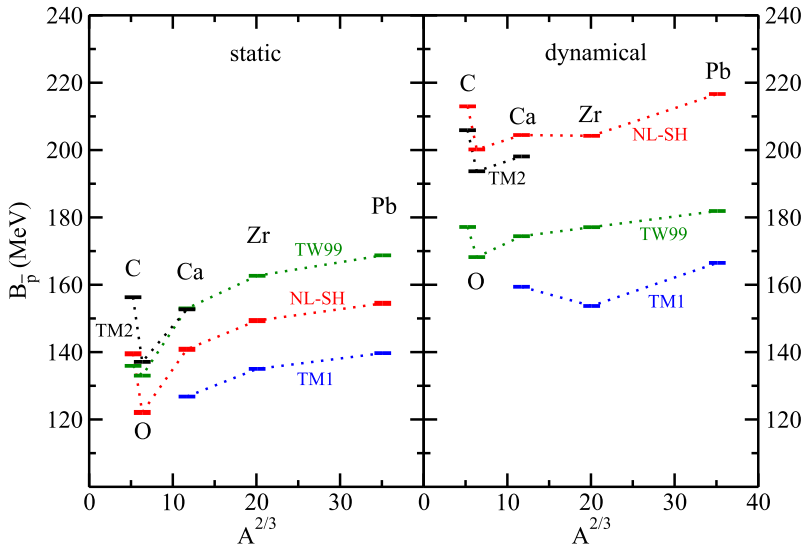

Fig. 7. Binding energies of $1s$ $\bar{p}$-nuclear states across the periodic table calculated statically (left) and dynamically (right) using the TM2 (black), TM1 (blue), NL-SH (red) and TW99 (green) models. (For interpretation of the references to color in this figure legend, the reader is referred to the web version of this article.)

The effect of the $\bar{p}$ self-interaction starts to be considerable for really deep $\bar{p}$ potentials, i.e. for $\xi \geq 0.5$. Correspondingly, the $\bar{p}$ binding energies and the total binding energies of $\bar{p}$ nuclei are larger when the $\bar{p}$ self-interaction is subtracted and the effect increases with ξ – for $\xi = 1$ the difference is more than 200 MeV in $^{208}\mathrm{Pb}_{\bar{p}}$.

It is to be stressed that the available experimental data constrain the depth of the $\bar{p}$ potential at much lower values than the G-parity transformation. The corresponding scaling factor of the $\bar{p}$ coupling constants which gives the potential consistent with the data is $\xi \approx 0.2$, which is safely in the region where the effect of the $\bar{p}$ self-interaction is negligible. From now on we will discuss the results of our calculations for the value of $\xi = 0.2$ only.

Binding energies $B_{\bar{p}}$ of $1s$ $\bar{p}$-nuclear states in core nuclei from ^{12}C to ^{208}Pb are plotted in Fig. 7, where the results of static as well as dynamical calculations for various RMF models are presented. Substantial differences between the $\bar{p}$ binding energies calculated statically and dynamically indicate that the polarization of the nuclear core is, even for $\xi = 0.2$, still significant. Indeed, the central nuclear core densities are almost twice larger than the saturation density. The $\bar{p}$ binding energies shown in the figure were calculated using the TM1, TM2, NL-SH and TW99 models. They evince a strong model dependence. In this work we often used the TM model [38] which consists of two parameter sets – the TM2 model designed to account for properties of light nuclei and the TM1 model describing heavy nuclei. However, these two TM parametrizations yield quite different characteristics of $\bar{p}$ nuclei, as illustrated in the figure. There is a large inconsistency between $B_{\bar{p}}$ in light nuclei calculated using the TM2 model and $B_{\bar{p}}$ for the TM1 model in heavy nuclei (compare also $B_{\bar{p}}$ in Ca for both TM1 and TM2). In the case of the NL-SH and TW99 models the $\bar{p}$ binding energy grows with increasing A, as expected, since the antiproton feels attraction from larger amount of nucleons (except ^{12}C with an extreme central density). The differences between the $\bar{p}$ binding energies calculated statically and dynamically indicate that the response of the nuclear core to the extra antiproton varies with the applied RMF model, where nuclear compressibility seems to be the decisive factor. The TW99 model gives the lowest value of the nuclear compressibility ($K = 240$ MeV) out of the models used in our calculations. Consequently, there is a smallest difference between $B_{\bar{p}}$ calculated statically and

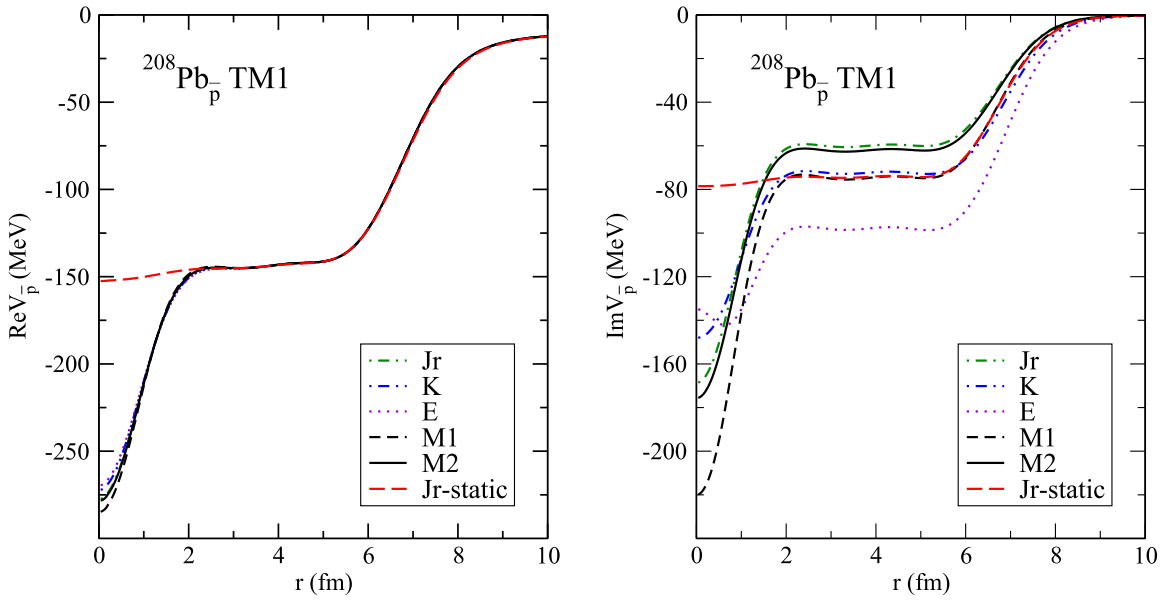

Fig. 8. The real Re$V_{\rm opt}$ and imaginary Im$V_{\rm opt}$ part of the $\bar{p}$ potential in ^{208}Pb, calculated dynamically using the TM1 model and different procedures of handling self-consistently $\sqrt{s}$ (see text for details). The $\bar{p}$ potential calculated statically for selected $\sqrt{s}$ (Jr-static) is shown for comparison.

dynamically. Then follow the TM1 and TM2 models with compressibilities $K = 280$ MeV and $K = 344$ MeV, respectively. The largest dynamical change of the $\bar{p}$ binding energy is observed for the NL-SH model with $K = 355$ MeV.

As demonstrated in Fig. 7, the $\bar{p}$ binding energies calculated using the above RMF models remain sizable even for the reduced $\bar{p}$ couplings ($\xi = 0.2$), which has consequences for the evaluation of the widths of $\bar{p}$-nuclear states discussed in the following subsection.

3.2. $\bar{p}$ annihilation in a nucleus

We performed first fully self-consistent calculations of $\bar{p}$-nuclear states including antiproton absorption in a nucleus. The $\bar{p}$ annihilation was described by the imaginary part of a phenomenological optical potential, parameters of which were determined from global fits to antiproton atom data [14]. The effective scattering length Imb_0 (see Eq. (14)) accounts for the $\bar{p}$ absorption at threshold. However, the energy available for $\bar{p}$ annihilation products in the medium is lowered for the deeply bound antiproton. As a consequence, many annihilation channels may be considerably suppressed, which could result in significantly reduced widths of the deeply bound $\bar{p}$-nuclear states [18]. We evaluated the phase space suppression factors for considered annihilation channels as described in Section 2. They are presented in Fig. 1 as a function of the center-of-mass energy. As $\sqrt{s}$ decreases many channels become suppressed or even closed, especially channels with massive particles in the final state and multi-particle decay channels. The range of $\sqrt{s}$ relevant for our calculations, $\sqrt{s} \approx 1.55$–1.72 GeV, is denoted by the shaded area in Fig. 1. Unlike Ref. [18], we considered also kaon annihilation channels in our calculations. However, their contribution to the total $\bar{p}$ width was found negligible (5 MeV at most).

We considered various procedures for handling $\sqrt{s}$ which controls the phase space reduction and consequently the $\bar{p}$ widths. First, we adopted $\sqrt{s}$ defined by Eq. (18) which was applied by Mishustin et al. [18]. We also assumed two scenarios – the annihilation with a proton in the $1s$ state, $B_N = B_{p1s}$, (denoted by M2) and the case when B_N was replaced by the aver-

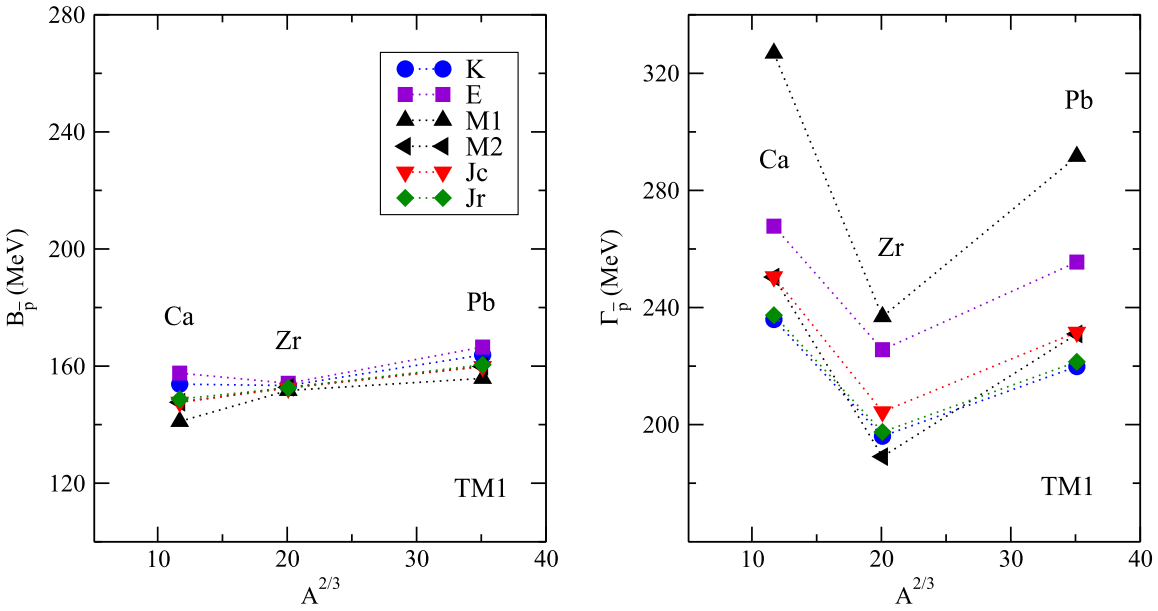

Fig. 9. Binding energies (left panel) and widths (right panel) of $1s$ $\bar{p}$-nuclear states in selected nuclei, calculated dynamically using the TM1 model and different forms of $\sqrt{s}$ (see text for details).

age binding energy per nucleon B_{Nav} (denoted by M1). Next, we used $\sqrt{s}$ transformed into the antiproton–nucleus system (19) with non-negligible contribution from kinetic energies of annihilating partners. To explore the effect of the medium, we calculated the underlying kinetic energies for constant (Jc) as well as reduced (Jr) (anti)nucleon masses. Finally, we applied the forms of $\sqrt{s}$ used in the calculations of kaonic nuclei (20), and η nuclei as well as kaonic atoms (21) (denoted by K and E, respectively). In Fig. 8, we present the real and imaginary parts of the $\bar{p}$ potential in ^{208}Pb, calculated dynamically in the TM1 model for the above forms of $\sqrt{s}$. The real parts of the $\bar{p}$ potentials calculated dynamically for $\xi = 0.2$ and $\mathrm{Im}b_0 = 1.9$ fm have approximately the same depth for all considered procedures for evaluating $\sqrt{s}$. On the other hand, the absorptive $\bar{p}$ potentials $\mathrm{Im}V_{\mathrm{opt}}$ exhibit strong dependence on the applied form of $\sqrt{s}$. The $\bar{p}$ potential calculated statically is shown in the figure as well. Both $\mathrm{Re}V_{\mathrm{opt}}$ and $\mathrm{Im}V_{\mathrm{opt}}$ are much shallower than the dynamically calculated potentials in the central region of the nucleus which illustrates the importance of a dynamical, self-consistent treatment during antiproton–nucleus bound states calculations using an optical potential describing the $\bar{p}$ absorption.

In Fig. 9, we compare binding energies (left panel) and widths (right panel) of $1s$ $\bar{p}$-nuclear states in ^{40}Ca, ^{90}Zr, and ^{208}Pb, calculated dynamically for $\xi = 0.2$ and $\mathrm{Im}b_0 = 1.9$ fm using the same RMF model (TM1) but different forms of $\sqrt{s}$. As can be seen, the $\bar{p}$ energies in a given nucleus calculated using different forms of $\sqrt{s}$ do not deviate much from each other since the real parts of the underlying $\bar{p}$ potential are approximately the same (see Fig. 8, left panel). The $\bar{p}$ widths are sizable and exhibit much larger dispersion. The largest widths are predicted for $\sqrt{s} =$ M1 and the corresponding $\bar{p}$ binding energies are thus the smallest. The $\bar{p}$ widths are significantly reduced after including the non-negligible momentum dependent term in $\sqrt{s}$. It is due to the additional sizable downward energy shift coming from the $\bar{p}$ and nucleon kinetic energies.[2] The kinetic energies calculated with reduced masses ($\sqrt{s} =$ Jr) are larger and consequently the $\bar{p}$

[2] Similarly reduced $\bar{p}$ widths are obtained for $\sqrt{s} =$ M2. However, in this case the annihilation of $\bar{p}$ with a proton in the $1s$ state is assumed ($B_{p1s} \gg B_{Nav}$).

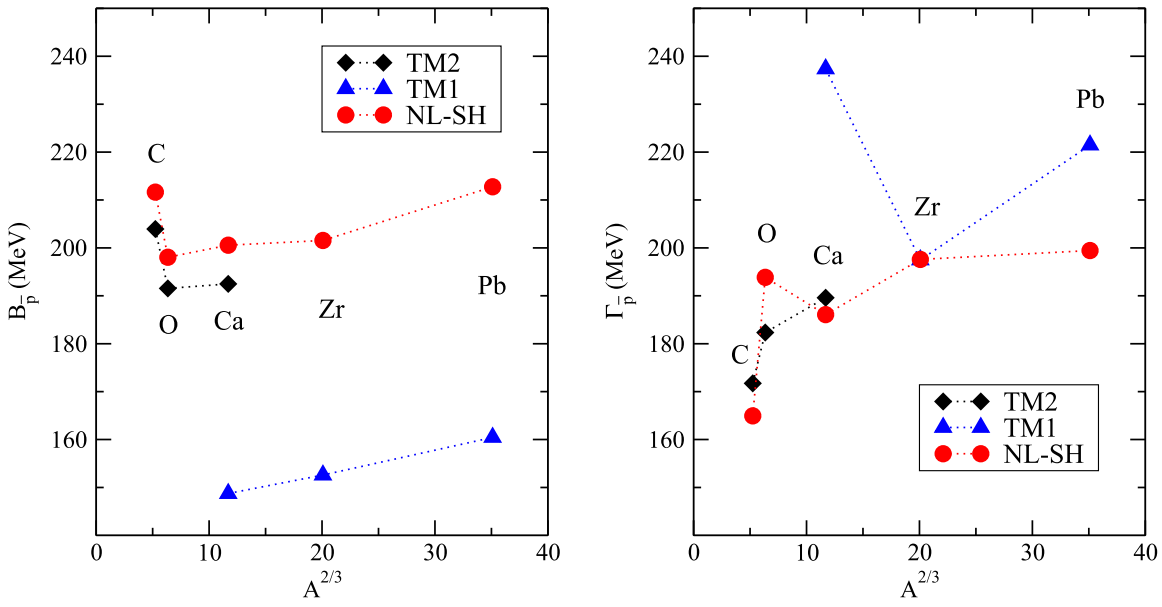

Fig. 10. Binding energies (left panel) and widths (right panel) of $1s$ $\bar{p}$-nuclear states across the periodic table calculated dynamically for $\sqrt{s} =$ Jr using the TM2 (black), TM1 (blue) and NL-SH (red) models. (For interpretation of the references to color in this figure legend, the reader is referred to the web version of this article.)

Table 2
Binding energies $B_{\bar{p}}$ and widths $\Gamma_{\bar{p}}$ (in MeV) of the $1s$ $\bar{p}$-nuclear state in ^{16}O, calculated dynamically (Dyn) and statically (Stat) within the TM2 model using the real and complex potentials consistent with $\bar{p}$-atom data (see text for details).

	Real		Complex		f_s(M1)		f_s(Jr)	
	Dyn	Stat	Dyn	Stat	Dyn	Stat	Dyn	Stat
$B_{\bar{p}}$	193.7	137.1	175.6	134.6	190.2	136.1	191.5	136.3
$\Gamma_{\bar{p}}$	–	–	552.3	293.3	232.5	165.0	182.3	147.0

widths are smaller than those calculated using constant masses ($\sqrt{s} =$ Jc); the difference is up to 15 MeV in the TM1 model. The $\bar{p}$ widths calculated using $\sqrt{s} =$ K and Jr are comparable. However, when the low density limit is taken into account ($\sqrt{s} =$ E) the $\bar{p}$ widths become by ≈ 30 MeV larger.

The model dependence of the $\bar{p}$ binding energies and widths of $1s$ $\bar{p}$-nuclear states across the periodic table calculated dynamically for $\xi = 0.2$, Im$b_0 = 1.9$ fm, and $\sqrt{s} =$ Jr is illustrated in Fig. 10. The TM2 and NL-SH models give similar $\bar{p}$ binding energies in ^{12}C, ^{16}O and ^{40}Ca. The corresponding $\bar{p}$ widths are also quite close to each other. On the other hand, the TM1 model, which yields considerably lower values of $B_{\bar{p}}$ predicts larger $\bar{p}$ widths than the TM2 and NL-SH models (except the case of ^{90}Zr).

In Table 2, we present binding energies $B_{\bar{p}}$ and widths $\Gamma_{\bar{p}}$ of the $1s$ $\bar{p}$-nuclear state in ^{16}O, calculated using the real and complex potentials consistent with $\bar{p}$-atom data ($\xi = 0.2$, Im$b_0 = 1.9$ fm). To illustrate the role of the suppression factors f_s we show the results of calculations without f_s ('Complex'), as well as including f_s for $\sqrt{s}$ due to $B_{\bar{p}}$ and B_{Nav} ('f_s(M1)') and for $\sqrt{s}$ with the additional downward energy shift caused by the momenta of annihilating partners ('f_s(Jr)'). The static calculations, which do not account for the core polarization effects, give approximately the same values of the $\bar{p}$ binding energy for all cases. The binding energies

calculated dynamically are much larger, which indicates that the polarization of the core nucleus is significant. When the phase space suppression is taken into account the $\bar{p}$ width is reduced by more than twice (compare 'Complex' and 'f_s(M1)' in the last row of Table 2). When treating $\sqrt{s}$ self-consistently including the $\bar{p}$ and N momenta (see 'f_s(Jr)'), the $\bar{p}$ width is reduced by additional ≈ 50 MeV, but still remains sizable. The corresponding lifetime of the antiproton in the nucleus is $\simeq 1$ fm/c.

4. Conclusions

In this work, we studied the sub-threshold antiproton interaction with the nuclear medium. The real part of the $\bar{p}$-nucleus potential was constructed within the RMF approach using G parity as a starting point. Since the empirical $\bar{p}$-nucleus interaction is much weaker than that derived from G-parity transformed $\bar{p}$ coupling constants, a uniform scaling factor ξ was introduced to control the strength of the $\bar{p}$-nucleus interaction.

We explored dynamical effects caused by the presence of the strongly interacting $\bar{p}$ in the $1s_{1/2}$ state of selected nuclei across the periodic table and confirmed sizable changes in the nuclear structure. The central density of the nuclear core considerably increases – it reaches about 3 times the normal nuclear density. While in light nuclei the antiproton affects the entire nucleus, in heavier nuclei the increase in the core density distribution is significant only in the central region where $\bar{p}$ is localized, $r \leq 2$ fm. Since various RMF models give quite different equation of state at such high densities, we employed several RMF parametrizations including the density-dependent TW99 model to check the model dependence of our results. The response of the nuclear core to the strongly bound antiproton varies with the applied RMF model as it is affected by the corresponding nuclear compressibility.

In the RMF approach, the antiproton as well as each nucleon moves in mean fields created by all (anti)nucleons in the nucleus, including itself. The effect of the $\bar{p}$ self-interaction increases with the strength of the $\bar{p}$ couplings. It causes saturation of the antiproton and nuclear core density distributions and subsequent decrease at some critical value of the scaling factor ξ. We checked that for the values of $\xi \sim 0.2$–0.3, consistent with empirical $\bar{p}$-nucleus potentials with depths $\approx$150–200 MeV, the effect is tiny and can thus be neglected. This finding is general enough to be applied in RMF calculations of other nuclear systems with a strongly interacting hadron.

In order to include the $\bar{p}$ annihilation in the nuclear medium, we adopted the imaginary part of a phenomenological optical potential with parameters constrained by fits to $\bar{p}$-atom data. We considered various relevant decay channels of $\bar{p}N$ annihilation at rest and took into account the phase space suppression for annihilation products of the deeply bound antiproton in the nuclear medium. We performed dynamical calculations of $\bar{p}$-nuclear bound states using a complex optical potential consistent with $\bar{p}$-atom data. We explored in detail the interplay between the underlying dynamical processes and the relevant kinematical conditions that determine the annihilation width of $\bar{p}$ bound states in the nuclear medium. The $\bar{p}$ widths decrease by factor 2 when the suppression of the phase space is considered and they are further reduced by ≈ 50 MeV when the momenta of annihilating partners are taken into account. However, the $\bar{p}$ widths still remain sizeable for a realistic $\bar{p}$-nucleus interaction. We noticed that the $\bar{p}$ absorption remarkably influenced the polarization of the nuclear core. It is therefore mandatory to perform the calculations with a complex $\bar{p}$-nucleus potential fully self-consistently. Such calculations were performed in this work for the first time ever.

It is desirable to use the self-consistent techniques applied in this work in calculations of $\bar{p}$-nucleus interaction based on a more fundamental $\bar{N}N$ potential model, such as the Paris $\bar{N}N$ potential [16] used in the most recent study of $\bar{p}$ atoms [15], and compare them with the calculations within the RMF approach. We are currently finalizing such calculations and the results will be published elsewhere. It is also desirable to study in detail the $\bar{p}$-nucleus interaction above threshold to describe $\bar{p}$-nucleus scattering processes because knowledge of such processes, of the $\bar{p}$ behavior in the nuclear medium, as well as post $\bar{p}$ annihilation dynamics of the nuclear core is expected to be in great demand in view of future experiments at FAIR [17]. Considering anticipated production of hyperon–antihyperon pairs in $\bar{p}$-nucleus collisions at FAIR it is timely to extend the present model to calculations of nuclear systems with (anti)hyperons.

Acknowledgements

This work was supported by the GACR grant No. P203/15/04301S. J.M. acknowledges financial support within the agreement on scientific collaboration between the Czech Academy of Sciences and the Israel Academy of Sciences and Humanities. Both J.H. and J.M. acknowledge the hospitality extended to them at the Racah Institute of Physics, The Hebrew University of Jerusalem, during a collaboration visit in April/May 2015. We wish to thank E. Friedman, A. Gal, and S. Wycech for valuable discussions, and P. Tlustý for his assistance during Monte Carlo simulations using PLUTO.

References

[1] O. Chamberlaine, et al., Phys. Rev. 100 (1955) 947.
[2] R. Armenteros, B. French, High-Energy Physics, vol. 4, Academic Press, New York, 1969.
[3] E. Klempt, C.J. Batty, J.-M. Richard, Phys. Rep. 413 (2005) 197.
[4] R. Machleidt, Adv. Nucl. Phys. 19 (1988) 189.
[5] T. Bürvenich, I.N. Mischustin, L.M. Satarov, J.A. Maruhn, H. Stöcker, W. Greiner, Phys. Lett. B 542 (2002) 261.
[6] C.Y. Wong, A.K. Kerman, G.R. Satchler, A.D. Mackellar, Phys. Rev. C 29 (1984) 574.
[7] A.J. Baltz, C.B. Dover, M.E. Sainio, A. Gal, G. Toker, Phys. Rev. C 32 (1985) 1272.
[8] G.E. Walker, Ch.D. Goodman, C. Olmer (Eds.), Antinucleon– and Nucleon–Nucleus Interaction, Plenum Press, 1985.
[9] S. Teis, W. Cassing, T. Maruyama, U. Mosel, Phys. Rev. C 50 (1994) 388.
[10] B. Loiseau, S. Wycech, Phys. Rev. C 72 (2005) 011001.
[11] X.-W. Kang, J. Haidenbauer, U.-G. Meissner, Phys. Rev. D 91 (2015) 074003.
[12] C.J. Batty, E. Friedman, A. Gal, Phys. Rep. 287 (1997) 385.
[13] E. Friedman, A. Gal, Phys. Rep. 452 (2007) 89.
[14] E. Friedman, A. Gal, J. Mareš, Nucl. Phys. A 761 (2005) 283.
[15] E. Friedman, A. Gal, B. Loiseau, S. Wycech, Nucl. Phys. A 943 (2015) 101.
[16] B. El-Bennich, M. Lacombe, B. Loiseau, S. Wycech, Phys. Rev. C 79 (2009) 054001.
[17] The FAIR facility [online], URL: http://www.fair-center.eu/index.php?id=1.
[18] T.J. Bürvenich, W. Greiner, I.N. Mishustin, L.M. Satarov, H. Stöcker, Phys. Rev. C 71 (2005) 035201.
[19] A.B. Larionov, I.N. Mishustin, L.M. Satarov, W. Greiner, Phys. Rev. C 78 (2008) 014604.
[20] A.B. Larionov, I.N. Mishustin, I.A. Pschenichnov, L.M. Satarov, W. Greiner, Acta Phys. Pol. B 41 (2010) 299.
[21] A.B. Larionov, I.A. Pschenichnov, I.N. Mishustin, W. Greiner, Phys. Rev. C 80 (2009) 021601.
[22] A.B. Larionov, I.N. Mishustin, L.M. Satarov, W. Greiner, Phys. Rev. C 82 (2010) 024602.
[23] T. Gaitanos, M. Kaskulov, H. Lenske, Phys. Lett. B 703 (2011) 193.
[24] B.D. Serot, J.D. Walecka, Adv. Nucl. Phys. 16 (1986) 1.
[25] P.-G. Reinhardt, Rep. Prog. Phys. 52 (1989) 439.
[26] The GiBUU model [online], URL: http://gibuu.physik.uni-giessen.de/GiBUU.
[27] K. Nakamura, et al., Phys. Rev. Lett. 52 (1984) 731.
[28] T. Gaitanos, M. Kaskulov, U. Mosel, Nucl. Phys. A 828 (2009) 9.

[29] T. Gaitanos, M. Kaskulov, Nucl. Phys. A 899 (2013) 133.
[30] T. Gaitanos, M. Kaskulov, Nucl. Phys. A 940 (2015) 181.
[31] S. Typel, H.H. Wolter, Nucl. Phys. A 656 (1999) 331.
[32] A. Cieplý, E. Friedman, A. Gal, D. Gazda, J. Mareš, Phys. Lett. B 702 (2011) 402.
[33] D. Gazda, J. Mareš, Nucl. Phys. A 881 (2012) 159.
[34] E. Friedman, A. Gal, Nucl. Phys. A 899 (2013) 60.
[35] A. Gal, Nucl. Phys. A 914 (2013) 270.
[36] E. Friedman, A. Gal, J. Mareš, Phys. Lett. B 725 (2013) 334.
[37] A. Cieplý, E. Friedman, A. Gal, J. Mareš, Nucl. Phys. A 925 (2014) 126.
[38] Y. Sugahara, H. Toki, Nucl. Phys. A 579 (1994) 557.
[39] M.M. Sharma, M.A. Nagarajan, P. Ring, Phys. Lett. B 312 (1993) 377.
[40] Particle data group [online], http://pdg.lbl.gov/2013/reviews/rpp2013-rev-kinematics.pdf.
[41] C. Amsler, Rev. Mod. Phys. 70 (1998) 1293.
[42] A Monte Carlo Simulation tool PLUTO [online], http://www-hades.gsi.de/?q=pluto.

Available online at www.sciencedirect.com

ScienceDirect

Nuclear Physics A 969 (2018) 45–59

NUCLEAR PHYSICS A

www.elsevier.com/locate/nuclphysa

Calculations of antiproton–nucleus quasi-bound states using the Paris $\bar{N}N$ potential

Jaroslava Hrtánková *, Jiří Mareš

Nuclear Physics Institute, 250 68 Řež, Czech Republic

Received 21 August 2017; received in revised form 21 September 2017; accepted 22 September 2017
Available online 28 September 2017

Abstract

An optical potential constructed using the $\bar{p}N$ scattering amplitudes derived from the 2009 version of the Paris $\bar{N}N$ potential is applied in calculations of $\bar{p}$ quasi-bound states in selected nuclei across the periodic table. A proper self-consistent procedure for treating energy dependence of the amplitudes in a nucleus appears crucial for evaluating $\bar{p}$ binding energies and widths. Particular attention is paid to the role of P-wave amplitudes. While the P-wave potential nearly does not affect calculated $\bar{p}$ binding energies, it reduces considerably the corresponding widths. The Paris S-wave potential supplemented by a phenomenological P-wave term yields in dynamical calculations $\bar{p}$ binding energies $B_{\bar{p}} \approx 200$ MeV and widths $\Gamma_{\bar{p}} \sim$ 200–230 MeV, which is very close to the values obtained within the RMF model consistent with $\bar{p}$-atom data.

Keywords: Antiproton–nucleus interaction; Paris $\bar{N}N$ potential; Antiproton–nuclear bound states

1. Introduction

The elastic part of an $\bar{N}N$ potential constructed from a boson exchange NN potential using the G-parity transformation is strongly attractive (see, e.g. [1]). This fact stimulated speculations about existence of $\bar{p}$-nuclear bound states [2–4]. The $\bar{p}N$ and $\bar{p}$-nucleus interactions, as well as their capability of forming corresponding bound states have been explored extensively in

* Corresponding author.
E-mail address: hrtankova@ujf.cas.cz (J. Hrtánková).

https://doi.org/10.1016/j.nuclphysa.2017.09.011
0375-9474/

LEAR experiments at CERN [5,6]. Complementary information about the $\bar{p}$ optical potential near threshold was acquired within the study of strong interaction energy shifts and widths in antiprotonic atoms [7–9]. Analyses of $\bar{p}$-atom data and $\bar{p}$ scattering off nuclei at low energies disclosed that the antiproton interaction with a nucleus is dominated by $\bar{p}$ annihilation which governs propagation of the antiproton in nuclear matter. It was found that the experimental data could be well fitted by a $\bar{p}$-nuclear optical potential, imaginary part of which greatly outweighs the strongly attractive real part. However, if the antiproton is deeply bound in the nuclear medium the situation might change. In fact, the phase space for $\bar{p}$ annihilation products gets considerably reduced, which could lead to relatively long $\bar{p}$ lifetime in nuclear matter [10]. Nonetheless, no definite evidence of forming a $\bar{p}N$ or $\bar{p}$-nucleus quasi-bound state has been reported so far.

The study of $\bar{p}$ interactions with a nucleon and the nuclear medium is still topical. One example worth mentioning is the very recent analysis of J/Ψ events collected by the BESIII experiment which supports the existence of either a $\bar{p}p$ molecule-like state or a bound state [11]. It is to be noted that one of the observed resonant states, $X(1835)$, was described by the 2009 version of the Paris $\bar{N}N$ potential, assuming that it originates from a $\bar{p}p$ bound state [20,11]. Furthermore, the knowledge of $\bar{p}$-nucleus interaction at various densities and under different kinematical conditions will be utilized and further expanded in forthcoming experiments with $\bar{p}$-beams at FAIR [12]. Simulations of the considered processes in a wide range of $\bar{p}$-beam momenta, providing experimentalists with valuable hints, are being performed within the Giessen Boltzmann–Ueling–Uhlenbeck (GiBUU) transport model [13] in which the $\bar{p}$ potential in nuclear matter serves as input.

Properties of $\bar{p}$-nuclear quasi-bound states have been calculated within the Relativistic Mean Field (RMF) model [4,10,14–17] using the G-parity transformation of coupling constants involved. A scaling factor representing departure from G-parity together with a phenomenological imaginary part were introduced to construct an optical potential consistent with experimental data. In Ref. [17], the $\bar{p}$ annihilation was treated dynamically and fully self-consistently, taking into account the reduced phase-space for annihilation products as well as compression of the nuclear core caused by the antiproton. Though the calculated $\bar{p}$ widths in the nuclear medium were found to be suppressed significantly, they remained considerable. Recently, Gaitanos et al. have developed a non-linear derivative (NLD) model [18,19]. It incorporates momentum dependence of mean fields acting on $\bar{p}$ which yields the depth of the $\bar{p}$-nucleus potential in accord with experimental data, without introducing any additional scaling factor.

Several microscopic $\bar{N}N$ potential models, such as those based on one- and two-pion exchange [20,21] or chiral EFT [22,23] have been developed recently. Friedman et al. [24] confronted the 2009 version of the Paris $\bar{N}N$ potential [20] with the $\bar{p}$-atom data across the periodic table and antinucleon interactions with nuclei up to 400 MeV/c, including elastic scattering and annihilation cross sections. Their analysis revealed necessity to include the P-wave part of the $\bar{p}N$ interaction to make the real $\bar{p}$ potential attractive in the relevant low density region of the nucleus, as required by experiment. However, it was found that the Paris S-wave potential supplemented by the contribution of the Paris P-wave amplitudes fails to achieve reasonable fit to $\bar{p}$ atom data. On the other hand, the Paris S-wave potential with a purely phenomenological P-wave term accounts well for the data on the low-density, near-threshold $\bar{p}$-nucleus interaction. From this point of view, it is tempting to apply the S-wave amplitudes derived from the Paris $\bar{N}N$ potential and either the Paris or phenomenological P-wave amplitudes to the description of $\bar{p}$ interactions in the nuclear interior, i.e., farther down below threshold and at higher nuclear densities.

In the present work we employ the 2009 version of the Paris $\bar{N}N$ model in the construction of an optical potential which is then used in calculations of $\bar{p}$-nuclear quasi-bound states for the first time. We demonstrate the role of a proper self-consistent treatment of the energy dependence of scattering amplitudes involved. The adopted procedure for evaluating the sub-threshold energy shift has been applied before in calculations of kaonic and $\bar{p}$ atoms, as well as K^--, η- and $\bar{p}$-nuclear states [17,24–32]. We take into account the P-wave part of the $\bar{p}N$ potential aiming at exploring its impact on calculated $\bar{p}$ binding energies and widths. Finally, we compare present results with those obtained within the RMF approach constrained by $\bar{p}$-atom data [17].

The paper is organized as follows. In Section 2, we briefly describe applied methodology. We present construction of the in-medium $\bar{p}N$ S-wave amplitudes from the free-space amplitudes derived within the Paris $\bar{N}N$ potential. We discuss a self-consistent procedure for treating the energy dependence of the amplitudes and construct a relevant $\bar{p}$ optical potential. Moreover, we introduce the P-wave interaction term which supplements the S-wave part of the potential. In Section 3, we present selected results of our calculations of $\bar{p}$ quasi-bound states in various nuclei across the periodic table, illustrating dynamical effects in the nuclear core caused by the antiproton and the role of the P-wave part of the $\bar{p}N$ potential. Summary of the present study is given in Section 4.

2. Model

The binding energy $B_{\bar{p}}$ and width $\Gamma_{\bar{p}}$ of a $\bar{p}$ quasi-bound state in a nucleus are obtained by solving the Dirac equation

$$[-i\vec{\alpha}\cdot\vec{\nabla}+\beta m_{\bar{p}}+V_{\rm opt}(r)]\psi_{\bar{p}}=\epsilon_{\bar{p}}\psi_{\bar{p}}, \tag{1}$$

where $m_{\bar{p}}$ is the mass of the antiproton, $\epsilon_{\bar{p}}=-B_{\bar{p}}-{\rm i}\Gamma_{\bar{p}}/2$, $(B_{\bar{p}}>0)$, and $V_{\rm opt}(r)$ is a complex optical potential which enters the Dirac equation as a time component of a 4-vector.[1]

2.1. S-wave interaction

First, we consider only the S-wave optical potential which is constructed in a '$t\rho$' form as follows:

$$2E_{\bar{p}}V^{\rm S}_{\rm opt}(r)=-4\pi\left(F_0\frac{1}{2}\rho_p(r)+F_1\left(\frac{1}{2}\rho_p(r)+\rho_n(r)\right)\right), \tag{2}$$

where $E_{\bar{p}}=m_{\bar{p}}-B_{\bar{p}}$, F_0 and F_1 are isospin 0 and 1 in-medium amplitudes in the $\bar{p}$-nucleus frame, and $\rho_p(r)$ $[\rho_n(r)]$ is the proton (neutron) density distribution calculated within the RMF model NL-SH [33].[2] The amplitudes F_0 and F_1 entering Eq. (2) are constructed from the free-space $\bar{p}N$ amplitudes in the two-body frame using the multiple scattering approach of Wass et al. [34] (WRW) which accounts for Pauli correlations in the nuclear medium

[1] As a test, we solved the Schrödinger equation for the same potential $V_{\rm opt}(r)$ and got $\bar{p}$ energies and widths which differ by less than 1 MeV from those obtained by solving Eq. (1).

[2] The NL-SH model contains non-linear scalar self-interactions comprising of the cubic and quadratic terms in the σ field. The model has proven successful in reproducing the binding energies and charge radii of nuclei, as well as neutron-skin thickness. In addition, it describes well saturation properties of nuclear matter, such as the binding energy per nucleon $a_{\rm v}=-16.33$ MeV, nuclear matter density $\rho_0=0.146$ fm^{-3}, and compressibility $K=355$ MeV.

$$F_1 = \frac{\frac{\sqrt{s}}{m_N} f^{\rm S}_{\bar{p}n}(\delta\sqrt{s})}{1 + \frac{1}{4}\xi_k \frac{\sqrt{s}}{m_N} f^{\rm S}_{\bar{p}n}(\delta\sqrt{s})\rho(r)} \,, \quad F_0 = \frac{\frac{\sqrt{s}}{m_N}[2 f^{\rm S}_{\bar{p}p}(\delta\sqrt{s}) - f^{\rm S}_{\bar{p}n}(\delta\sqrt{s})]}{1 + \frac{1}{4}\xi_k \frac{\sqrt{s}}{m_N}[2 f^{\rm S}_{\bar{p}p}(\delta\sqrt{s}) - f^{\rm S}_{\bar{p}n}(\delta\sqrt{s})]\rho(r)} \,. \quad (3)$$

Here, $f^{\rm S}_{\bar{p}n}$ ($f^{S}_{\bar{p}p}$) denotes the free-space $\bar{p}n$ ($\bar{p}p$) S-wave two-body cm scattering amplitude as a function of $\delta\sqrt{s} = \sqrt{s} - E_{\rm th}$, where s is the Mandelstam variable and $E_{\rm th} = m_N + m_{\bar{p}}$. The factor $\sqrt{s}/m_N$ transforms the amplitudes from the two-body frame to the $\bar{p}$-nucleus frame. The nuclear density distribution $\rho(r) = \rho_p(r) + \rho_n(r)$ and the Pauli correlation factor ξ_k is defined as follows

$$\xi_k = \frac{9\pi}{k_{\rm F}^2} \left(4 \int_0^\infty \frac{dr}{r} \exp(ikr) j_1^2(k_{\rm F} r) \right) \,, \quad (4)$$

where $j_1(k_{\rm F} r)$ is the spherical Bessel function, $k_{\rm F}$ is the Fermi momentum, and

$$k = \sqrt{(\epsilon_{\bar{p}} + m_{\bar{p}})^2 - m_{\bar{p}}^2}.$$

The integral in Eq. (4) can be solved analytically. The resulting expression is of the form

$$\xi_k = \frac{9\pi}{k_{\rm F}^2} \left[1 - \frac{q^2}{6} + \frac{q^2}{4}\left(2 + \frac{q^2}{6}\right) \ln\left(1 + \frac{4}{q^2}\right) - \frac{4}{3} q \left(\frac{\pi}{2} - \arctan\left(\frac{q}{2}\right)\right) \right] \,, \quad (5)$$

where $q = -ik/k_{\rm F}$.

The free-space S-wave scattering amplitudes are derived from the 2009 version of the Paris $\bar{N}N$ potential [20]. The $\bar{p}n$ and $\bar{p}p$ amplitudes are expressed as appropriate mixtures of isospin $T = 0$ and $T = 1$ $\bar{N}N$ amplitudes, evaluated as angular momentum averages of fixed-T amplitudes [24].

In Fig. 1 the free-space $\bar{p}p$ (top panel) and $\bar{p}n$ (bottom panel) amplitudes plotted as a function of energy are compared with the in-medium amplitudes at saturation density $\rho_0 = 0.17$ fm^{-3}. Both free and WRW modified amplitudes manifest strong energy dependence for $\delta\sqrt{s} = E - E_{\rm th} \leq 0$. While the in-medium $\bar{p}p$ amplitude is attractive in the entire energy range below threshold, the real part of the in-medium $\bar{p}n$ amplitude is attractive for $\delta\sqrt{s} \leq -70$ MeV and with slightly repulsive dip near threshold. The peaks of both in-medium amplitudes are lower in comparison with the free-space amplitudes and shifted by ≈ 30 MeV towards the $\bar{p}N$ threshold.

We explored the effect of the WRW procedure on $\bar{p}$ binding energies and widths and performed, out of curiosity, also calculation with the free-space S-wave amplitudes. In Table 1 we present $1s$ $\bar{p}$ binding energies and widths in ^{208}Pb calculated with the free-space amplitudes and WRW modified (in-medium) amplitudes, using static RMF densities. The in-medium modifications significantly reduce the $\bar{p}$ widths whereas the $\bar{p}$ binding energies are affected only slightly. This could be anticipated upon closer inspection of Fig. 1. The differences between the free-space and WRW-modified real $\bar{p}N$ amplitudes at $\delta\sqrt{s} = E - E_{\rm th} \sim -200$ MeV (which is the energy shift relevant to static calculations) is almost negligible (see left panels). On the other hand, the imaginary amplitudes (right panels) are evidently reduced at $\delta\sqrt{s} \sim -200$ MeV when in-medium modifications are taken into account. Consequently, the $\bar{p}$ widths are reduced as well.

The energy argument of the $\bar{p}N$ scattering amplitudes is expressed by Mandelstam variable

$$s = (E_N + E_{\bar{p}})^2 - (\vec{p}_N + \vec{p}_{\bar{p}})^2 \,, \quad (6)$$

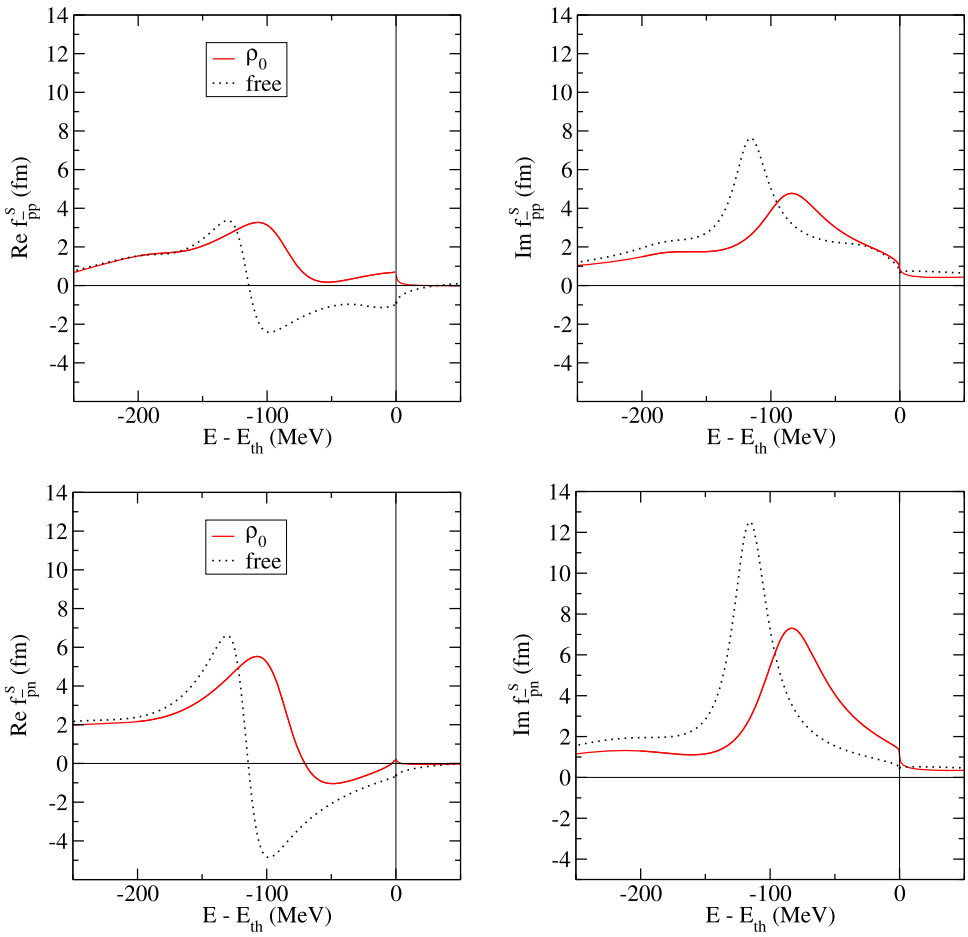

Fig. 1. Energy dependence of the Paris 09 $\bar{p}p$ (top) and $\bar{p}n$ (bottom) S-wave two-body cm amplitudes: in-medium (Pauli blocked) amplitudes for $\rho_0 = 0.17$ fm^{-3} (solid line) are compared with the free-space amplitude (dotted line).

Table 1
$1s$ $\bar{p}$ binding energies and widths (in MeV) in ^{208}Pb, calculated using static RMF densities with the free-space (free) and in-medium (WRW) S-wave amplitudes.

	free	WRW
$B_{\bar{p}}$ (MeV)	184.8	188.6
$\Gamma_{\bar{p}}$ (MeV)	318.5	233.8

where $E_N = m_N - B_{N\mathrm{av}}$ with $B_{N\mathrm{av}} = 8.5$ MeV being the average binding energy per nucleon. In the two-body c.m. frame $\vec{p}_N + \vec{p}_{\bar{p}} = 0$ and Eq. (6) reduces to

$$\sqrt{s}_{\mathrm{M}} = m_{\bar{p}} + m_N - B_{\bar{p}} - B_{N\mathrm{av}} \,. \tag{7}$$

However, when the interaction of the antiproton with a nucleon takes place in a nucleus, the momentum dependent term in Eq. (6) does not vanish and gives rise to an additional downward energy shift [25]. Taking into account averaging over the angles $(\vec{p}_N + \vec{p}_{\bar{p}})^2 \approx \vec{p}_N^{\,2} + \vec{p}_{\bar{p}}^{\,2}$, Eq. (6) can be rewritten as

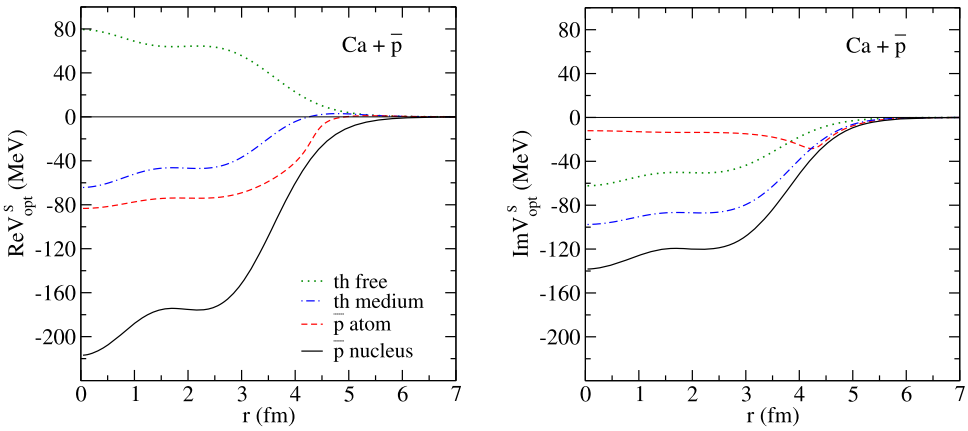

Fig. 2. The potential felt by $\bar{p}$ at threshold ('th medium'), in the $\bar{p}$ atom and $\bar{p}$ nucleus, calculated for ^{40}Ca+$\bar{p}$ with in-medium Paris S-wave amplitudes and static RMF densities. The $\bar{p}$ potential calculated using free-space amplitudes at threshold is shown for comparison ('th free').

$$\sqrt{s}_{\rm J} = E_{\rm th}\left(1 - \frac{2(B_{\bar{p}} + B_{N\rm av})}{E_{\rm th}} + \frac{(B_{\bar{p}} + B_{N\rm av})^2}{E_{\rm th}^2} - \frac{T_{\bar{p}}}{E_{\rm th}} - \frac{T_{N\rm av}}{E_{\rm th}}\right)^{1/2}, \tag{8}$$

where $T_{N\rm av}$ is the average kinetic energy per nucleon and $T_{\bar{p}}$ represents the kinetic energy of the antiproton. The kinetic energies were calculated as the corresponding expectation values of the kinetic energy operator $\hat{T} = -\frac{\hbar^2}{2m_N}\triangle$.

We note that the $\bar{p}$ binding energy $B_{\bar{p}}$ appears as an argument in the expression for $\sqrt{s}$, which in turn serves as an argument for $V_{\rm opt}$ in Eq (1). Therefore, $\sqrt{s}$ has to be determined self-consistently, namely its value obtained by solving the Dirac equation (1) should agree with the value of $\sqrt{s}$ which serves as input in Eqs. (2) and (3). An additional self-consistency scheme has to be considered in dynamical calculations: The RMF densities entering the expression (2) for $V_{\rm opt}$ are modified by the $\bar{p}$ bound in a nucleus and thus by the solution of the Dirac equation (1).

The $\bar{p}N$ amplitudes are strongly energy and density dependent, as was shown in Fig. 1. Consequently, the depth and shape of the $\bar{p}$-nuclear potential depend greatly on the energies and densities pertinent to the processes under consideration. This is demonstrated in Fig. 2 where we present the $\bar{p}$ potential in ^{40}Ca calculated using the free-space amplitudes at threshold and in-medium Paris S-wave amplitudes in three different energy regions: At threshold, for $\delta\sqrt{s} = 0$, the $\bar{p}$ potential constructed using the free space amplitudes (denoted by 'th free') has a repulsive real part and fairly absorptive imaginary part. When medium modifications of the amplitudes are taken into account ('th medium'), the $\bar{p}$ potential becomes attractive and more absorptive. At energies relevant to $\bar{p}$ atoms the $\bar{p}$ potential, constructed following Ref. [24], is more attractive and weakly absorptive. At energies relevant to $\bar{p}$ nuclei ($\sqrt{s}_{\rm J}$), the $\bar{p}$ potential is strongly attractive, however, also strongly absorptive. Clearly, proper self-consistent evaluation of the energy shift $\delta\sqrt{s}$ is crucial.

2.2. *P-wave interaction*

Recent calculations of $\bar{p}$ atoms and scattering of 48 MeV antiprotons [24] showed that a sizable contribution from the P-wave part of the $\bar{p}N$ interaction is needed to get reasonable description of the experimental data. In order to examine the effect of the P-wave interaction on the binding energies and widths of $\bar{p}$-nuclear quasi-bound states, we supplement the S-wave

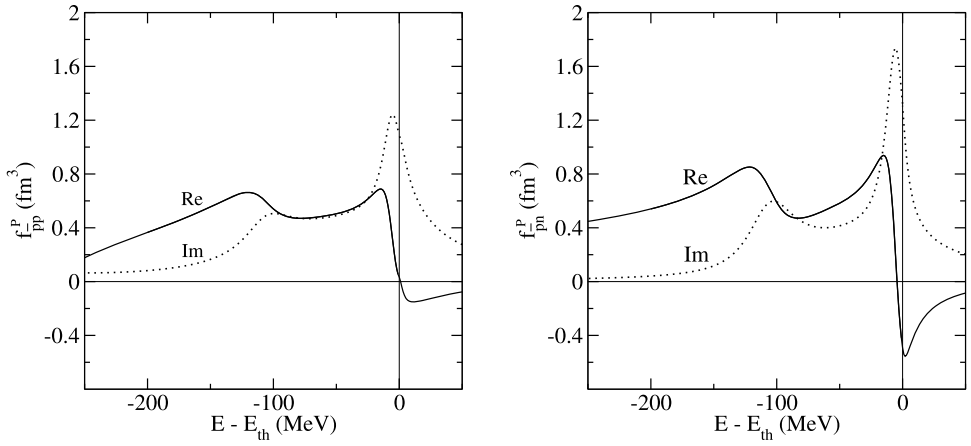

Fig. 3. Energy dependence of the Paris 09 $\bar{p}p$ (left) and $\bar{p}n$ (right) P-wave free-space amplitudes.

optical potential in Eq. (2) [$q(r) = 2E_{\bar{p}} V^{\mathrm{S}}_{\mathrm{opt}}(r)$] by a gradient term which stands for the P-wave interaction [24,35,36]

$$2E_{\bar{p}} V_{\mathrm{opt}}(r) = q(r) + 3\vec{\nabla} \cdot \alpha(r) \vec{\nabla} \,. \tag{9}$$

The factor $2l + 1 = 3$ in the P-wave part is introduced to match the normalization of the Paris $\bar{N}N$ scattering amplitudes and

$$\alpha(r) = 4\pi \frac{m_N}{\sqrt{s}} \left(f^P_{\bar{p}p}(\delta\sqrt{s})\rho_p(r) + f^P_{\bar{p}n}(\delta\sqrt{s})\rho_n(r) \right) \,. \tag{10}$$

Here, $f^P_{\bar{p}p}(\delta\sqrt{s})$ and $f^P_{\bar{p}n}(\delta\sqrt{s})$ denote the P-wave $\bar{p}p$ and $\bar{p}n$ free-space scattering amplitudes, respectively. We assume that the P-wave interaction contributes mainly near the nuclear surface where the nuclear densities are relatively low, and further in the interior its effect should decrease due to gradient form of the P-wave potential. Therefore, we do not consider medium modifications of the Paris P-wave amplitudes. The free-space $\bar{p}p$ and $\bar{p}n$ P-wave scattering amplitudes derived from the latest version of the Paris $\bar{N}N$ potential are shown as a function of energy in Fig. 3. Again, we witness a strong energy dependence of the amplitudes.

The analysis of Friedman et al. [24] revealed that the potential constructed from the Paris S- and P-wave amplitudes fails to fit the antiproton atom data and that it is through the fault of the P-wave part. Their analysis also showed that the potential based on the Paris S-wave and phenomenological P-wave amplitude $f^P_{\bar{p}N} = 2.9 + i1.8$ fm^3 [24] does fit the data well. Therefore, we performed calculations exploring the effect of the P-wave interaction using both the Paris and phenomenological P-wave interactions.

3. Results

In this section, we present selected results of our self-consistent calculations of $\bar{p}$ quasi-bound states in nuclei across the periodic table using an optical potential constructed from the $\bar{p}N$ scattering amplitudes derived from the 2009 version of the Paris $\bar{N}N$ potential [20]. First, we performed calculations using only the S-wave optical potential and explored its energy and density dependence. Then, we took into account the P-wave $\bar{p}N$ interaction and studied its effect on the $\bar{p}$ binding energies and widths.

We performed static, as well as dynamical calculations. In the static calculations, the nuclear core is unaffected by the presence of the antiproton and its structure thus remains the same. In the

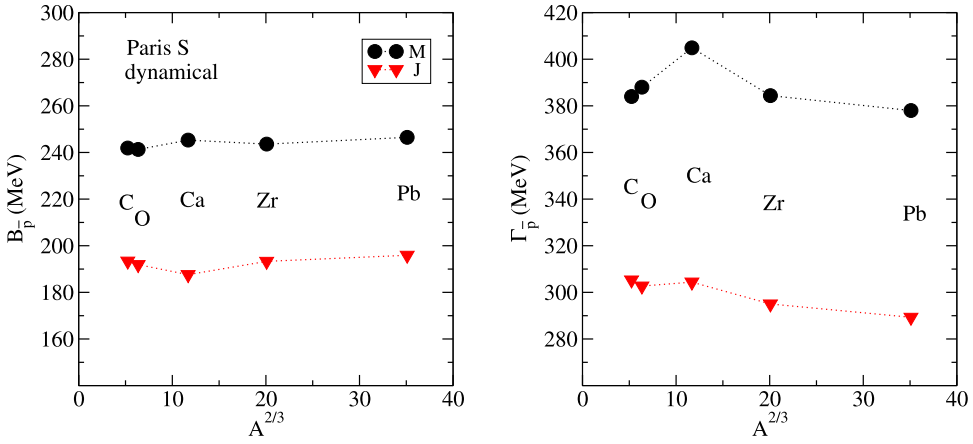

Fig. 4. Binding energies (left panel) and widths (right panel) of $1s$ $\bar{p}$ bound states in selected nuclei, calculated dynamically with S-wave Paris potential and different forms of $\sqrt{s}$ [M (J) denotes $\sqrt{s}_{\rm M}$ ($\sqrt{s}_{\rm J}$), see text for details].

dynamical calculations, the $\bar{p}$ polarizes the nuclear core, causing changes in the nuclear density distribution and nucleon single-particle energies. In our previous calculations of $\bar{p}$ quasi-bound states within the RMF model [17] it was demonstrated that the nuclear core is significantly affected by the extra antiproton – the nuclear density in the central region reaches 2–3 times the saturation density. Since the $\bar{p}$ optical potential is density dependent, such increase in the density would result in a considerable increase of the $\bar{p}$ binding energies and widths. In fact, there is a competing effect, energy dependence of the imaginary part of the phenomenological $\bar{p}N$ scattering amplitude, coming from the phase space suppression for the $\bar{p}$ annihilation products, which partly compensates the effect of the increased density. The corresponding lifetime of the $\bar{p}$ inside a nucleus is then ~ 1 fm/c [17]. However, the response of the nuclear core to the extra $\bar{p}$ is not instant – it could possibly last longer than the lifetime of $\bar{p}$ inside a nucleus [14,15]. As a result, the antiproton annihilates before the nuclear core is fully polarized. Our static and dynamical calculations of $\bar{p}$ binding energies and widths may thus be considered as two limiting scenarios.

As was shown in Figs. 1 and 3, the $\bar{p}N$ scattering amplitudes strongly depend on energy. It is thus very important to evaluate the $\bar{p}$-nucleus potential self-consistently in the appropriate reference frame. This is demonstrated in Fig. 4, where we present $1s$ $\bar{p}$ binding energies (left panel) and corresponding widths (right panel) in various nuclei calculated dynamically using the Paris S-wave potential and two forms of the energy factor: $\sqrt{s}_{\rm M}$ [Eq. (7)] and $\sqrt{s}_{\rm J}$ [Eq. (8)]. The two forms of $\sqrt{s}$ yield very different binding energies and widths. As for the $\sqrt{s}_{\rm M}$, the $\bar{p}$ binding energies are sizable and show weak A-dependence. The corresponding $\bar{p}$ widths are huge (≤ 400 MeV), much larger than the binding energies. Including momentum dependent terms in $\sqrt{s}_{\rm J}$ causes additional considerable downward energy shift, which leads to lower values of $\bar{p}N$ scattering amplitudes (see Fig. 1; the relevant energy shift $\delta\sqrt{s} \leq -200$ MeV) and, consequently, shallower $\bar{p}$-nucleus optical potential. The $\bar{p}$ widths are strongly reduced, yet remain sizable. The $\bar{p}$ binding energies decrease as well (up to $\sim 20\%$) and are again almost A-independent. Finally, it is to be noted that in static calculations, the effect of the momentum dependent terms in $\sqrt{s}_{\rm J}$ on $\bar{p}$ binding energies and widths is about half of that effect in the dynamical case.

Next, we consider the P-wave part of the $\bar{p}N$ interaction. We adopt the Paris $\bar{p}p$ and $\bar{p}n$ P-wave scattering amplitudes as well as the phenomenological P-wave potential fitted by Friedman and Gal to $\bar{p}$ atom data [24] and construct the $S+P$-wave $\bar{p}$-nucleus optical potential [Eq. (9)] which is further applied in self-consistent calculations of $\bar{p}$-nuclear quasi-bound states.

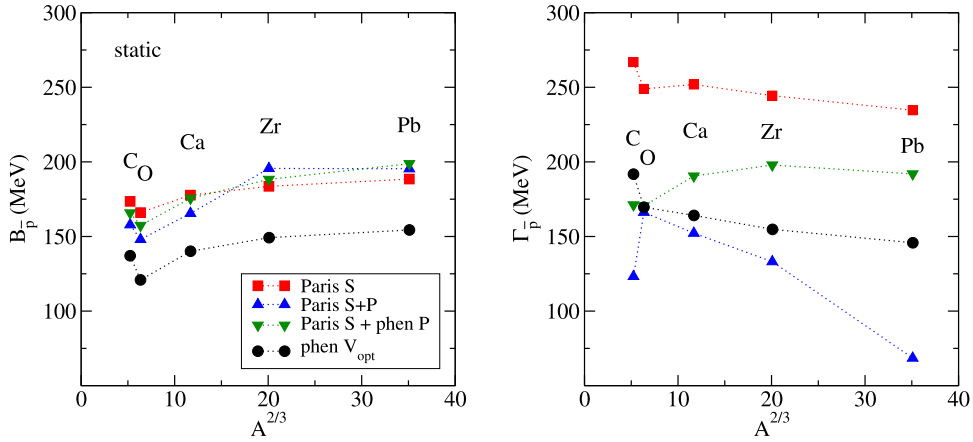

Fig. 5. 1s $\bar{p}$ binding energies (left panel) and widths (right panel) in various nuclei, calculated statically for $\sqrt{s}_{\rm J}$ using S-wave Paris potential (red squares), including phenomenological P-wave potential (green triangles down), Paris P-wave potential (blue triangles up) and phenomenological RMF potential (black circles). (For interpretation of the references to color in this figure legend, the reader is referred to the web version of this article.)

Table 2
Self-consistent energy shifts $\delta\sqrt{s}_{\rm J}$ in ^{208}Pb+$\bar{p}$ relevant to static calculations within the Paris S-wave, Paris $S+P$-wave and Paris S-wave + phen. P-wave potentials.

^{208}Pb+$\bar{p}$	Paris S	Paris $S+P$	Paris S + phen. P
$\delta\sqrt{s}_{\rm J}$ (MeV)	−210.6	−238.9	−223.6

In Fig. 5, we present 1s $\bar{p}$ binding energies (left) and widths (right) as a function of mass number A, calculated statically with the Paris S-wave (squares), Paris $S+P$-wave (triangles up), Paris S-wave + phen. P-wave (triangles down) potentials for $\sqrt{s}_{\rm J}$ [Eq. (8)]. The $\bar{p}$ binding energies and widths calculated statically with a phenomenological optical potential ('phen $V_{\rm opt}$', circles) [17] are shown for comparison. The real part of this $\bar{p}$-nucleus potential was constructed within the RMF approach using G-parity motivated $\bar{p}$-meson coupling constants which were multiplied by a scaling factor to account for available experimental data. The $\bar{p}$ absorption was described by the imaginary part of a purely phenomenological optical potential fitted to strong interaction energy shifts and widths in $\bar{p}$-atoms. The reduced phase space available for annihilation of $\bar{p}$ deeply bound in the nuclear medium was taken into account by introducing corresponding suppression factors (see Ref. [17] for more details).

As can be seen from Fig. 5, both P-wave interaction terms, Paris as well as phenomenological, do not affect much the $\bar{p}$ binding energies – they are comparable with binding energies evaluated using only the S-wave potential. On the other hand, the $\bar{p}$ widths decrease noticeably when the phenomenological P-wave term is included in the $\bar{p}$ optical potential. The effect is even more pronounced for the Paris P-wave interaction. We observe strong A-dependence of $\bar{p}$ widths for the Paris $S+P$-wave potential. On the contrary, the widths calculated with the phenomenological P-wave term, as well as only with the S-wave potential vary much less with A (starting oxygen).

To better understand this behavior, we show in Table 2 the energy shifts $\delta\sqrt{s}_{\rm J}$ in ^{208}Pb+$\bar{p}$ evaluated self-consistently in static calculations with Paris S-wave, Paris $S+P$-wave and Paris S-wave + phen. P-wave potentials. The S-wave potential yields the smallest energy shift with respect to threshold, which implies stronger $\bar{p}N$ amplitudes (see Fig. 1) and thus larger $\bar{p}$ binding

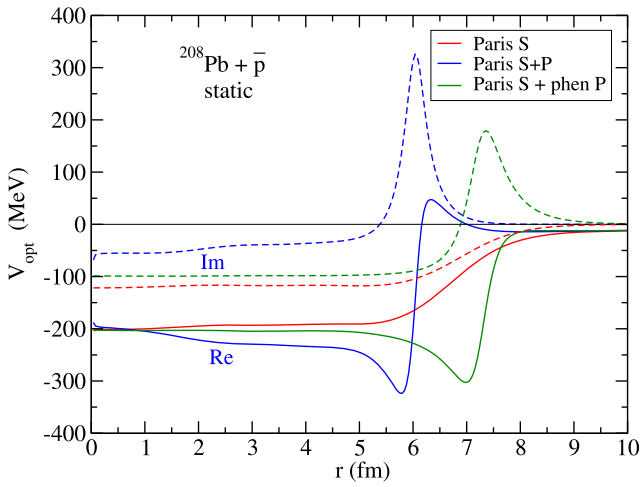

Fig. 6. The real (solid curves) and imaginary (dashed curves) parts of the S-wave Paris potential (red) and the local (Krell–Ericson [37]) forms of the Paris $S+P$-wave (green) and Paris S-wave + phen. P-wave (blue) potentials felt by $\bar{p}$ in ^{208}Pb, calculated statically for $\sqrt{s}_{\rm J}$ (see text for details). (For interpretation of the references to color in this figure legend, the reader is referred to the web version of this article.)

energies and widths. When the P-wave interaction is taken into account, the downward energy shift increases. As a result, the S-wave part of the $\bar{p}$ potential becomes weaker. However, this decrease of the S-wave attraction is more than compensated by the real part of the P-wave potential as illustrated in Fig. 6. Here we present the Paris S-wave, Paris $S+P$-wave and Paris S-wave + phen. P-wave $\bar{p}$ potentials in ^{208}Pb, calculated statically for $\sqrt{s}_{\rm J}$.[3] As a result, the $\bar{p}$ binding energies shown in Fig. 5 are very close to each other. On the other hand, the weaker imaginary part of the S-wave potential is not fully compensated by the P-wave part, particularly the Paris P-wave which is very weakly absorptive for the corresponding $\delta\sqrt{s}_{\rm J}$ (see Fig. 3 and Table 2). The imaginary part of the $S+P$ potential is thus shallower than that of pure S-wave potential. On top of that, the range of the Paris $S+P$-wave potential is smaller than the range of the Paris S-wave + phen. P-wave potential (see Fig. 6). Therefore, the $\bar{p}$ widths in heavier nuclei calculated using the Paris $S+P$-wave potential decrease considerably.

It is to be noted that the depth of the $S+P$-wave potential is a result of delicate interplay between the S- and P-wave parts which are linked together. Very important is also the balance between the real and imaginary parts of the P-wave amplitudes since their strength controls the range of the potential.

Dynamical effects are illustrated in Fig. 7 where we compare $1s$ $\bar{p}$ binding energies (left panel) and corresponding widths (right panel) in various nuclei, calculated statically and dynamically for $\sqrt{s}_{\rm J}$ using the Paris S-wave and Paris S-wave + phen. P-wave optical potentials. In both cases, the binding energies $B_{\bar{p}}$ calculated dynamically are somewhat larger than those obtained in static calculations and the polarization effects decrease with the mass number A. In dynamical and static calculations alike, the $\bar{p}$ binding energies calculated for the Paris S + phen. P-wave potential are comparable with those obtained with the Paris S-wave potential. The P-wave interaction slightly increases the $\bar{p}$ binding energies in heavier nuclei (^{40}Ca, ^{90}Zr, and ^{208}Pb) and decreases them in light nuclei (^{16}O and ^{12}C). The $\bar{p}$ widths calculated dynamically are no-

[3] Fig. 6 shows local forms of the $S+P$-wave potentials obtained from nonlocal Kisslinger potential of Eq. (9) using the Krell–Ericson transformation [37].

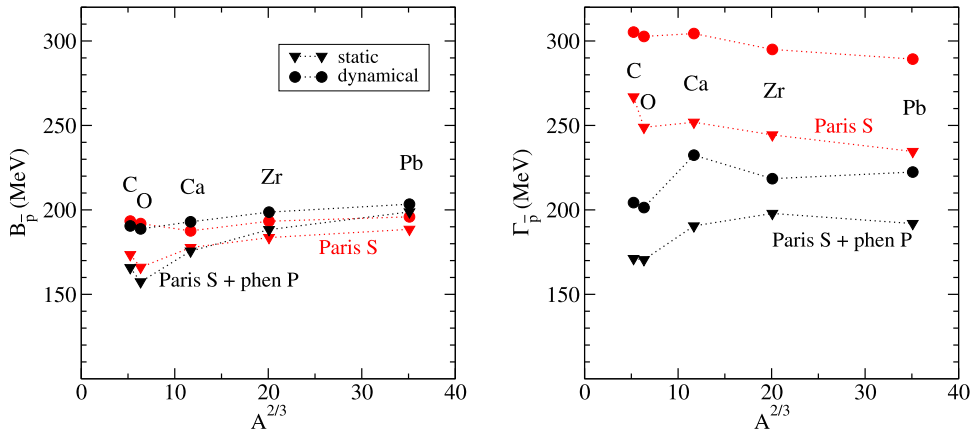

Fig. 7. 1s $\bar{p}$ binding energies (left panel) and widths (right panel) in various nuclei, calculated statically (triangles) and dynamically (circles) for $\sqrt{s}_J$ using S-wave Paris potential (red) and including phenomenological P-wave potential (black). (For interpretation of the references to color in this figure legend, the reader is referred to the web version of this article.)

ticeably larger than the widths calculated statically. It is caused mainly by the increase of the central nuclear density, which outweighs the decrease of the $\bar{p}N$ amplitudes due to the larger energy shift with respect to threshold ($\delta\sqrt{s}_{\rm dyn} \sim -255$ MeV vs. $\delta\sqrt{s}_{\rm stat} \sim -200$ MeV). The Paris S-wave + phen. P-wave potential yields again smaller $\bar{p}$ widths than the S-wave potential. Still, the $\bar{p}$ widths calculated dynamically are larger or at least comparable with the corresponding $\bar{p}$ binding energies. The lifetime of the antiproton inside the nucleus is consistent with $\simeq 1$ fm/c.

It is to be noted that in our previous RMF calculations [17] we found strong model dependence of the dynamical effects caused by the extra $\bar{p}$ inside the nucleus. It could be attributed to different values of nuclear compressibility given by applied RMF models (models with larger compressibility predict larger dynamical changes in $\bar{p}$ binding energies). In order to explore model dependence in the present study, we performed calculations also using the RMF model TM(1)2 [38]. We found that unlike the phenomenological RMF approach the present static as well as dynamical calculations based on Paris $\bar{N}N$ amplitudes yield quite similar results within the TM and NL-SH models, the differences in $\bar{p}$ binding energies and widths are up to 10 MeV. It is due to energy dependence of the $\bar{p}N$ amplitudes which compensates the increase of the nuclear density. Namely, larger dynamical changes imply larger subthreshold energy shift and thus weaker $\bar{p}N$ amplitudes (see Fig. 1). We preferred the NL-SH model in the present work since the TM model consists of two different parameter sets – TM2 for light nuclei and TM1 for heavy nuclei.

Next, we compare the predictions for $\bar{p}$ binding energies and widths calculated dynamically using the 2009 version of the Paris $\bar{N}N$ potential with our former calculations based on the RMF model [17]. The 1s $\bar{p}$ binding energies (left) and corresponding widths (right) in selected nuclei calculated using the phenomenological RMF approach (circle), Paris S-wave potential (square), Paris $S+P$-wave potential (triangle up) and Paris S-wave + phen. P-wave potential (triangle down) are shown in Fig. 8. The binding energies are very close to each other in all cases, $B_{\bar{p}} \sim 200$ MeV, and rather weakly A-dependent. The $\bar{p}$ widths exhibit considerably larger dispersion for the different potentials. The Paris S-wave potential yields sizable widths in all nuclei, $\Gamma_{\bar{p}} \sim 300$ MeV. The Paris P-wave interaction again reduces the $\bar{p}$ widths significantly, to less than one half. The Paris S-wave + phen. P-wave potential yields very similar $\bar{p}$ widths as the phenomenological approach. They are in the range of ~ 200–230 MeV and comparable

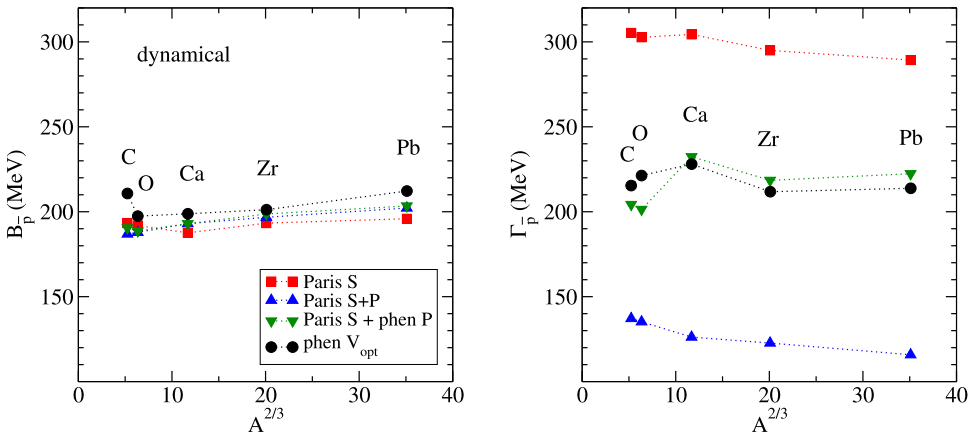

Fig. 8. Binding energies (left panel) and widths (right panel) of $1s$ $\bar{p}$-nuclear states in selected nuclei, calculated dynamically for $\sqrt{s}_{\mathrm{J}}$ using the Paris $\bar{N}N$ S-wave potential (red), Paris S-wave + phen. P-wave (green) and phenomenological approach within the RMF model NL-SH (black). (For interpretation of the references to color in this figure legend, the reader is referred to the web version of this article.)

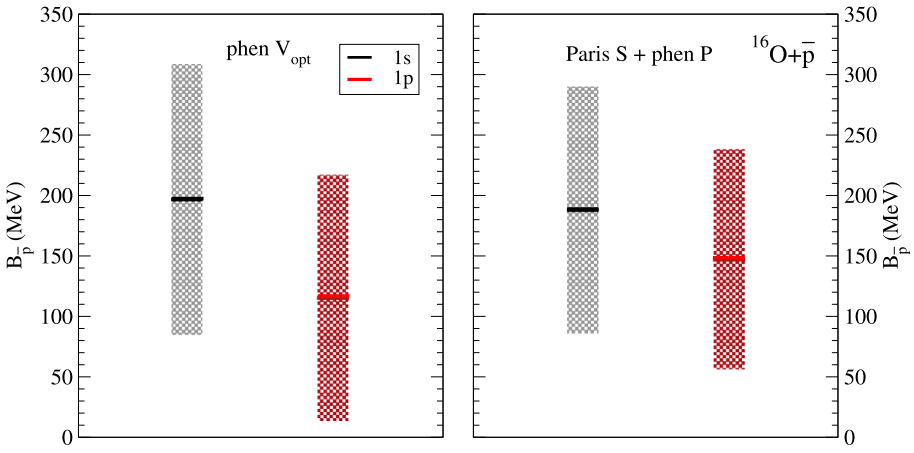

Fig. 9. $1s$ and $1p$ binding energies (lines) and widths (boxes) of $\bar{p}$ in ^{16}O calculated dynamically within the NL-SH model for $\sqrt{s}_{\mathrm{J}}$ with phenomenological $\bar{p}$ optical potential (left panel) and Paris S-wave + phen. P-wave potential (right panel). (For interpretation of the references to color in this figure, the reader is referred to the web version of this article.)

with the corresponding binding energies. The agreement between the phenomenological RMF and Paris S-wave + phen. P-wave potentials is quite impressive.

One has to mention that in the dynamical calculations, the depths of the Paris $S + P$-wave and Paris S-wave + phen. P-wave potentials in the central region of all nuclei are very similar to each other. However, the range of the Paris $S + P$-wave potential (in the local form) is again much smaller than the range of the Paris $S +$ phen. P-wave potential. Consequently, the $\bar{p}$ widths calculated using the Paris $S + P$ potential are considerably smaller.

We may thus infer that the real and imaginary parts of the Paris P-wave amplitudes are not well balanced in the energy region relevant to $\bar{p}$-nuclear states calculations. Anyway, it was demonstrated by Friedman and Gal (see Table 1 in Ref. [24]) that the real and imaginary parts of the Paris P-wave had to be scaled by different factors in order to obtain satisfactory fit to $\bar{p}$ atom data.

Besides the $\bar{p}$ ground states we calculated also $\bar{p}$ excited states in selected nuclei. In Fig. 9 we compare the binding energies and widths of the $1s$ and $1p$ $\bar{p}$ states in ^{16}O, calculated dynamically

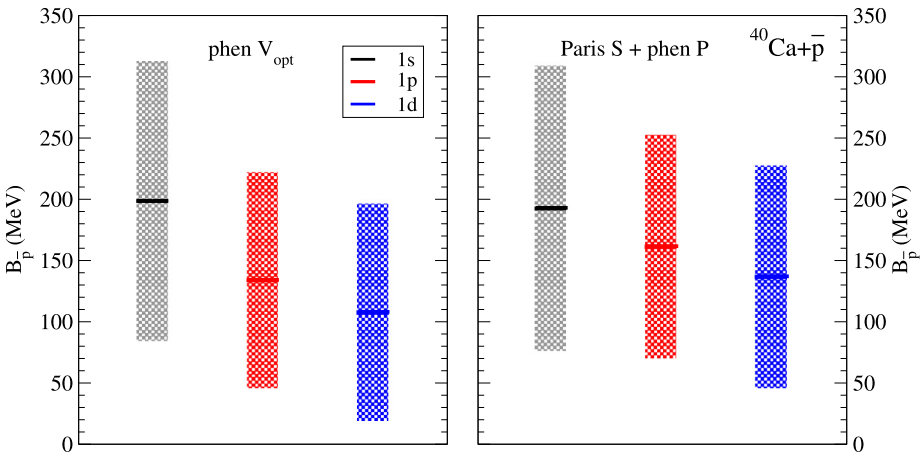

Fig. 10. $1s$, $1p$ and $1d$ binding energies (lines) and widths (boxes) of $\bar{p}$ in ^{40}Ca calculated dynamically within the NL-SH model for $\sqrt{s}_{\mathrm{J}}$ with phenomenological $\bar{p}$ optical potential (left panel) and Paris S-wave + phen. P-wave potential (right panel). (For interpretation of the references to color in this figure, the reader is referred to the web version of this article.)

using the Paris S-wave + phen. P-wave potential (right) and within the phenomenological RMF approach (left). The Paris S-wave + phen. P-wave potential yields similar spectrum of the $\bar{p}$ bound states as the RMF potential, however the $1p$ binding energy is about 20% larger and the width is slightly smaller than in the RMF model. Nevertheless, the agreement of the two spectra, which were obtained within two different approaches, is surprisingly good.

Fig. 10 shows similar $\bar{p}$ spectra in ^{40}Ca. The $1p$ and $1d$ binding energies calculated with the Paris S-wave + phen. P-wave potential are again slightly larger (and $s-p$ and $s-d$ level spacing smaller) than in the phenomenological RMF approach. It is due to a broader $\bar{p}$ potential well of the Paris S-wave + phen. P-wave potential. Both approaches yield comparable $\bar{p}$ widths.

It is to be noted that in the present calculations, V_{opt} is a central potential constructed from angular momentum-averaged scattering amplitudes and thus there is no spin-orbit splitting of p and d levels presented in Figs. 9 and 10. In the RMF approach, the $\bar{p}$ binding energies in $1p$ and $1d$ spin doublets are nearly degenerate, the difference in $\bar{p}$ energies (as well as $\bar{p}$ widths) is up to ~ 1 MeV. These findings are in agreement with spin symmetry predicted for antinucleon spectra [39–42]. In the left panels of Figs. 9 and 10 we show spin-averaged $1p$ and $1d$ $\bar{p}$ binding energies and widths.

4. Summary

We performed fully self-consistent calculations of $\bar{p}$-nuclear quasi-bound states using an optical potential constructed from the S- and P-wave $\bar{p}N$ scattering amplitudes obtained within the 2009 version of the Paris $\bar{N}N$ potential [24]. The free-space S-wave scattering amplitudes were modified by WRW procedure [34] in order to account for Pauli correlations in the medium. A self-consistent scheme for proper dealing with the energy and density dependence of the in-medium amplitudes was adopted in evaluation of the $\bar{p}$-nuclear optical potential. To our knowledge, such calculations based on a microscopic model were carried out for the first time. Previous studies of $\bar{p}$-nuclear states were performed within phenomenological (RMF) approaches [4,10,14–17].

First, we explored the S-wave part of the $\bar{p}$ optical potential and showed that its form depends strongly on energy and density at which it is evaluated. The potential derived from free-space $\bar{p}N$ amplitudes is repulsive and moderately absorptive at threshold. After applying in-medium

modifications of the amplitudes, the potential becomes strongly attractive and absorptive at energies and densities relevant to $\bar{p}$-nuclear states calculations. As a result, $\bar{p}$ binding energies in the $1s$ state amount to almost 200 MeV, and the corresponding widths $\Gamma_{\bar{p}} \sim 300$ MeV in the dynamical calculations.

Then we took into account the P-wave part of the $\bar{p}$ optical potential. Recent analysis by Friedman et al. [24] revealed that the optical potential based on the Paris S- and P-wave scattering amplitudes fails to fit the $\bar{p}$ atom data. On the other hand, the Paris S-wave potential supplemented by a phenomenological P-wave term reproduces the data well. We adopted both the Paris and phenomenological P-wave terms in our calculations. We performed static calculations (neglecting modifications of the nuclear core) as well as dynamical calculations (nuclear core is polarized by $\bar{p}$) which yield lower and upper estimates of $\bar{p}$ binding energies and widths. We found that the P-wave interaction almost does not affect the binding energies of $\bar{p}$-nuclear quasi-bound states. This is in sharp contrast to the case of $\bar{p}$ atoms where it was found necessary to include the P-wave term of the Paris $\bar{p}N$ interaction in order to increase attraction of the $\bar{p}$ optical potential [24]. This again illustrates how the form of the potential depends on energy and density.

The widths of $\bar{p}$-nuclear states are reduced substantially when the P-wave interaction part is considered. The Paris P-wave potential reduces the widths much more than the phenomenological one. It is a result of a delicate balance between the S- and P-wave parts of the total $\bar{p}$ optical potential. The strength of the P-wave part which acts mainly near the nuclear surface and thus controls the range of the optical potential seems to be decisive.

Finally, we compared results of our present calculations using the Paris $\bar{N}N$ potential with our previous calculations of $\bar{p}$-nuclear quasi-bound states performed within the RMF model tuned to the $\bar{p}$-atom data [17]. The $\bar{p}$ binding energies and widths calculated dynamically with the Paris S-wave potential supplemented by the phenomenological P-wave term were found to be in good agreement with the RMF model calculations. Both approaches yield the $1s$ $\bar{p}$ binding energies $B_{\bar{p}} \approx 200$ MeV and the widths $\Gamma_{\bar{p}} \sim 200$–$230$ MeV in considered nuclei. We find this agreement rewarding as it shows that the $\bar{p}$ atoms fits not only define the form of the $\bar{p}$ optical potential near threshold and at low density region but, moreover, quite sufficiently constrain extrapolations to higher densities and farther down below threshold – to the region relevant to $\bar{p}$-nuclear states.

In conclusion, it is to be noted that the present work based on the 2009 version of the Paris $\bar{N}N$ potential was inspired by the recent study of Friedman and Gal [24]. They examined this very potential in the analysis of experimental results for antiprotonic atoms across the periodic table as well as antinucleon interactions with nuclei up to 400 MeV/c. Other realistic $\bar{N}N$ models, such as the Bonn–Jülich chiral NNLO [22] and N^{3}LO [23] EFT potential models or Zhou–Timmermans model [21], could be applied in the study of $\bar{p}$ interactions with the nuclear medium. It would be desirable to perform such calculations and compare between different $\bar{N}N$ interaction models.

Acknowledgements

We thank E. Friedman, A. Gal and S. Wycech for valuable discussions, and B. Loiseau for providing us with the free $\bar{N}N$ amplitudes. This work was supported by the GACR Grant No. P203/15/04301S.

References

[1] R. Machleidt, Adv. Nucl. Phys. 19 (1988) 189.
[2] C.Y. Wong, A.K. Kerman, G.R. Satchler, A.D. Mackellar, Phys. Rev. C 29 (1984) 574.

[3] A.J. Baltz, C.B. Dover, M.E. Sainio, A. Gal, G. Toker, Phys. Rev. C 32 (1985) 1272.
[4] T. Bürvenich, I.N. Mischustin, L.M. Satarov, J.A. Maruhn, H. Stöcker, W. Greiner, Phys. Lett. B 542 (2002) 261.
[5] G.E. Walker, Ch.D. Goodman, C. Olmer (Eds.), Antinucleon– and Nucleon–Nucleus Interaction, Plenum Press, 1985.
[6] E. Klempt, C. Batty, J.-M. Richard, Phys. Rep. 413 (2005) 197.
[7] C.J. Batty, E. Friedman, A. Gal, Phys. Rep. 287 (1997) 385.
[8] E. Friedman, A. Gal, Phys. Rep. 452 (2007) 89.
[9] E. Friedman, A. Gal, J. Mareš, Nucl. Phys. A 761 (2005) 283.
[10] T.J. Bürvenich, W. Greiner, I.N. Mishustin, L.M. Satarov, H. Stöcker, Phys. Rev. C 71 (2005) 035201.
[11] M. Ablikim, et al., BESIII Collaboration, Phys. Rev. Lett. 117 (2016) 042002.
[12] The FAIR facility [online], http://www.fair-center.eu/index.php?id=1.
[13] The GiBUU model [online], http://gibuu.physik.uni-giessen.de/GiBUU.
[14] A.B. Larionov, I.N. Mishustin, L.M. Satarov, W. Greiner, Phys. Rev. C 78 (2008) 014604.
[15] A.B. Larionov, I.N. Mishustin, L.M. Satarov, W. Greiner, Phys. Rev. C 82 (2010) 024602.
[16] T. Gaitanos, M. Kaskulov, H. Lenske, Phys. Lett. B 703 (2011) 193.
[17] J. Hrtánková, J. Mareš, Nucl. Phys. A 945 (2016) 197.
[18] T. Gaitanos, M. Kaskulov, U. Mosel, Nucl. Phys. A 828 (2009) 9.
[19] T. Gaitanos, M. Kaskulov, Nucl. Phys. A 940 (2015) 181.
[20] B. El-Bennich, M. Lacombe, B. Loiseau, S. Wycech, Phys. Rev. C 79 (2009) 054001.
[21] D. Zhou, R.G.E. Timmermans, Phys. Rev. C 86 (2012) 044003.
[22] K.W. Kang, J. Haidenbauer, U.-G. Meißner, J. High Energy Phys. 1402 (2014) 113.
[23] L.-Y. Dai, J. Haidenbauer, U.-G. Meißner, J. High Energy Phys. 1707 (2017) 78.
[24] E. Friedman, A. Gal, B. Loiseau, S. Wycech, Nucl. Phys. A 934 (2015) 101.
[25] A. Cieplý, E. Friedman, A. Gal, D. Gazda, J. Mareš, Phys. Lett. B 702 (2011) 402.
[26] D. Gazda, J. Mareš, Nucl. Phys. A 881 (2012) 159.
[27] E. Friedman, A. Gal, Nucl. Phys. A 899 (2013) 60.
[28] E. Friedman, A. Gal, J. Mareš, Phys. Lett. B 725 (2013) 334.
[29] A. Cieplý, E. Friedman, A. Gal, J. Mareš, Nucl. Phys. A 925 (2014) 126.
[30] E. Friedman, A. Gal, Nucl. Phys. A 959 (2017) 66.
[31] J. Hrtánková, J. Mareš, Phys. Lett. B 770 (2017) 342.
[32] J. Hrtánková, J. Mareš, Phys. Rev. C 96 (2017) 015205.
[33] M.M. Sharma, M.A. Nagarajan, P. Ring, Phys. Lett. B 312 (1993) 377.
[34] T. Wass, M. Rho, W. Weise, Nucl. Phys. A 617 (1997) 449.
[35] M.B. Johnson, G.R. Satchler, Ann. Phys. 248 (1996) 134.
[36] M. Ericson, T.E.O. Ericson, Ann. Phys. 36 (1966) 323.
[37] M. Krell, T.E.O. Eriscon, Nucl. Phys. B 11 (1969) 521.
[38] Y. Sugahara, H. Toki, Nucl. Phys. A 579 (1994) 557.
[39] J.N. Ginocchio, Phys. Rep. 414 (2005) 165.
[40] X.T. He, S.G. Zhou, J. Meng, E.G. Zhao, W. Scheid, Eur. Phys. J. A 28 (2006) 265.
[41] H. Liang, W.H. Long, J. Meng, N. Van Giai, Eur. Phys. J. A 44 (2010) 119.
[42] R. Lisboa, M. Malheiro, P. Alberto, M. Fiolhais, A.S. de Castro, Phys. Rev. C 81 (2010) 064324.

Physics Letters B 770 (2017) 342–347

Contents lists available at ScienceDirect

Physics Letters B

www.elsevier.com/locate/physletb

Are there any narrow K^--nuclear states?

Jaroslava Hrtánková [a,b,*], Jiří Mareš [a]

[a] Nuclear Physics Institute, 250 68 Řež, Czech Republic
[b] Czech Technical University in Prague, Faculty of Nuclear Sciences and Physical Engineering, Břehová 7, 115 19 Prague 1, Czech Republic

ARTICLE INFO

Article history:
Received 6 March 2017
Received in revised form 12 April 2017
Accepted 23 April 2017
Available online 27 April 2017
Editor: J.-P. Blaizot

Keywords:
Antikaon–nucleus interaction
Antikaon annihilation
Kaonic nuclear bound states

ABSTRACT

We performed self-consistent calculations of K^--nuclear quasi-bound states using a single-nucleon K^- optical potential derived from chiral meson–baryon coupled-channel interaction models, supplemented by a phenomenological K^- multinucleon potential introduced recently to achieve good fits to kaonic atom data [1]. Our calculations show that the effect of K^- multinucleon interactions on K^- widths in nuclei is decisive. The resulting widths are considerably larger than corresponding binding energies. Moreover, when the density dependence of the K^--multinucleon interactions derived in the fits of kaonic atoms is extended to the nuclear interior, the only two models acceptable after imposing as additional constraint the single-nucleon fraction of K^- absorption at rest do not yield any kaonic nuclear bound state in majority of considered nuclei.

1. Introduction

Interaction between the K^- meson and nucleon(s) has been object of increased interest in recent years [2–6]. The K^-N interaction is closely related to such issues as the nature of the $\Lambda(1405)$ resonance, propagation of the antikaon in nuclear matter, production of strangeness or existence of K^--nuclear quasi-bound states. Despite much effort in the last decade [7–9], the question of kaonic nuclear states is still not resolved.

The K^-N interaction has recently been described in the framework of chirally motivated meson–baryon interaction models, parameters of which have been tuned to fit low-energy experimental data. As was shown in Ref. [1], commonly accepted models provide quite diverse K^-N scattering amplitudes below threshold. However, the amplitudes from this very energy region enter the construction of a K^--nucleus potential relevant for calculations of kaonic nuclear states.

A distinctive feature of the K^-p amplitudes is their strong energy dependence originating from the presence of the $\Lambda(1405)$ resonance, which is generated dynamically in the chiral coupled-channel models of meson–baryon interactions. It is thus imperative to treat the energy dependence of scattering amplitudes properly and evaluate the K^--nucleus optical potential self-consistently [10,11].

The chiral meson–baryon interaction models discussed in this work, Prague (P) [12] and Kyoto–Munich (KM) [13], include only K^- absorption on a single-nucleon, $K^-N \to \pi Y$ ($Y = \Lambda, \Sigma$). Calculations of K^--nuclear bound states based solely on these chiral models yield K^- absorption widths quite small due to the proximity of $\pi\Sigma$ threshold [10,11,14]. However, in the nuclear medium K^- multinucleon interactions take place as well [1,15,16] and their role increases with density and K^- binding energy. Therefore, the K^- multinucleon processes, absorption in particular, have to be taken into account in any realistic assessment of the K^- widths (to lesser extent also K^- binding energies) in the nuclear medium. In Refs. [10,11,14], the K^-NN absorption was incorporated using a phenomenological potential fitted to kaonic atom data since the applied chiral model did not address such processes. Recently Sekihara et al. [17] described the non-mesonic K^- interaction channels within a chiral unitary approach for the s-wave $\bar{K}N$ amplitude and evaluated the ratio of mesonic to non-mesonic K^- absorption at rest inside the medium. The experimental information about this ratio comes from bubble chamber experiments [18–20]. Friedman and Gal performed fits of kaonic atom data for several recent chirally motivated meson–baryon coupled-channel interaction models [1]. Subsequent comparison with the single-nucleon fractions of K^- absorption at rest provided strict constraint on the meson–baryon interaction models describing the single-nucleon K^- potential as well as on the corresponding phenomenological K^- multinucleon optical potentials. Only the P and KM models were found acceptable by this analysis.

* Corresponding author.
E-mail address: hrtankova@ujf.cas.cz (J. Hrtánková).

http://dx.doi.org/10.1016/j.physletb.2017.04.052

In this work, we apply the above two interaction models in calculations of K^-- nuclear quasi bound states. The single-nucleon K^- potential is supplemented by a corresponding phenomenological optical potential which describes K^- multinucleon interactions. We demonstrate that the K^- multinucleon interactions in the nuclear medium affect crucially the K^- widths. For the first time, we perform calculations of kaonic nuclear states using K^--nuclear potentials containing both K^- single-nucleon and multinucleon interactions, while the multinucleon potential was fitted for each chiral K^-N amplitude model to kaonic atom data separately and further confronted with branching rations of K^- absorption at rest.

2. Methodology

The self-consistent calculations of K^--nuclear quasi-bound states are based on solving the Klein–Gordon equation for K^- in the medium

$$\left[\vec{\nabla}^2 + \tilde{\omega}^2_{K^-} - m^2_{K^-} - \Pi_{K^-}(\omega_{K^-}, \rho)\right]\phi_{K^-} = 0\,, \tag{1}$$

which yields kaon binding energies B_{K^-} and widths Γ_{K^-}. Here, m_{K^-} denotes the K^- mass, $\tilde{\omega}_{K^-} = m_{K^-} - B_{K^-} - \mathrm{i}\Gamma_{K^-}/2 - V_C = \omega_{K^-} - V_C$, V_C is the Coulomb potential, and ρ is the nuclear density distribution. In the present work, the energy- and density-dependent kaon self-energy operator Π_{K^-} is constructed from scattering amplitudes derived within chiral SU(3) meson–baryon coupled-channel interaction models: Prague (P) [12] and Kyoto–Munich (KM) [13]. These models capture physics of the $\Lambda(1405)$ resonance and reproduce low energy K^-N observables, consisting of cross-sections for low-energy K^-p processes (listed in Ref. [13]), three accurately determined threshold branching ratios [21], as well as the $1s$ level shift and width in the K^- hydrogen atom from the SIDDHARTA experiment [22].

The self-energy operator Π_{K^-} entering Eq. (1) is constructed in a "$t\rho$" form as follows:

$$\Pi_{K^-} = 2\mathrm{Re}(\omega_{K^-})V^{(1)}_{K^-} = -4\pi\frac{\sqrt{s}}{m_N}\left(F_0\frac{1}{2}\rho_p + F_1\left(\frac{1}{2}\rho_p + \rho_n\right)\right)\,. \tag{2}$$

Here, F_0 and F_1 denote the isospin 0 and 1 s-wave in-medium amplitudes, respectively, m_N is the nucleon mass, $\sqrt{s}$ is the K^-N total energy, and $V^{(1)}_{K^-}$ denotes the (single-nucleon) K^--nucleus optical potential corresponding to the K^-N amplitudes. The kinematical factor $\sqrt{s}/m_N$ transforms the scattering amplitudes from the two-body frame to the K^--nucleus frame. The proton and neutron density distributions ρ_p and ρ_n in a given core nucleus are obtained within the relativistic mean-field model NL-SH [23].

The in-medium amplitudes F_0 and F_1 are derived from the free-space amplitudes, $F_{K^-n}(\sqrt{s})$ and $F_{K^-p}(\sqrt{s})$, using the multiple scattering approach (WRW) [24] which accounts for Pauli correlations in the nuclear medium:

$$F_1 = \frac{F_{K^-n}(\sqrt{s})}{1 + \frac{1}{4}\xi_k\frac{\sqrt{s}}{m_N}F_{K^-n}(\sqrt{s})\rho}\,,$$
$$F_0 = \frac{[2F_{K^-p}(\sqrt{s}) - F_{K^-n}(\sqrt{s})]}{1 + \frac{1}{4}\xi_k\frac{\sqrt{s}}{m_N}[2F_{K^-p}(\sqrt{s}) - F_{K^-n}(\sqrt{s})]\rho}\,, \tag{3}$$

where ξ_k is adopted from Ref. [1].

The distinctive feature of K^-p amplitudes constructed in chirally motivated coupled-channel models is their strong energy (and density) dependence near and below threshold due to dynamically generated subthreshold s-wave resonance $\Lambda(1405)$. The energy dependence of in-medium scattering amplitudes calls for a proper self-consistent evaluation of corresponding K^- optical potentials used in genuine calculations of K^- atomic as well as nuclear states, as shown in Refs. [1,10,14,16].

Table 1
Values of the complex amplitude B and exponent α used to evaluate $V^{(2)}_{K^-}$ for chiral meson–baryon interaction models considered in this work.

	P1	KM1	P2	KM2
α	1	1	2	2
ReB (fm)	-1.3 ± 0.2	-0.9 ± 0.2	-0.5 ± 0.6	0.3 ± 0.7
ImB (fm)	1.5 ± 0.2	1.4 ± 0.2	4.6 ± 0.7	3.8 ± 0.7

The energy argument of in-medium amplitudes entering Eq. (3) is defined by Mandelstam variable

$$s = (E_N + E_{K^-})^2 - (\vec{p}_N + \vec{p}_{K^-})^2\,, \tag{4}$$

where $E_N = m_N - B_N$, $E_{K^-} = m_{K^-} - B_{K^-}$ and $\vec{p}_{N(K^-)}$ is the nucleon (kaon) momentum. The momentum dependent term in Eq. (4) is no longer zero in the K^--nucleus cm frame and generates additional downward energy shift [10]. The K^-N amplitudes are expressed as a function of energy $\sqrt{s} = E_{th} + \delta\sqrt{s}$ where the energy shift $\delta\sqrt{s}$ can be approximated as

$$\delta\sqrt{s} = -B_N\frac{\rho}{\bar{\rho}} + \beta_{K^-}\mathrm{Re}V_{K^-}(r)$$
$$- \beta_N\left[B_{K^-}\frac{\rho}{\rho_{\max}} + T_N\left(\frac{\rho}{\bar{\rho}}\right)^{2/3} + V_C\left(\frac{\rho}{\rho_{\max}}\right)^{1/3}\right]\,. \tag{5}$$

Here, $B_N = 8.5$ MeV is the average binding energy per nucleon, $\bar{\rho}$ is the average nuclear density, $\rho_{\max}$ is the maximal value of the nuclear density, and $\beta_{N(K^-)} = m_{N(K^-)}/(m_N + m_{K^-})$. $T_N = 23$ MeV is the average nucleon kinetic energy in Fermi Gas Model. The energy shift respects the low-density limit, i.e. $\delta\sqrt{s} \to 0$ as $\rho \to 0$ and the minimal substitution requirement $E \to E - V_C$ [25]. Self-consistency is ensured by dependence of $\delta\sqrt{s}$ on B_{K^-}, as well as on the K^- optical potential V_{K^-} determined by the energy dependent K^-N in-medium amplitudes.

The K^- interactions with two and more nucleons are an indispensable component of a K^--nucleus interaction [26–29]. Recent analyses by Friedman and Gal have confirmed that the optical potential constructed from in-medium chirally motivated K^-N amplitudes have to be supplemented by a phenomenological term representing K^- multinucleon processes in order to achieve good fit to kaonic atom data [1,16]. Therefore, we supplement the single-nucleon potential $V^{(1)}_{K^-}$ by a phenomenological potential $V^{(2)}_{K^-}$ of the form

$$2\mathrm{Re}(\omega_{K^-})V^{(2)}_{K^-} = -4\pi B(\frac{\rho}{\rho_0})^\alpha\rho\,, \tag{6}$$

where B is a complex amplitude and α is a positive number. The parameters of the potential were fitted to kaonic atom data for both P and KM chiral meson–baryon interaction models separately. It has been shown in Ref. [1] that only these two models are capable to reproduce simultaneously kaonic atom data and K^- single-nucleon absorption fractions determined in bubble chamber experiments [18–20]. The corresponding values of the parameters α, ReB and ImB including uncertainties are listed in Table 1. In view of the uncertainties (noticeably larger for $\alpha = 2$), the P and KM models could be regarded as equivalent.

The full K^- optical potential V_{K^-} used in a self-consistent evaluation of the subthreshold energy shift $\delta\sqrt{s}$ and in calculations of kaonic nuclear states is then constructed as a sum of the single- and multinucleon optical potentials $V_{K^-} = V^{(1)}_{K^-} + V^{(2)}_{K^-}$.

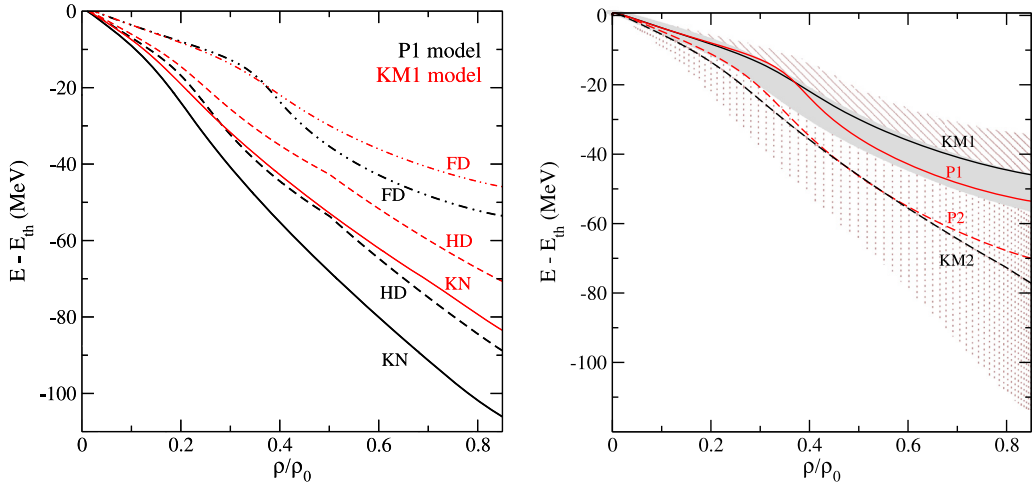

Fig. 1. Subthreshold energies probed in the $^{208}\mathrm{Pb}+K^-$ nucleus as a function of relative density ρ/ρ_0, calculated self-consistently in the P1 and KM1 models for both options of the K^- multinucleon interaction potential (see text for details) (left) compared with the energy shift calculated with the single-nucleon K^- potential (KN, solid line). The right panel shows comparison of subthreshold energies probed in considered K^-N amplitude models, supplemented by the FD variant of $V_{K^-}^{(2)}$. The dashed and dotted areas stand for uncertainties and the gray band denotes their overlap. (For interpretation of the references to color in this figure legend, the reader is referred to the web version of this article.)

In our calculations, we consider the conversion of K^- on two nucleons $K^-NN \to \Sigma N$ to be the dominant mode of K^- absorption in the nuclear interior [17,27,30]. The amplitudes ImB for multinucleon processes are multiplied by a suppression factor which reflects the phase space reduction for decay products in $K^-NN \to \Sigma N$ absorption in the nuclear medium [27].

Experiments with kaonic atoms probe the real part of the K^- optical potential reliably only up to $\sim 25\%$ of ρ_0 and the imaginary part, that is dominant in causing strong interaction effects in kaonic atoms, is determined up to $\sim 50\%$ of ρ_0 [1,26]. Further in the nuclear interior, the shape of the phenomenological K^- optical potential $V_{K^-}^{(2)}$ is mere extrapolation or analytic continuation of the empirical formula applied in the kaonic atom fit. Moreover, the larger value of the exponent α in Eq. (6), the larger is sensitivity of extrapolations to the nuclear interior. Therefore, we consider two limiting options for $V_{K^-}^{(2)}$ beyond the half density limit $\rho(r) = 0.5\rho_0$ in our calculations. First, we apply the form (6) in the entire nucleus (full density option – FD). Second, we fix the potential $V_{K^-}^{(2)}$ at constant value $V_{K^-}^{(2)}(0.5\rho_0)$ for $\rho(r) \geq 0.5\ \rho_0$ (half density limit – HD).

3. Results

The formalism outlined in Section 2 was adopted to self-consistent calculations of K^- nuclear quasi-bound states in selected nuclei across the periodic table. Here we present results for the P and KM models, supplemented by a phenomenological K^- multinucleon potential $V_{K^-}^{(2)}$ determined in the fits of kaonic atom data. We took into account uncertainties of the parameters of $V_{K^-}^{(2)}$ shown in Table 1. Results for other K^-N interaction models considered in Ref. [1] including more details will be discussed elsewhere [31].

A characteristic feature of the self-consistently evaluated energy shift $\delta\sqrt{s}$ from Eq. (5) is its strong density dependence which plays important role in calculations of kaonic nuclear, as well as atomic states using energy dependent chirally motivated K^-N amplitudes. The left panel of Fig. 1 illustrates the strong density dependence of $\delta\sqrt{s}$ in ^{208}Pb, calculated self-consistently within the P and KM models for $\alpha = 1$ (P1 and KM1). These models yield for both HD and FD options of $V_{K^-}^{(2)}$ smaller energy shift with respect to the K^-N threshold than the original single-nucleon potential $V_{K^-}^{(1)}$ (KN). The smallest $\delta\sqrt{s}$ is obtained for the full density option FD. The P2 and KM2 models (not shown in the figure) yield energy shifts closer to the original KN case. The KM2 model gives even slightly larger $\delta\sqrt{s}$ for the HD option than the K^- single-nucleon potential due to attractive Re$V_{K^-}^{(2)}$ (positive ReB, see Table 1). However, the uncertainties for $\alpha = 2$ shown in Table 1 are so large that the sign of Re$B(\alpha = 2)$ is insignificant. The energy shift for the FD option is in any case shallower than for the original K^- single-nucleon potential owing to very strong absorption.

In the right panel of Fig. 1, we present subthreshold energies probed by the K^--nuclear potential as a function of the nuclear density in ^{208}Pb, calculated in P and KM interaction models with the FD version of the K^- multinucleon potential. The dashed and dotted areas denote uncertainties involved in the K^- multinucleon potential $V_{K^-}^{(2)}$ calculated for the KM1 and KM2 models, respectively; the gray band stands for their overlap. The figure illustrates the extent of the uncertainties as well as model dependence. The energy shifts range from ≈ -35 to -115 MeV in the nuclear center. The P1 and KM1 models yield smaller spread in $\delta\sqrt{s}$ due to the uncertainties than the models with $\alpha = 2$. For both values of α, the energy shifts calculated using the P and KM models are lying within the corresponding uncertainty band, which suggests that the models could be regarded as equivalent. It is to be noted that in the P2 model, we had to scale the imaginary part of the total K^- potential entering the Klein–Gordon equation by factor 0.8 in order to get numerically stable solution (converged iteration loop). Without the scaling of ImV_{K^-} the energy shift would be smaller than the one presented in the right panel of Fig. 1 (for more details see footnote [1]).

Fig. 2 shows real (left) and imaginary (right) parts of the total K^- potential, calculated self-consistently for $^{208}\mathrm{Pb} + K^-$ in the KM1 (top) and KM2 (bottom) model. The gray shaded areas stand for uncertainties in $V_{K^-}^{(2)}$. The K^- multinucleon interactions affect the real part of the K^- optical potential markedly less than its imaginary part in all considered models, which has crucial consequences for the widths of K^- nuclear states. The ReV_{K^-} potentials for HD and FD options differ by ≈ 20 MeV in each interaction model. On the other hand, the imaginary parts of V_{K^-} exhibit much larger dispersion for different versions of $V_{K^-}^{(2)}$, as illustrated in Fig. 2, right panels. The K^- multinucleon absorption significantly deepens the imaginary part of the K^- op-

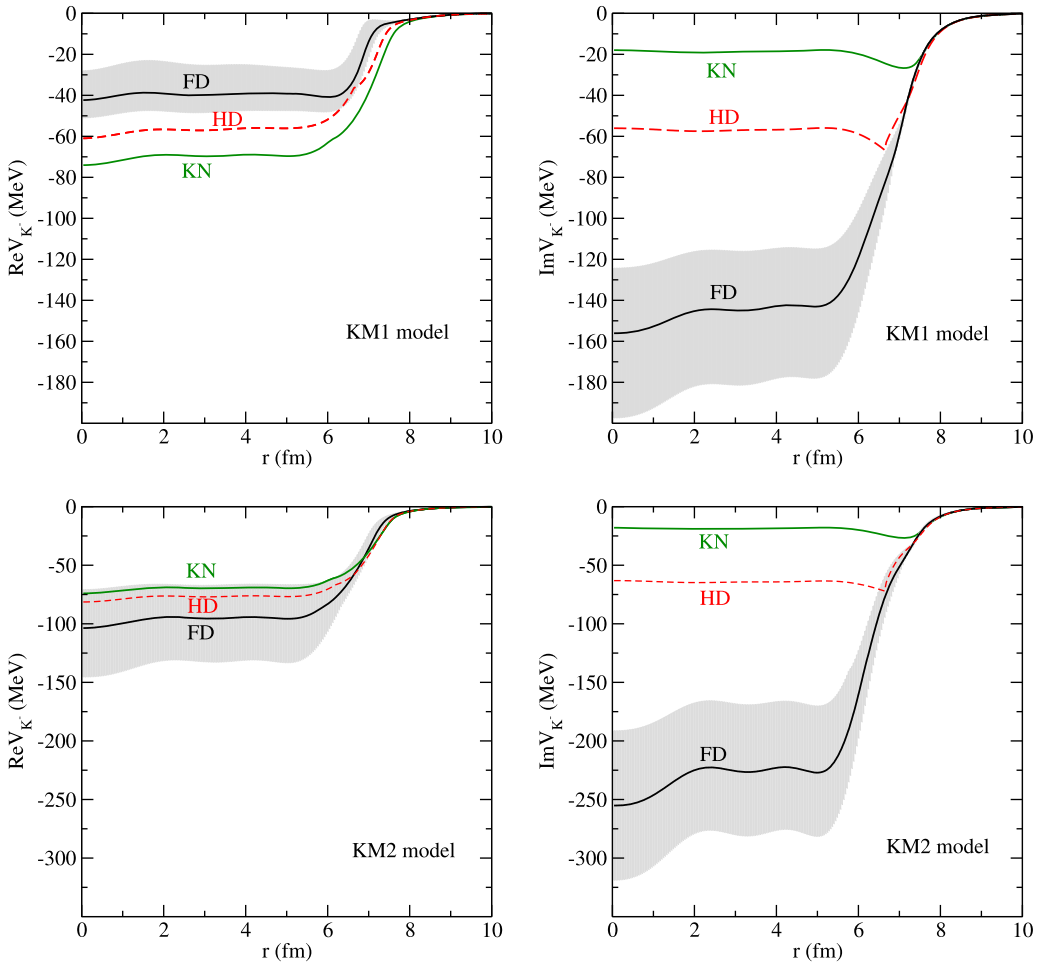

Fig. 2. The real (left) and imaginary (right) parts of the K^- optical potential in the $^{208}\mathrm{Pb} + K^-$ nucleus, calculated self-consistently in the KM1 (top) and KM2 (bottom) model, for two different versions of the K^- multinucleon potential (see text for details). The shaded area stands for uncertainties. The single-nucleon K^- potential (KN, green solid line) calculated in the KM model is shown for comparison. (For interpretation of the references to color in this figure legend, the reader is referred to the web version of this article.)

tical potential. For the FD option of $V^{(2)}_{K^-}$, the KM model yields $|\,\mathrm{Im}V_{K^-}\,| \gg |\,\mathrm{Re}V_{K^-}\,|$ inside the nucleus for both values of α, even when the uncertainties of the K^- multinucleon potential are taken into account. The same holds for the P model (not shown in the figure).

The particular role of K^- single- and multinucleon absorptions with respect to the nuclear density is illustrated in Fig. 3. Here we compare individual contributions of K^- single-nucleon and multinucleon absorptions to the total K^- absorption, expressed as a fraction of $\mathrm{Im}V^{(1)}_{K^-}$ and $\mathrm{Im}V^{(2)}_{K^-}$ with respect to the total imaginary K^- potential $\mathrm{Im}V_{K^-}$, calculated self-consistently for $^{208}\mathrm{Pb} + K^-$ in the P and KM models. The density ρ/ρ_0 (thin dotted line) is shown for comparison. The relative contribution of $\mathrm{Im}V^{(1)}_{K^-}$ and $\mathrm{Im}V^{(2)}_{K^-}$ to K^- absorption is changing with radius (density) because of the different range of corresponding potentials. At the nuclear surface, the K^- absorption on a single nucleon dominates, while it is reduced in the nuclear interior due to vicinity of $\pi\Sigma$ threshold and the multinucleon absorption prevails. The single-nucleon K^-N absorption in the nuclear medium is more suppressed in the models with $\alpha = 2$ since the self-consistent value of $\sqrt{s}$ at ρ_0 is closer to the $\pi\Sigma$ threshold than in the models with $\alpha = 1$. The analysis of Friedman and Gal [1] showed that the fractions of K^- absorption on a single nucleon ($\sim 75\%$) and several nucleons ($\sim 25\%$) from the bubble chamber experiments are sensitive to about 15% of nuclear density (denoted in Fig. 3 by vertical black line). At this density,

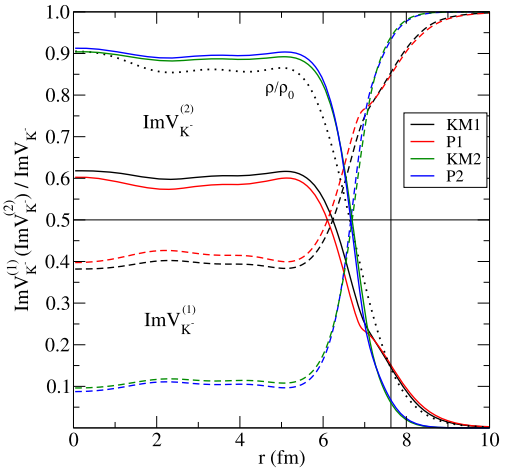

Fig. 3. The ratio of $\mathrm{Im}V^{(1)}_{K^-}$ (dashed line) and $\mathrm{Im}V^{(2)}_{K^-}$ (solid line) potentials to the total K^- imaginary potential $\mathrm{Im}V_{K^-}$ as a function of radius, calculated self-consistently for $^{208}\mathrm{Pb} + K^-$ system within different meson–baryon interaction models and FD option of the K^- multinucleon potential. The relative nuclear density ρ/ρ_0 (dotted line) and vertical lines denoting 15% of ρ_0 are shown for comparison.

the ratios $\mathrm{Im}V^{(2)}_{K^-}/\mathrm{Im}V^{(1)}_{K^-}$ are lower than experimental fractions of K^- absorption at rest [18–20] due to different self-consistent values of $\delta\sqrt{s}$ for kaonic and nuclear states. However, we stress that

Table 2
1s K^- binding energies B_{K^-} and widths Γ_{K^-} (in MeV) in various nuclei calculated using the single nucleon K^-N amplitudes (denoted KN); plus a phenomenological amplitude $B(\rho/\rho_0)^\alpha$, where $\alpha = 1$ and 2, for 'half-density limit' (HD) and 'full density' option (FD) (see text for details).

KM model			$\alpha = 1$		$\alpha = 2$	
		KN	HD	FD	HD	FD
^{16}O	B_{K^-}	45	34	not	48	not
	Γ_{K^-}	40	109	bound	121	bound
^{40}Ca	B_{K^-}	59	50	not	64	not
	Γ_{K^-}	37	113	bound	126	bound
^{208}Pb	B_{K^-}	78	64	33	80	53
	Γ_{K^-}	38	108	273	122	429
P model			$\alpha = 1$		$\alpha = 2$	
^{16}O	B_{K^-}	64	49	not	63	not
	Γ_{K^-}	25	94	bound	117	bound
^{40}Ca	B_{K^-}	81	67	not	82	not
	Γ_{K^-}	14	95	bound	120	bound
^{208}Pb	B_{K^-}	99	82	36	96	47*
	Γ_{K^-}	14	92	302	117	412*

* The solution of Eq. (1) for $\mathrm{Im}V_{K^-}$ scaled by factor 0.8.

one has to compare corresponding widths, rather than $\mathrm{Im}V^{(1)}_{K^-}$ and $\mathrm{Im}V^{(2)}_{K^-}$, for proper confrontation with experiment.

In Table 2 we present 1s K^- binding energies B_{K^-} and widths Γ_{K^-}, calculated in the KM and P models. The K^- binding energies and widths calculated only with the underlying K^- single-nucleon potential are shown for comparison. When K^- multinucleon interactions are included, the K^- widths increase considerably. For the HD option the K^- widths are of order ~ 100 MeV and exceed significantly the corresponding K^- binding energies.

For the K^- interaction models with the FD multinucleon potentials $V^{(2)}_{K^-}$, the antikaon is unbound in the majority of nuclei. We found 1s K^- quasi-bound states in ^{208}Pb, however, the K^- widths are huge, one order of magnitude larger than the binding energies.[1] These conclusions remain valid even when the uncertainties in the K^- multinucleon potential are taken into account.

4. Conclusions

This work reports on calculations of K^- nuclear quasi-bound states performed using a K^- single-nucleon potential derived within two chirally motivated meson–baryon coupled-channel models P and KM, supplemented by a phenomenological potential representing the K^- multinucleon interactions. Parameters of the phenomenological potential were recently fitted by Friedman and Gal [1] to kaonic atom data for each meson–baryon interaction model separately. Moreover, in the analysis of Ref. [1] the single-nucleon K^- potential constructed within the P and KM chiral models together with a phenomenological K^- multinucleon potential $V^{(2)}_{K^-}$ was confronted with the branching ratios of K^- single-nucleon absorption at rest for the first time. The fractions of K^- single-nucleon absorption calculated within these two models are in agreement with the data from bubble chamber experiments.

Since the kaonic atom data probe the K^- optical potential reliably up to at most $\sim 50\%$ of ρ_0, two scenarios for extrapolating $V^{(2)}_{K^-}$ to higher densities $\rho \geq 0.5\rho_0$ were considered. Moreover, uncertainties of the parameters of the phenomenological K^- multinucleon potentials were taken into account in order to verify that the results are sufficiently robust.

The fractions of K^- single-nucleon and multinucleon absorption in the medium were evaluated. At the surface of a nucleus, the fractions are in accordance with experimental data. In the nuclear interior, the K^- single-nucleon absorption is reduced due to the vicinity of $\pi\Sigma$ threshold and the K^- multinucleon absorption prevails.

The K^- multinucleon interactions were found to cause radical increase of K^- widths. In vast majority of nuclei the widths exceed considerably K^- binding energies. The FD variant of the phenomenological potential does not even yield any K^- bound states in most of the nuclei. Calculations performed for other nuclei and other recent K^-N interaction models considered in Ref. [1] confirmed our conclusions concerning the decisive effect of K^- multinucleon interactions on K^- widths in nuclei [31]. In view of our results, it would be desirable to explore the role of the K^- multinucleon processes in few-body systems as well.

The main message of the present study is that the K^--nuclear quasi-bound states in many-body nuclear systems, if they ever exist, have huge widths, considerably exceeding K^- binding energies. Their identification in experiment thus seems impossible.

[1] In the case of the P2 model, we present the solution of the Klein–Gordon equation (1) for ^{208}Pb with $\mathrm{Im}V_{K^-}$ scaled by factor 0.8 since the calculation with the full imaginary potential is not numerically stable due to extremely strong K^- absorption – the non-converged $\Gamma_{K^-} > 500$ MeV while the corresponding $B_{K^-} < 15$ MeV.

Acknowledgements

We wish to thank E. Friedman and A. Gal for valuable discussions, and A. Cieplý and M. Mai for providing us with the free K^-N scattering amplitudes. This work was supported by the GACR Grant No. P203/15/04301s.

J. Hrtánková acknowledges financial support from the CTU-SGS Grant No. SGS16/243/OHK4/3T/14.

Both J.H. and J.M. acknowledge the hospitality extended to them at the Racah Institute of Physics, The Hebrew University of Jerusalem, during their collaboration visit in November 2016. J.M. acknowledges financial support of his visit provided by the Racah Institute of Physics. J.H. acknowledges financial support of the Czech Academy of Sciences which enabled her stay at the Hebrew University.

References

[1] E. Friedman, A. Gal, Nucl. Phys. A 959 (2017) 66.
[2] See contributions in: A. Gal, O. Hashimoto, J. Pochodzalla (Eds.), Special Issue on Progress in Strangeness Nuclear Physics, Nucl. Phys. A 881 (2012) 1–338.
[3] See contributions in: B. Juliá Díaz, V. Magas, E. Oset, A. Parreño, A. Polls, L. Tolós, I. Vidaña, À. Ramos (Eds.), Proc. 11th Int. Conf. on Hypernuclear and Strange Particle Physics, HYP2012, Barcelona, 1–5 October, 2012, Nucl. Phys. A 914 (2013) 1–567.
[4] See contributions in: P. Bühler, J. Marton, K. Suzuki, E. Widmann, J. Zmeskal (Eds.), Proc. Int. Conf. on Exotic Atoms and Related Topics, EXA2014, Wien, 14–19 September, 2014, Hyperfine Interact. 233 (1–3) (2015), Hyperfine Interact. 234 (1–3) (2015).
[5] See contributions in: A. Gal, J. Pochodzalla (Eds.), Recent Progress in Strangeness and Charm Hadronic and Nuclear Physics, Nucl. Phys. A 954 (2016) 1–422.
[6] See contributions in: Proc. 12th Int. Conf. on Hypernuclear and Strange Particle Physics, HYP2015, Sendai, 7–12 September, 2015, in: JPS Conf. Proc., 2017, in press.
[7] W. Weise, Nucl. Phys. A 835 (2010) 51, and references therein.
[8] A. Gal, E.V. Hungerford, D.J. Millener, Rev. Mod. Phys. 88 (2016) 035004, and references therein.
[9] N.V. Shevchenko, Few-Body Syst. 58 (2017) 6, and references therein.
[10] A. Cieplý, E. Friedman, A. Gal, D. Gazda, J. Mareš, Phys. Lett. B 702 (2011) 402.
[11] A. Cieplý, E. Friedman, A. Gal, D. Gazda, J. Mareš, Phys. Rev. C 84 (2011) 045206.
[12] A. Cieplý, J. Smejkal, Nucl. Phys. A 881 (2012) 115.
[13] Y. Ikeda, T. Hyodo, W. Weise, Nucl. Phys. A 881 (2012) 98.
[14] D. Gazda, J. Mareš, Nucl. Phys. A 881 (2012) 159.
[15] E. Friedman, A. Gal, C.J. Batty, Phys. Lett. B 308 (1993) 6.
[16] E. Friedman, A. Gal, Nucl. Phys. A 899 (2013) 60.

[17] T. Sekihara, J. Yamagata-Sekihara, D. Jido, Y. Kanada-En'yo, Phys. Rev. C 86 (2012) 065205.
[18] H. Davis, F. Oppenheimer, W.L. Knight, F.R. Stannard, O. Treutler, Nuovo Cimento A 53 (1968) 313.
[19] J.W. Moulder, N.E. Garret, L.M. Tucker, W.M. Bugg, G.T. Condo, H.O. Cohn, R.D. McCulloch, Nucl. Phys. B 35 (1971) 332.
[20] C. Vander Velde-Wilquet, J. Sacton, J.H. Wickens, D.N. Tovee, D.H. Davis, Nuovo Cimento A 39 (1977) 539.
[21] A.D. Martin, Nucl. Phys. B 179 (1981) 33, and references therein.
[22] M. Bazzi, et al., SIDDHARTA Collaboration, Phys. Lett. B 704 (2011) 113.
[23] M.M. Sharma, M.A. Nagarajan, P. Ring, Phys. Lett. B 312 (1993) 377.
[24] T. Wass, M. Rho, W. Weise, Nucl. Phys. A 617 (1997) 449.
[25] E.E. Kolomeitsev, N. Kaiser, W. Weise, Phys. Rev. Lett. 90 (2013) 092501.
[26] C.J. Batty, E. Friedman, A. Gal, Phys. Rep. 287 (1997) 385.
[27] J. Mareš, E. Friedman, A. Gal, Phys. Lett. B 606 (2005) 295.
[28] E. Friedman, A. Gal, J. Mareš, Nucl. Phys. A 761 (2005) 283.
[29] E. Friedman, A. Gal, Phys. Rep. 452 (2007) 89.
[30] T. Sekihara, D. Jido, Y. Kanada-En'yo, Phys. Rev. C 79 (2009) 062201(R).
[31] J. Hrtánková, J. Mareš, arXiv:1704.07205 [nucl-th], Phys. Rev. C, submitted for publication.

K^- nuclear states: Binding energies and widths

J. Hrtánková* and J. Mareš†
Nuclear Physics Institute, 25068 Řež, Czech Republic

(Received 24 April 2017; revised manuscript received 8 June 2017; published 24 July 2017)

K^- optical potentials relevant to calculations of K^- nuclear quasibound states were developed within several chiral meson-baryon coupled-channels interaction models. The applied models yield quite different K^- binding energies and widths. Then the K^- multinucleon interactions were incorporated by a phenomenological optical potential fitted recently to kaonic atom data. Though the applied K^- interaction models differ significantly in the K^-N subthreshold region, our self-consistent calculations of kaonic nuclei across the periodic table lead to conclusions valid quite generally. Due to K^- multinucleon absorption in the nuclear medium, the calculated widths of K^- nuclear states are sizable, $\Gamma_{K^-} \geqslant 90$ MeV, and exceed substantially their binding energies in all considered nuclei.

DOI: 10.1103/PhysRevC.96.015205

I. INTRODUCTION

The near-threshold $\bar{K}N$ attraction seems to be strong enough to bind the antikaon in the nuclear medium and form a kaonic nucleus [1–4]. However, strong absorption of K^- in nuclear matter, as well as in-medium modifications and distinct energy dependence of the K^-N scattering amplitudes attributed to the $\Lambda(1405)$ resonance could call this presumption into question and thus have to be carefully accounted for in relevant calculations.

Unique information allowing us to fix the K^-p interaction at and above threshold is provided by low-energy $\bar{K}N$ scattering data (summarized, e.g., in Ref. [5]), threshold branching ratios [6], and, in particular, strong interaction energy shift and width of kaonic hydrogen atom [7]. The K^-n interaction is much poorly determined due to the lack of sufficiently accurate data. Considerably less is known about the K^-N interaction below threshold. Information about the subthreshold interaction of K^- with nucleons comes from the analyses of $\pi\Sigma$ spectra in the region of $\Lambda(1405)$ and especially from the measurement of energy shifts and widths of K^- atomic states throughout the periodic table [8,9].

The theoretical description of the K^-N interaction is currently provided by chirally motivated meson-baryon interaction models. Parameters of these models are tuned to reproduce the above low-energy K^-N observables. In the present study, the free-space K^-N scattering amplitudes derived within various chiral SU(3) meson-baryon coupled-channels interaction models: Prague (P) [10], Kyoto-Munich (KM) [5], Murcia (M1 and M2) [11], and Bonn (B2 and B4) [12] are used to construct the kaon self-energy operator Π_{K^-}. The free s-wave scattering amplitudes $F_{K^-p}(\sqrt{s})$ and $F_{K^-n}(\sqrt{s})$ considered in this work are shown in Fig. 1. Being constrained by the data, the $F_{K^-p}(\sqrt{s})$ amplitudes [Fig. 1 (top)] agree with each other at threshold and, except the Bonn model amplitudes, also above threshold. The form of B2 and B4 amplitudes deviates from the others because higher partial waves were included in the Bonn model fits. All the K^-p amplitudes differ considerably below threshold, which implies the region relevant for K^--nuclear bound-state calculations. Moreover, they are significantly energy dependent below threshold due to existence of $\Lambda(1405)$ resonance which is dynamically generated in these models. It is thus important to evaluate the K^--nucleus potential self-consistently [13,14]. The K^-n amplitudes [Fig. 1 (bottom)] differ appreciably from each other in the entire energy range considered here. Figure 1 illustrates significant model dependence of the input scattering amplitudes. As a result, binding energies B_{K^-} and widths Γ_{K^-} of kaonic nuclear states calculated within the above K^-N interaction models are expected to differ substantially from each other.

The implications of self-consistent treatment of energy dependence of chirally inspired K^-N amplitudes near threshold for calculations of K^--nuclear states were discussed in Ref. [15]. Due to a sizable downward energy shift towards $\pi\Sigma$ threshold, the K^- potential constructed within the P model yields relatively small K^- widths because only the K^- absorption on a single nucleon, $K^-N \to \pi Y$ ($Y = \Lambda, \Sigma$), is involved in this model [13–15]. In nuclear medium, K^- multinucleon interactions, such as $K^-NN \to YN$, take place as well [16–18] and should thus be considered in any realistic study of K^--nuclear quasibound states. Indeed, recent analyses of kaonic atoms have confirmed that a phenomenological term representing K^- multinucleon processes has to be added to the optical potential constructed from in-medium chirally motivated K^-N amplitudes in order to achieve good fit to the data [17,18]. In Refs. [13–15], the K^-NN absorption was included using a phenomenological potential and, as a consequence, the K^- widths increased and became comparable with K^- binding energies. Although the chiral K^-N interaction models do not involve the K^- multinucleon processes explicitly, Sekihara *et al.* [19] derived nonmesonic K^- interaction channels within a chiral unitary approach for the s-wave $\bar{K}N$ amplitude and calculated the ratio of mesonic to nonmesonic K^- absorption at rest in nuclear matter. The experimental information about this ratio comes from bubble chamber experiments [20–22]. Recently, Friedman and Gal have supplemented the K^- single-nucleon

*hrtankova@ujf.cas.cz
†mares@ujf.cas.cz

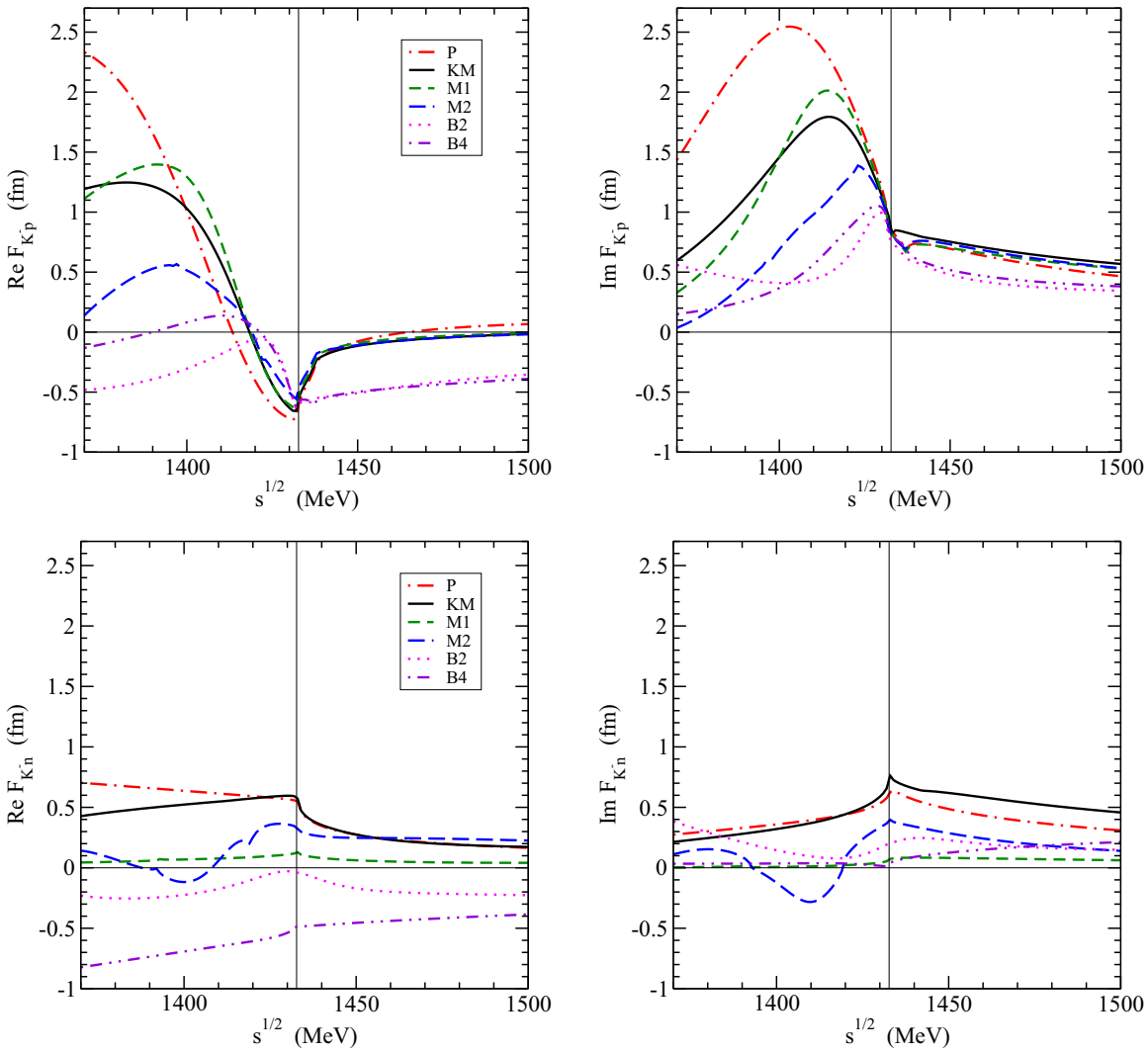

FIG. 1. Energy dependence of real (left) and imaginary (right) parts of free-space K^-p (top) and K^-n (bottom) amplitudes in considered chiral models (see text for details). Thin vertical lines mark threshold energies.

potential constructed from several chiral K^-N amplitude models by a phenomenological term representing the K^- multinucleon interactions and fitted its parameters to kaonic atom data for each meson-baryon interaction model separately [18]. Moreover, they confronted the total K^- optical potential with experimental fractions of K^- absorption at rest. They found that only the P and KM models supplemented by the K^- multinucleon potential are able to reproduce both experimental constraints simultaneously. These two models were recently used in calculations of K^- quasibound states [23] and the K^- multinucleon interactions were found to cause radical increase of the widths of K^--nuclear states.

In this work, we apply all six chirally motivated meson-baryon coupled-channels interaction models considered in Ref. [18] to calculations of K^--nuclear quasibound states, aiming at exploring model dependence of predicted K^- binding energies and widths. Then we supplement the K^- single-nucleon potential by a corresponding phenomenological optical potential describing the K^- multinucleon interactions in order to study in detail their impact on K^- binding energies and widths. Unlike previous calculations, we consider various K^-N interaction models presented in recent years. Most of them were never applied in such studies before. We perform unique calculations of kaonic nuclear quasibound states using the K^--nuclear potentials containing both K^- single-nucleon and multinucleon interactions which were fitted to available data for each meson-baryon interaction model.

The paper is organized as follows. In Sec. II we present construction of the in-medium K^-N amplitudes from the free-space amplitudes derived within chirally inspired coupled-channels models of meson-baryon interactions. We introduce a self-consistent scheme for treating energy dependence of these amplitudes and derive for each interaction model a relevant K^--nuclear potential. We discuss results of our calculations of K^--nuclear quasi-bound states using these potentials. In Sec. III, we present phenomenological potentials describing K^- multinucleon interactions and explore their impact on the widths and binding energies of kaonic nuclear quasibound states. A brief summary is given in Sec. IV.

II. CHIRALLY MOTIVATED K^- NUCLEAR POTENTIALS

The binding energies B_{K^-} and widths Γ_{K^-} of K^--nuclear quasibound states are determined by solving self-consistently the Klein-Gordon equation

$$\left[\vec{\nabla}^2 + \tilde{\omega}_{K^-}^2 - m_{K^-}^2 - \Pi_{K^-}(\omega_{K^-},\rho)\right]\phi_{K^-} = 0, \qquad (1)$$

where $\tilde{\omega}_{K^-} = m_{K^-} - B_{K^-} - i\Gamma_{K^-}/2 - V_C = \omega_{K^-} - V_C$, m_{K^-} is the K^- mass, V_C is the Coulomb potential introduced via the minimal substitution [24], and ρ is the nuclear density distribution. The energy- and density-dependent kaon self-energy operator Π_{K^-} describes K^- interactions with the nuclear medium.

The self-energy operator Π_{K^-} in Eq. (1) is constructed in a "$t\rho$" form with the in-medium amplitudes derived from the chirally motivated K^-N scattering amplitudes presented in Fig. 1. It is expressed as

$$\begin{aligned}\Pi_{K^-} &= 2\mathrm{Re}(\omega_{K^-})V_{K^-}^{(1)} \\ &= -4\pi\frac{\sqrt{s}}{m_N}\left[F_0\frac{1}{2}\rho_p + F_1\left(\frac{1}{2}\rho_p + \rho_n\right)\right], \end{aligned} \qquad (2)$$

where F_0 and F_1 are the isospin 0 and 1 s-wave in-medium amplitudes, respectively, $\sqrt{s}$ is the total energy of the K^-N system, m_N is the nucleon mass, and $V_{K^-}^{(1)}$ stands for the (single-nucleon) K^--nucleus optical potential. The kinematical factor $\sqrt{s}/m_N$ comes from transforming amplitudes from the two-body center-of-mass frame to the laboratory frame. The ρ_p and ρ_n denote proton and neutron density distributions, respectively, in a given core nucleus obtained within the relativistic mean-field model NL-SH [25]. We consider static nuclear density distribution, which means that core polarization effects are not included in our calculations. The polarization effects are A dependent—for instance, within the P model, they increase B_{K^-} by $\approx$6 MeV in Li, by $\leqslant$2 MeV in Ca, and by $\leqslant$0.5 MeV in Pb [15]. In any case, the role of the nuclear polarization is less pronounced than the model dependence.

The modifications of the free-space amplitudes due to Pauli principle in the medium are accounted for by using the multiple scattering approach (WRW) [26]. The in-medium amplitudes F_0 and F_1 are then given in the following form:

$$\begin{aligned} F_1 &= \frac{F_{K^-n}(\sqrt{s})}{1 + \frac{1}{4}\xi_k\frac{\sqrt{s}}{m_N}F_{K^-n}(\sqrt{s})\rho}, \\ F_0 &= \frac{[2F_{K^-p}(\sqrt{s}) - F_{K^-n}(\sqrt{s})]}{1 + \frac{1}{4}\xi_k\frac{\sqrt{s}}{m_N}[2F_{K^-p}(\sqrt{s}) - F_{K^-n}(\sqrt{s})]\rho}, \end{aligned} \qquad (3)$$

where

$$\xi_k = \frac{9\pi}{p_{\mathrm{F}}^2}4I_q, \quad I_q = \int_0^\infty \frac{dt}{t}\exp(iqt)j_1^2(t). \qquad (4)$$

Here p_{F} is the Fermi momentum corresponding to density $\rho = 2p_{\mathrm{F}}^3/(3\pi^2)$, $j_1(t)$ is the spherical Bessel function, and $q = \sqrt{\omega_{K^-}^2 - m_{K^-}^2}/p_{\mathrm{F}}$. The integral I_q in Eq. (4) can be evaluated analytically as [18]

$$\begin{aligned} 4I_q = 1 - \frac{q^2}{6} + \frac{q^2}{4}\left(2 + \frac{q^2}{6}\right)\ln\left(1 + \frac{4}{q^2}\right) \\ - \frac{4}{3}q\left[\frac{\pi}{2} - \arctan(q/2)\right]. \end{aligned} \qquad (5)$$

In Fig. 2, we present the K^-p and K^-n amplitudes in the considered models, modified by the WRW procedure at saturation density $\rho_0 = 0.17\,\mathrm{fm}^{-3}$ plotted as a function of energy. It follows from comparison with Fig. 1 that the K^-p amplitudes are affected significantly by Pauli correlations: The real part of the amplitudes becomes attractive in the entire energy region below threshold (except the B2 and B4 models) and the imaginary part is considerably lowered below threshold. On the other hand, the K^-n amplitudes are modified by Pauli correlations only moderately.

In previous calculations [13,15], the in-medium modifications of the K^-N amplitudes in the P model [10] were accounted for in a different way. The integration over the intermediate meson-baryon momenta in the underlying Green's function was restricted to a region ensuring the nucleon intermediate energy to be above the Fermi level (denoted further "Pauli"). Moreover, the in-medium hadron self-energies (denoted "Pauli+SE") were considered in some cases as well. In Fig. 3, we compare the Pauli correlated amplitudes with the WRW modified amplitudes in the P model. Both approaches, WRW and Pauli, yield similar K^-N in-medium reduced amplitudes[1] $f_{K^-N} = \frac{1}{2}(f_{K^-p} + f_{K^-n})$ in the subthreshold energy region. Above threshold, the behavior of Pauli and WRW modified amplitudes is different. The effect of hadron self-energies is illustrated in Fig. 3 as well. The Pauli correlated and Pauli+SE amplitudes are again quite similar to each other farther below threshold (in the region relevant to K^--nuclear bound state calculations), but they differ appreciably near and above threshold.

The existence of the subthreshold resonance $\Lambda(1405)$, which is dynamically generated in chirally motivated coupled-channels models, causes that the K^-p amplitudes exhibit strong energy (and density) dependence near and below threshold. This feature requires a proper self-consistent scheme for evaluating the K^- optical potential in both calculations of K^- atomic as well as nuclear states [13,15,17,18].

The in-medium amplitudes entering Eq. (3) are a function of energy $\sqrt{s}$ given by Mandelstam variable

$$s = (E_N + E_{K^-})^2 - (\vec{p}_N + \vec{p}_{K^-})^2, \qquad (6)$$

where $E_N = m_N - B_N$, $E_{K^-} = m_{K^-} - B_{K^-} - V_C$, and $\vec{p}_{N(K^-)}$ is the nucleon (kaon) momentum. Unlike the free two-body center-of-mass system, the momentum-dependent term $(\vec{p}_N + \vec{p}_{K^-})^2 \neq 0$ in the K^--nucleus center-of-mass frame, which generates additional substantial downward energy shift [13]. The non-negligible momentum term is on averaging over angles equal to $p_{K^-}^2 + p_N^2$. This averaging, i.e., dropping the term $\sim\vec{p}_{K^-}\cdot\vec{p}_N$, has been meant to provide a mean value

[1] $F_{K^-N} = g(p)f_{K^-N}g(p')$, where $g(p)$ is a momentum-space form factor (see Ref. [13]).

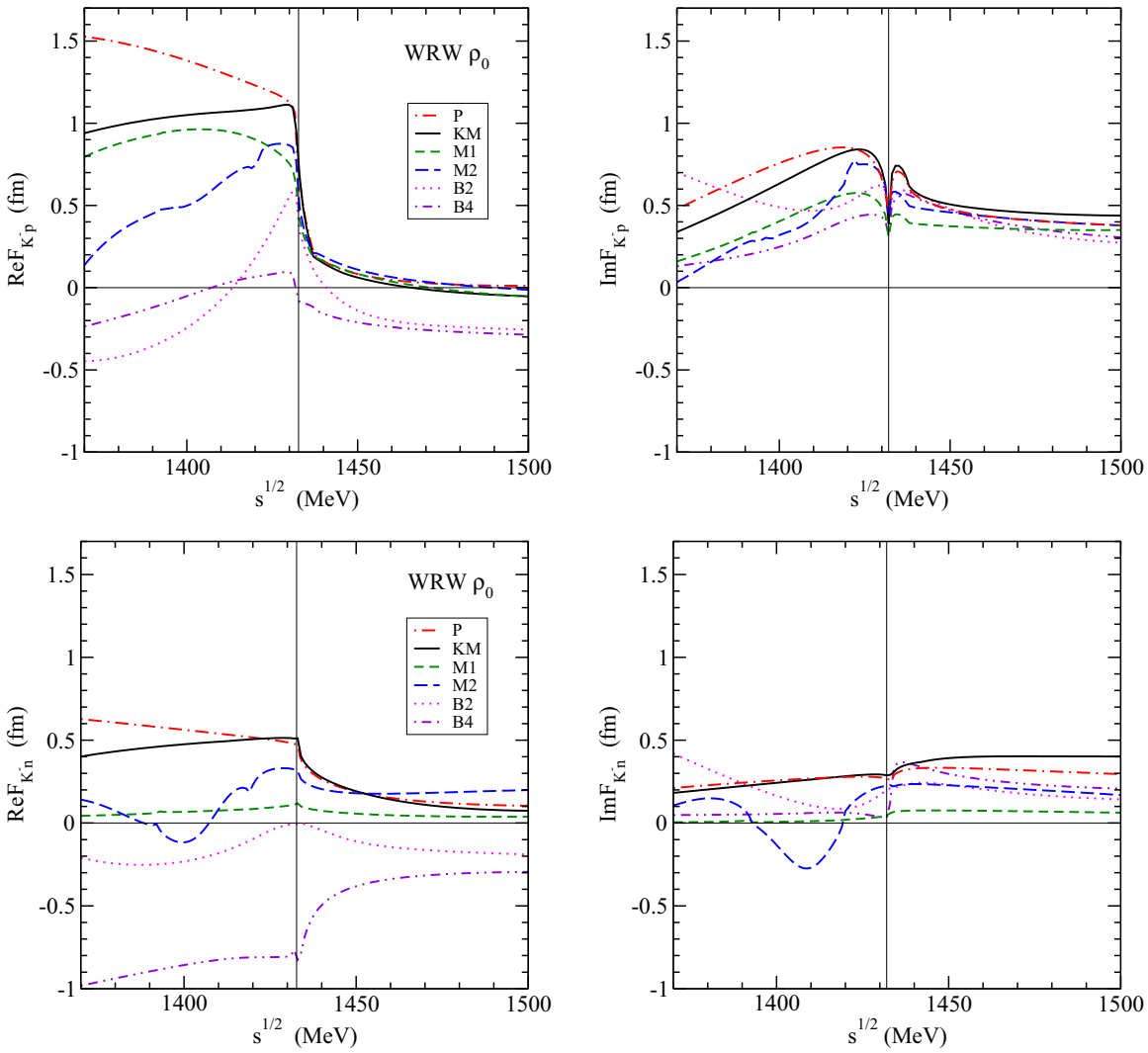

FIG. 2. Energy dependence of real (left) and imaginary (right) parts of WRW modified K^-p (top) and K^-n (bottom) amplitudes at $\rho_0 = 0.17\,\mathrm{fm}^{-3}$ in considered models. Thin vertical lines mark threshold energies.

of the energy $\sqrt{s}$ for a given density. It is not a substitute for a proper treatment of Fermi motion. The effect of Fermi motion was studied in detail in Ref. [27] where it was demonstrated that the Fermi averaging has a small effect on the K^- binding energy. Nevertheless, we performed calculations using averaging on the level of K^-N amplitudes instead of angular averaging. We verified that both approaches yield very similar results—K^- binding energies differ by $\leqslant 2\%$ and the widths by $\leqslant 10\%$.

The kaon kinetic energy is given in the local density approximation by

$$\frac{p_{K^-}^2}{2m_{K^-}} = -B_{K^-} - \mathrm{Re}V_{K^-} - V_C, \tag{7}$$

where V_{K^-} is the K^--nuclear optical potential. The nucleon kinetic energy is expressed within the Fermi gas model as

$$\frac{p_N^2}{2m_N} = T_N\left(\frac{\rho}{\bar{\rho}}\right)^{2/3}, \tag{8}$$

where $T_N = 23$ MeV is the average nucleon kinetic energy and $\bar{\rho}$ is the average nuclear density distribution.

Finally, the K^-N amplitudes can be expressed as a function of energy $\sqrt{s} = E_{\mathrm{th}} + \delta\sqrt{s}$ where $E_{\mathrm{th}} = m_N + m_{K^-}$ and the energy shift $\delta\sqrt{s}$ is expanded near threshold in terms of binding and kinetic energies (to leading order):

$$\delta\sqrt{s} \approx -B_N - B_{K^-} - V_C - \beta_N T_N\left(\frac{\rho}{\bar{\rho}}\right)^{2/3} - \beta_{K^-}[-B_{K^-} - \mathrm{Re}V_{K^-}(r) - V_C], \tag{9}$$

where $\beta_{N(K^-)} = m_{N(K^-)}/(m_N + m_{K^-})$ and $B_N = 8.5$ MeV is the average binding energy per nucleon. After introducing specific forms of density dependence ensuring that $\delta\sqrt{s} \to 0$ as $\rho \to 0$ in agreement with the low-density limit (for details, see Ref. [17]) the energy shift $\delta\sqrt{s}$ in Eq. (9) has the following form:

$$\delta\sqrt{s} = -B_N\frac{\rho}{\bar{\rho}} - \beta_N\left[B_{K^-}\frac{\rho}{\rho_{\max}} + T_N\left(\frac{\rho}{\bar{\rho}}\right)^{2/3} + V_C\left(\frac{\rho}{\rho_{\max}}\right)^{1/3}\right] + \beta_{K^-}\mathrm{Re}V_{K^-}(r), \tag{10}$$

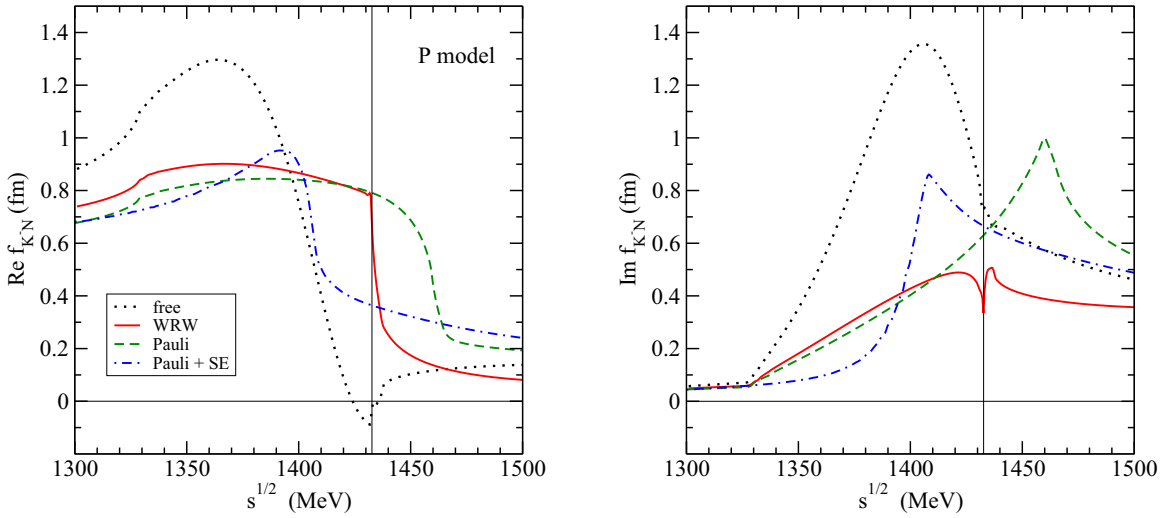

FIG. 3. Energy dependence of free-space (dotted line) amplitude $f_{K^-N} = \frac{1}{2}(f_{K^-p} + f_{K^-n})$ compared with WRW modified amplitude (solid line), Pauli (dashed line), and Pauli + SE (dot-dashed line) modified amplitude for $\rho_0 = 0.17\,\mathrm{fm}^{-3}$ in the P model (left: real parts, right: imaginary parts). The thin vertical line indicates the K^-N threshold.

where $\rho_{\max}$ is the maximal value of the nuclear density. The K^- binding energy B_{K^-} is multiplied by $\rho/\rho_{\max}$, which ensures that the K^- kinetic energy expressed in Eq. (7) in terms of local density approximation is positive at any nuclear density.

It is to be noted that since the input of our work was adopted from the kaonic atoms analysis of Friedman and Gal [18], it is desirable to keep consistent and use similar kinematics in our calculations.

In Fig. 4 we present the downward energy shift $\delta\sqrt{s} = E - E_{\mathrm{th}}$ as a function of relative density ρ/ρ_0 probed in the self-consistent calculations with in-medium K^- optical potential $V_{K^-}^{(1)}$ based on amplitudes from chiral models P, KM, M1, and M2. The calculations were performed for the $^{16}\mathrm{O} + K^-$ system. The models considered here predict quite different energy shifts, reaching at the saturation density values between $\sim$−40 MeV for the M2 model and $\sim$−100 MeV for the P model. The energy shifts corresponding to the Bonn models B2 and B4 are not plotted in the figure since these models do not yield any K^--nuclear bound state. It is to be noted that though the free-space amplitudes in Fig. 1 are shown only to $\sqrt{s} = 1370$ MeV, the amplitudes for KM and P models are available down to 1300 MeV. The energy shifts $\delta\sqrt{s}$ in the models shown in Fig. 4 are thus safely in the available energy region.

In calculations presented in this work, we take into account only Pauli correlations in the medium expressed within the WRW approach. One might argue that the effect of hadron self-energies should be included as well. In Fig. 5 we demonstrate the role of hadron self-energies in ^{40}Ca. We compare the K^- potential $V_{K^-}^{(1)}$ calculated in the P model within the WRW method (left panel) with the K^- potential calculated using the Pauli and Pauli +SE in-medium amplitudes, used in previous calculations of K^--nuclear bound states [15] (right panel). The hadron self-energies modify considerably the potential evaluated at threshold while their effect becomes rather small in self-consistent treatment of the energy shift. Then the WRW, Pauli, and Pauli+SE options for in-medium modifications of K^-N amplitudes give nearly identical K^--nucleus potentials.

As was shown in Figs. 1 and 2, the chiral K^-N amplitudes differ considerably below threshold, thus in the region relevant to calculations of kaonic nuclear states. As a consequence, corresponding K^--nucleus potentials derived using these amplitudes differ significantly as well. In Fig. 6, we present real (left) and imaginary (right) parts of the K^--nuclear optical

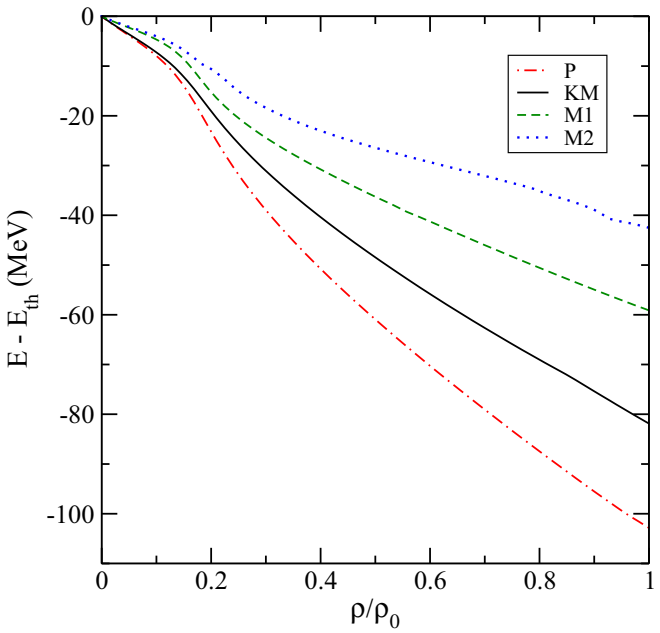

FIG. 4. Subthreshold energies probed in the $^{16}\mathrm{O} + K^-$ nucleus as a function of relative density ρ/ρ_0, calculated self-consistently using K^-N amplitudes in the P (dot-dashed line), KM (solid line), M1 (dashed line), and M2 (dotted line) models.

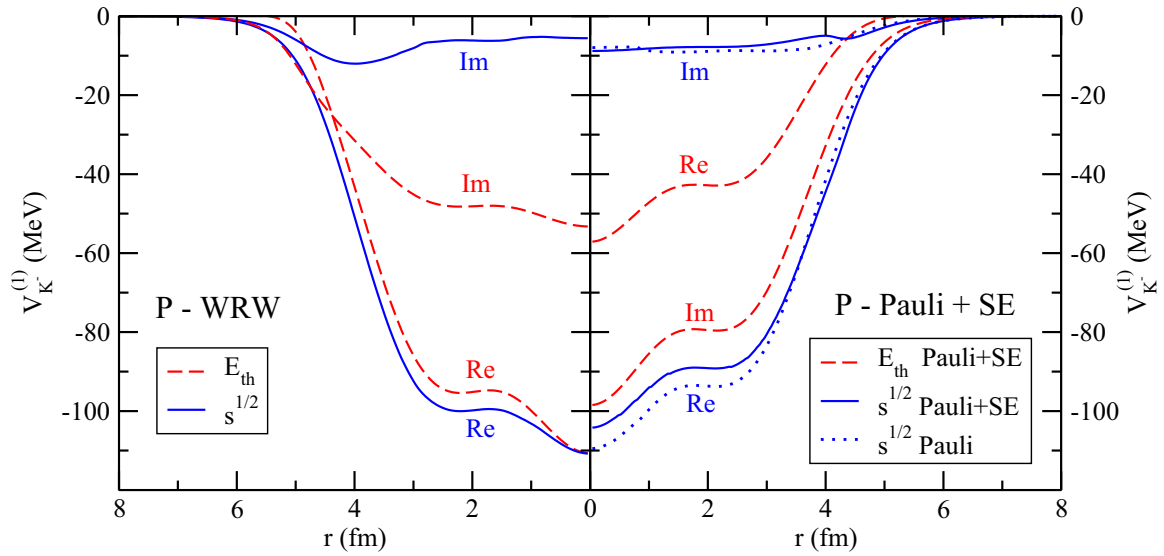

FIG. 5. K^- nuclear potential $V^{(1)}_{K^-}$ in ^{40}Ca calculated using chiral K^-N P amplitudes at threshold (dashed lines) and with $\sqrt{s}$ (Eq. (8) of Ref. [15]) (solid lines) in two in-medium versions: WRW (left panel) and Pauli+SE (right panel). The Pauli version (right panel, dotted line) for $\sqrt{s}$ from [15] is shown as well (see text for details).

potential $V^{(1)}_{K^-}$ in ^{40}Ca, calculated self-consistently within P, KM, M1, and M2 models. The depths of $\mathrm{Re}V^{(1)}_{K^-}$ are ranging from 30 MeV in the M2 model to 110 MeV in the P model. The imaginary parts of the K^- potentials are rather shallow inside the nucleus, which reflects sizable downward energy shift to the vicinity of threshold of the main decay channel $K^-N \to \pi\Sigma$. The apparent dip in the surface region is due to the low-density limit adopted in $\delta\sqrt{s}$ [see Eq. (10)].

The $1s$ binding energies B_{K^-} and widths Γ_{K^-} in selected nuclei are presented in Fig. 7. The calculated K^- binding energies are strongly model dependent due to different depths of $\mathrm{Re}V^{(1)}_{K^-}$ in various K^-N interaction models. However, they exhibit similar A dependence in all models considered. The K^- widths are rather small and weakly A dependent. The KM model predicts widths up to three times larger than the P and M1 models. The M2 model yields similar widths as the KM model for ^{208}Pb and ^{90}Zr, while the widths in lighter nuclei are comparable with the P model widths. It is to be noted that we get no kaonic nuclear bound states for the Bonn models B2 and B4 because the real parts of the in-medium K^-N amplitudes are repulsive in the relevant subthreshold region (see Figs. 1 and 2).

In Fig. 8 (left panel) we compare K^--nuclear single-particle spectra in ^{40}Ca, calculated using various K^-N interaction models. Again, the K^- binding energies B_{K^-} strongly depend on the model used. The relative position of the K^- spectra is in accordance with the depths of the K^--nucleus potentials $V^{(1)}_{K^-}$ shown in Fig. 6. The corresponding $K^-N \to \pi Y$ conversion

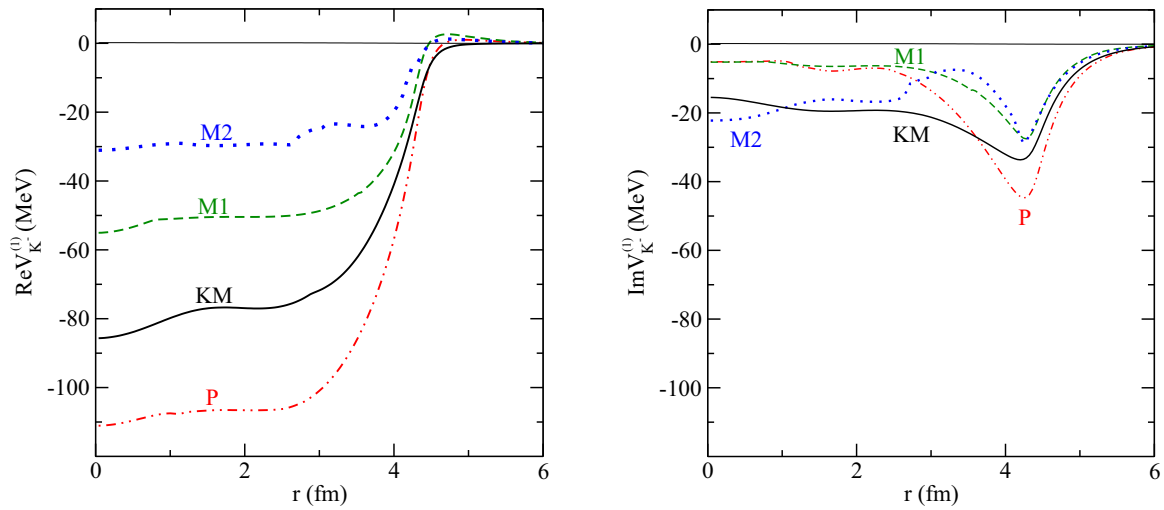

FIG. 6. Real (left) and imaginary (right) parts of the K^- nuclear potential $V^{(1)}_{K^-}$ in ^{40}Ca calculated self-consistently using chiral P (dot-dashed line), KM (solid line), M1 (dashed line), and M2 (dotted line) amplitudes.

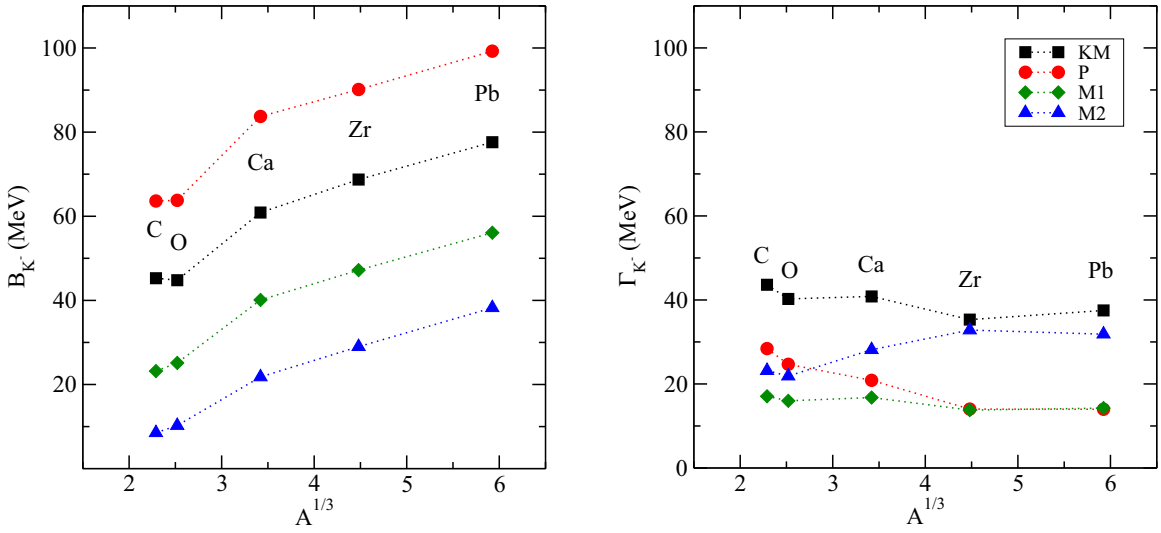

FIG. 7. 1s K^- binding energies (left) and corresponding widths (right) in various nuclei calculated self-consistently in P (circles), KM (squares), M1 (diamonds), and M2 (triangles) models. K^--multinucleon interactions are not considered.

widths are presented in Fig. 8 (right panel). In the P and KM models, the 1s-state widths are reduced due to considerable energy shift towards the $\pi\Sigma$ threshold and become smaller than the widths of excited states, for which $\sqrt{s}$ is farther from the $\pi\Sigma$ threshold. On the other hand, the K^- widths calculated in M1 and M2 models follow the opposite trend. It is because $\sqrt{s}$ in these models is much closer to the K^-N threshold where the (dominant) imaginary part of the K^-p amplitudes starts to decrease towards the threshold (see Fig. 2). This feature is more pronounced in the M2 model, which gives a smaller downward energy shift due to the shallower K^- potential (1d and 2s states are unbound).

Following results of calculations presented so far, one might conclude that at least some K^-N interaction models predict sufficiently bound kaonic nuclear states with relatively narrow widths. In the nuclear medium, however, K^- multinucleon processes take place as well. They are becoming more and more important with increasing nuclear density and K^- binding energy [28,29]. We will demonstrate their significant role in self-consistent calculations of kaonic nuclei in the next section.

III. THE ROLE OF K^- MULTINUCLEON INTERACTIONS

The K^- multinucleon interactions are an inseparable component of every realistic description of K^--nucleus interactions. As was shown in recent analysis by Friedman and Gal [18], the single-nucleon K^- potential constructed within all chiral meson-baryon interaction models considered in this work has to be supplemented by a phenomenological term representing K^- multinucleon processes in order to obtain good fit to kaonic atom data. The total K^- optical potential is then a sum of single-nucleon and multinucleon potential $V_{K^-} = V_{K^-}^{(1)} + V_{K^-}^{(2)}$, where the single-nucleon potential $V_{K^-}^{(1)}$ is

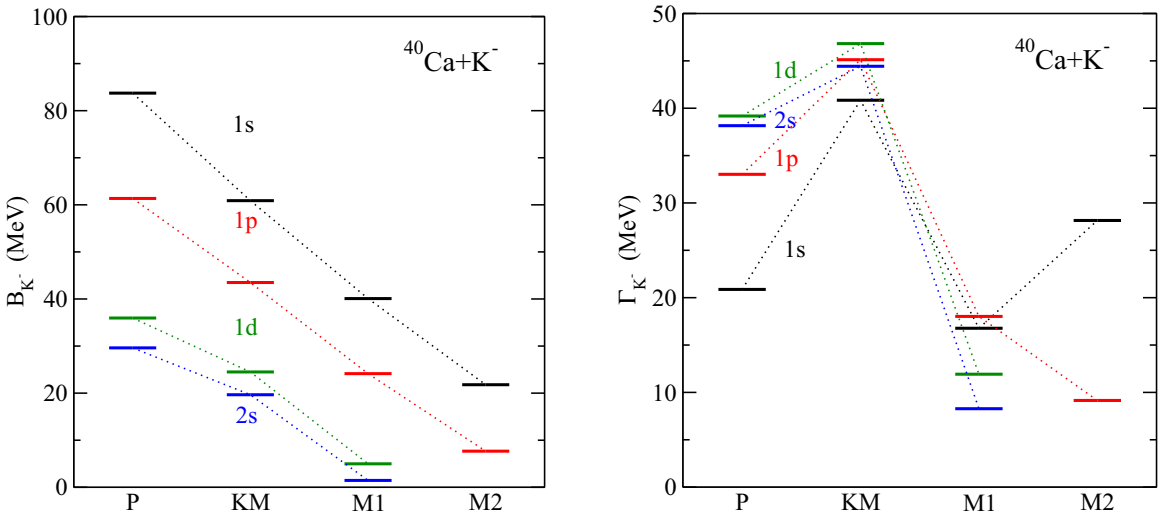

FIG. 8. K^- binding energies (left) and widths (right) in s, p, and d levels in ^{40}Ca calculated self-consistently in P, KM, M1, and M2 models. K^--multinucleon interactions are not considered.

TABLE I. Values of the complex amplitude B and exponent α used to evaluate $V_{K^-}^{(2)}$ for all chiral meson-baryon interaction models considered in this work.

	P1	KM1	P2	KM2
α	1	1	2	2
ReB (fm)	-1.3 ± 0.2	-0.9 ± 0.2	-0.5 ± 0.6	0.3 ± 0.7
ImB (fm)	1.5 ± 0.2	1.4 ± 0.2	4.6 ± 0.7	3.8 ± 0.7
	B2	B4	M1	M2
α	0.3	0.3	0.3	1
ReB (fm)	2.4 ± 0.2	3.1 ± 0.1	0.3 ± 0.1	2.1 ± 0.2
ImB (fm)	0.8 ± 0.1	0.8 ± 0.1	0.8 ± 0.1	1.2 ± 0.2

given by Eq. (2) and the multinucleon term $V_{K^-}^{(2)}$ is of the form

$$2\mathrm{Re}(\omega_{K^-})V_{K^-}^{(2)} = -4\pi B\left(\frac{\rho}{\rho_0}\right)^{\alpha}\rho. \tag{11}$$

The values of the complex amplitude B and positive exponent α listed in Table I were obtained by fitting kaonic atom data for each K^-N amplitude model separately [18]. Moreover, the total K^- optical potentials V_{K^-} were then confronted with branching ratios of K^- absorption at rest. Only two models, P and KM, were found to reproduce simultaneously the fractions of K^- single-nucleon absorption from bubble chamber experiments [20–22] and kaonic atom data. Yet we performed calculations for all six discussed K^-N amplitude models. It is to be noted that the P and KM models could be regarded as equivalent within the uncertainties shown in Table I.

The dominant mode of K^- absorption on two nucleons in the nuclear interior is the nonpionic conversion $K^-NN \to \Sigma N$ [19,28,30]. Since the amplitude ImB is constant, we multiply it by kinematical suppression factor to account for phase space reduction for decay products in $K^-NN \to \Sigma N$ absorption in the nuclear medium. The suppression factor used in our calculation is of the form

$$f_{\Sigma N} = \frac{M^3}{s_m^{3/2}}\sqrt{\frac{[s_m-(m_N+m_\Sigma)^2][s_m-(m_N-m_\Sigma)^2]}{[M^2-(m_N+m_\Sigma)^2][M^2-(m_N-m_\Sigma)^2]}} \times \Theta(\sqrt{s}_m - m_N - m_\Sigma), \tag{12}$$

where $M = 2m_N + m_{K^-}$ and $\sqrt{s}_m = M - \delta\sqrt{s}$ [28].

It is to be noted that for processes on a single nucleon, the proper energy dependence is embedded directly in the K^-N amplitudes constructed within chirally motivated coupled-channels models.

Analyses of Friedman and Gal have shown that kaonic atom data constrain reliably the real part of the K^- optical potential up to ∼25% of ρ_0 and its imaginary part up to ∼50% of ρ_0. The shape of the phenomenological K^- optical potential $V_{K^-}^{(2)}$ in the nuclear interior is thus a matter of extrapolation to higher densities. In order to allow for more flexibility, we consider different options for $V_{K^-}^{(2)}$ beyond the half density limit $\rho(r) = 0.5\rho_0$ in our calculations. First, the form (11) is applied in the entire nucleus (full density option, FD). Second, the potential $V_{K^-}^{(2)}$ is fixed at constant value $V_{K^-}^{(2)}(0.5\rho_0)$ for $\rho(r) \geqslant 0.5\rho_0$ (half density limit, HD). In the third approximation (TR), the $t\rho$ form of $V_{K^-}^{(2)}$ is assumed for densities $\rho(r) \geqslant 0.5\rho_0$ in Eq. (11), i.e., $V_{K^-}^{(2)} \sim -4\pi B(0.5)^{\alpha}\rho$ for $\rho(r) \geqslant 0.5\rho_0$.

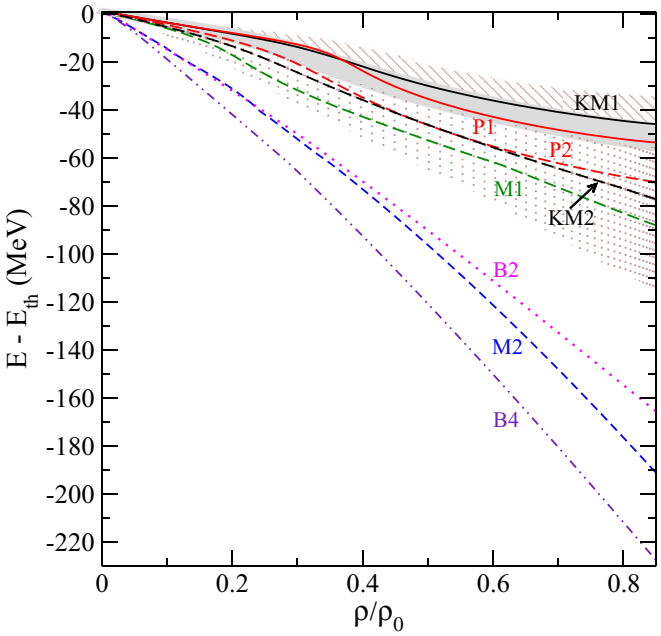

FIG. 9. Subthreshold energies probed in the ^{208}Pb + K^- nucleus as a function of relative density ρ/ρ_0, calculated self-consistently in all K^-N amplitude models considered, supplemented by the FD variant of $V_{K^-}^{(2)}$. The dashed and dotted areas denote the uncertainty bands calculated in the KM1 and KM2 models and the shaded gray band represents their overlap.

In Fig. 9, we present subthreshold energy shift $\delta\sqrt{s} = E - E_{\mathrm{th}}$ as a function of the nuclear density in ^{208}Pb, calculated in all K^-N interaction models considered in this work, with the FD version of the K^- multinucleon potential. For illustration, we show also the uncertainties involved in the KM1 and KM2 multinucleon potentials. They are denoted by dashed and dotted areas and the gray shaded band denotes their overlap. After including the K^- multinucleon interactions in the KM and P models (the only two models accepted by analysis of Ref. [18]), the energy shift $\delta\sqrt{s}$ for a particular density becomes smaller and moves back towards the K^-N threshold (compare Fig. 4 and Fig. 9). On the other hand, the B2, B4, and M2 models supplemented by a strongly attractive K^- multinucleon potential Re$V_{K^-}^{(2)}$ (see Table I) probe much deeper energy region below threshold than the KM and P models. In fact, fairly deep Re$V_{K^-}^{(2)}$, (200–300) MeV, causes that K^- will be bound even in the Bonn models B2 and B4.

We witness large model dependence of the downward energy shifts $\delta\sqrt{s}$, ranging from −35 to −230 MeV in the nuclear center. This suggests that the models yield considerably different K^- optical potentials. Yet, the KM and P models could be regarded as equivalent since they all lie in corresponding uncertainty bands and describe kaonic atom data equally well. We note that the free-space amplitudes in the M1, M2, B2, and B4 models were available only for

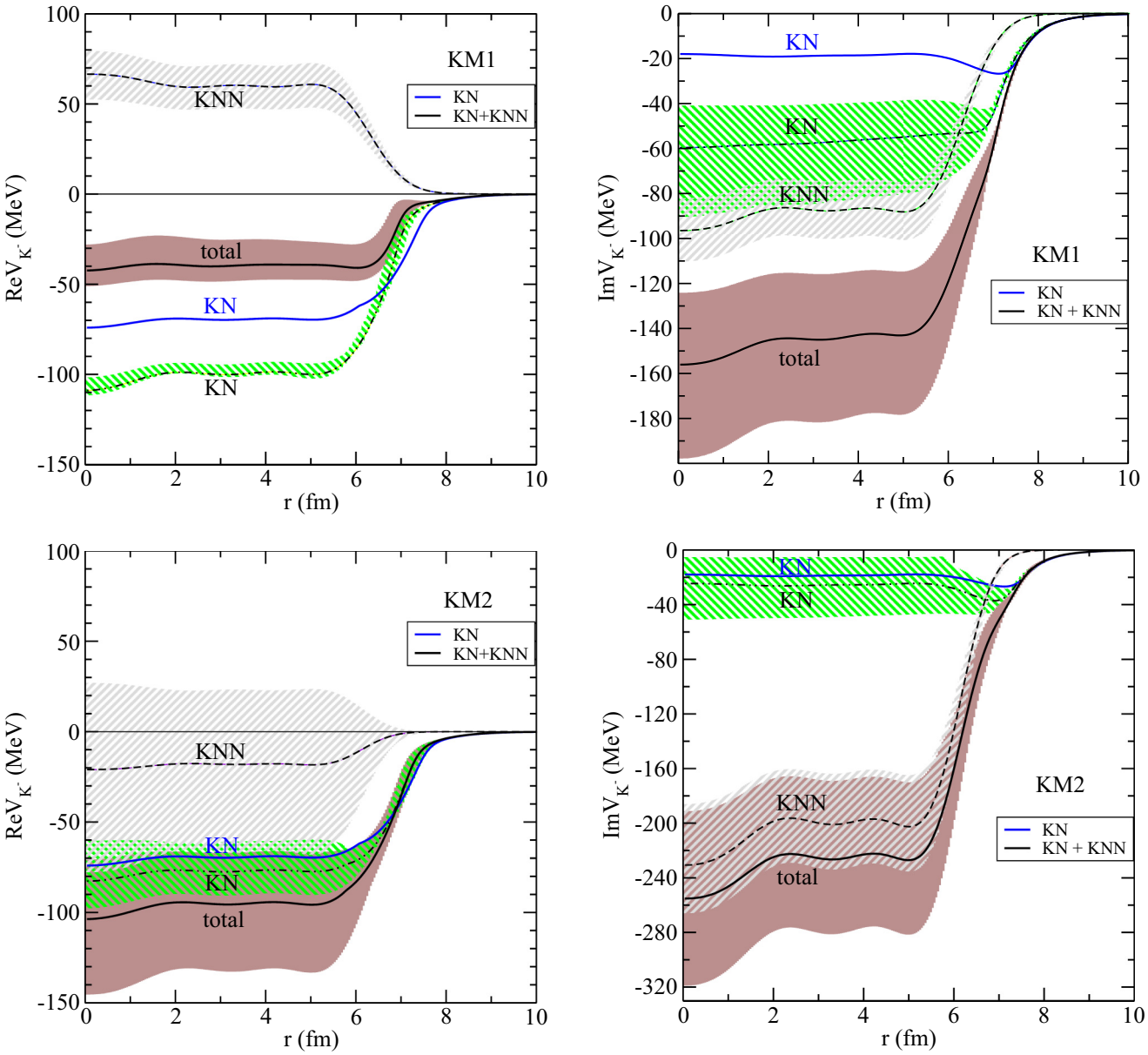

FIG. 10. The respective contributions from K^-N (dashed dotted line) and K^-NN (dashed line) potentials to the total real (left) and imaginary (right) K^- optical potential in the $^{208}\mathrm{Pb} + K^-$ nucleus, calculated self-consistently in the FD version of KM1 (top) and KM2 (bottom) models. The shaded areas denote the uncertainty bands. The K^- single-nucleon potential (KN, blue solid line) calculated in the KM model (i.e., without multinucleon interactions) is shown for comparison.

$\sqrt{s} \geqslant 1370$ MeV. Therefore, we fixed the K^-N amplitudes at constant value $F_{K^-N}(1370)$ when $\sqrt{s}$ got below 1370 MeV in our self-consistent calculations.

The individual contributions from single-nucleon $V_{K^-}^{(1)}$ and multinucleon $V_{K^-}^{(2)}$ potentials to the total K^- optical potential V_{K^-} including their uncertainties (shaded areas) are shown in Fig. 10, calculated self-consistently for $^{208}\mathrm{Pb} + K^-$ in the KM1 (top panels) and KM2 model (bottom panels) and the FD version of $V_{K^-}^{(2)}$. For comparison, we present the single-nucleon K^-N potential (KN, blue solid line) derived from the K^-N amplitude model KM without considering multinucleon interactions. The contribution from $\mathrm{Re}\,V_{K^-}^{(2)}$ to the total real K^--nucleus potential is repulsive in the KM1 model, as well as in the P1 and P2 models (not shown in the figure). As a result, the total K^--nucleus potential including multinucleon processes is less attractive than the original single-nucleon K^--nucleus potential. In the KM2 model the contribution from $V_{K^-}^{(2)}$ brings additional attraction to the total potential due to positive sign of the effective amplitude $\mathrm{Re}B$ (see Table I). However, the extensive uncertainty band in Fig. 10 proves that the sign of $\mathrm{Re}B$ in the KM2 model is insignificant. The $V_{K^-}^{(1)}$ part of the optical potential in the KM1 and KM2 models (as well as in other models) differs from the original single-nucleon K^-N potential due to the different subthreshold energy shift (see Fig. 9 and Fig. 4). The uncertainties in the K^-N part arise from variations of $\delta\sqrt{s}$ caused by the uncertainties in total

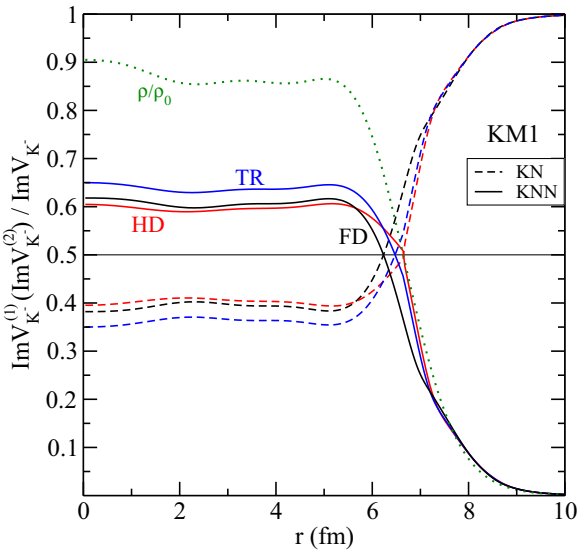

FIG. 11. The ratio of $\mathrm{Im}V_{K^-}^{(1)}$ (dashed line) and $\mathrm{Im}V_{K^-}^{(2)}$ (solid line) potentials to the total K^- imaginary potential $\mathrm{Im}V_{K^-}$ as a function of radius, calculated self-consistently for the $1s$ K^- state in ^{208}Pb using the KM1 model and different options for the K^- multinucleon potential. The relative nuclear density ρ/ρ_0 (dotted line) is shown for comparison.

K^--nuclear potential. The depths of the total $\mathrm{Re}V_{K^-}$ in the KM1(2), P1(2), and M1 models including the multinucleon potential $V_{K^-}^{(2)}$ are of the range $\simeq$(50–100) MeV (not quoting uncertainties).

Adding K^- multinucleon absorptions dramatically increases the depth of the total imaginary K^- potential as illustrated in the right panels of Fig. 10. In the KM models (as well as P models, not shown in the figure), $\mathrm{Im}V_{K^-}$ is much deeper than $\mathrm{Re}V_{K^-}$ for both values of α even when the uncertainties are taken into account. The K^- multinucleon processes contribute substantially to K^- absorption mainly in the interior of a nucleus. As a result, the depth of $\mathrm{Im}V_{K^-}$ $\simeq$(70–170) MeV in the KM1, P1, and M1 models and $\mathrm{Im}V_{K^-}$ $\simeq$ 270 MeV in the KM2 and P2 models (not quoting uncertainties). The range of $V_{K^-}^{(2)}$ potential is considerably smaller than the range of the $V_{K^-}^{(1)}$ potential and thus in the surface region of a nucleus, K^- single-nucleon absorption dominates in accordance with experimental findings [20–22].

The B2, B4, and M2 models yield the real part of the total K^--nucleus potential extremely deep, $\sim$(200–300) MeV in the nuclear interior, thanks to a strongly attractive $\mathrm{Re}V_{K^-}^{(2)}$. On the contrary, the imaginary part of the V_{K^-} potentials in these models is shallower than in the KM1 model.

Next, we evaluated the fractions of the K^- single- and multinucleon absorptions as a ratio of $\mathrm{Im}V_{K^-}^{(1)}$ and $\mathrm{Im}V_{K^-}^{(2)}$ with respect to the total imaginary K^- potential $\mathrm{Im}V_{K^-}$. These ratios are depicted in Fig. 11 as a function of radius, calculated self-consistently for the $1s$ K^- state in ^{208}Pb using the KM1 model and HD, TR, and FD options for $V_{K^-}^{(2)}$. For comparison, the relative density ρ/ρ_0 (thin dotted line) is shown here as well. Since the range and density dependence

TABLE II. $1s$ K^- binding energies and widths (in MeV) in various nuclei calculated using the single-nucleon K^-N KM amplitudes (denoted KN); plus a phenomenological amplitude $B(\rho/\rho_0)^\alpha$, where $\alpha = 1$ and 2, for "half-density limit" (HD), $t\rho$ option (TR), and full density option (FD).

KM model			$\alpha = 1$			$\alpha = 2$		
		KN	HD	TR	FD	HD	TR	FD
^{6}Li	B_{K^-}	25	11	Not	Not	23	19	Not
	Γ_{K^-}	45	116	bound	bound	122	160	bound
^{12}C	B_{K^-}	45	34	20	Not	48	44	Not
	Γ_{K^-}	44	114	182	bound	125	191	bound
^{16}O	B_{K^-}	45	34	25	Not	48	46	Not
	Γ_{K^-}	40	109	158	bound	121	167	bound
^{40}Ca	B_{K^-}	59	50	40	Not	64	63	Not
	Γ_{K^-}	37	113	164	bound	126	175	bound
^{90}Zr	B_{K^-}	69	56	47	17	72	71	30
	Γ_{K^-}	36	107	156	312	120	167	499
^{208}Pb	B_{K^-}	78	64	56	33	80	80	53
	Γ_{K^-}	38	108	153	273	122	163	429
P model			$\alpha = 1$			$\alpha = 2$		
		KN	HD	TR	FD	HD	TR	FD
^{6}Li	B_{K^-}	38	21	Not	Not	36	28	Not
	Γ_{K^-}	40	112	bound	bound	133	183	bound
^{12}C	B_{K^-}	64	50	35	Not	64	57	Not
	Γ_{K^-}	28	96	165	bound	122	196	bound
^{16}O	B_{K^-}	64	50	39	Not	63	59	Not
	Γ_{K^-}	25	94	142	bound	117	169	bound
^{40}Ca	B_{K^-}	81	67	56	Not	82	79	Not
	Γ_{K^-}	14	95	145	bound	120	175	bound
^{90}Zr	B_{K^-}	90	74	62	19	87	85	Not
	Γ_{K^-}	12	88	136	340	114	164	bound
^{208}Pb	B_{K^-}	99	82	70	37	96	92	47[a]
	Γ_{K^-}	14	92	137	302	117	163	412[a]

[a]the solution of the Klein-Gordon equation for $\mathrm{Im}V_{K^-}$ scaled by factor 0.8.

of $V_{K^-}^{(1)}$ and $V_{K^-}^{(2)}$ potentials is different (see Fig. 10) the relative contribution of $\mathrm{Im}V_{K^-}^{(1)}$ and $\mathrm{Im}V_{K^-}^{(2)}$ to K^- absorption is changing with the radius (density). In the surface region of a nucleus, the dominant process is the K^- absorption on a single nucleon, while in the nuclear interior, the single-nucleon absorption is reduced due to the vicinity of the $\pi\Sigma$ threshold and multinucleon absorption prevails. All three higher-density versions of $V_{K^-}^{(2)}$ yield the same fractions of single- and multinucleon absorption at the nuclear surface and differ slightly from each other inside the nucleus.

The above-discussed K^-N amplitude models supplemented by K^- multinucleon interactions described by the phenomenological potential $V_{K^-}^{(2)}$ were applied to calculations of K^--nuclear bound states in various nuclei across the periodic table. We considered all three extrapolations HD, TR, and FD of $V_{K^-}^{(2)}$.

In Table II, we present $1s$ K^- binding energies B_{K^-} and widths Γ_{K^-}, calculated in the KM and P models, respectively. For comparison, we show also K^- binding energies and widths calculated only with the underlying chirally inspired

TABLE III. 1s K^- binding energies and widths (in MeV) in ^{16}O and ^{208}Pb calculated using the single-nucleon K^-N amplitudes M1, M2, B2, B4 plus a phenomenological amplitudes $B(\rho/\rho_0)^\alpha$ from Table I.

		M1		M2		B2		B4	
		KN	FD	KN	FD	KN	FD	KN	FD
^{16}O	B_{K^-}	25	48	10	135	Not	98	Not	170
	Γ_{K^-}	16	117	22	244	bound	271	bound	190
^{208}Pb	B_{K^-}	56	80	38	170	Not	146	Not	200
	Γ_{K^-}	14	121	32	214	bound	259	bound	174

TABLE IV. K^- binding energies and widths (in MeV) in ^{208}Pb calculated using the single-nucleon K^-N KM amplitudes (denoted KN); plus a phenomenological amplitude $B(\rho/\rho_0)^\alpha$, where $\alpha = 1$, for half density (HD) and full density (FD) options (see text for details).

^{208}Pb + K^-		1s	1p	1d	1f	1g	1h	1i
KN	B_{K^-}	78	70	61	52	42	31	20
	Γ_{K^-}	38	38	40	42	45	46	47
HD	B_{K^-}	64	58	51	42	33	22	8
	Γ_{K^-}	108	110	112	115	120	127	143
FD	B_{K^-}	33	24	9	Not bound	Not bound	Not bound	Not bound
	Γ_{K^-}	273	285	306				

K^- single-nucleon potential. In these models, which provide reasonable description of kaonic atom data and fractions of K^- single- and multinucleon absorptions at rest, K^- widths increase considerably after including K^- multinucleon processes, while K^- binding energies change only slightly (they decrease in KM1, P1, and P2[2] models and increase in KM2 model). For the FD multinucleon potentials $V^{(2)}_{K^-}$, the antikaon is unbound in the vast majority of nuclei. In ^{90}Zr and ^{208}Pb, we found 1s K^- quasibound states, however, the K^- binding energies of such states are small and widths are huge, one order of magnitude larger than the binding energies. For other variants of $V^{(2)}_{K^-}$ potential, HD and TR, K^- widths are of order ∼100 MeV but, again, the binding energies are much smaller than the widths in most nuclei. The smallest K^- widths are predicted in the P model for $\alpha = 1$ and the HD option; nevertheless, they still exceed noticeably the binding energies. These results hold generally and remain valid even when the uncertainties in the multinucleon potential $V^{(2)}_{K^-}$ are taken into account.

For completeness, we show in Table III binding energies and widths of the K^- 1s states in ^{16}O and ^{208}Pb, calculated in M1, M2, B2, and B4 models and FD variant of $V^{(2)}_{K^-}$. Unlike KM and P models, these models give K^- quasibound states for the FD option also in ^{16}O due to strongly attractive K^- multinucleon interactions. However, the predicted K^- binding energies are again much smaller than the widths (except the B4 model, which yields comparable binding energies and widths). However, it is to be stressed that none of the models in Table III reproduces experimental values of the fractions of K^- single- and multinucleon absorptions at rest.

Table IV presents the binding energies and widths of K^- quasibound states in ^{208}Pb, calculated in the KM1 model with FD and HD options of the multinucleon potential. The binding energies and widths of K^- states calculated with the underlying K^-N single-nucleon potentials (KN) are presented here for comparison. The $K^-N \to \pi Y$ conversion widths are gradually increasing in excited states as $\delta\sqrt{s}$ is moving away from the $\pi\Sigma$ threshold. However, the increase in the KM model is not as pronounced as in the P model [15], where the difference between the K^- widths due to K^- single-nucleon absorption in the 1s and 1i states is ≃35 MeV (compare also Γ_{K^-} of excited states in ^{40}Ca for various K^-N amplitude models in Fig. 8). For the HD option of multinucleon potential, the K^- binding energies are smaller and widths are more than twice larger than in the KN case. In the FD version of $V^{(2)}_{K^-}$, the number of excited K^- quasibound states is considerably reduced because of strong K^- absorption.

IV. CONCLUSIONS

We performed calculations of K^- nuclear quasi-bound states using K^--nucleus optical potentials derived self-consistently from K^-N amplitudes, obtained within several recent chirally-motivated meson-baryon coupled-channels models. Following analyses of Friedman and Gal [17,18] these models need to be supplemented by a phenomenological term representing K^- multinucleon interactions in order to fit kaonic atom data. Though only the P and KM models are able to reproduce at the same time the experimentally determined fractions of K^- single-nucleon absorption at rest [18], we considered also the other K^-N amplitude models in order to explore model dependence of our calculations. The main aim of our work was to assess the effect of the K^- multinucleon processes on binding energies and widths of kaonic nuclear states.

First, we constructed the chirally motivated K^- single-nucleon part of the optical potential using six different sets of K^-N amplitudes. In order to account for Pauli correlations in the nuclear medium, we applied the multiple-scattering WRW procedure [26]. We verified that hadron self-energies, considered in previous calculations of in-medium K^-N amplitudes [13,14], affect the K^- single-nucleon potential only slightly in the energy region relevant to our current calculations. An important aspect of chirally motivated K^-N amplitudes is their energy dependence, which has to be treated self-consistently, taking into account the non-negligible contribution from K^- and N momenta. Each of the considered models gives different depths of ReV_{K^-} in a nucleus and thus probes different energy regions below the K^-N threshold. The resulting K^- binding energies B_{K^-} are then strongly model dependent. The widths of the 1s K^--nuclear states come out quite small. The smallest widths Γ_{K^-} are predicted by the

[2]For the FD variant of the P2 model, we had to scale huge imaginary part ImV_{K^-} by factor 0.8 in order to get fully converged self-consistent solution of the Klein-Gordon equation Eq. (1). The calculation with the unscaled imaginary potential is not numerically stable due to extremely strong K^- absorption—the nonconverged $\Gamma_{K^-} > 500$ MeV while the corresponding $B_{K^-} < 15$ MeV.

Murcia model M1, whereas the KM model predicts the K^- widths three times as large.

Next, we added to each K^- single-nucleon potential $V^{(1)}_{K^-}$ a corresponding phenomenological multinucleon potential $V^{(2)}_{K^-}$, parameters of which were recently fitted to kaonic atom data [18]. Since the kaonic-atom data probe the K^- optical potential reliably up to at most $\sim$50% of ρ_0, we considered three different scenarios for extrapolating $V^{(2)}_{K^-}$ to higher densities, $\rho \geqslant 0.5\rho_0$. Though the applied models differ widely in the subthreshold region, our calculations lead to some quite general conclusions, valid for each of the K^--nucleus interaction models. We found that the K^- multinucleon absorption gives rise to substantial increase of the widths of K^--nuclear states. The K^- widths exceed considerably the K^- binding energies in the vast majority of nuclei. In the KM and P models, the only models accepted by the analysis of Friedman and Gal [18], the FD variant of $V^{(2)}_{K^-}$ even does not yield any K^--nuclear bound state in most of the nuclei under consideration. We verified that these conclusions remain valid even after taking into account the uncertainties in the multinucleon potential $V^{(2)}_{K^-}$.

After exploring various chirally inspired coupled-channels models of meson-baryon interactions together with a phenomenological K^- multinucleon part fitted to reproduce the experimental data, we feel free to conclude that the widths of K^--nuclear quasibound states in nuclei with $A \geqslant 6$ are considerably larger than their binding energies. Therefore, observation of such states in experiment seems highly unlikely. We believe that our results will stimulate theoretical studies of the role of K^- multinucleon processes in lighter K^--nuclear systems in which few-body techniques are applicable.

ACKNOWLEDGMENTS

We thank E. Friedman and A. Gal for valuable discussions and A. Cieplý and M. Mai for providing us with the free K^-N scattering amplitudes. This work was supported by the GACR Grant No. P203/15/04301s. J.H. acknowledges support from the CTU-SGS Grant No. SGS16/243/OHK4/3T/14. Both J.H. and J.M. acknowledge the hospitality extended to them at the Racah Institute of Physics, The Hebrew University of Jerusalem, during their collaboration visit in November 2016. J.M. acknowledges financial support of his visit provided by the Racah Institute of Physics. J.H. acknowledges financial support of the Czech Academy of Sciences which enabled her stay at the Hebrew University.

[1] Y. Akaishi and T. Yamazaki, Phys. Rev. C **65**, 044005 (2002).
[2] T. Yamazaki and Y. Akaishi, Phys. Lett. B **535**, 70 (2002).
[3] W. Weise, Nucl. Phys. A **835**, 51 (2010).
[4] N. V. Shevchenko, Few Body Syst. **58**, 6 (2017).
[5] Y. Ikeda, T. Hyodo, and W. Weise, Nucl. Phys. A **881**, 98 (2012).
[6] A. D. Martin, Nucl. Phys. B **179**, 33 (1981).
[7] M. Bazzi *et al.* (SIDDHARTA Collaboration), Phys. Lett. B **704**, 113 (2011).
[8] C. J. Batty, E. Friedman, and A. Gal, Phys. Rept. **287**, 385 (1997).
[9] E. Friedman and A. Gal, Phys. Rept. **452**, 89 (2007).
[10] A. Cieplý and J. Smejkal, Nucl. Phys. A **881**, 115 (2012).
[11] Z. H. Guo and J. A. Oller, Phys. Rev. C **87**, 035202 (2013).
[12] M. Mai and U.-G. Meißner, Nucl. Phys. A **900**, 51 (2013).
[13] A. Cieplý, E. Friedman, A. Gal, D. Gazda, and J. Mareš, Phys. Lett. B **702**, 402 (2011).
[14] A. Cieplý, E. Friedman, A. Gal, D. Gazda, and J. Mareš, Phys. Rev. C **84**, 045206 (2011).
[15] D. Gazda and J. Mareš, Nucl. Phys. A **881**, 159 (2012).
[16] E. Friedman, A. Gal, and C. J. Batty, Phys. Lett. B **308**, 6 (1993).
[17] E. Friedman and A. Gal, Nuc. Phys. A **899**, 60 (2013).
[18] E. Friedman and A. Gal, Nucl. Phys. A **959**, 66 (2017).
[19] T. Sekihara, J. Yamagata-Sekihara, D. Jido, and Y. Kanada-En'yo, Phys. Rev. C **86**, 065205 (2012).
[20] H. Davis, F. Oppenheimer, W. L. Knight, F. R. Stannard, and O. Treutler, Nuovo Cimento **53A**, 313 (1968).
[21] J. W. Moulder, N. E. Garret, L. M. Tucker, W. M. Bugg, G. T. Condo, H. O. Cohn, and R. D. McCulloch, Nucl. Phys. B **35**, 332 (1971).
[22] C. Vander Velde-Wilquet, J. Sacton, J. H. Wickens, D. N. Tovee, and D. H. Davis, Nuovo Cimento **39A**, 538 (1977).
[23] J. Hrtánková and J. Mareš, Phys. Lett. B **770**, 342 (2017).
[24] E. E. Kolomeitsev, N. Kaiser, and W. Weise, Phys. Rev. Lett. **90**, 092501 (2003).
[25] M. M. Sharma, M. A. Nagarajan, and P. Ring, Phys. Lett. B **312**, 377 (1993).
[26] T. Wass, M. Rho, and W. Weise, Nucl. Phys. A **617**, 449 (1997).
[27] T. Waas, N. Kaiser, and W. Weise, Phys. Lett. B **379**, 34 (1996); **365**, 12 (1996).
[28] J. Mareš, E. Friedman, and A. Gal, Phys. Lett. B **606**, 295 (2005).
[29] E. Friedman, A. Gal, and J. Mareš, Nucl. Phys. A **761**, 283 (2005).
[30] T. Sekihara, D. Jido, and Y. Kanada-En'yo, Phys. Rev. C **79**, 062201(R) (2009).